Generation and Application of Squeezed States of Light in Quantum Sensing

Nielsen, Jens Arnbak Holbøll

Publication date:
2021

Document Version
Publisher's PDF, also known as Version of record

Technical University of Denmark

Department of Physics

PhD Thesis

Generation and Application of Squeezed States of Light in Quantum Sensing

Author
Jens Arnbak Holbøll Nielsen

Supervisor
Professor Ulrik Lund Andersen
Associate Professor Tobias Gehring
Senior Researcher Jonas Schou Neergaard-Nielsen

November, 2021

A thesis submitted in partial fulfilment of the requirements for the degree of Doctor of Philosophy at the Technical University of Denmark.

Title: Generation and Application of Squeezed States of Light in Quantum Sensing.
Author: Jens Arnbak Holbøll Nielsen.
Supervisors:
Professor Ulrik Lund Andersen
Associate Professor Tobias Gehring
Senior Researcher Jonas Schou Neergaard-Nielsen
Period: April 2018 - November 2021.

Center for Macroscopic Quantum States, BigQ.
DTU Physics
Technical University of Denmark
Fysikvej 307, 2800 Lyngby, Denmark

Abstract

Quantum technology has seen a surge in attention throughout the 21st century in part due to the promise of superior performance in many fields of science and technology compared to classical counterparts. One of the areas that show much potential is the field of quantum metrology, where systems exploiting quantum mechanical principles can overcome the limitations of classical metrology systems and reach extreme levels of precision enabling the exploration of domains previously unavailable.

A subfield of quantum metrology is quantum phase estimation, where a system is probed by an optical field and information about said system is extracted by subsequent estimation of the optical phase. Classical phase estimation systems are limited by the quantum mechanical nature of light, leading to a measurement sensitivity which scales as $\sim 1/\sqrt{N}$, where N is the number of photons in the optical field. Using quantum entangled states like the famous NOON states, allows for theoretical performance beyond this classical limit with sensitivities scaling as $\sim 1/N$. Entangled states are, however, very difficult to generate and extremely fragile making them quite impractical in a real world implementation.

In this thesis, I will be working with quantum mechanical states of light called squeezed states. The thesis will go into great detail of the theoretical and practical aspects of squeezed light, explaining how optical loss and phase noise in the squeezed quadrature measurement are the two main limitations to generating high degrees of squeezed light. The thesis will cover the construction of a small footprint squeezed light source and the initial attempt at building an extremely high performing squeezed light source.

The main results of the thesis come in the form of two phase estimation experiments. In the first experiment, squeezed vacuum states of light are shown both theoretically and experimentally to not only break the classical limit, but also give better performance than the before mentioned NOON states. An important figure of merit for phase estimation experiments is the Fisher Information per photon, and in our experiment we reach $15.8(6)\,\mathrm{rad}^{-2}$, which to the best of our knowledge is higher than has ever been measured in other phase estimation systems. Finally, as an extension of the estimation protocol, the squeezed vacuum states of light are also used to sense a small 3 kHz sine wave phase modulation.

The second experiment implements a variational quantum algorithm to optimize a general squeezed state probe for phase estimation in noisy, practical systems. The preliminary results presented in this thesis seem to suggest that the addition of displacement in the case of thermal noise could lead to better performance, but certain problems in the algorithm together with phase instability of the experiment, means that the performance of the system will have to be improved, before this hypothesis can be fully tested.

Dansk resumé

Kvanteteknologi har oplevet en stigning i opmærksomhed gennem det 21. århundrede, delvist som følge af løftet om overlegen ydeevne sammenlignet med klassiske modparter inden for mange videnskabs- og teknologiområder. Et af de områder der viser stort potentiale er kvantemetrologi, hvor systemer der udnytter kvantemekaniske principper kan overvinde klassiske metrologisystemers begrænsninger og opnå ekstreme præcisionsniveauer, der muliggør udforskning af domæner, der tidligere ikke har været tilgængelige.

Et underfelt af kvantemetrologi er kvantefaseestimering, hvor et system sonderes af et optisk felt, og information om systemet udvindes ved efterfølgende estimering af den optiske fase. Klassiske faseestimeringssystemer er begrænset af lysets kvantemekaniske natur, hvilket fører til en måleføl somhed, som skaleres som $\sim 1/\sqrt{N}$, hvor N er antallet af fotoner i det optiske felt. Ved at bruge kvantesammenfiltrede tilstande, som de berømte NOON-tilstande, giver det mulighed for en teoretisk ydeevne ud over klassiske grænse med en måleføl somhed der skalerer som $\sim 1/N$. Sammenfiltrede tilstande er imidlertid meget vanskelige at generere og ekstremt skrøbelige, hvilket gør dem meget upraktiske i virkeligt implementeringer.

I denne afhandling vil jeg arbejde med kvantemekaniske lystilstande kaldet klemte-lystilstande. Afhandlingen vil gå i detaljer med de teoretiske og praktiske aspekter af klemt-lys, og forklare, hvordan optisk tab og fasestøj i målingen af den klemte kvadratur er de to vigtigste begrænsninger af genereringen af høje grader af klemt lys. Afhandlingen vil dække konstruktionen af en lille klemt-lyskilde og det indledende forsøg på at bygge en ekstremt højtydende klemt-lyskilde.

Hovedresultaterne af afhandlingen kommer i form af to faseestimeringseksperimenter. I det første eksperiment er klemte vakuumtilstande af lys vist, både teoretisk og eksperimentelt, ikke kun at bryde den klassiske grænse, men også give bedre ydeevne end de før nævnte NOON-tilstande. Et vigtigt nøgletal inden for faseestimeringseksperimenter er Fisher Information per foton, og i vores experiment når vi $15.8(6)\,\mathrm{rad}^{-2}$, hvilket til det bedste af vores viden er højere, end hvad der nogensinde ellers er blevet målt i andre faseestimeringssystemer. Til sidst blev de klemte vakuumtilstande, i forlængelse af faseestimeringsprotokollen, også brugt til at måle en lille 3 kHz sinusbølge fasemodulation.

Det andet eksperiment implementerer en variationskvantealgoritme for at optimere en generel klemt-lyssonde til faseestimering i støjende, praktiske systemer. De foreløbige resultater præsenteret i denne afhandling synes at antyde, at tilføjelse af forskydning i tilfælde af termisk støj kunne føre til bedre ydeevne, men visse problemer i algoritmen sammen med faseustabilitet af eksperimentet betyder, at ydeevnen af systemet skal forbedres, før denne hypotese kan testes fuldt ud.

Acknowledgement

Having now finished my PhD over a three and a half year period in the Quantum Physics and Information Technology (QPIT) group at the physics institute of the Technical University of Denmark (DTU), I can confidently say that I have no regrets of applying for the position back in the winter of 2018, when I was finishing my Master's degree. In fact, I am very grateful to Professor Ulrik Lund Andersen for giving me the opportunity to do a PhD in his group and for assuming the role of my main supervisor. I am thankful for the supervision, I have received from Ulrik and would like to thank him for placing a great deal of trust in me and my decisions throughout the project. I would also like to thank my co-supervisors Tobias Gehring and Jonas Schou Neergaard-Nielsen. Tobias, who is in charge of the CVLAB, was in charge of my day-to-day supervision. Tobias always made time to help me in the lab, when I stumbled upon a problem, I could not solve, and I have learned a great deal about electronics and experimental techniques from him. Jonas, who is in charge of the CATLAB next door from us, is a great source of knowledge, and I am very grateful to him for always having time for me to stop by his office for stupid questions and theoretical discussions. I would also like to thank Tine Hougaard Klitmøller, the group "Mom", without whom nothing would function.

The QPIT group has grown to be a big and culturally diverse group over the period of my PhD. I would like to thank all my colleagues at QPIT for contributing to making this group a comfortable place of work (despite a certain pandemic being thrown in to the mix half way through). Firstly, I would like to thank Christian for showing me the ropes and helping me get to know the lab, when I first started. I did all of my experimental work in the CVLAB, and I would like to thank my lab mates Casper, Iyad, Rayssa, Renato for their contribution in making the CVLAB the greatest (and cleanest !) lab in all of QPIT. Rayssa and I worked together during the first year of my thesis, and she deserves special thanks for being a joy to work together with and for working hard in helping me assemble a certain infamous OPO. Both Casper and Rayssa I would also like to thank for being great friends and also for having dedicated a lot of time to give me detailed feedback on my thesis. I am also thankful to Tummas, who worked hard in getting the VQA code ready for me to get some results of that experiment in time.

Besides my lab colleagues, I would like to extend a special thanks to some of my colleagues and friends in the neighbouring lab CATLAB. I would like to thank Mikkel and Shuro for being great friends and for always having time to listen to me complaining, when something was not working in the lab. To Shuro: 日本語の練習を手伝ってくれたのは本当にありがとうございました！ (translated: thank you very much for helping me practice my Japanese!) .

In the winter of 2020 I had the privilege of being able to visit the LIGO group at the Kavli institute of the Massachusetts Institute of Technology (MIT) in Boston, US, and I would like to thank professor Nergis Mavalvala for agreeing to host me. I would in general like to thank everyone at the MIT LIGO group for making me feel welcome during my stay, but special thanks must be extended to Álvaro Fernández Galiana for allowing me to share his office during my stay and for being an extremely kind and helpful colleague and friend and Lee McCuller for teaching me a lot about control systems and for great theoretical discussions.

I would like to extend a heartfelt thanks to my wife and the love of my life Majken. Majken has supported me through thick and thin, sun and rain and ups and downs and has been very understanding during these last couple of months, where I have had to basically confine myself to either the office or the lab in order to finish this thesis. Finally, I would like to thank my family and friends for having my back throughout the entire process.

Contents

List of Figures

List of Tables

The more important fundamental laws and facts of physical science have all been discovered, and these are now so firmly established that the possibility of their ever being supplanted in consequence of new discoveries is exceedingly remote.

Light Waves and Their Uses
by Albert A. Michelson, 1903

1 Introduction

At the end of the 19th century the general consensus among physicists was that most if not all aspects of the world had been discovered and understood. However, certain experimental observations such as black body radiation, the photoelectric effect and the emission lines of the hydrogen atom could not be explained theoretically in the frame work of classical thermodynamic and electrodynamic theory.

Max Planck solved the first problem in 1900 [1] by introducing the idea that vibrations of atoms were quantized and would therefore emit light with quantized energy. Albert Einstein built upon this theory by postulating that the electromagnetic wave itself was quantized and used this to explain the photoelectric effect in 1905 [2], and Niels Bohr explained the hydrogen emission spectrum with his atomic model using quantized electron orbits in 1913 [3]. These, together with other examples where quantization had to be introduced heuristically to make theory fit experimental observations, are coined the "old quantum mechanics", even though they never formed a cohesive theory.

In 1923 Louis de Broglie lay the foundation for modern quantum mechanics with his matter wave theory [4], which was continued by Werner Heisenberg (together with Born and Jordan) in 1925 [5] and Erwin Schrödinger in 1926 [6], who independently of each other developed the theories (pictures) of quantum mechanics that we still use today. Wolfgang Pauli, Paul Dirac, Niels Bohr, Albert Einstein, John Von Neumann and many others also contributed to the theory of quantum mechanics, which has proved to be one of the most successful theories ever developed.

With the formulation of the theory of quantum mechanics came also a surge in technological development, which has been coined the first quantum revolution [7]. This technology, also coined "quantum 1.0 technology", includes lasers, transistors, atomics clocks and semiconductors, all of which has been instrumental in propelling us into and through the information age.

As information technology continued to develop, seemingly according to Moore's law [8], a rising concern developed that information would be encoded into smaller and smaller physical systems, where the laws of physics stop obeying classical mechanics and start behaving according to quantum mechanics. Several people started building on the ideas of Rolf Landaur [9] and Charles Bennett [10] of building a computer based on the principles of quantum mechanics. In 1982, Richard Feynman [11] famously created an abstract model to show, how a quantum mechanical system could do computations similar to classical computer and also argued that a quantum computer could simulate nature much more efficiently than any classical computer [12].

David Deutsch formalised the universal quantum computer compatible with the Church-

Turing principle in 1985 [13] and built on the framework of Feynman to create, what is know as the circuit model of quantum computation [14].

Throughout the early 1990s several prominent quantum algorithms were developed that promised to outperform their classical counterparts. The most celebrated being Shor's algorithm of factoring in 1994 [15]. This accelerated the interest in quantum computation, and since the 2000s the field of quantum information has exploded in size. Today we are in the middle of a "second quantum revolution". Whereas the first quantum revolution was about understanding and probing the quantum realm, this second revolution revolves around the manipulation and control of quantum systems. Controlling quantum systems, however, is very difficult, and our current technology level is defined by noisy operations and measurements on quantum system of limited circuit size (10-60 qubits) and of limited quality. This technology regime was dubbed "Noisy-Intermediate-Scale-Quantum" (NISQ) technology by John Preskill in 2018 [16], and while most researchers agree that we will not have a universal quantum computer for many years to come, the hope is that NISQ technology will be able to outperform classical computers in certain tasks. This goal might have been reached already with a quantum supremacy claim from Google in 2019 [17] and three claims from Jian-Wei Pans research group at the University of Science and Technology of China, one in 2020 [18] and two in 2021 [19, 20].

In the extensive toolbox of quantum technology we find quantum metrology - the science of precision measurements. Quantum metrology was in part developed due to precision measurements playing a central role in quantum information science (and quantum science in general) [7], but has also come into its own, in part due to the potential advantages it promises in various fields of science such as biology and medical sciences [21]. As implied by the name, quantum metrology employs the principles of quantum mechanics such as superposition, entanglement etc. to overcome the limitations that quantum mechanics itself imposes on classical measurement techniques.

Important platforms in quantum metrology are quantum optical systems, where a system under test is probed by a light field (usually in the form of a laser beam), and from the measurement of the light field information of the system can be extracted. Quantum interferometry (also known as quantum phase estimation/sensing) is a central field of optical quantum metrology [22], and here the sample is probed by one arm of an optical interferometer, and the parameter in focus is encoded into the phase of the light. The phase is measured at the output of the interferometer, and from this measurement the target parameter is extracted. Quantum interferometry has seen tremendous success in the improvement of gravitational wave measurements in LIGO [23–25] and GEO600 [26] gravitational wave observatories.

The main focus of this thesis will be a certain type of continuous variable, quantum state of light called squeezed light, and how this quantum state can be used in quantum phase estimation applications. The thesis will go into great detail with the theoretical and practical generation, control and measurement of squeezed states of light. The thesis will cover the design and construction of two squeezed light sources; one with a small footprint and one designed to be extremely high performing. The main results of the thesis covers two phase estimation experiments using squeezed states of light. The first will experimentally investigate the optimal Gaussian quantum state for phase estimation in ideal systems with low noise, and the second will investigate the optimal Gaussian quantum state in a more practical setting of systems with excess noise.

1.0.1 Structure of the thesis

The thesis is structured in the following way:

- Chapter (2) introduces the basic theory and concepts of quantum optics. This includes an introduction to the quantized electromagnetic field, a description of the quantum states of light used in this thesis, and how the most common optical components of our laboratories transform these quantum states of light.
- Chapter (3) goes into detail with the generation of squeezed light in an optical parametric oscillator, and how squeezed light is measured in a homodyne detector. This chapter will also deal with the most common sources of imperfections and noise and how these affect the detection of squeezed light.
- Chapter (4) introduces the theory behind the feedback techniques used in the experiments and the technique used to characterize and optimize these systems.
- Chapter (5) describes an experiment that was published in optics express in 2019 under the title " Compact, low-threshold squeezed light source ", where we built a small footprint, high performance squeezed light source. This chapter will introduce the experimental setup, go through the necessary design considerations when building a squeezed light source and finally include the paper in its entirety.
- Chapter (6) describes, what was for a long time the main project of my thesis. This project centers on the design and construction of an optical parametric oscillator designed to produce high degrees of squeezed light. This chapter describes the noise and loss budgets that went into the design and the geometric design of the cavity. Finally, this chapters describes the initial tests of the source and the problems that caused us to have to pivot to other experiments.
- Chapter (7) describes the a phase estimation and sensing experiment using squeezed states of light that resulted in a paper, titled "Deterministic quantum phase estimation beyond the ideal NOON state limit", which was submitted to arXiv shortly before finalizing this thesis. This chapter includes the supplementary material introducing the basic theory of quantum metrology, the experimental setup and the estimation protocol. The chapter ends with including the manuscript in its entirety.
- Chapter (8) describes an experimental realization of a variational quantum algorithm assisted phase estimation protocol using squeezed light. The chapter introduces variational quantum algorithms and describes the experiment and the implemented algorithm. The chapter ends with a presentation of the initial results of the experiment and an outlook.
- Chapter (9) will conclude on the thesis and give an outlook on the experiments.

The aim of science is to make difficult things understandable in a simpler way; the aim of poetry is to state simple things in an incomprehensible way. The two are incompatible.

Paul Dirac
Dirac: A Scientific Biography
by Helge Kragh, 1990

2

Introduction to quantum optics

In this chapter, I will give a brief overview of the basic theory of quantum optics relevant to this thesis. I will very briefly go through the quantum mechanical theory of the electromagnetic field and then make a brief overview of important Gaussian quantum states of light. I will then move on to describe how important optical components that will be used many times throughout the thesis interact with an optical field. Throughout this chapter, I will use theory from common laser and quantum optics books such as Milonni and Eberly [27], Gerry and Knight [28], and Bachor and Ralph [29]. I will also make references to previous PhD theses such as the theses of my supervisors Tobias Gehring [30] and Jonas Schou Neergaard-Nielsen [31].

2.1 The electromagnetic field

The quantization of the classical electromagnetic field is a stable of just about every quantum optics thesis. In this thesis, this will be left as an exercise to the reader, and we shall skip directly to the generalized quantum mechanical multimode electromagnetic wave operator [28]

$$\hat{\mathbf{E}}(r,z,t)=\sum_{i=1}^{N}\mathcal{E}_i(r,z)\left\{\hat{\mathbf{a}}_i^{\dagger}(t)e^{-i(k_iz+\Omega_it+\phi_i)}+\hat{\mathbf{a}}_i(t)e^{i(k_iz+\Omega_it+\phi_i)}\right\}, \tag{2.1}$$

where ϕ_i is the phase, $k_i=2\pi n_i/\lambda_i$ is the spatial angular frequency with n_i being the refractive index, and $\Omega_i=2\pi\nu_i$ is the temporal angular frequency of the i_{th} mode. The wavelength (λ) and the frequency (ν) are connected by the velocity of light in vacuum (c) via $\lambda\nu=c$.

$\mathcal{E}_i(r,z)=\hat{\mathbf{e}}A_i(r,z)\sqrt{\hbar\Omega_i/2\epsilon_0V}$ with $\hbar=h/2\pi$ being the reduced Planck's constant, ϵ_0 is the vacuum permittivity and V is a quantization volume. $\hat{\mathbf{e}}$ is the polarization unit vector, and $A_i(z,r)$ is a spatial field distribution function ($A_i=1$ for plane waves and more complicated for Gaussian beam shapes [27]).

Finally, $\hat{\mathbf{a}}_i$ and $\hat{\mathbf{a}}_i^{\dagger}$ are annihilation and creation operators of the quantum mechanical harmonic oscillators that describe the excitation of each field mode. These operators obey the commutator relation

$$\left[\hat{\mathbf{a}}_i,\hat{\mathbf{a}}_j^{\dagger}\right]=\delta_{ij}, \tag{2.2}$$

where δ is the Kronecker delta function. We can also define canonical position and momentum

quadrature operators in the time domain

$$\hat{\mathbf{X}}(t) \equiv \Big(\hat{\mathbf{a}}^\dagger(t) + \hat{\mathbf{a}}(t)\Big), \tag{2.3a}$$

$$\hat{\mathbf{P}}(t) \equiv i\Big(\hat{\mathbf{a}}^\dagger(t) - \hat{\mathbf{a}}(t)\Big), \tag{2.3b}$$

and in the frequency domain via a Fourier transform of the field operators

$$\widetilde{\mathbf{X}}(\omega) \equiv \Big(\widetilde{\mathbf{a}}^\dagger(-\omega) + \widetilde{\mathbf{a}}(\omega)\Big), \tag{2.4a}$$

$$\widetilde{\mathbf{P}}(\omega) \equiv i\Big(\widetilde{\mathbf{a}}^\dagger(-\omega) - \widetilde{\mathbf{a}}(\omega)\Big). \tag{2.4b}$$

Following the definition of the electrical field as written in equation (2.1), these operators can be interpreted as describing excitations of the electrical field component ($\hat{\mathbf{E}} \propto \hat{\mathbf{X}}$) and the magnetic field component ($\hat{\mathbf{B}} \perp \hat{\mathbf{E}} \propto \hat{\mathbf{P}}$) of the electromagnetic field. Since the quadrature operators do not commute, they have to obey the Heisenberg uncertainty relation [32]. The definition of the operators equations (2.3a) and (2.3b) ensure that the associated Heisenberg uncertainty relation is unity

$$\sigma_X^2 \sigma_P^2 \geq \frac{1}{4}\left|\left\langle\left[\hat{\mathbf{X}}, \hat{\mathbf{P}}\right]\right\rangle\right|^2 = 1. \tag{2.5}$$

This definition of the operators corresponds to setting $\hbar = 2$ in the standard quantum mechanical position-momentum commutator, simplifying future calculations.

The eigenstates of these operators span the continuous variable phase space, and the free evolution of the optical field mode $\propto \exp(-i\omega t)$ will cause a rotation around the origin of the phase space. As an extension of this, we can write up the generalized (rotated) quadrature operators.

$$\hat{\mathbf{X}}(\theta) \equiv \left(\hat{\mathbf{a}}^\dagger e^{i\theta} + \hat{\mathbf{a}} e^{-i\theta}\right) \tag{2.6}$$

$$\hat{\mathbf{P}}(\theta) \equiv i\Big(\hat{\mathbf{a}}^\dagger e^{i\theta} - \hat{\mathbf{a}} e^{-i\theta}\Big). \tag{2.7}$$

The phase space will be used to visualize quantum states later in the next section.

Finally we can write up the energy of the electromagnetic field defined in equation (2.1) via the Hamilton operator

$$\hat{\mathbf{H}} = \sum_{i=1}^{N} \hbar\Omega_i \left(\hat{\mathbf{a}}_i^\dagger \hat{\mathbf{a}}_i + \frac{1}{2}\right) = \sum_{i=1}^{N} \hbar\Omega_i \left(\hat{\mathbf{n}}_i + \frac{1}{2}\right), \tag{2.8}$$

where we have defined the photon number operator $\hat{\mathbf{n}} = \hat{\mathbf{a}}^\dagger \hat{\mathbf{a}}$.

2.2 Gaussian quantum states

In this section, I will describe Gaussian states in general as well as highlight the most relevant ones for this thesis. In order to define Gaussian states, I will briefly have to introduce the concepts of the density operator and the Wigner function. For the analysis below, I will limit myself to one optical mode to keep things simple, but this formalism can without much difficulty be generalized to multimode states.

2.2.1 The density operator and Wigner function

A quantum state is described by its state vector $|x\rangle$ in a given basis, and many different bases can be used to describe quantum states, e.g. the energy eigenstate basis (Fock basis) $|\psi\rangle$

$$\hat{\mathbf{H}}\,|n\rangle = E_n\,|n\rangle\,, \tag{2.9}$$

where $\langle n|m\rangle = \delta_{nm}$, and E_n is the eigenenergy of the state $|n\rangle$.

In general, a quantum state can be described by a state vector, only if the state is pure. For statistical mixtures, such as thermal states, one needs to represent the state via other means, and a convenient way of doing this is by using the density operator $\hat{\rho}$

$$\hat{\rho} = \sum_{n=0}^{N} p_n\,|n\rangle\,\langle n|\,, \tag{2.10}$$

where the summation is over all possible energy eigenstates, and p_n is an associated probability of finding the system in the corresponding state $\hat{\rho}\,|n\rangle = p_n\,|n\rangle$.

The density operator is Hermitian $\hat{\rho}^\dagger = \hat{\rho}$, positive semi-definite $\hat{\rho} \geq 0$, and trace-preserving $\mathrm{tr}(\hat{\rho}) = 1$. Finally, there are two very convenient uses of the density operator; firstly, the expectation value of an arbitrary operator is given by $\left\langle \hat{\mathbf{A}} \right\rangle = \mathrm{tr}\left(\hat{\rho}\hat{\mathbf{A}}\right)$, and secondly, the purity of a quantum state can be determined by $\mathrm{tr}\left(\hat{\rho}^2\right) \leq 1$, where it is only 1 for a pure state.

Through the density operator, a quantum state can be visualized via the Wigner function, a quasi-probability distribution, in the phase space. The Wigner function is defined as [31]

$$W(X,P) \equiv \frac{1}{4\pi}\int e^{iPx/2}\left\langle X+\frac{x}{2}\middle|\hat{\rho}\middle|X+\frac{x}{2}\right\rangle \mathrm{d}x\,, \tag{2.11}$$

where $\hat{\mathbf{X}}\,|X\rangle = X\,|X\rangle$, with $|X\rangle$ being an eigenstate of the quadrature operator. The Wigner function is a semi-probability distribution, as it can have negative values for certain non-Gaussian quantum states. For all the states of this thesis however, the Wigner function will be positive and can serve as a probability of finding the quantum state with a given position in the phase space. With the Wigner function available, we can define Gaussian quantum states, as states that have Gaussian Wigner functions. Gaussian Wigner functions are fully defined by the first (expectation value) and second (covariance matrix) statistical moments, with the covariance matrix given by

$$\underline{\underline{\Gamma}} = \begin{pmatrix} \left\langle \hat{\mathbf{X}}^2 \right\rangle - \left\langle \hat{\mathbf{X}} \right\rangle^2 & \left\langle \hat{\mathbf{X}}\hat{\mathbf{P}} \right\rangle - \left\langle \hat{\mathbf{X}} \right\rangle \left\langle \hat{\mathbf{P}} \right\rangle \\ \left\langle \hat{\mathbf{X}}\hat{\mathbf{P}} \right\rangle - \left\langle \hat{\mathbf{X}} \right\rangle \left\langle \hat{\mathbf{P}} \right\rangle & \left\langle \hat{\mathbf{P}}^2 \right\rangle - \left\langle \hat{\mathbf{P}} \right\rangle^2 \end{pmatrix}, \tag{2.12}$$

and by using this and the expectation value, the Wigner function of a Gaussian state can be written as [30]

$$W(\vec{X}) = \frac{1}{2\pi\sqrt{\det(\Gamma)}} e^{-\frac{1}{2}(\vec{X}-\langle\vec{X}\rangle)^T\Gamma^{-1}(\vec{X}-\langle\vec{X}\rangle)}, \tag{2.13}$$

$$\vec{X} = \begin{pmatrix} X \\ P \end{pmatrix}. \tag{2.14}$$

2.2.2 The coherent state

The first Gaussian state I will introduce, is the coherent state $|\alpha\rangle$. This state is very useful, as it is the state generated by an ideal laser. The coherent state is an eigenstate of the annihilation operator $\hat{\mathbf{a}}|\alpha\rangle = \alpha|\alpha\rangle$ and forms an "overcomplete" basis, meaning two basis states are not orthonormal $\langle\beta|\alpha\rangle = \exp\left(-\left|\beta^2 - \alpha^2\right|\right)$.

The eigenvalue α of the operator is related to the photon expectation value $\langle\alpha|\hat{\mathbf{n}}|\alpha\rangle = \langle\alpha|\hat{\mathbf{a}}^\dagger\hat{\mathbf{a}}|\alpha\rangle = |\alpha|^2$. This relation is even clearer when calculating the photon probability distribution by projecting the coherent state onto the Fock state basis

$$P(n) = |\langle n|\alpha\rangle|^2 = e^{-2|\alpha|}\frac{|\alpha|^{2n}}{n!}, \tag{2.15}$$

which is a Poisson distribution with expectation value and variance $|\alpha|^2$. For sufficiently large α the Poisson distribution is known to be well approximated by a Gaussian distribution. In figure (2.1a) 10^6 samples of a coherent state photon distribution are shown(For this figure the mean photon number is 10000). The figure also shows the corresponding Gaussian approximation.

In terms of the quadrature operators the expectation values are $\left\langle\hat{\mathbf{X}}\right\rangle = \mathrm{Re}\{\alpha\}$ and $\left\langle\hat{\mathbf{P}}\right\rangle = \mathrm{Im}\{\alpha\}$, and the covariance matrix is the identity matrix $\underline{\underline{\Gamma}} = \underline{\underline{\mathcal{I}}}$, which means the coherent state is a minimum uncertainty state. The Wigner function equation (2.13) of a coherent state with $\alpha = 50$ is shown in figure (2.1b).

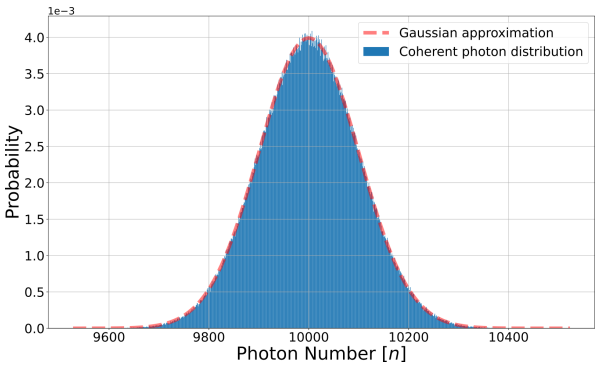

(a) Coherent state photon distribution with $\langle\hat{\mathbf{n}}\rangle = 10000$. The red outline is the corresponding Gaussian approximation.

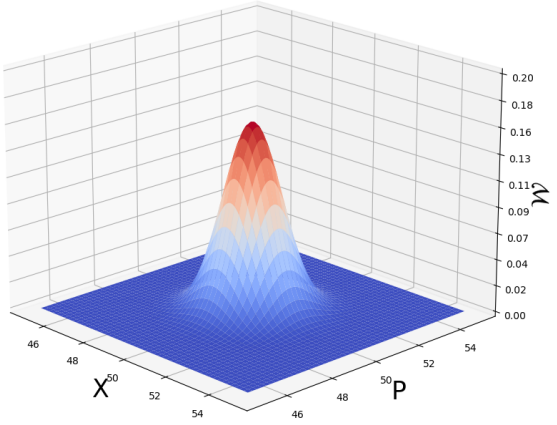

(b) Wigner function of a coherent state with displacement $\alpha = 50$.

Figure 2.1

A very important point to note about this visualization method is that there exists a plot similar to figure (2.1b) for each sideband frequency in the frequency domain, and the displacement from origin at a given sideband frequency is determined by number of photons at the given frequency and not by the carrier amplitude at DC (in the rotating frame of the carrier). When more modes at different sideband frequencies are relevant, it can be helpful to go to the so-called "sideband picture" by extending the phase space into a third dimension as shown in figure (2.2).

Finally, a very important coherent state is the vacuum state $|\alpha = 0\rangle$. This state has zero mean $\alpha = 0$, but since the variance of the coherent state is independent of the photon occupation, the vacuum state will still exhibit an uncertainty in photon number- and quadrature-operators.

This uncertainty is referred to as vacuum fluctuations or shot noise. The coherent state is created mathematically from the vacuum state via a displacement operation $|\alpha\rangle = \hat{\mathbf{D}}(\alpha)\,|0\rangle$, where the displacement operator is defined as

$$\hat{\mathbf{D}}(\alpha) = \exp\Big(\alpha\hat{\mathbf{a}}^\dagger + \alpha^*\hat{\mathbf{a}}\Big). \tag{2.16}$$

In practice, as mentioned before, the coherent state is generated in the linear gain process of a laser, but will only be a coherent state above a certain sideband frequency. Below this frequency the laser will have excess technical noise from the laser process and electronics.

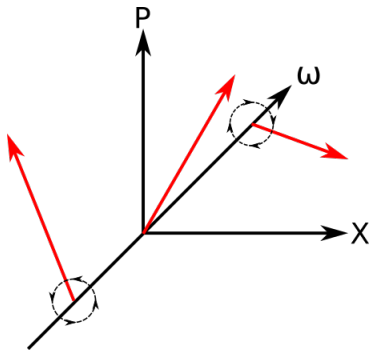

Figure 2.2: Example of the sideband picture representation. Here the uncertainty circles have been neglected for simplicity. The dotted circles note the direction of revolution of the sideband modes in the rotating frame of the DC carrier.

2.2.3 The thermal state

The second Gaussian state is the thermal state, which is the optical state produced by a perfect black body. This state is a statistical mixture of photons with no coherence and cannot be written as a quantum mechanical state vector. In stead it is described via the density matrix as [31]

$$\hat{\rho}_{th} = \frac{1}{n_{th}+1}\sum_{n=0}^{\infty}\left(\frac{n_{th}}{n_{th}+1}\right)^n |n\rangle\langle n|\,, \tag{2.17}$$

where n_{th} is the mean photon occupation. The thermal state hos no displacement in phase space $\langle X\rangle = \langle P\rangle = 0$, but has covariance matrix

$$\Gamma_{th} = \begin{pmatrix} 2n_{th}+1 & 0 \\ 0 & 2n_{th}+1 \end{pmatrix}, \tag{2.18}$$

meaning it has noise greater than shot noise and symmetric in the quadratures.

2.2.4 The squeezed state

The last Gaussian state to be introduced is the squeezed state $|\xi\rangle = \hat{\mathbf{S}}(\xi))\,|0\rangle$, where $\xi = re^{i\phi}$ is a complex squeezing parameter with r being the squeezing strength and ϕ being a phase determining the orientation of the squeezed state in phase space. Squeezed states are generated from the vacuum state by the squeezing operator

$$\hat{\mathbf{S}}(\xi) = \exp\Big(1/2(\xi^*\hat{\mathbf{a}}^2 - \xi\hat{\mathbf{a}}^{\dagger 2})\Big). \tag{2.19}$$

As suggested by the form of the squeezing operator, squeezed vacuum states can only be generated by non-linear processes that are at minimum quadratic in the field operators, and the practical generation of these states of light will be described in detail in chapter (3).

If we project the squeezed state onto the photon basis

$$\langle n|\xi\rangle\,|n\rangle = \frac{1}{\sqrt{\cosh(r)}}\frac{\sqrt{n!}}{(n/2)!}\left(\frac{e^{i\phi}\tanh(r)}{2}\right)^{n/2}|2n\rangle\,, \tag{2.20}$$

we see that the squeezed state contains only even photon number components. $|\langle n|\xi\rangle|^2$ is visualized in figure (2.3a) for a squeezing strength $r = 0.68$.

It is also possible to create a displaced squeezed state by applying the displacement operator in addition to the squeezing operator $|\alpha,\xi\rangle = \hat{\mathbf{D}}(\alpha)\hat{\mathbf{S}}(\xi)\,|0\rangle$.

Looking at the quadrature operators, in the case of a squeezed vacuum state the expectation value of the quadrature operator is zero $\left\langle\hat{\mathbf{X}}\right\rangle = \left\langle\hat{\mathbf{P}}\right\rangle = 0$. In the case of a displaced squeezed state, the expectation value is the same as with the coherent state. More interestingly, the covariance matrix of a pure squeezed vacuum state has the following form

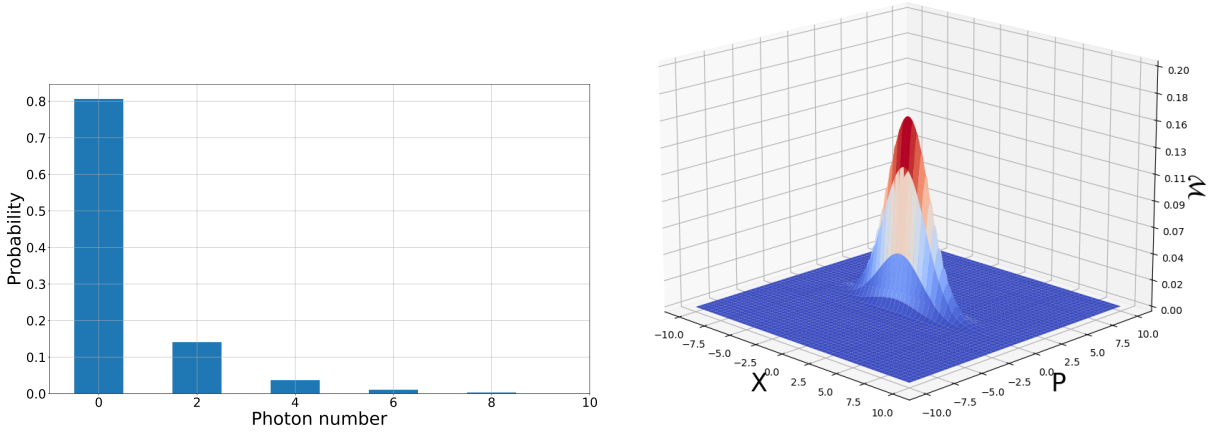

(a) Squeezed state photon distribution for $r = 0.68$.

(b) Wigner function of a squeezed vacuum state with $r = 0.68$ and $\phi = 0$

Figure 2.3

$$\underline{\underline{\Gamma}} = \hat{\mathbf{R}}(\phi/2)^{\dagger}\begin{pmatrix} e^{2r} & 0 \\ 0 & e^{-2r}\end{pmatrix}\hat{\mathbf{R}}(\phi/2), \tag{2.21}$$

where $\hat{\mathbf{R}}(\phi/2)$ is a rotation operator

$$\hat{\mathbf{R}}(\phi) = \begin{pmatrix} \cos(\phi) & \sin(\phi) \\ -\sin(\phi) & \cos(\phi)\end{pmatrix}, \tag{2.22}$$

where the phase angle ϕ is the angle of the squeezing operator defined above.

From equation (2.21) we see that the pure squeezed state is also a minimum uncertainty state. Unlike the coherent state, however, the squeezed state has asymmetric variance in the quadrature operators, the variance of one quadrature operator can be reduced compared to the shot noise variance, at the expense of increasing the variance of the complementary operator

since the Heisenberg uncertainty relation must be obeyed. For $r \to 0$, the variance goes back to shot noise, as we would expect. The Wigner function of a pure squeezed state with $r = 0.68$ and $\phi = 0$ is shown as a scatter plot in figure (2.3b).

Losing one photon of a squeezed photon pair leaves the remaining photon in a thermal state [33]. A lossy squeezed state can therefore be modelled as thermal squeezed state, which has a modified covariance matrix of

$$\underline{\underline{\Gamma}}_{th} = (2\langle n \rangle_{th} + 1)\hat{\mathbf{R}}(\phi/2)^{\dagger}\begin{pmatrix} e^{2r_{th}} & 0 \\ 0 & e^{-2r_{th}} \end{pmatrix}\hat{\mathbf{R}}(\phi/2), \tag{2.23}$$

where r_{th} is an effective squeezing parameter, and $\langle \hat{\mathbf{n}} \rangle_{th}$ is the average number of thermal photons in the squeezed state.

2.2.5 Brief comment on the linearization of field operators

Throughout the thesis, I will assume the operators to be linearizable. This means that the operators can be expanded to first order around a "classical" mean value to give us a zero-variance mean value and a zero-mean quantum mechanical fluctuation part

$$\hat{\mathbf{a}} = (\alpha + \delta\hat{\mathbf{a}})e^{-i\phi}, \tag{2.24}$$

where ϕ is a phase that can be time-dependent. The mean value of the operator will then be equal to the classical part $\langle \hat{\mathbf{a}} \rangle = \alpha$, and the variance will be equal to the variance of the fluctuation part $\sigma_a^2 = \langle \hat{\mathbf{a}}^2 \rangle - \langle \hat{\mathbf{a}} \rangle^2 = \langle \delta\hat{\mathbf{a}}^2 \rangle$. Since this version of the operator assumes quantum limited fluctuations, it is useful to cast this operator into a form that also includes the classical (excess) amplitude- and phase-noise. We allow a small time fluctuating part in both the classical phase $\phi \to \phi + \delta\phi$ and the classical mean amplitude $\alpha \to \alpha + \delta\alpha$, and we expand to first order in the fluctuations around the phase ϕ

$$\begin{aligned}(\alpha + \delta\alpha(t) + \delta\hat{\mathbf{a}})e^{-i(\phi+\delta\phi(t))} &\approx (\alpha + \delta\alpha(t) - i\alpha\delta\phi(t) + \delta\hat{\mathbf{a}})e^{-i\phi} \\ &\equiv \left(\alpha + \delta\hat{\tilde{\mathbf{a}}}\right)e^{-i\phi},\end{aligned} \tag{2.25}$$

where we have redefined the operator fluctuation term to also include the classical fluctuations. We see, as we would expect, that the amplitude fluctuations belong to the real part of the fluctuations and the phase fluctuations belong to the imaginary part (but scaled by the carrier amplitude). We drop the tilde and only look at the fluctuation term. From equations (2.3a) and (2.3b), we see that the real and imaginary parts of the field operator are equal to the quadrature operators $\mathrm{Re}\{\hat{\mathbf{a}}\} = 1/2\hat{\mathbf{X}}$ and $\mathrm{Im}\{\hat{\mathbf{a}}\} = 1/2\hat{\mathbf{P}}$ (using our shot noise normalization). If we measure the power spectral density (PSD) of the quadrature operators, we get

$$\mathrm{PSD}\left(\hat{\mathbf{X}}\right) = 4\mathrm{PSD}(\mathrm{Re}\{\delta\hat{\mathbf{a}}\}) = 4|\alpha|^2\mathrm{RIN}, \tag{2.26a}$$

$$\mathrm{PSD}\left(\hat{\mathbf{P}}\right) = 4\mathrm{PSD}(\mathrm{Im}\{\delta\hat{\mathbf{a}}\}) = 4|\alpha|^2\mathrm{PSD}(\delta\phi), \tag{2.26b}$$

where $\mathrm{RIN} = \mathrm{PSD}(|\delta\alpha|^2/|\alpha|^2)$ is the relative intensity noise power spectral density and $\delta\phi$ is the phase noise we introduced above. From equations (2.26a) and (2.26b) we see that measurements of the noise of the quadrature operators give us information about the intensity noise and phase noise of the optical field (both quantum mechanical and classical).

2.3 Important quantum optics components

I will go through the mathematics of how the most important optical components of this thesis interact with light fields. I will begin with covering the simpler optical components such as the beam splitter, the phase shifter and the photodetector, and then end by covering optical modulators and cavities that require a more thorough analysis.

2.3.1 Beam splitters

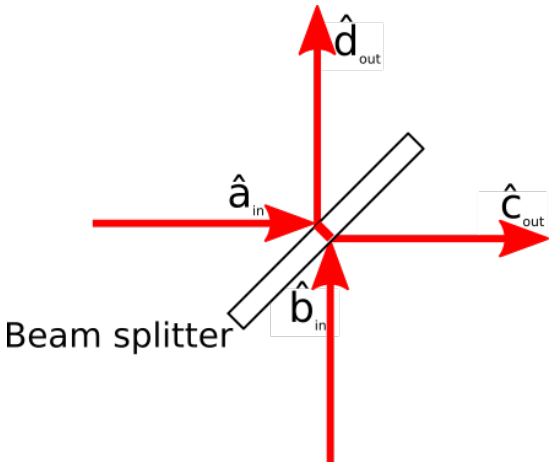

Figure 2.4: Sketch of a beam splitter.

The (power) beam splitter (BS) is a semi-transparent mirror with transmittance $\sqrt{\tau}$ and reflectance $\sqrt{1-\tau}$. The splitter has two input ports and two output ports as shown in figure (2.4). The input and output operators are related by the following input-output relations

$$\begin{pmatrix} \hat{\mathbf{c}}_{out} \\ \hat{\mathbf{d}}_{out} \end{pmatrix} = \begin{pmatrix} \sqrt{\tau} & i\sqrt{1-\tau} \\ i\sqrt{1-\tau} & \sqrt{\tau} \end{pmatrix} \begin{pmatrix} \hat{\mathbf{a}}_{in} \\ \hat{\mathbf{b}}_{in} \end{pmatrix}. \tag{2.27}$$

If the $\hat{\mathbf{b}}$ input is left empty (vacuum is injected), then the model for a beam splitter can be used to model the effect of optical loss on an optical quantum state [29]. The effect on the expectation value, can be directly analysed using equation (2.27), but in the case of analysing the effect on the quantum noise, it is easier to look at how the beam splitter affects the two-mode covariance matrix of the quadrature operators.

$$\underline{\underline{\Gamma}} = \begin{pmatrix} \sigma_{a,X}^2 & 0 & 0 & 0 \\ 0 & \sigma_{a,P}^2 & 0 & 0 \\ 0 & 0 & \sigma_{b,X}^2 & 0 \\ 0 & 0 & 0 & \sigma_{b,P}^2 \end{pmatrix} = \begin{pmatrix} \sigma_{a,X}^2 & 0 & 0 & 0 \\ 0 & \sigma_{a,P}^2 & 0 & 0 \\ 0 & 0 & 1 & 0 \\ 0 & 0 & 0 & 1 \end{pmatrix}. \tag{2.28}$$

Writing the beam splitter input/output matrix in a symplectic form [30]

$$\underline{\underline{S_{BS}}} = \begin{pmatrix} \sqrt{1-\tau} & 0 & 0 & \sqrt{\tau} \\ 0 & \sqrt{1-\tau} & \sqrt{\tau} & 0 \\ 0 & -\sqrt{\tau} & \sqrt{1-\tau} & 0 \\ -\sqrt{\tau} & 0 & 0 & \sqrt{1-\tau} \end{pmatrix}, \tag{2.29}$$

and applying it to the covariance matrix $\underline{\underline{\Gamma'}} = \underline{\underline{S_{BS}}}\,\underline{\underline{\Gamma}}\,\underline{\underline{S_{BS}}}^T$ yields

$$\underline{\underline{\Gamma'}} = \begin{pmatrix} \sigma_{a,X}^2(1-\tau)+\tau & 0 & (1-\sigma_{a,X}^2)\sqrt{(1-\tau)\tau} & 0 \\ 0 & \sigma_{a,P}^2(1-\tau)+\tau & 0 & (1-\sigma_{a,P}^2)\sqrt{(1-\tau)\tau} \\ (1-\sigma_{a,X}^2)\sqrt{(1-\tau)\tau} & 0 & \sigma_{a,X}^2\tau+(1-\tau) & 0 \\ 0 & (1-\sigma_{a,P}^2)\sqrt{(1-\tau)\tau} & 0 & \sigma_{a,P}^2\tau+(1-\tau) \end{pmatrix}. \tag{2.30}$$

This new covariance matrix has the form $\begin{pmatrix} \underline{\underline{A}} & \underline{\underline{C}} \\ \underline{\underline{C}} & \underline{\underline{B}} \end{pmatrix}$. The $\underline{\underline{A}}$ matrix represents the reflected (or lost) mode. We have no way of recovering this and therefore have to trace this mode out. What we are left with is the transmitted mode represented by the $\underline{\underline{B}}$ matrix, which will have the form

$$\tau\begin{pmatrix} \sigma_X^2 & 0 \\ 0 & \sigma_P^2 \end{pmatrix} + (1-\tau)\begin{pmatrix} 1 & 0 \\ 0 & 1 \end{pmatrix}. \tag{2.31}$$

We will be using equation (2.31) later, when we have to analyze the effect of loss on the squeezed state.

2.3.2 Phase shifters

A phase shifter is usually a piezo-electric-transducer that is used to actuate the position of a mirror or slightly stretch a fiber thereby changing the path length of a laser beam slightly. From equation (2.1), we can see that a change in the path length will result in a phase shift of the form $\Delta\phi = k\Delta l + \arctan(\Delta l/(z_R))$, where the second term comes from the Gouy phase shift of a Gaussian beam with $z_R = \pi\omega^2 n/\lambda$ being the Rayleigh length. The result of inducing such a phase shift is a rotation of the quadrature operators similar to equations (2.6) and (2.7)

$$\begin{pmatrix} \hat{\mathbf{X}}(\Delta\phi) \\ \hat{\mathbf{P}}(\Delta\phi) \end{pmatrix} = \begin{pmatrix} \cos(\Delta\phi) & \sin(\Delta\phi) \\ -\sin(\Delta\phi) & \cos(\Delta\phi) \end{pmatrix}\begin{pmatrix} \hat{\mathbf{X}} \\ \hat{\mathbf{P}} \end{pmatrix}. \tag{2.32}$$

2.3.3 Photodetectors

The photodetector is an electrical device containing a photo-diode, which is a semiconductor that converts a stream of photons into a current by absorbing a photon and promoting an electron from the valence band to the conduction band [34]. This current is the electronic charge e^- multiplied by the number operator of electrons excited into the conduction band $\hat{\mathbf{n}}_e(t)$ and divided by the detection time interval Δt

$$\hat{\mathbf{i}}(t) = \frac{\hat{\mathbf{n}}_e(t)\mathrm{e}^-}{\Delta t}. \tag{2.33}$$

The efficiency of the photodetector is determined by the number of electrons excited every time a photon impinges on the detector $\eta_{QE} = \langle\hat{\mathbf{n}}_e\rangle / \langle\hat{\mathbf{n}}_p\rangle \leq 1$. The current can therefore be related to the photon flux operator $\hat{\mathbf{A}} = \hat{\mathbf{a}}/\sqrt{\Delta t}$ via

$$\hat{\mathbf{i}}(t) = \mathrm{e}^-\eta_{QE}\hat{\mathbf{A}}^\dagger\hat{\mathbf{A}}. \tag{2.34}$$

This expression can then be put into its final form by introducing the spectral-responsivity $R = \mathrm{e}^-/\hbar\Omega_c$, where Ω_c is once again the photon carrier frequency

$$\hat{\mathbf{i}}(t) = R\hbar\Omega_c\eta_{QE}\hat{\mathbf{A}}^\dagger\hat{\mathbf{A}} \approx R\hbar\Omega_c\Big(|\alpha|^2 + |\alpha|\delta\hat{\mathbf{X}}_a\Big), \tag{2.35}$$

where we have ignored the non-linear fluctuation terms. We see that the expectation value of the photocurrent is proportional to the power of the impinging light and the variance is proportional

to the variance of the fluctuations of the amplitude quadrature amplified by the power impinging on the detector.

A single photodetector is phase insensitive, but phase sensitivity can be added by putting an interferometer before the photodetector or by employing more advanced detection schemes such as heterodyne or homodyne measurements.

2.3.4 Optical modulators

In section (2.2.2) it was mentioned how displacing a quantum state at a frequency side band was only possible by putting photons into the mode with the corresponding frequency. Optical modulators give us a way to achieve this. They can in general be separated into active and passive modulators, and in this thesis I will only go into the theory of the passive ones, specifically electro-optic phase modulators and acousto-optic amplitude modulators. I will begin this section with the latter; the acousto-optic modulator.

2.3.4.1 Amplitude modulation and acousto-optic modulators (AOM)

Acousto-optic modulators work by inducing vibrations at a given frequency ω_m in a crystal that light is propagating through. These vibrational modes (phonons) scatter some of the photons via a third-order Stokes/anti-Stokes Brillouin scattering processes. In general, both processes will take place, and depending on the process, the scattered photon will either be red detuned ($\omega = \Omega_c - \omega_m$) or blue detuned ($\omega = \Omega_c + \omega_m$), thus creating a sideband on either side of the carrier frequency.
Mathematically, assuming a cosine-wave drive of angular frequency ω_m, modulation depth m and modulation phase ϕ_m, the resulting electronic field operator(ignoring the spatial variations) will be amplitude modulated

$$\begin{aligned}\hat{\mathbf{a}}(t) &= \hat{\mathbf{a}}e^{-i\Omega_c t}\Big(\Big(1-\frac{m}{2}\Big)+\frac{m}{2}\cos(\omega_m t+\phi_m)\Big),\\ &= \hat{\mathbf{a}}e^{-i\Omega_c t}\Big(\Big(1-\frac{m}{2}\Big)+\frac{m}{4}\Big(e^{-i(\omega_m t+\phi_m)}+e^{i(\omega_m t+\phi_m)}\Big)\Big),\end{aligned} \tag{2.36}$$

creating the sidebands as described above. For an AOM the photons scattered into the sidebands are separated spatially from the carrier mode, meaning that it is actually possible to physically isolate and use one sideband leaving us basically with a new carrier mode at a shifted frequency

$$\hat{\mathbf{a}}_{\pm}(t) = \hat{\mathbf{a}}\frac{m}{4}e^{-i(\Omega_c\pm\omega_m)t\mp i\phi_m}. \tag{2.37}$$

If we return to equation (2.36), we can finally write up the quadrature operators in terms of the generalized quadrature operators equations (2.6) and (2.7)

$$\hat{\mathbf{X}}(t) = \Big(1-\frac{m}{2}\Big)\hat{\mathbf{X}}(\Omega_c t)+\frac{m}{4}\Big(\hat{\mathbf{X}}((\Omega_c-\omega_m)t-\phi_m)+\hat{\mathbf{X}}((\Omega_c+\omega_m)t+\phi_m)\Big), \tag{2.38a}$$

$$\hat{\mathbf{P}}(t) = \Big(1-\frac{m}{2}\Big)\hat{\mathbf{P}}(\Omega_c t)+\frac{m}{4}\Big(\hat{\mathbf{P}}((\Omega_c-\omega_m)t-\phi_m)+\hat{\mathbf{P}}((\Omega_c+\omega_m)t+\phi_m)\Big). \tag{2.38b}$$

2.3.4.2 Phase modulators

Phase modulators typically use the electro-optic effect to modify the refractive index of a crystal, thereby changing the optical path-length, inducing a phase shift similarly to the phase shifters described above. Since this shift is due to a modulation of the voltage difference over the crystal, this can be done much faster than a piezo-driven phase shifter, typically hundreds of

megahertz compared to kilohertz frequencies. If we modulate with a cosine drive like in the case of amplitude modulation, the modulation of the field operators will have the following form

$$\hat{\mathbf{a}}(t) = \hat{\mathbf{a}} e^{-i(\Omega_c t + m\cos(\omega_m t))}. \tag{2.39}$$

This exponential can be expanded into Bessel functions [35]

$$\hat{\mathbf{a}}(t) = \hat{\mathbf{a}} e^{-i\Omega_c t} \sum_{k=-\infty}^{\infty} -i^k \mathcal{J}_k(m) e^{-ik\omega_m t}, \tag{2.40a}$$

$$\mathcal{J}_k(m) = \frac{1}{k!}\frac{m}{2}^k + \mathcal{O}\Big(m^{k+2}\Big). \tag{2.40b}$$

We see that depending on the depth of the modulation, we can create a lot of sidebands around the carrier. If the modulation depth is small, then only the sidebands corresponding to lowest order in k (± 1) will be relevant and the field operators will take on the form

$$\hat{\mathbf{a}}(t) \approx \hat{\mathbf{a}} e^{-i\Omega_c t}\big(\mathcal{J}_0(m) + i\mathcal{J}_{-1}(m)e^{-i\omega_m t} - i\mathcal{J}_1(m)e^{i\omega_m t}\big), \tag{2.41a}$$

$$\approx \hat{\mathbf{a}} e^{-i\Omega_c t}\Big(1 - i\frac{m}{2}\big(e^{-i\omega_m t} + e^{i\omega_m t}\big)\Big). \tag{2.41b}$$

Since frequency is the derivative of phase, phase modulation and frequency modulation can be seen as the same effect. Phase modulation can be interpreted as frequency modulation by rewriting the modulation depth as $m = \Delta\omega/\omega_m$, where $\Delta\omega$ is the frequency shift. Finally, we can write up the quadrature operators again

$$\hat{\mathbf{X}}(t) = \hat{\mathbf{X}}(\Omega_c t) + \frac{m}{2}\Big(\hat{\mathbf{P}}((\Omega_c - \omega_m)t) + \hat{\mathbf{P}}((\Omega_c + \omega_m)t)\Big), \tag{2.42a}$$

$$\hat{\mathbf{P}}(t) = \hat{\mathbf{P}}(\Omega_c t) - \frac{m}{2}\Big(\hat{\mathbf{X}}((\Omega_c - \omega_m)t) + \hat{\mathbf{X}}((\Omega_c + \omega_m)t)\Big). \tag{2.42b}$$

2.3.5 Optical cavities

The final and maybe most important piece of optical equipment, we need to touch upon, is the optical cavity. An optical cavity consists of two or more reflective surfaces placed in a configuration that allows light to be caught in between them. An optical cavity is also called an optical resonator, as light caught between the mirrors will resonate and allow for a strong optical field to be built-up in between the them.

The build-up of the optical field inside the cavity is called a resonance, and stems from constructive interference between the light-field entering the cavity and light the light field already in the cavity having completed one or more round-trips. The condition for this constructive interference to build up is therefore that the phase of the light-field need to be the same each time, it makes a round-trip of the cavity (modulo 2π) or in other words the length of the cavity needs to be an integer number of wavelengths of the field $L_{cav} = n\lambda$. Given a certain cavity length, a number of frequencies of the light field will fulfil the above condition and will resonate. These are called resonance frequencies and are given by $\Omega_{cav} = 2\pi nc/(2L_{cav})$. The frequency difference between two cavity resonances is called the free spectral range (FSR) $\omega_{FSR} = 2\pi c/(2L_{cav})$.

There are two distinct types of optical cavities; the first is a standing wave cavity (or a Fabry-Pérot cavity) as shown in figure (2.5) (a). This cavity type is made up of two mirrors placed opposite of each other, and light caught between these two mirrors will form a standing wave pattern. The other type is a running wave cavity and is sketched in figure (2.5) (b). Running wave cavities a made up of three or more mirrors placed in patterns of triangles,

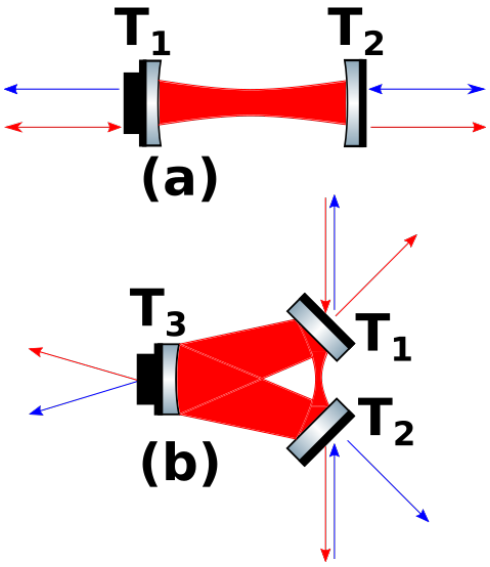

Figure 2.5: Sketch of a Fabry-Pérot cavity (a) and a running wave cavity (b)

squares, butterflies etc. to guide the light around in the cavity. Each type of cavity has its own strengths and weaknesses, and I will return to this in section (5.1.2).

For the following analysis, I will assume a linear cavity with each mirror having a finite power transmissivity T_i and is treated using the same formalism as a beam splitter, having two input modes and two output modes, where the intra-cavity transmitted input and reflected output modes feed into the intra-cavity field. The relevant modes for each mirror are then the external input and reflected output mode. The dynamics of the intra-cavity field of an optical cavity can be described in the rotating frame of the laser frequency using the Langevin formalism of the Heisenberg picture [29]

$$\frac{\mathrm{d}}{\mathrm{d}t}\hat{\mathbf{a}} = -(\gamma - i\Delta)\hat{\mathbf{a}} + \sum_k \sqrt{2\gamma^k}\hat{\mathbf{A}}^k_{in}, \tag{2.43}$$

where $\gamma^k = \left(1 - \sqrt{1-T_k}\right)/\tau_{cav} \approx \frac{T_k}{2\tau_{cav}}$ is the decay rate through the k'th mirror with τ_{cav} being the cavity roundtrip time given by $\tau_{cav} = 2L_{cav}/c$ for a linear cavity. The approximation is valid for transmittances much less than 1.

$\gamma = \sum_k \gamma^k = 2\pi\nu_{HWHM}$ is the total decay rate of the cavity and represents the half-width-half-maximum (HWHM) bandwidth of the cavity.

$\Delta = \Omega_c - \Omega_{cav}$ is the detuning of the cavity resonance from the carrier frequency of the field.

Finally, $\hat{\mathbf{A}}^k_{in}$ is the photon flux operator defined in section (2.3.3) entering the k'th port. The photon flux operators have units of $\sqrt{\text{Photon Number}/s}$ for which calculating the power comes very easily $P = \hbar\Omega_c \left\langle \hat{\mathbf{A}}^\dagger \hat{\mathbf{A}} \right\rangle$. The intra-cavity field is a steady state field with units of $\sqrt{\text{Photon Number}}$ and therefore in order to calculate the intra-cavity power, you have to include the cavity round-trip time $P_{cav} = \hbar\Omega_c \left\langle \hat{\mathbf{a}}^\dagger \hat{\mathbf{a}} \right\rangle / \tau_{cav}$.

We will use equation (2.43) as the starting point of analyzing the strengths of an optical cavity. For this analysis, we will assume equation (2.24) to be valid, meaning $\hat{\mathbf{a}} = \alpha + \delta\hat{\mathbf{a}}$ and $\hat{\mathbf{A}} = A + \delta\hat{\mathbf{A}}$. We will start by analysing the mean field equations, ignoring all fluctuation terms.

2.3.5.1 Mean-field equations: Power build-up

The mean-field version of equation (2.43) is

$$\frac{\mathrm{d}}{\mathrm{d}t}\alpha = -(\gamma - i\Delta)\alpha + \sum_k \sqrt{2\gamma^k} A_{in}^k. \tag{2.44}$$

The two mirror ports are denoted as $k = \{in, out\}$, and we assume a coherent input only at the input port, $A_{in}^{out} = 0$. If we assume the intra-cavity field to be in a steady-state, then the time derivative is zero, and we can solve the dynamics

$$\alpha = \frac{\sqrt{2\gamma^{in}}}{\gamma - i\Delta} A_{in}^{in} = \frac{\sqrt{2\gamma^{in}}(\gamma + i\Delta)}{\gamma^2 + \Delta^2} A_{in}^{in}. \tag{2.45}$$

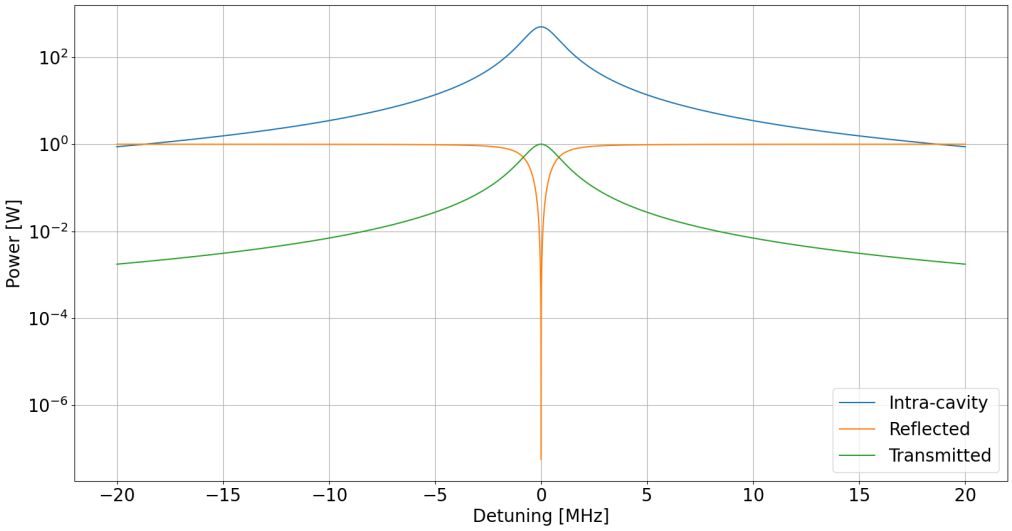

Figure 2.6: Intra-cavity power build-up, transmitted power and reflected power as a function of cavity detuning for an impedance matched cavity of finesse 1570 and HWHM bandwidth of 800 kHz.

We can also calculate the fields exiting the two ports

$$\begin{aligned} A_{out}^{in} &= \sqrt{2\gamma^{in}}\alpha - \sqrt{1 - T_{in}} A_{in}^{in} \approx \sqrt{2\gamma^{in}}\alpha - A_{in}^{in}, \\ &= \left(2\gamma^{in}\frac{\gamma + i\Delta}{\gamma^2 + \Delta^2} - 1\right) A_{in}^{in}, \end{aligned} \tag{2.46a}$$

$$\begin{aligned} A_{out}^{out} &= \sqrt{2\gamma^{out}}\alpha - \sqrt{1 - T_{out}} A_{in}^{out} \approx \sqrt{2\gamma^{in}}\alpha - A_{in}^{out}, \\ &= \sqrt{4\gamma^{in}\gamma^{out}}\frac{\gamma + i\Delta}{\gamma^2 + \Delta^2} A_{in}^{in}, \end{aligned} \tag{2.46b}$$

where the approximation is only valid for $R = 1 - T \approx 1$. This case is also known as the high finesse regime. The finesse of a cavity is a measure of how well the light is stored inside the cavity and is defined by $F = 2\omega_{FSR}/\gamma = \omega_{FSR}/\omega_{HWHM}$. There are three distinct behaviours of the cavity depending on the mirror reflectivities; under-coupled ($\gamma^{in} > \gamma^{out} + \gamma^L$), impedance-matched ($\gamma^{in} = \gamma^{out} + \gamma^L$) and over-coupled($\gamma^{in} < \gamma^{out} + \gamma^L$). Here I have included the intra-cavity loss decay rate γ^L, which is necessary when considering a physical cavity. The power build-up of an impedance-matched cavity is shown in figure (2.6) as a function of cavity detuning.

The cavity in this calculation has a finesse of 1570 and a HWHM bandwidth of 800 kHz. The intra-cavity field can be orders of magnitude larger than the input and transmitted powers. This allows amplification of very weak non-linear processes and will be very relevant in chapter (3).

2.3.5.2 Fluctuation equations: Noise filtering

The next part of this analysis also starts with equation (2.43), but this time we will ignore the mean-value parts and only concentrate on the fluctuations. In the analysis above, we ignored the input fields that we did not actively use, but this time we allow both classical and quantum mechanical fluctuations which means that even if we do not actively input fields through the mirrors, vacuum fluctuations will still enter the empty inputs. The differential equation then becomes

$$\frac{\mathrm{d}}{\mathrm{d}t}\delta\hat{\mathbf{a}} = -(\gamma - i\Delta)\delta\hat{\mathbf{a}} + \sqrt{2\gamma^{in}}\delta\hat{\mathbf{A}}^{in}_{in} + \sqrt{2\gamma^{out}}\delta\hat{\mathbf{A}}^{out}_{in} + \sqrt{2\gamma^{L}}\delta\hat{\mathbf{A}}^{L}. \tag{2.47}$$

We can rewrite this differential equation in terms of quadrature operators

$$\frac{\mathrm{d}}{\mathrm{d}t}\delta\hat{\mathbf{X}} = -\gamma\delta\hat{\mathbf{X}} + \Delta\delta\hat{\mathbf{P}} + \sqrt{2\gamma^{in}}\delta\hat{\mathbf{X}}^{in}_{in} + \sqrt{2\gamma^{out}}\delta\hat{\mathbf{X}}^{out}_{in} + \sqrt{2\gamma^{L}}\delta\hat{\mathbf{X}}^{L}, \tag{2.48a}$$

$$\frac{\mathrm{d}}{\mathrm{d}t}\delta\hat{\mathbf{P}} = -\gamma\delta\hat{\mathbf{P}} - \Delta\delta\hat{\mathbf{X}} + \sqrt{2\gamma^{in}}\delta\hat{\mathbf{P}}^{in}_{in} + \sqrt{2\gamma^{out}}\delta\hat{\mathbf{P}}^{out}_{in} + \sqrt{2\gamma^{L}}\delta\hat{\mathbf{P}}^{L}. \tag{2.48b}$$

Using the general property of Fourier transforms that $\mathcal{F}\left(\frac{\mathrm{d}}{\mathrm{d}t}f(t)\right) = -i\omega\widetilde{f}(\omega)$, we can find the steady state frequency domain solution of the intra-cavity operators

$$\delta\widetilde{\mathbf{X}} = \frac{1}{\gamma - i\omega}\left(\Delta\delta\widetilde{\mathbf{P}} + \sqrt{2\gamma^{in}}\delta\widetilde{\mathbf{X}}^{in}_{in} + \sqrt{2\gamma^{out}}\delta\widetilde{\mathbf{X}}^{out}_{in} + \sqrt{2\gamma^{L}}\delta\widetilde{\mathbf{X}}^{L}\right), \tag{2.49a}$$

$$\delta\widetilde{\mathbf{P}} = \frac{1}{\gamma - i\omega}\left(-\Delta\delta\widetilde{\mathbf{X}} + \sqrt{2\gamma^{in}}\delta\widetilde{\mathbf{X}}^{in}_{in} + \sqrt{2\gamma^{out}}\delta\widetilde{\mathbf{X}}^{out}_{in} + \sqrt{2\gamma^{L}}\delta\widetilde{\mathbf{X}}^{L}\right). \tag{2.49b}$$

From equations (2.49a) and (2.49b) we see that for non-zero detunings the quadrature fluctuations will couple, mixing a little bit of X into P and vice versa. We can also calculate the transmitted and reflected fluctuations

$$\delta\widetilde{\mathbf{X}}^{out}_{out} = \frac{\sqrt{2\gamma^{out}}}{\gamma - i\omega}\left(-\Delta\delta\widetilde{\mathbf{P}} + \sqrt{2\gamma^{in}}\delta\widetilde{\mathbf{X}}^{in}_{in} + \sqrt{2\gamma^{out}}\delta\widetilde{\mathbf{X}}^{out}_{in} + \sqrt{2\gamma^{L}}\delta\widetilde{\mathbf{X}}^{L}\right) - \delta\widetilde{\mathbf{X}}^{out}_{in}, \tag{2.50a}$$

$$\delta\widetilde{\mathbf{P}}^{out}_{out} = \frac{\sqrt{2\gamma^{out}}}{\gamma - i\omega}\left(\Delta\delta\widetilde{\mathbf{X}} + \sqrt{2\gamma^{in}}\delta\widetilde{\mathbf{P}}^{in}_{in} + \sqrt{2\gamma^{out}}\delta\widetilde{\mathbf{P}}^{out}_{in} + \sqrt{2\gamma^{L}}\delta\widetilde{\mathbf{P}}^{L}\right) - \delta\widetilde{\mathbf{P}}^{out}_{in}, \tag{2.50b}$$

$$\delta\widetilde{\mathbf{X}}^{in}_{out} = \frac{\sqrt{2\gamma^{in}}}{\gamma - i\omega}\left(-\Delta\delta\widetilde{\mathbf{P}} + \sqrt{2\gamma^{in}}\delta\widetilde{\mathbf{X}}^{in}_{in} + \sqrt{2\gamma^{out}}\delta\widetilde{\mathbf{X}}^{out}_{in} + \sqrt{2\gamma^{L}}\delta\widetilde{\mathbf{X}}^{L}\right) - \delta\widetilde{\mathbf{X}}^{in}_{in}, \tag{2.50c}$$

$$\delta\widetilde{\mathbf{P}}^{in}_{out} = \frac{\sqrt{2\gamma^{in}}}{\gamma - i\omega}\left(\Delta\delta\widetilde{\mathbf{X}} + \sqrt{2\gamma^{in}}\delta\widetilde{\mathbf{P}}^{in}_{in} + \sqrt{2\gamma^{out}}\delta\widetilde{\mathbf{P}}^{out}_{in} + \sqrt{2\gamma^{L}}\delta\widetilde{\mathbf{P}}^{L}\right) - \delta\widetilde{\mathbf{P}}^{in}_{in}. \tag{2.50d}$$

For the next part of the analysis, we will assume zero detuning, meaning we have linear, decoupled equations that we can cast in form of transfer functions that link the fluctuations exiting a given port with the fluctuations entering a given port

$$\delta\widetilde{\mathbf{X}}^{out}_{out} = \Theta_{[in;out]}\delta\widetilde{\mathbf{X}}^{in}_{in} + \Theta_{[out;out]}\delta\widetilde{\mathbf{X}}^{out}_{in} + \Theta_{[L;out]}\delta\widetilde{\mathbf{X}}^{L}, \tag{2.51a}$$

$$\delta\widetilde{\mathbf{P}}^{out}_{out} = \Theta_{[in;out]}\delta\widetilde{\mathbf{P}}^{in}_{in} + \Theta_{[out;out]}\delta\widetilde{\mathbf{P}}^{out}_{in} + \Theta_{[L;out]}\delta\widetilde{\mathbf{P}}^{L}, \tag{2.51b}$$

$$\delta\widetilde{\mathbf{X}}^{in}_{out} = \Theta_{[in;in]}\delta\widetilde{\mathbf{X}}^{in}_{in} + \Theta_{[out;in]}\delta\widetilde{\mathbf{X}}^{out}_{in} + \Theta_{[L;in]}\delta\widetilde{\mathbf{X}}^{L}, \tag{2.51c}$$

$$\delta\widetilde{\mathbf{P}}^{in}_{out} = \Theta_{[in;in]}\delta\widetilde{\mathbf{P}}^{in}_{in} + \Theta_{[out;in]}\delta\widetilde{\mathbf{P}}^{out}_{in} + \Theta_{[L;in]}\delta\widetilde{\mathbf{P}}^{L}, \tag{2.51d}$$

where the index on the transfer functions $[i;j]$ refers to the input of the i'th ports effect on the output of the j'th port, with the specific transfer functions given by

$$\Theta_{[i;j]} = \frac{2\sqrt{\gamma^i \gamma^j}}{\gamma + i\omega} - \delta_{ij}. \tag{2.52}$$

We plot the amplitude and phase response of the transfer functions in figure (2.7) for the two distinct cases reflection from the same port of $i = j$ and transmission through another port $i \neq j$ using the same cavity parameters as in figure (2.6).

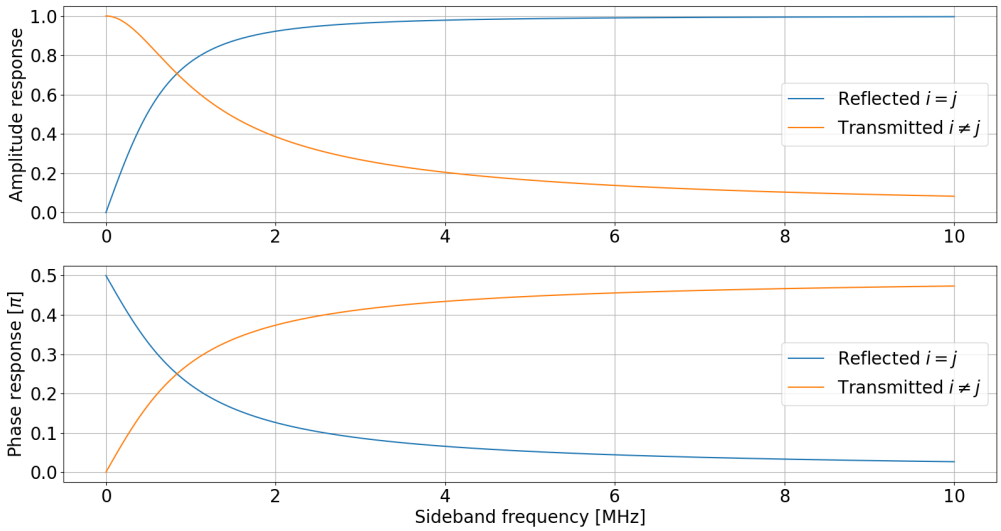

Figure 2.7: Top figure: The amplitude response of the cavity transfer function equation (2.52) for the cases of transmission from one port to the other $i \neq j$ and reflection from the same input port $i = j$. **Bottom figure**: The phase response of the same transfer function. For both figures the cavity parameters are the same as in figure (2.6).

We see that for the transmitted fields, the cavity acts as a low-pass filter, attenuating noise above the cavity bandwidth and transmitting fluctuations below. Inversely, the reflected fields are high-pass filtered by the cavity. This shows that optical cavities can work very effectively as an optical filter, removing unwanted technical (classical) noise from an optical mode. The cavity cannot remove quantum noise, however, inputting shot noise in all ports will only return shot noise through all ports.

2.3.5.3 Spatial filtering

We have previously seen that an optical cavity can filter amplitude and phase noise by engineering the cavity bandwidth. An optical cavity can however also work as a spatial filter, and in order to analyse this we first need to introduce the concept of Laguerre-Gauss and Hermite-Gauss modes in more detail.

Hermite-Gauss modes:
The Hermite-Gauss basis is a complete set of orthogonal spatial eigenmodes of a laser beam with symmetry in x- and/or y-directions. These modes are characterized by two indices n and

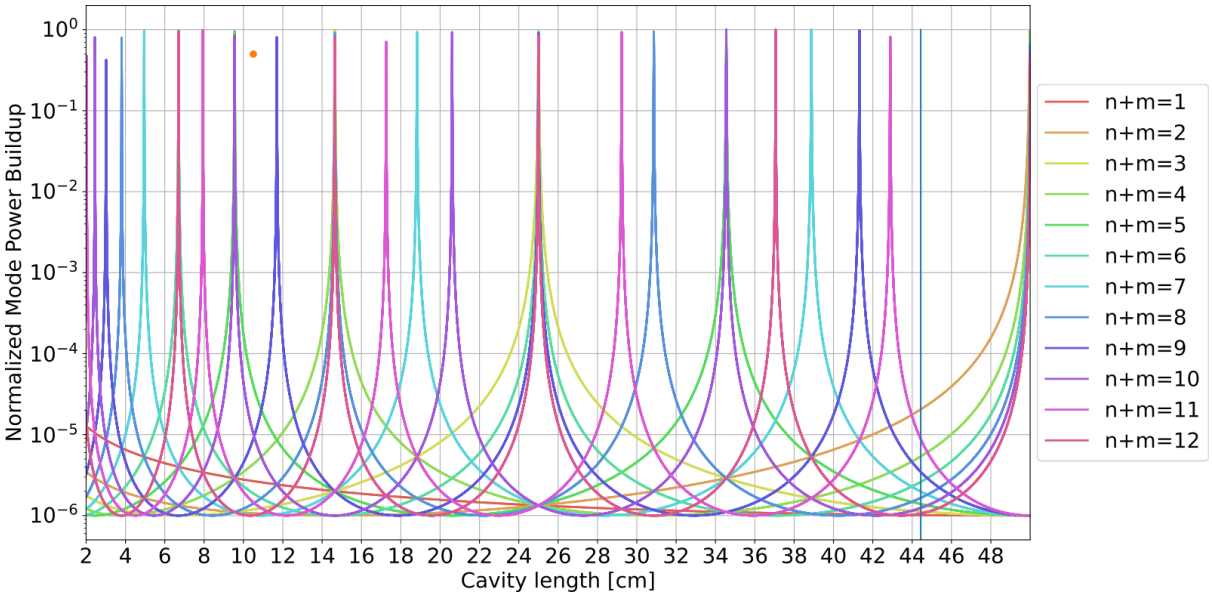

Figure 2.8: Normalized power build-up for higher-order modes as a function of cavity length. The cavity has the same parameters as in figure (2.6). The orange dot marks a cavity length which would provide good isolation. This simulation is done using Finesse [35].

m describing the order in the x- and y-directions, and the spatial mode function is in general given by [27]

$$A_{n,m}(x,y,z) = C^{HG}_{m,n}\frac{w_0}{w(z)}H_n\left(\frac{\sqrt{2}x}{w(z)}\right)H_m\left(\frac{\sqrt{2}y}{w(z)}\right) \times \exp\left(-\frac{x^2+y^2}{w^2(z)}\right)\exp\left(ik\frac{x^2+y^2}{2R^2(z)}\right)\exp(-i\phi^n_m(z)), \tag{2.53}$$

where $C^{HG}_{m,n}$ is a normalization factor, $H_n(u)$ is a generalized Hermite polynomial, $w(z) = w_0\sqrt{1+(z/z_R)^2}$ is the beam radius with w_0 being the waist size and $z_R = \pi w_o^2 n/\lambda$ being the Rayleigh length. $R(z) = z(1+(z_R/z)^2)$ is the radius of curvature of the wave front, and finally $\phi^n_m(z) = (1+n+m)\,\mathrm{atan}(z/z_R)$ is the Gouy phase. Setting $n = m = 0$ gives us the fundamental Gaussian mode shape

$$A_{0,0}(x,y,z) = \sqrt{\frac{2}{\pi}}\frac{w_0}{w(z)}\exp\left(-\frac{x^2+y^2}{w^2(z)}\right)\exp\left(-ik\frac{x^2+y^2}{2R(z)}\right)\exp\big(-i\phi^0_0(z)\big). \tag{2.54}$$

Laguerre-Gauss modes:
The Laguerre-Gauss basis is a complete set of orthogonal, rotationally symmetric eigenmodes defined with indices l describing azimuthal order and p describing the radial order. In this we consider only optical modes without angular momentum for which $l = 0$. In this case, the spatial mode functions for Laguerre-Gauss modes are defined as

$$A_{0,p}(r,z) = C^{LG}_{0,p}\frac{1}{w(z)}L^0_p\left(\frac{2r^2}{w^2(z)}\right)\exp\left(-\frac{r^2}{w^2(z)}\right)\exp\left(-ik\frac{r^2}{2R(z)}\right)\exp\big(-i\phi^0_2 p(z)\big), \tag{2.55}$$

where once again, $C^{LG}_{0,p}$ is a normalization factor, and $L^0_p(u)$ is a generalized Laguerre Polynomial. Similarly to Hermite-Gauss modes, setting $p = 0$ return the fundamental Gaussian mode shape equation (2.54) with $r^2 = x^2 + y^2$, and in general every Laguerre-Gauss mode can be expressed as a super position of Hermite-Gauss modes and vice versa.

Knowledge of these modes are in general very useful in aligning optical cavities, as [36] showed that angular and translational mismatches (alignment) of the beam will cause excitations of Hermite-Gauss modes in the cavity, and position and size mismatches of the beam waist (mode-match) of the beam will cause excitation of Laguerre-Gauss modes in the cavity. Due to a difference in phase, the different modes will resonate with different resonance frequencies and identifying these different types of modes in the cavity spectrum will give hints as to what needs to be improved in order to get the best alignment of the fundamental Gaussian mode into the cavity (by removing these higher order modes).

For certain cavity configurations, more than just the fundamental Gaussian mode will resonate in the cavity. This is usually undesirable and has to be taken into account when designing an optical cavity. The laser beam exiting a laser usually contains components of higher order Hermite-Gauss or Laguerre-Gauss modes due to imperfections, and an optical cavity, where care is taken to isolate the fundamental Gaussian mode from the other higher order modes, can therefore be used to spatially filter the beam to make sure, it will only contain the fundamental mode to a high degree. The parameter that is often tuned to ensure this, is the length of the cavity, and in figure (2.8) the power build-up of higher order Hermite-Gaussian modes (compared to the fundamental mode) as a function of cavity length is shown for the same cavity used in figures (2.6) and (2.7).

An alternative way of spatially filtering a laser beam is to couple it into a single mode (SM) fiber, as the only mode to be supported by the SM fiber has a very high fidelity to the fundamental Gaussian mode, and all other modes will not be coupled into the fiber.

An expert is a person who has found out by his own painful experience all the mistakes that one can make in a very narrow field.

Niels Bohr
Dr. Edward Teller's Magnificent Obsession
by Robert Coughlan, 1954

3

Optical parametric oscillator theory

In this chapter, I will go through the mathematics behind squeezed light generation in an optical parametric oscillator and detection in a balanced homodyne detector. The analysis will include the most important sources of imperfection, and how these will affect the squeezed light.

3.1 Squeezing generation, nonlinear interactions and quasi-phase matching

In order to generate squeezed light, we need to generate an interaction producing an operator of the form equation (2.19). For this we need an interaction Hamiltonian of the form

$$\hat{\mathbf{H}}_{int} = \frac{1}{2} i\hbar \Big(K^* \hat{\mathbf{a}}^2 - K \hat{\mathbf{a}}^{\dagger 2} \Big) \tag{3.1}$$

where K is a complex number. This interaction Hamiltonian will lead to the squeezing operator when applying the time evolution operator $\hat{\mathbf{U}}(t) = \exp\Big(-i/\hbar \hat{\mathbf{H}}_{int} t\Big)$. Interactions, which are quadratic or of higher order in the field operators, are called nonlinear interactions and arises from nonlinear terms in the material polarization. Squeezed light requires interactions of at least second order.

The general interaction Hamiltonian for this type of nonlinear process is given by

$$H_{int}^{TWM} = i\hbar g (\hat{\mathbf{b}} \hat{\mathbf{a}}_i^\dagger \hat{\mathbf{a}}_s^\dagger - \hat{\mathbf{b}}^\dagger \hat{\mathbf{a}}_i \hat{\mathbf{a}}_s), \tag{3.2}$$

where $\hat{\mathbf{a}}_s$ is called the signal field, $\hat{\mathbf{a}}_i$ is called the idler field and $\hat{\mathbf{b}}$ is called the pump field.

There are two conditions that need to be satisfied for this type of process to take place: $\Omega_s + \Omega_i = \Omega_p$ (energy conservation) and $\hat{\mathbf{k}}_s + \hat{\mathbf{k}}_i = \hat{\mathbf{k}}_p$ (momentum conservation).

In the case where the pump-field is empty, the process that will take place is called sum-frequency-generation (SFG); the signal and idler photons will annihilate to create a pump photon. If one of the signal or idler fields are empty, the process taking place will be called difference-frequency-generation (DFG); a pump photon will annihilate and create a photon at both the idler and signal frequencies.

A special case of these processes is if $1/2\Omega_p = \Omega_s = \Omega_i$. In this case, the process generating the pump field is called second harmonic generation (SHG), and the process generating the signal field is called parametric down-conversion (PDC). If the signal field is vacuum in the

PDC process, then the pump can interact with the vacuum modes in what is called spontaneous parametric down-conversion (SPDC), and it is from the SPDC process that squeezed light is generated.

The factor g is the interaction strength given by [37]

$$g = \epsilon_0 \chi^{(2)}_{eff} \sqrt{\frac{1}{2}\eta_s \eta_i \eta_p \hbar \Omega_s \Omega_i \Omega_p} L_c \mathrm{sinc}\left(\Delta\hat{\mathbf{k}} L_c/2\right) e^{iL_c \Delta\hat{\mathbf{k}}/2}, \tag{3.3}$$

where $\eta_i = \sqrt{\mu_i/\epsilon_i}$ is called the wave impedance. For a dielectric material with weak magnetic properties the impedance is $\eta_i \approx 377\,\Omega/\sqrt{\epsilon_{r,i}}$. L_c is the propagation length of the nonlinear medium (usually a dielectric crystal) and $\Delta\hat{\mathbf{k}} = \hat{\mathbf{k}}_p - \hat{\mathbf{k}}_s - \hat{\mathbf{k}}_i$ is the phase-mismatch. The form of g in equation (3.3) is however only valid for plane waves, and in the case of strongly focussed laser beams we have to use the framework developed by Boyd and Kleinman in 1968 [38], which includes spatial mode overlap, Gouy phase and loss. We will revisit Boyd-Kleinman theory in section (5.1.2.3)

$\chi^{(2)}_{eff} = 2/(\pi m)\chi^{(2)}_{zzz}$ is the effective second order nonlinear susceptibility coefficient, which describes the strength of the nonlinear process. $\chi^{(2)}_{zzz}$ is the nonlinear coefficient in the case of non-critical phase matching, where momentum conservation naturally occurs for fields propagating along the relevant axis (z-axis in this case) of the crystal. This is in general not possible, and the nonlinear process is severely limited if $\Delta\hat{\mathbf{k}}$ is non-zero. In order to overcome this, we exploit what is called quasi-phase-matching through periodic poling, where a strong electrical field is applied to the nonlinear crystal periodically to create inverted crystal domains and effectively change the sign of the nonlinear interaction. What it does in terms of phase matching, is that it adds a term $\Delta\hat{\mathbf{k}} = \hat{\mathbf{k}}_p - \hat{\mathbf{k}}_s - \hat{\mathbf{k}}_i - G$, where $G = 2\pi m/\Lambda$ is an effective wave-vector added by the periodic structure. m is an integer and Λ is the period of the structure. By choosing the period intelligently the periodic poling can compensate the natural dispersion of the material to allow for partial access to the desired tensor component with a $2/(\pi m)$ penalty.

The crystals, used in the experiments of this thesis, are (periodically poled) kalium titanyl phosphate $KTiOPO_4$ (PPKTP).

3.2 The nonlinear equations of motion

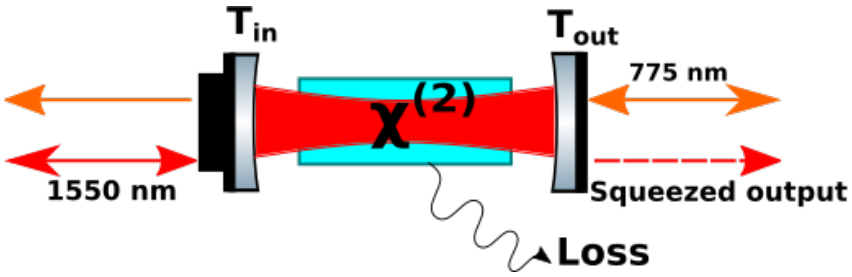

Figure 3.1: Theoretical model of the OPO. The (1550 nm) signal mode is inserted through the input mirror, the (1550 nm) squeezed mode is extracted through the output mirror, and the (775 nm) pump mode is inserted through the output mirror. Both mirrors have different transmissivity for the different wavelengths as well as the intra-cavity loss being different. This figure represents a theoretical model and does not necessarily reflect the exact physical configuration of the experimental system.

In order to increase the nonlinear interaction from the PPKTP, the crystal is put into a double-resonant cavity, which enhances both the signal/idler mode and the second harmonic

pump mode. Cavity enhancement of the PDC process is in general called optical parametric oscillation (OPO). The analysis in this section will largely follow the analysis done in section (2.3.5): I will once again assume a linear cavity coupled to three input/output channels; input, output and intra-cavity loss as shown in figure figure (3.1).

3.2.1 The basic equations of motion

The SPDC process can in general be subdivided into three types. In type 0 SPDC, the signal and idler fields are indistinguishable as they both have the same polarization, which is identical to the pump field polarization. In type 1 SPDC, the signal and idler fields still have the same polarization, but orthogonal to the pump field polarization. Finally, in type 2 SPDC the signal and idler fields are distinguishable with different polarizations, one of which will also match the pump polarization. We set up equations of motion without any assumption on whether the SPDC process is type 0, 1 or 2.

We start with a total Hamiltonian on the form

$$\hat{\mathbf{H}}_{tot} = \hbar\Omega_s \hat{\mathbf{a}}_s^\dagger \hat{\mathbf{a}}_s + \hbar\Omega_i \hat{\mathbf{a}}_i^\dagger \hat{\mathbf{a}}_i + \hbar\Omega_p \hat{\mathbf{b}}^\dagger \hat{\mathbf{b}} + \frac{i\hbar g}{2}\Big(\hat{\mathbf{b}}\hat{\mathbf{a}}_s^\dagger \hat{\mathbf{a}}_i^\dagger - \hat{\mathbf{b}}^\dagger \hat{\mathbf{a}}_s \hat{\mathbf{a}}_i\Big), \tag{3.4}$$

where $2\Omega_1 = \Omega_s + \Omega_i$. In the rotating frame of the signal frequency the equations of motion are

$$\dot{\hat{a}}_s = -(\gamma_s - i\Delta_s)\hat{\mathbf{a}}_s + \frac{g^*}{2}\hat{\mathbf{a}}_i^\dagger \hat{\mathbf{b}} + \sqrt{2\gamma_s^{in}}\hat{\mathbf{A}}_{s,in}^{in} + \sqrt{2\gamma_s^{out}}\hat{\mathbf{A}}_{s,in}^{out} + \sqrt{2\gamma_s^{L}}\hat{\mathbf{A}}_s^{L}, \tag{3.5a}$$

$$\dot{\hat{a}}_i = -(\gamma_i - i\Delta_i)\hat{\mathbf{a}}_i + \frac{g^*}{2}\hat{\mathbf{a}}_s^\dagger \hat{\mathbf{b}} + \sqrt{2\gamma_i^{in}}\hat{\mathbf{A}}_{i,in}^{in} + \sqrt{2\gamma_i^{out}}\hat{\mathbf{A}}_{i,in}^{out} + \sqrt{2\gamma_i^{L}}\hat{\mathbf{A}}_i^{L}, \tag{3.5b}$$

$$\dot{\hat{b}} = -(\gamma_p - i\Delta_p)\hat{\mathbf{b}} - \frac{g}{2}\hat{\mathbf{a}}_s\hat{\mathbf{a}}_i + \sqrt{2\gamma_p^{in}}\hat{\mathbf{B}}_{in}^{in} + \sqrt{2\gamma_p^{out}}\hat{\mathbf{B}}_{in}^{out} + \sqrt{2\gamma_p^{L}}\hat{\mathbf{B}}^{L}, \tag{3.5c}$$

where the detunings and decay rates follow the formalism introduced in section (2.3.5). Since the OPO that we work with is degenerate, we now make the assumption that $\Omega_s = \Omega_i$, and we drop the index on the operators. The equations of motion thus reduce to

$$\dot{\hat{a}} = -(\gamma_s - i\Delta_s)\hat{\mathbf{a}} + g^*\hat{\mathbf{a}}^\dagger \hat{\mathbf{b}} + \sqrt{2\gamma_s^{in}}\hat{\mathbf{A}}_{in}^{in} + \sqrt{2\gamma_s^{out}}\hat{\mathbf{A}}_{in}^{out} + \sqrt{2\gamma_s^{L}}\hat{\mathbf{A}}^{L}, \tag{3.6a}$$

$$\dot{\hat{b}} = -(\gamma_p - i\Delta_p)\hat{\mathbf{b}} - \frac{g}{2}\hat{\mathbf{a}}\hat{\mathbf{a}} + \sqrt{2\gamma_p^{in}}\hat{\mathbf{B}}_{in}^{in} + \sqrt{2\gamma_p^{out}}\hat{\mathbf{B}}_{in}^{out} + \sqrt{2\gamma_p^{L}}\hat{\mathbf{B}}^{L}. \tag{3.6b}$$

We once again assume linearisation of the operators equation (2.24). This allows us to set up separate equations for the classical mean value and the quantum fluctuations, and we will start analysing the behaviour of the former.

3.2.2 Mean-value equations of motion

The classical mean behaviour of the OPO is described by the following equations of motion,

$$\dot{\alpha} = -(\gamma_s - i\Delta_s)\alpha + g^*\alpha^*\beta + \sqrt{2\gamma_s^{in}}A_{in}^{in}, \tag{3.7a}$$

$$\dot{\beta} = -(\gamma_p - i\Delta_p)\beta - \frac{g}{2}\alpha^2 + \sqrt{2\gamma_p^{out}}B_{in}^{out}, \tag{3.7b}$$

where we have allowed the second harmonic pump field to enter the cavity from the output-coupler and the fundamental field from the input-coupler. If we solve these equations in the

steady state

$$\beta = \frac{\sqrt{2\gamma_p^{out}}}{\gamma_p - i\Delta_p} B_{in}^{out} - \frac{g\alpha^2}{2(\gamma_p - i\Delta_p)}, \tag{3.8a}$$

$$\alpha = \frac{\sqrt{2\gamma_s^{in}} A_{in}^{in}}{((\gamma_s - i\Delta_s) - g^*\beta)}, \tag{3.8b}$$

where we have assumed α to be real without loss of generality. The two equations are coupled by the nonlinear interaction that allows energy to be exchanged between the two fields. We are going to decouple these equations, however, by assuming $\alpha \ll \beta$, which means we can ignore the effect of the fundamental field on the second harmonic field. The second harmonic field will therefore remain undepleted, and the equations then reduce to the following

$$\beta \approx \frac{\sqrt{2\gamma_p^{out}}}{\gamma_p - i\Delta_p} B_{in}^{out}, \tag{3.9a}$$

$$\begin{aligned} \alpha &\approx \frac{\sqrt{2\gamma_s^{in}} A_{in}^{in}}{(\gamma_s - i\Delta_s)\left(1 - g^* \frac{\sqrt{2\gamma_p^{out}}}{(\gamma_s - i\Delta_s)(\gamma_p - i\Delta_p)} B_{in}^{out}\right)}, \\ &= \frac{\sqrt{2\gamma_s^{in}} A_{in}^{in}}{(\gamma_s - i\Delta_s)\left(1 - \frac{|g|\sqrt{2\gamma_p^{out}(\gamma_s^2+\Delta_s^2)(\gamma_p^2+\Delta_p^2)}}{(\gamma_s^2+\Delta_s^2)(\gamma_p^2+\Delta_p^2)} |B_{in}^{out}| e^{-i\left(\phi_p + \phi_{\Delta s} + \phi_{\Delta p} - \phi_g\right)}\right)}. \end{aligned} \tag{3.9b}$$

Here we have split up the complex numbers into amplitudes and arguments with $\phi_g = \arg g$, $\phi_{\Delta i} = \arctan(\Delta_i/\gamma_i)$ and ϕ_p being the phase of the pump field with respect to the fundamental field.

From here we can identify a threshold-point as the point, where the creation of photons in the fundamental mode is perfectly balanced by the total loss of photons in the fundamental mode (in the case where the complex exponent is equal to zero)

$$\begin{aligned} 1 &= \frac{|g|\sqrt{2\gamma_p^{out}(\gamma_s^2 + \Delta_s^2)(\gamma_p^2 + \Delta_p^2)}}{(\gamma_s^2 + \Delta_s^2)(\gamma_p^2 + \Delta_p^2)} |B_{in}^{out}|, \\ &= \frac{|B_{in}^{out}|}{|B^{thr}|}, \end{aligned} \tag{3.10}$$

which gives us the threshold value of the input field $B^{thr} = \left(|g|\sqrt{2\gamma_p^{out}(\gamma_s^2 + \Delta_s^2)(\gamma_p^2 + \Delta_p^2)}/\left((\gamma_s^2 + \Delta_s^2)(\gamma_p^2 + \Delta_p^2)\right)\right)^{-1}$. The ratio between the input pump power and the threshold pump power is then $P_p/P_p^{thr} = \left|B_{in}^{out}/B^{thr}\right|^2$. This allows us to rewrite equation (3.9b) as

$$\begin{aligned} \alpha &\approx \frac{2\sqrt{\gamma_s^{in}} A_{in}^{in}}{(\gamma_s - i\Delta_s)\left(1 - \sqrt{\frac{P_p}{P_p^{thr}}} e^{-i\left(\phi_p + \phi_{\Delta s} + \phi_{\Delta p} - \phi_g\right)}\right)}, \\ &= g_{PG} \frac{\sqrt{2\gamma_s^{in}}}{\gamma_s - i\Delta_s} A_{in}^{in} = g_{PG}\alpha_0, \end{aligned} \tag{3.11}$$

where we have defined the parametric gain constant g_{PG}, and α_0 is the intracavity field without parametric gain. We see that in the case of the complex exponent being zero, the parametric

gain will work as to amplify the fundamental intra-cavity field with gain values approaching infinite as the pump power approaches the threshold.

If the complex exponent is π the parametric gain will de-amplify the fundamental field with gain going towards 1/2 close to the threshold. If we re-write equation (3.11) in terms of field powers, then we see that $P = |g_{PG}|^2 P_0$, and this is shown in figure (3.2).

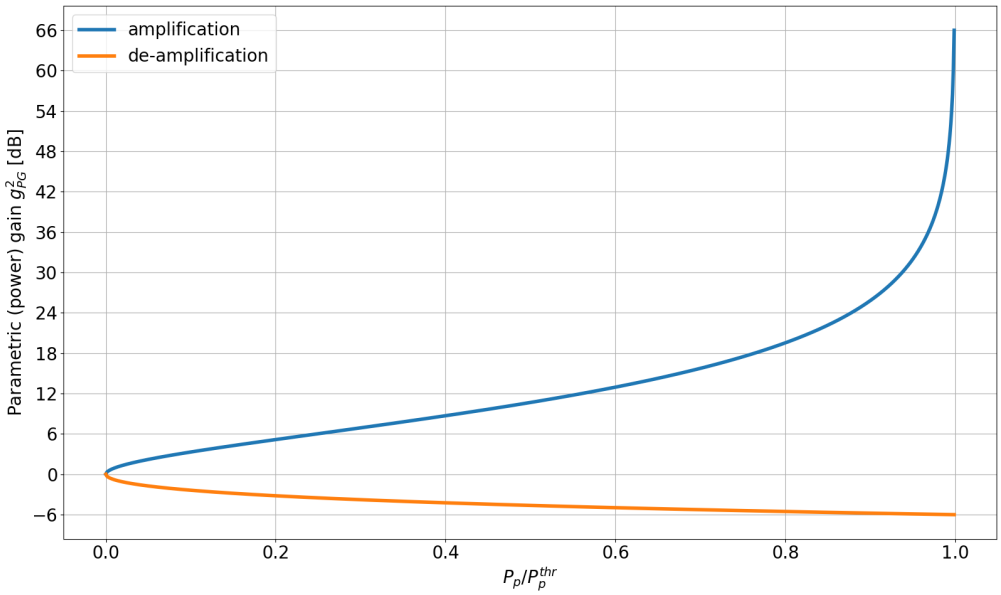

Figure 3.2: Parametric gain in the cases of amplification and de-amplification as a function of pump power to threshold power ratio.

Above the threshold, the pump field will amplify the quantum fluctuations to create a fundamental coherent field, even when no seed is present. This is not reflected in this analysis and will require including the fluctuation terms.

3.2.3 Fluctuation-equations of motion

We now return to the equations of motion and focus on the quantum fluctuations. In order to solve these, we linearize the equations of motion, meaning we only keep terms that are first-order in fluctuation operators. We will keep the pump field quantum mechanical and allow for a pump field to enter through the output-coupler and a seed field to enter through the input-coupler. The linearized equations of motion are then

$$\delta\dot{\hat{a}} = -(\gamma_s - i\Delta_s)\delta\hat{\mathbf{a}} + g^*\delta\hat{\mathbf{a}}^\dagger\beta + g^*\delta\hat{\mathbf{b}}\alpha^* + \sqrt{2\gamma_s^{in}}\delta\hat{\mathbf{A}}_{in}^{in} + \sqrt{2\gamma_s^{out}}\delta\hat{\mathbf{A}}_{in}^{out} + \sqrt{2\gamma_s^{L}}\delta\hat{\mathbf{A}}^{L}, \quad (3.12a)$$

$$\delta\dot{\hat{b}} = -(\gamma_p - i\Delta_p)\delta\hat{\mathbf{b}} - g\delta\hat{\mathbf{a}}\alpha + \sqrt{2\gamma_p^{in}}\delta\hat{\mathbf{B}}_{in}^{in} + \sqrt{2\gamma_p^{out}}\delta\hat{\mathbf{B}}_{in}^{out} + \sqrt{2\gamma_p^{L}}\delta\hat{\mathbf{A}}^{L}. \quad (3.12b)$$

We assume no detuning and rewrite the equations in terms of quadrature operators equations (2.3a) and (2.3b)

$$\delta\dot{\hat{X}}_s = -\gamma_s\delta\hat{\mathbf{X}}_s + g^*\delta\hat{\mathbf{X}}_s\beta + g^*\delta\hat{\mathbf{X}}_p\alpha^* + \sqrt{2\gamma_s^{in}}\delta\hat{\mathbf{X}}_{s,in}^{in} + \sqrt{2\gamma_s^{out}}\delta\hat{\mathbf{X}}_{s,in}^{out} + \sqrt{2\gamma_s^{L}}\delta\hat{\mathbf{X}}_s^{L}, \tag{3.13a}$$

$$\delta\dot{\hat{X}}_p = -\gamma_p\delta\hat{\mathbf{X}}_p - g\delta\hat{\mathbf{X}}_s\alpha + \sqrt{2\gamma_p^{in}}\delta\hat{\mathbf{X}}_{p,in}^{in} + \sqrt{2\gamma_p^{out}}\delta\hat{\mathbf{X}}_{p,in}^{out} + \sqrt{2\gamma_p^{L}}\delta\hat{\mathbf{X}}_p^{L}, \tag{3.13b}$$

$$\delta\dot{\hat{P}}_s = -\gamma_s\delta\hat{\mathbf{P}}_s - g^*\delta\hat{\mathbf{P}}_s\beta + g^*\delta\hat{\mathbf{P}}_p\alpha^* + \sqrt{2\gamma_s^{in}}\delta\hat{\mathbf{P}}_{s,in}^{in} + \sqrt{2\gamma_s^{out}}\delta\hat{\mathbf{P}}_{s,in}^{out} + \sqrt{2\gamma_s^{L}}\delta\hat{\mathbf{P}}_s^{L}, \tag{3.13c}$$

$$\delta\dot{\hat{P}}_p = -\gamma_p\delta\hat{\mathbf{X}}_p - g\delta\hat{\mathbf{P}}_s\alpha + \sqrt{2\gamma_p^{in}}\delta\hat{\mathbf{P}}_{p,in}^{in} + \sqrt{2\gamma_p^{out}}\delta\hat{\mathbf{P}}_{p,in}^{out} + \sqrt{2\gamma_p^{L}}\delta\hat{\mathbf{P}}_p^{L}. \tag{3.13d}$$

In order to finally solve the equations of motion for these quadrature operators, we assume a steady-state solution and transform to the frequency domain, for which we have $\mathcal{F}\left(\delta\hat{\mathbf{X}}\right) \to \delta\widetilde{\mathbf{X}}$ and $\mathcal{F}\left(\delta\dot{\hat{X}}\right) \to i\omega\delta\widetilde{\mathbf{X}}$. This allows us to set up the equations of motion as a matrix equation

$$\begin{pmatrix} i\omega+\gamma_s-g\beta & -g^*\alpha^* & 0 & 0 \\ g\alpha & i\omega+\gamma_p & 0 & 0 \\ 0 & 0 & i\omega+\gamma_s+g\beta & -g^*\alpha^* \\ 0 & 0 & g\alpha & i\omega+\gamma_p \end{pmatrix} \begin{pmatrix} \delta\widetilde{\mathbf{X}}_s \\ \delta\widetilde{\mathbf{X}}_p \\ \delta\widetilde{\mathbf{P}}_s \\ \delta\widetilde{\mathbf{P}}_p \end{pmatrix} = \begin{pmatrix} \widetilde{\mathbf{N}}_s^x \\ \widetilde{\mathbf{N}}_p^x \\ \widetilde{\mathbf{N}}_s^p \\ \widetilde{\mathbf{N}}_p^p \end{pmatrix}, \tag{3.14}$$

where we have introduced "collected" noise operators

$$\widetilde{\mathbf{N}}_i^x = \sqrt{2\gamma_i^{in}}\delta\widetilde{\mathbf{X}}_{i,in}^{in} + \sqrt{2\gamma_i^{out}}\delta\widetilde{\mathbf{X}}_{i,in}^{out} + \sqrt{2\gamma_i^{L}}\delta\widetilde{\mathbf{X}}_i^{L}, \tag{3.15a}$$

$$\widetilde{\mathbf{N}}_i^p = \sqrt{2\gamma_i^{in}}\delta\widetilde{\mathbf{P}}_{i,in}^{in} + \sqrt{2\gamma_i^{out}}\delta\widetilde{\mathbf{P}}_{i,in}^{out} + \sqrt{2\gamma_i^{L}}\delta\widetilde{\mathbf{P}}_i^{L}, \tag{3.15b}$$

to simplify the notation. Inverting the matrix and solving the equation yields the following solutions for $\delta\widetilde{\mathbf{X}}_s$ and $\delta\widetilde{\mathbf{P}}_s$ (the operators of interest)

$$\begin{pmatrix} \delta\widetilde{\mathbf{X}}_s \\ \delta\widetilde{\mathbf{P}}_s \end{pmatrix} = \begin{pmatrix} \Big(|g|^2|\alpha|^2 + (\gamma_s+i\omega-g\beta)(\gamma_p+i\omega)\Big)^{-1} \\ \Big(|g|^2|\alpha|^2 + (\gamma_s+i\omega+g\beta)(\gamma_p+i\omega)\Big)^{-1} \end{pmatrix} \begin{pmatrix} \gamma_p+i\omega & g\alpha & 0 & 0 \\ 0 & 0 & \gamma_p+i\omega & g\alpha \end{pmatrix} \begin{pmatrix} \widetilde{\mathbf{N}}_s^x \\ \widetilde{\mathbf{N}}_p^x \\ \widetilde{\mathbf{N}}_s^p \\ \widetilde{\mathbf{N}}_p^p \end{pmatrix}, \Rightarrow$$

$$\delta\widetilde{\mathbf{X}}_s = \frac{\left[\gamma_p+i\omega\right]\widetilde{\mathbf{N}}_s^x + g\alpha\widetilde{\mathbf{N}}_p^x}{|g|^2|\alpha|^2 + (\gamma_s+i\omega-g\beta)\,(\gamma_p+i\omega)}, \tag{3.16a}$$

$$\delta\widetilde{\mathbf{P}}_s = \frac{\left[\gamma_p+i\omega\right]\widetilde{\mathbf{N}}_s^p + g\alpha\widetilde{\mathbf{N}}_p^p}{|g|^2|\alpha|^2 + (\gamma_s+i\omega+g\beta)\,(\gamma_p+i\omega)}. \tag{3.16b}$$

If we try to calculate the variance of equations (3.16a) and (3.16b) for $\alpha \to 0$ and $\omega \to 0$

$$\gamma_s\left\langle\delta\widetilde{\mathbf{X}}_s^\dagger\delta\widetilde{\mathbf{X}}_s\right\rangle = \frac{2}{\left(1-\frac{g\beta}{\gamma_s}\right)^2}, \tag{3.17a}$$

$$\gamma_s\left\langle\delta\widetilde{\mathbf{P}}_s^\dagger\delta\widetilde{\mathbf{P}}_s\right\rangle = \frac{2}{\left(1+\frac{g\beta}{\gamma_s}\right)^2}, \tag{3.17b}$$

and identify $g\beta/\gamma_s = \sqrt{P_p/P_p^{thr}}$, then we can see that we indeed do have squeezing in the P-quadrature, but that this is limited to at best to 3 dB of squeezing as the pump power goes to the threshold.

If we try to calculate the variance of the fluctuations exiting the cavity, we will see that we can measure much more squeezing. This is due to a destructive interference between the exiting field fluctuations and the vacuum outside the cavity. This part of the analysis starts by calculating the transmitted fluctuations, and as we defined above, we will look at the fluctuations exiting the output coupler

$$\delta\widetilde{\mathbf{X}}^{out}_{s,out} = \sqrt{2\gamma_s^{out}}\frac{\left[\gamma_p + i\omega\right]\widetilde{\mathbf{N}}^x_s + g\alpha\widetilde{\mathbf{N}}^x_p}{|g|^2|\alpha|^2 + (\gamma_s + i\omega - g\beta)(\gamma_p + i\omega)} - \delta\widetilde{\mathbf{X}}^{out}_{s,in}, \tag{3.18a}$$

$$\delta\widetilde{\mathbf{P}}^{out}_{s,out} = \sqrt{2\gamma_s^{out}}\frac{\left[\gamma_p + i\omega\right]\widetilde{\mathbf{N}}^p_s + g\alpha\widetilde{\mathbf{N}}^p_p}{|g|^2|\alpha|^2 + (\gamma_s + i\omega + g\beta)(\gamma_p + i\omega)} - \delta\widetilde{\mathbf{P}}^{out}_{s,in}. \tag{3.18b}$$

Next step is to calculate the variance of the field fluctuations. This calculation is however quite heavy and can be found in appendix (A). I will directly skip to the result equations (A.8a) and (A.8b)

$$\begin{aligned}\sigma^2\left(\delta\widetilde{\mathbf{X}}^{out}_{s,out}\right) = 1 &+ \eta_{esc}\frac{4\sqrt{\frac{P_p}{P_{th}}}}{\left[1-\sqrt{\frac{P_p}{P_{th}}}\right]^2 + \left[\frac{\omega}{\gamma_s}\right]^2} + \eta_{esc}\frac{4\frac{\gamma_s^{in}}{\gamma_s}\mathcal{V}_s^x}{\left[1-\sqrt{\frac{P_p}{P_{th}}}\right]^2 + \left[\frac{\omega}{\gamma_s}\right]^2} \\ &+ \eta_{esc}\frac{4|g|^2|\alpha|^2\left[\frac{\gamma_p}{\gamma_s} + \frac{\gamma_p^{out}}{\gamma_s}\mathcal{V}_p^x\right]}{\gamma_p^2\left[\frac{|g|^2|\alpha|^2-\omega^2}{\gamma_s\gamma_p} + \left(1-\sqrt{\frac{P_p}{P_{th}}}\right)\right]^2 + \omega^2\left[1-\sqrt{\frac{P_p}{P_{th}}} + \frac{\gamma_p}{\gamma_s}\right]^2},\end{aligned} \tag{3.19a}$$

$$\begin{aligned}\sigma^2\left(\delta\widetilde{\mathbf{P}}^{out}_{s,out}\right) = 1 &- \eta_{esc}\frac{4\sqrt{\frac{P_p}{P_{th}}}}{\left[1+\sqrt{\frac{P_p}{P_{th}}}\right]^2 + \left[\frac{\omega}{\gamma_s}\right]^2} + \eta_{esc}\frac{4\frac{\gamma_s^{in}}{\gamma_s}\mathcal{V}_s^p}{\left[1+\sqrt{\frac{P_p}{P_{th}}}\right]^2 + \left[\frac{\omega}{\gamma_s}\right]^2} \\ &+ \eta_{esc}\frac{4|g|^2|\alpha|^2\left[\frac{\gamma_p}{\gamma_s} + \frac{\gamma_p^{out}}{\gamma_s}\mathcal{V}_p^p\right]}{\gamma_p^2\left[\frac{|g|^2|\alpha|^2-\omega^2}{\gamma_s\gamma_p} + \left(1+\sqrt{\frac{P_p}{P_{th}}}\right)\right]^2 + \omega^2\left[1+\sqrt{\frac{P_p}{P_{th}}} + \frac{\gamma_p}{\gamma_s}\right]^2}.\end{aligned} \tag{3.19b}$$

These equations assume uncorrelated noise for both pump and fundamental fields, but besides this allows for excess noise in both amplitude $\mathcal{V}_i^x$ and phase quadrature $\mathcal{V}_i^p$. The above equations also assume the coherent amplitude of the fundamental field to be much smaller than that of the pump (no pump depletion) $|\alpha| \ll |\beta|$. Finally, we have introduced the OPO escape efficiency $\eta_{esc} = \gamma_s^{out}/\gamma_s$.

From this expression we see that if we have a non-zero coherent amplitude in the fundamental mode (also called seeding the OPO), then noise from the second harmonic pump will be coupled to the squeezing. Another disadvantage to using a seed is that excess noise in the seed will also be transferred to the squeezed light.

We will therefore assume no seed, which gives us the final result

$$\sigma^2\left(\delta\widetilde{\mathbf{X}}^{out}_{s,out}\right) = V_+ = 1 + \eta_{esc}\frac{4\sqrt{\frac{P_p}{P_p^{thr}}}}{\left(1-\sqrt{\frac{P_p}{P_p^{thr}}}\right)^2 + \left(\frac{\omega}{\gamma_s}\right)^2}, \tag{3.20a}$$

$$\sigma^2\left(\delta\widetilde{\mathbf{P}}^{out}_{s,out}\right) = V_- = 1 - \eta_{esc}\frac{4\sqrt{\frac{P_p}{P_p^{thr}}}}{\left(1+\sqrt{\frac{P_p}{P_p^{thr}}}\right)^2 + \left(\frac{\omega}{\gamma_s}\right)^2}, \tag{3.20b}$$

where we have switched notation of the variances to V_+ for anti-squeezing and V_- for squeezing for simplicity. As can be seen, these equations represent phase quadrature squeezing from an OPO. For an escape efficiency of $\eta_{esc} = 0.98$ and a signal cavity bandwidth of $\gamma_s = 2\pi\ 100\,\text{MHz}$, the expected squeezing and anti-squeezing as a function of pump power and frequency can be seen in figure (3.3).

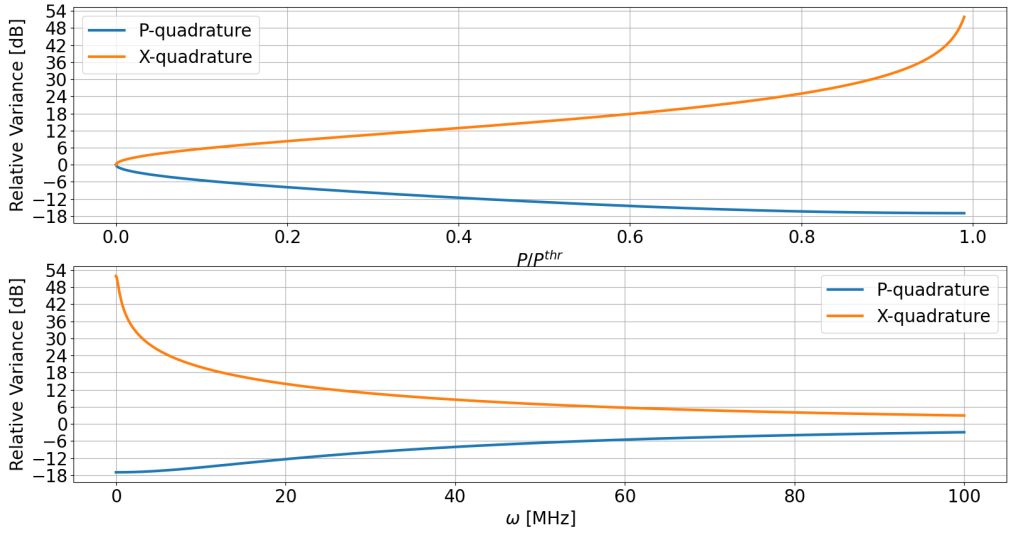

Figure 3.3: Top: Squeezing and anti-squeezing as a function of pump power for a sideband frequency of 0 Hz. **Bottom**: Squeezing and anti-squeezing as a function of sideband frequency for a pump power of $99\,\%P_p^{thr}$. Both graphs have $\eta_{esc} = 0.98$ and $\gamma_s = 2\pi\ 100\,\text{MHz}$

3.2.4 Effect of optical loss

Optical loss from the OPO to the detector can be very well modelled using equation (2.31), setting $\tau = 1 - \mathcal{L}_{opt} = \eta_{opt}$, where $\mathcal{L}_{opt}$ is the optical loss, and therefore η_{opt} is the optical efficiency. Evaluating the variances after the beamsplitter gives us

$$V_+ = 1 + \eta_{opt}\eta_{esc}\frac{4\sqrt{\frac{P_p}{P_p^{thr}}}}{\left(1 - \sqrt{\frac{P_p}{P_p^{thr}}}\right)^2 + \left(\frac{\omega}{\gamma_s}\right)^2}, \tag{3.21a}$$

$$V_- = 1 - \eta_{opt}\eta_{esc}\frac{4\sqrt{\frac{P_p}{P_p^{thr}}}}{\left(1 + \sqrt{\frac{P_p}{P_p^{thr}}}\right)^2 + \left(\frac{\omega}{\gamma_s}\right)^2}. \tag{3.21b}$$

The effect of optical loss is visualized in figure (3.4), where it is evident that the squeezing is quite fragile to loss, whereas the anti-squeezing is less so.

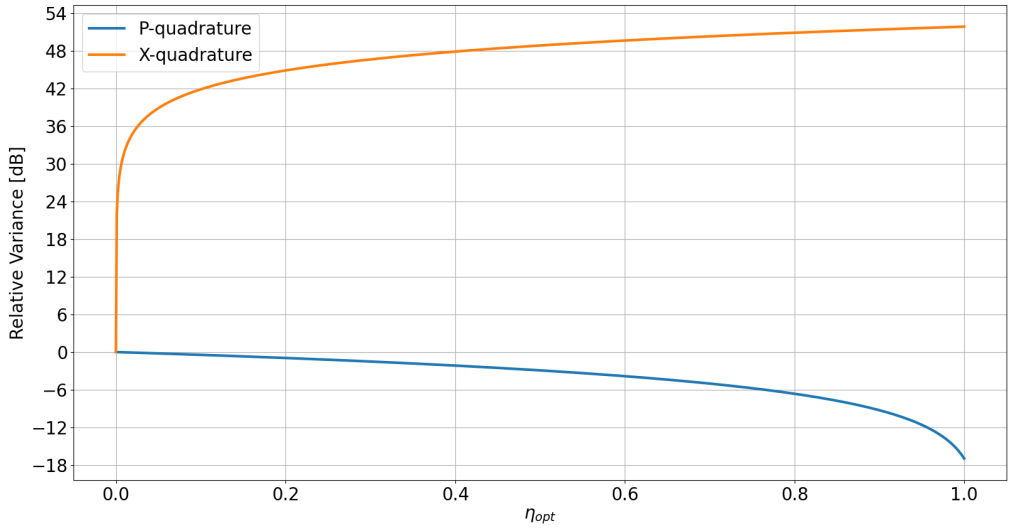

Figure 3.4: Simulation of squeezing and anti-squeezing as a function of optical loss. The other parameters are the same as in figure (3.3).

3.3 Detection of squeezed light via homodyne detection

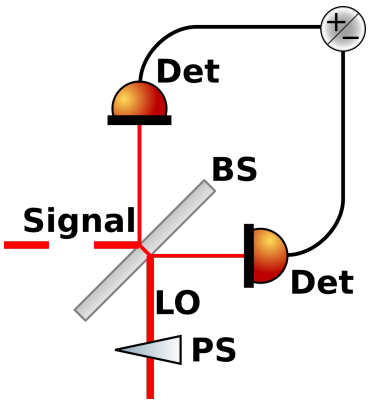

Figure 3.5: Sketch of a homodyne setup. BS: Beamsplitter, DET: Photodetector, PS: Phase shifter, LO: local oscillator.

Squeezed light is generally detected via a quadrature operator sensitive measurement technique. In section (2.3.3), we introduced the simple photodetector, but this is in general not enough to detect squeezed light, since a single photo detector only has access to the amplitude quadrature, and if squeezed vacuum is to be measured, it can be very difficult to get good signal clearance of the detector electronic noise. We therefore need a detection scheme that can allow us to measure the entire phase space and boost the signal high above the electronic noise.

The two most popular techniques for accomplishing these two tasks are homodyning and heterodyning. Homodyning allows for the measurement of all quadratures of the signal field, but not simultaneously, while heterodyning allows for the simultaneous measurement of two orthogonal quadratures of the signal field, but comes at the expense of a 50 % loss penalty, which is undesirable for squeezed light detection. Homodyning is therefore the preferred method, and

in the following section I will go through the mathematics behind homodyne detection.

3.3.1 Detection of squeezing and the effect of imperfect homodyne detection

A schematic representation is shown in figure (3.5), where the squeezed light enters in one input-port of the beam-splitter and a bright local oscillator enters from the second input-port. To begin with, we will consider the output modes $\hat{\mathbf{c}}$ and $\hat{\mathbf{d}}$ of the beam-splitter with power transmittance $\sqrt{\tau}$.

$$\hat{\mathbf{c}} = \sqrt{\tau}\hat{\mathbf{a}} + \sqrt{1-\tau}\hat{\mathbf{b}}e^{i\pi/2}, \tag{3.22a}$$

$$\hat{\mathbf{d}} = \sqrt{1-\tau}\hat{\mathbf{a}}e^{i\pi/2} + \sqrt{\tau}\hat{\mathbf{b}}. \tag{3.22b}$$

If the quantum efficiency of the diodes is imperfect, then we can insert another beam-splitter model with power transmittance η_{QE} to take into account the vacuum added by this additional loss

$$\hat{\mathbf{c}}_{imp} = \sqrt{\eta_{QE}}\hat{\mathbf{c}} + \sqrt{1-\eta_{QE}}\hat{\mathbf{v}}_c e^{i\pi/2}, \tag{3.23a}$$

$$\hat{\mathbf{d}}_{imp} = \sqrt{\eta_{QE}}\hat{\mathbf{d}} + \sqrt{1-\eta_{QE}}\hat{\mathbf{v}}_d e^{i\pi/2}. \tag{3.23b}$$

For simplicity, we assume the photo-diodes to have the same efficiency. The power of the light impinging on the photodiodes is given by

$$\begin{aligned}\hat{\mathbf{P}}_c &= \hbar\Omega_c\left[\sqrt{\eta_{QE}}\hat{\mathbf{c}}^\dagger + \sqrt{1-\eta_{QE}}\hat{\mathbf{v}}_c^\dagger e^{-i\pi/2}\right]\left[\sqrt{\eta_{QE}}\hat{\mathbf{c}} + \sqrt{1-\eta_{QE}}\hat{\mathbf{v}}_c e^{i\pi/2}\right] \\ &= \hbar\Omega_c\eta_{QE}\left[\tau\hat{\mathbf{a}}^\dagger\hat{\mathbf{a}} + (1-\tau)\hat{\mathbf{b}}^\dagger\hat{\mathbf{b}} + \sqrt{\tau}\sqrt{1-\tau}\left(\hat{\mathbf{a}}\hat{\mathbf{b}}^\dagger e^{-i\pi/2} + \hat{\mathbf{a}}^\dagger\hat{\mathbf{b}}e^{i\pi/2}\right)\right] + \hbar\Omega_c\left(1-\eta_{QE}\right)\hat{\mathbf{v}}_c^\dagger\hat{\mathbf{v}}_c \\ &+ \hbar\Omega_c\sqrt{\eta_{QE}(1-\eta_{QE})}\left[\sqrt{\tau}\left(\hat{\mathbf{v}}_c\hat{\mathbf{a}}^\dagger e^{i\pi/2} + \hat{\mathbf{v}}_c^\dagger\hat{\mathbf{a}}e^{-i\pi/2}\right) + \sqrt{1-\tau}\left(\hat{\mathbf{v}}_c\hat{\mathbf{b}}^\dagger + \hat{\mathbf{v}}_c^\dagger\hat{\mathbf{b}}\right)\right],\end{aligned} \tag{3.24a}$$

$$\begin{aligned}\hat{\mathbf{P}}_d &= \hbar\Omega_c\left[\sqrt{\eta_{QE}}\hat{\mathbf{d}}^\dagger + \sqrt{1-\eta_{QE}}\hat{\mathbf{v}}_d^\dagger e^{-i\pi/2}\right]\left[\sqrt{\eta_{QE}}\hat{\mathbf{d}} + \sqrt{1-\eta_{QE}}\hat{\mathbf{v}}_d e^{i\pi/2}\right] \\ &= \hbar\Omega_c\eta_{QE}\left[\tau\hat{\mathbf{b}}^\dagger\hat{\mathbf{b}} + (1-\tau)\hat{\mathbf{a}}^\dagger\hat{\mathbf{a}} - \sqrt{\tau}\sqrt{1-\tau}\left(\hat{\mathbf{a}}\hat{\mathbf{b}}^\dagger e^{-i\pi/2} + \hat{\mathbf{a}}^\dagger\hat{\mathbf{b}}e^{i\pi/2}\right)\right] + \hbar\Omega_c\left(1-\eta_{QE}\right)\hat{\mathbf{v}}_d^\dagger\hat{\mathbf{v}}_d \\ &+ \hbar\Omega_c\sqrt{\eta_{QE}(1-\eta_{QE})}\left[\sqrt{1-\tau}\left(\hat{\mathbf{v}}_d\hat{\mathbf{a}}^\dagger + \hat{\mathbf{v}}_d^\dagger\hat{\mathbf{a}}\right) + \sqrt{\tau}\left(\hat{\mathbf{v}}_d\hat{\mathbf{b}}^\dagger e^{i\pi/2} + \hat{\mathbf{v}}_d^\dagger\hat{\mathbf{b}}e^{-i\pi/2}\right)\right].\end{aligned} \tag{3.24b}$$

Next step is to multiply by R to get the photo-currents and either subtract or sum the two inputs. We will start with the sum as this is the simplest, assuming the beamsplitter to be balanced $\tau = 1/2$

$$\begin{aligned}\hat{\mathbf{i}}_+ &= R\hbar\Omega_c\eta_{QE}\left[\hat{\mathbf{a}}^\dagger\hat{\mathbf{a}} + \hat{\mathbf{b}}^\dagger\hat{\mathbf{b}}\right] + R\hbar\Omega_c\left(1-\eta_{QE}\right)\left[\hat{\mathbf{v}}_c^\dagger\hat{\mathbf{v}}_c + \hat{\mathbf{v}}_d^\dagger\hat{\mathbf{v}}_d\right] \\ &+ R\hbar\Omega_c\sqrt{\eta_{QE}(1-\eta_{QE})}\left[\sqrt{\tau}\left(\hat{\mathbf{v}}_c\hat{\mathbf{a}}^\dagger e^{i\pi/2} + \hat{\mathbf{v}}_c^\dagger\hat{\mathbf{a}}e^{-i\pi/2}\right) + \sqrt{1-\tau}\left(\hat{\mathbf{v}}_c\hat{\mathbf{b}}^\dagger + \hat{\mathbf{v}}_c^\dagger\hat{\mathbf{b}}\right)\right] \\ &+ R\hbar\Omega_c\sqrt{\eta_{QE}(1-\eta_{QE})}\left[\sqrt{1-\tau}\left(\hat{\mathbf{v}}_d\hat{\mathbf{a}}^\dagger + \hat{\mathbf{v}}_d^\dagger\hat{\mathbf{a}}\right) + \sqrt{\tau}\left(\hat{\mathbf{v}}_d\hat{\mathbf{b}}^\dagger e^{i\pi/2} + \hat{\mathbf{v}}_d^\dagger\hat{\mathbf{b}}e^{-i\pi/2}\right)\right].\end{aligned} \tag{3.24c}$$

We now linearize the operators as $\hat{\mathbf{a}} = \alpha + \delta\hat{\mathbf{a}}$ and $\hat{\mathbf{b}} = \left(\beta + \delta\hat{\mathbf{b}}\right)e^{-i\phi_{LO}}$, only keeping terms to first order in fluctuations, and taking the expectation value and variance of the operator.

$$\langle i_+\rangle = R\hbar\Omega_c\eta_{QE}\left[|\alpha|^2 + |\beta|^2\right], \tag{3.24d}$$

$$\sigma^2(i_+) \approx R^2\hbar^2\Omega_c^2\left[|\alpha|^2\sigma^2\left(\delta\hat{\mathbf{X}}_s\right) + |\beta|^2\sigma^2\left(\delta\hat{\mathbf{X}}_{LO}\right)\right], \tag{3.24e}$$

where for the variance, we have neglected the vacuum terms. We see that the homodyne detector in "sum" mode works as a normal single diode detector with two input optical modes.

For the subtraction of the two detector currents $\hat{\mathbf{i}}_-$ we get,

$$\begin{aligned}\hat{\mathbf{i}}_- &= R\hbar\Omega_c\eta_{QE}\left[(\tau-(1-\tau))\hat{\mathbf{a}}^\dagger\hat{\mathbf{a}}+((1-\tau)-\tau)\hat{\mathbf{b}}^\dagger\hat{\mathbf{b}}+2\sqrt{\tau(1-\tau)}\left(\hat{\mathbf{a}}\hat{\mathbf{b}}^\dagger e^{-i\pi/2}+\hat{\mathbf{a}}^\dagger\hat{\mathbf{b}}e^{i\pi/2}\right)\right]\\ &+ R\hbar\Omega_c\left(1-\eta_{QE}\right)\left[\hat{\mathbf{v}}_c^\dagger\hat{\mathbf{v}}_c-\hat{\mathbf{v}}_d^\dagger\hat{\mathbf{v}}_d\right]\\ &+ R\hbar\Omega_c\sqrt{\eta_{QE}(1-\eta_{QE})}\left[\sqrt{1-\tau}\left(\hat{\mathbf{v}}_c\hat{\mathbf{b}}^\dagger+\hat{\mathbf{v}}_c^\dagger\hat{\mathbf{b}}\right)+\sqrt{\tau}\left(\hat{\mathbf{v}}_d\hat{\mathbf{b}}^\dagger e^{-i\pi/2}+\hat{\mathbf{v}}_d^\dagger\hat{\mathbf{b}}e^{i\pi/2}\right)\right]\\ &- R\hbar\Omega_c\sqrt{\eta_{QE}(1-\eta_{QE})}\left[\sqrt{\tau}\left(\hat{\mathbf{v}}_d\hat{\mathbf{a}}^\dagger+\hat{\mathbf{v}}_d^\dagger\hat{\mathbf{a}}\right)+\sqrt{1-\tau}\left(\hat{\mathbf{v}}_c\hat{\mathbf{a}}^\dagger e^{-i\pi/2}+\hat{\mathbf{v}}_c^\dagger\hat{\mathbf{a}}e^{i\pi/2}\right)\right]. \qquad (3.25)\end{aligned}$$

If we assume the beamsplitter to be balanced $\tau = 1/2$, the local oscillator to be a bright classical field and $\beta \gg \alpha$ and only keep terms first order in fluctuations and β, we end up with

$$\begin{aligned}\hat{\mathbf{i}}_- &\approx R\hbar\Omega_c\eta_{QE}|\beta|\left(\delta\hat{\mathbf{a}}e^{-i(\phi_{LO}+\pi/2)}+\delta\hat{\mathbf{a}}^\dagger e^{i(\phi_{LO}+\pi/2)}\right)\\ &+ \frac{R\hbar\Omega_c}{\sqrt{2}}\sqrt{\eta_{QE}(1-\eta_{QE})}|\beta|\left[\left(\hat{\mathbf{v}}_c e^{-i\phi_{LO}}+\hat{\mathbf{v}}_c^\dagger e^{i\phi_{LO}}\right)+\left(\hat{\mathbf{v}}_d e^{-i(\phi_{LO}+\pi/2)}+\hat{\mathbf{v}}_d^\dagger e^{i(\phi_{LO}+\pi/2)}\right)\right],\\ &= R\hbar\Omega_c\eta_{QE}|\beta|\delta\hat{\mathbf{X}}_s^{\phi+\pi/2}+\frac{R\hbar\Omega_c}{\sqrt{2}}\sqrt{\eta_{QE}(1-\eta_{QE})}|\beta|\left[\delta\hat{\mathbf{X}}_{c,v}^{\phi}+\delta\hat{\mathbf{X}}_{d,v}^{\phi+\pi/2}\right]. \qquad (3.26)\end{aligned}$$

From this equation we see that the mean of the difference current is zero, but the variance $\sigma^2\left(\hat{\mathbf{i}}_-\right)$ is

$$\sigma^2\left(\hat{\mathbf{i}}_-\right) \approx R^2\hbar^2\Omega_c^2|\beta|^2\eta_{QE}\left[\eta_{QE}\sigma^2\left(\delta\hat{\mathbf{X}}_s^{\phi_{LO}+\pi/2}\right)+1-\eta_{QE}\right]. \qquad (3.27)$$

In general, the proportionality factor between the detected voltage from a photo detector and the number of detected photons (or quadrature values) is either unknown or cumbersome to estimate. To circumvent this proportionality factor, the signal can be normalized to the shot noise (which is detected in a homodyne detector by leaving the signal port empty - the signal is a vacuum state), and from this ratio the mean photon number (or quadrature values) can be calculated.

If we assume the squeezing to be in the P-quadrature as defined earlier, then for $\phi_{LO} = 0$ we recover a variance proportional to the squeezed quadrature variance, and if $\phi_{LO} = \pi/2$ we recover the anti-squeezed quadrature variance. Due to the imperfect detection η_{QE} the variances are scaled as

$$V_+ = 1+\eta_{QE}\eta_{opt}\eta_{esc}\frac{4\sqrt{\frac{P_p}{P_p^{thr}}}}{\left(1-\sqrt{\frac{P_p}{P_p^{thr}}}\right)^2+\left(\frac{\omega}{\gamma_s}\right)^2}, \qquad (3.28a)$$

$$V_- = 1-\eta_{QE}\eta_{opt}\eta_{esc}\frac{4\sqrt{\frac{P_p}{P_p^{thr}}}}{\left(1+\sqrt{\frac{P_p}{P_p^{thr}}}\right)^2+\left(\frac{\omega}{\gamma_s}\right)^2}. \qquad (3.28b)$$

3.3.2 Effect of imperfect mode-matching

Imperfect mode-matching between the squeezed mode and the local oscillator can come from beam misalignment, polarization mismatch or mode-mismatch. The effect on the squeezing is the same for all these causes; whatever part of the signal and local oscillator that is not interacting

causes vacuum to leak into the signal mode. Polarization mismatch is the simplest to model, so in the following we will do this. For simplicity we will assume the detection to be perfect $\eta_{QE} = 1$ and beamsplitter balance to be perfect. The polarization mismatch is then modelled as a half-wave plate before the 50/50 beam-splitter. The local oscillator will be assumed to have perfect s-polarization, but the signal mode will be assumed to be a mix between s-and p-polarization (the reverse situation leads to the same result)

$$\hat{\mathbf{a}}_{s-pol} = \sqrt{\eta}\hat{\mathbf{a}} + \sqrt{1-\eta}\hat{\mathbf{v}}_a, \tag{3.29a}$$
$$\hat{\mathbf{a}}_{p-pol} = \sqrt{1-\eta}\hat{\mathbf{a}} + \sqrt{\eta}\hat{\mathbf{v}}_a, \tag{3.29b}$$
$$\hat{\mathbf{b}}_{s-pol} = \hat{\mathbf{b}}, \tag{3.29c}$$
$$\hat{\mathbf{b}}_{p-pol} = \hat{\mathbf{v}}_b. \tag{3.29d}$$

For this the photo-currents at both detectors (neglecting second-order fluctuation terms) will be

$$\begin{aligned}\hat{\mathbf{i}}_c &= R\hbar\Omega_c\left[\hat{\mathbf{c}}^\dagger_{s-pol}\hat{\mathbf{c}}_{s-pol} + \hat{\mathbf{c}}^\dagger_{p-pol}\hat{\mathbf{c}}_{p-pol}\right] = \frac{R\hbar\Omega_c}{2}\left[\hat{\mathbf{a}}^\dagger\hat{\mathbf{a}} + \hat{\mathbf{b}}^\dagger\hat{\mathbf{b}}\right] \\ &+ \frac{R\hbar\Omega_c}{2}\left[\sqrt{\eta}\left(\hat{\mathbf{a}}\hat{\mathbf{b}}^\dagger e^{-i\pi/2} + \hat{\mathbf{a}}^\dagger\hat{\mathbf{b}}e^{i\pi/2}\right) + \sqrt{1-\eta}\left(\hat{\mathbf{v}}_a\hat{\mathbf{b}}^\dagger e^{-i\pi/2} + \hat{\mathbf{v}}^\dagger_a\hat{\mathbf{b}}e^{i\pi/2}\right)\right] \\ &+ \frac{R\hbar\Omega_c}{2}\left[\sqrt{1-\eta}\hat{\mathbf{a}}^\dagger\left(2\sqrt{\eta}\hat{\mathbf{v}}_a + \hat{\mathbf{v}}_b e^{i\pi/2}\right) + \sqrt{1-\eta}\hat{\mathbf{a}}\left(2\sqrt{\eta}\hat{\mathbf{v}}^\dagger_a + \hat{\mathbf{v}}^\dagger_b e^{-i\pi/2}\right)\right],\end{aligned} \tag{3.30a}$$

$$\begin{aligned}\hat{\mathbf{i}}_d &= R\hbar\Omega_c\left[\hat{\mathbf{d}}^\dagger_{s-pol}\hat{\mathbf{d}}_{s-pol} + \hat{\mathbf{d}}^\dagger_{p-pol}\hat{\mathbf{d}}_{p-pol}\right] = \frac{R\hbar\Omega_c}{2}\left[\hat{\mathbf{a}}^\dagger\hat{\mathbf{a}} + \hat{\mathbf{b}}^\dagger\hat{\mathbf{b}}\right] \\ &- \frac{R\hbar\Omega_c}{2}\left[\sqrt{\eta}\left(\hat{\mathbf{a}}\hat{\mathbf{b}}^\dagger e^{-i\pi/2} + \hat{\mathbf{a}}^\dagger\hat{\mathbf{b}}e^{i\pi/2}\right) + \sqrt{1-\eta}\left(\hat{\mathbf{v}}_a\hat{\mathbf{b}}^\dagger e^{-i\pi/2} + \hat{\mathbf{v}}^\dagger_a\hat{\mathbf{b}}e^{i\pi/2}\right)\right] \\ &+ \frac{R\hbar\Omega_c}{2}\left[\sqrt{1-\eta}\hat{\mathbf{a}}^\dagger\left(2\sqrt{\eta}\hat{\mathbf{v}}_a - \hat{\mathbf{v}}_b e^{i\pi/2}\right) + \sqrt{1-\eta}\hat{\mathbf{a}}\left(2\sqrt{\eta}\hat{\mathbf{v}}^\dagger_a - \hat{\mathbf{v}}^\dagger_b e^{-i\pi/2}\right)\right].\end{aligned} \tag{3.30b}$$

The final terms are interference-terms between local oscillator and signal. The interference is proportional to $\sqrt{\eta}$, and in [39] this efficiency is identified as the fringe visibility $\sqrt{\eta} = \mathcal{V}$.

If we continue to look at the difference current and make the usual assumptions $\hat{\mathbf{b}} \to |\beta|e^{-i\phi_{LO}}$ and $\beta >> \alpha$, then we end up with

$$\hat{\mathbf{i}}_- \approx R\hbar\Omega_c\beta\left[\mathcal{V}\delta\hat{\mathbf{X}}_s^{\phi+\pi/2} + \sqrt{1-\mathcal{V}^2}\delta\hat{\mathbf{X}}_{a,v}^{\phi+\pi/2}\right] \tag{3.31}$$

with the variance given by (this time also including η_{QE})

$$\sigma^2\left(\hat{\mathbf{i}}_-\right) \approx R^2\hbar^2\Omega_c^2\beta^2\left[\mathcal{V}^2\left\langle\left(\delta\hat{\mathbf{X}}_s^{\phi+\pi/2}\right)^2\right\rangle + 1 - \mathcal{V}^2\right] \Rightarrow,$$

$$V_+ = 1 + \mathcal{V}^2\eta_{QE}\eta_{opt}\eta_{esc}\frac{4\sqrt{\frac{P_p}{P_p^{thr}}}}{\left(1-\sqrt{\frac{P_p}{P_p^{thr}}}\right)^2 + \left(\frac{\omega}{\gamma_s}\right)^2}, \tag{3.32a}$$

$$V_- = 1 - \mathcal{V}^2\eta_{QE}\eta_{opt}\eta_{esc}\frac{4\sqrt{\frac{P_p}{P_p^{thr}}}}{\left(1+\sqrt{\frac{P_p}{P_p^{thr}}}\right)^2 + \left(\frac{\omega}{\gamma_s}\right)^2}, \tag{3.32b}$$

if we choose the phase of the local oscillator correctly (and add imperfect diode efficiency back). The visibility is an important parameter to optimize since the loss scales quadratically with the efficiency.

3.3.3 Effect of phase noise between pump and local oscillator

The final thing to consider is the case, where we have fluctuations in the phase of the local oscillator relative to the squeezed light. As has been used above the general quadrature operator is defined as $\delta\hat{\mathbf{X}}_s^{\phi} = \delta\hat{\mathbf{a}}e^{-i\phi} + \delta\hat{\mathbf{a}}^{\dagger}e^{i\phi}$, where for $\phi = 0$ we recover the amplitude quadrature $\delta\hat{\mathbf{X}}$, and for $\phi = \pi/2$ we recover the phase quadrature $\delta\hat{\mathbf{P}}$. For phases between 0 and $\pi/2$ we recover a mix of the two quadratures, and this can have a detrimental effect on the squeezing as an imperfect phase will cause anti-squeezing to be mixed into the squeezing during the measurement.

In order to model this we will assume the phase noise to be normally distributed $P(\phi, \phi_{RMS})$ around 0 phase with width ϕ_{RMS}

$$P(\phi, \phi_{RMS}) = \frac{1}{\sqrt{2\pi}\phi_{RMS}} e^{\frac{-\phi^2}{2\phi_{RMS}^2}}. \tag{3.33}$$

We defined the general covariance matrix of a pure squeezed state in equation (2.21), and we can change this to our general squeezed state by exchanging the diagonal values with equations (3.32a) and (3.32b). The rotated covariance matrix being

$$\underline{\underline{\Gamma}}(\phi) = \begin{pmatrix} \cos^2(\phi)V_+ + \sin^2(\phi)V_- & (V_+ - V_-)\frac{\sin(2\phi)}{2} \\ (V_+ - V_-)\frac{\sin(2\phi)}{2} & \cos^2(\phi)V_- + \sin^2(\phi)V_+ \end{pmatrix}. \tag{3.34}$$

We now multiply with the phase-distribution and integrate over all ϕ to get the phase-noise affected covariance matrix

$$\begin{aligned} \underline{\underline{\Gamma}}_{PN} &= \int_0^{2\pi} \underline{\underline{\Gamma}}(\phi)P(\phi, \phi_{RMS})\mathrm{d}\phi \\ &= \begin{pmatrix} \frac{1}{2}\left[\left(1 + e^{-2\phi_{RMS}^2}\right)V_+ + \left(1 - e^{-2\phi_{RMS}^2}\right)V_-\right] & 0 \\ 0 & \frac{1}{2}\left[\left(1 + e^{-2\phi_{RMS}^2}\right)V_- + \left(1 - e^{-2\phi_{RMS}^2}\right)V_+\right] \end{pmatrix}. \end{aligned} \tag{3.35}$$

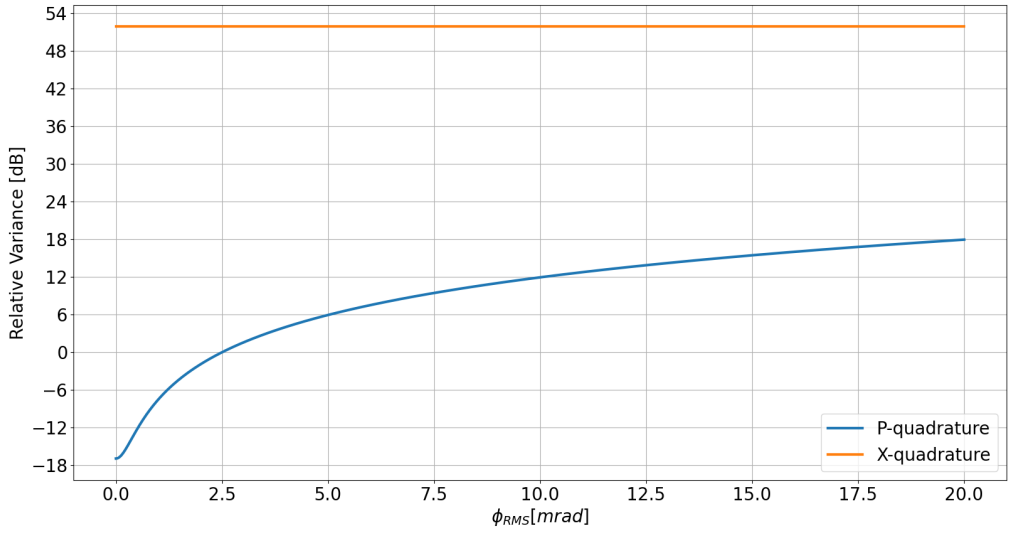

Figure 3.6: Squeezed and anti-squeezed variance as a function of phase noise. The pump power, frequency and total loss is the same as in figure (3.3).

$\left(1+e^{-2\phi_{RMS}^2}\right)/2 \approx \cos^2(\phi_{RMS})$ since they both have the same second-order expansion in ϕ, and the same is true for $\left(1-e^{-2\phi_{RMS}^2}\right)/2 \approx \sin^2(\phi_{RMS})$. We can therefore reduce the matrix to it's final approximate form

$$\underline{\underline{\Gamma}}_{PN} \approx \begin{pmatrix} \cos^2(\phi_{RMS})V_+ + \sin^2(\phi_{RMS})V_- & 0 \\ 0 & \cos^2(\phi_{RMS})V_- + \sin^2(\phi_{RMS})V_+ \end{pmatrix}. \tag{3.36}$$

The effect of phase noise on the squeezed and anti-squeezed variances can be seen in figure (3.6).

Any sufficiently advanced technology is indistinguishable from magic.

Science 158
by Arthur C. Clarke, 1967

4 Feedback systems

Most of the experiments done in our laboratory critically rely on keeping cavities on resonance for the entirety of the experiment duration. Futhermore, we need to be able to stabilize the relative phases between different optical fields. In this chapter, I will make an overview of the feedback systems used in chapters (5), (7) and (8) to stabilize cavities and relative phases.

4.1 Pound-Drever-Hall

The Pound-Drever-Hall (PDH) locking technique [40, 41] is probably the most popular cavity stabilization technique among several [42–44]. The issue with cavity stabilization is that even though the transmitted or reflected light from a cavity changes quickly away from resonance, the symmetry of these signals makes it impossible to differentiate between either side of the resonance. The phase, however, has a sharp zero crossing around the resonance and is therefore ideal to use as an error signal to feedback to either a piezo driven mirror in the cavity or to the laser itself.

Phase changes in a single optical field are ill-defined and cannot be measured with a single field alone. The main difference between different stabilization schemes is then the method used to provide a stable phase reference for which to compare the phase of the optical field as the detuning is changed.

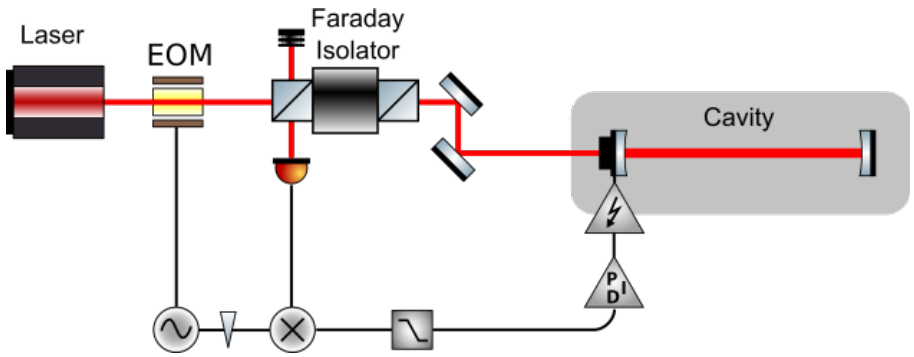

Figure 4.1: Sketch of a typical Pound-Drever-Hall cavity stabilization setup.

The PDH technique uses phase modulation to create sidebands in the optical field that can serve as this stable reference. A typical PDH setup is sketched in figure (4.1). An EOM creates

sidebands at a certain frequency ω_m ideally higher than the bandwidth of the cavity γ. The light then interacts with the cavity, is reflected and measured in a photo-detector. The starting point of the analysis is equation (2.41b), where we only look at the mean-field amplitudes. In the rotating field of the carrier, the field reflected off the cavity is

$$A_{in}^{out} = A_{in}^{in}\Big(R(\Delta) - i\frac{m}{2}R(\Delta+\omega_m)e^{-i\omega_m t} - i\frac{m}{2}R(\Delta-\omega_m)e^{i\omega_m t}\Big), \tag{4.1}$$

where the reflection coefficient $R(\Delta) = \big(2\gamma_{in}(\gamma+i\Delta)/\big(\gamma^2+\Delta^2\big) - 1\big)$.

The photodetector measures $\big|A_{in}^{out}\big|$ which will contain 3 types of contributions: I_{DC} proportional to the total power measured by the diodes, I_{ω_m} proportional to the interference between the sidebands and the carrier, and $I_{2\omega_m}$ proportional to the interference between the sidebands

$$I_{DC} \propto \big|A_{in}^{in}\big|^2\Big(|R(\Delta)|^2 + \frac{m^2}{4}|R(\Delta+\omega_m)|^2 + \frac{m^2}{4}|R(\Delta-\omega_m)|^2\Big), \tag{4.2a}$$

$$\begin{aligned} I_{\omega_m} \propto & -i\frac{m}{2}\big|A_{in}^{in}\big|^2\big(R^*(\Delta)R(\Delta+\omega_m)e^{-i\omega_m t} + R^*(\Delta)R(\Delta-\omega_m)e^{i\omega_m t}\big) \\ & - i\frac{m}{2}\big|A_{in}^{in}\big|^2\big(R(\Delta)R^*(\Delta+\omega_m)e^{i\omega_m t} - R(\Delta)R^*(\Delta-\omega_m)e^{-i\omega_m t}\big), \end{aligned} \tag{4.2b}$$

$$I_{2\omega_m} \propto \frac{m^2}{4}\big|A_{in}^{in}\big|^2\big(R^*(\Delta+\omega_m)R(\Delta-\omega_m)e^{2i\omega_m t} + R(\Delta+\omega_m)R^*(\Delta-\omega_m)e^{-2i\omega_m t}\big). \tag{4.2c}$$

We are interested in the terms oscillating at ω_m since these terms contain information about the relative phase between carrier and sidebands. If we expand the complex exponentials and reorder the terms, we get

$$\begin{aligned} I_{\omega_m} \propto & -m\big|A_{in}^{in}\big|^2\cos(\omega_m t)\,\mathbb{I}\mathrm{m}\left[R(\Delta)R^*(\Delta+\omega_m) + R(\Delta)R^*(\Delta-\omega_m)\right] \\ & - m\big|A_{in}^{in}\big|^2\sin(\omega_m t)\,\mathbb{R}\mathrm{e}\left[R(\Delta)R^*(\Delta+\omega_m) - R(\Delta)R^*(\Delta-\omega_m)\right]. \end{aligned} \tag{4.3}$$

The measured signal we mix with an electronic local oscillator (ELO) $I_{\omega_m}\cos(\omega_m t + \phi_{ELO})$ and lowpass filter with a cut-off frequency well below ω_m.

Depending on our choice of ϕ_{ELO}, we can pick either the cosine or sine term of equation (4.3), since

$$\cos(\omega_m t)\cos(\omega_m t) = 1/2 + 1/2\cos(2\omega_m t), \tag{4.4a}$$

$$\sin(\omega_m t)\sin(\omega_m t) = 1/2 - 1/2\cos(2\omega_m t), \tag{4.4b}$$

$$\cos(\omega_m t)\sin(\omega_m t) = 1/2\sin(2\omega_m t), \tag{4.4c}$$

and the lowpass filter will make sure to kill off any oscillating terms leaving only the DC term.

If the sideband frequency is smaller than the cavity bandwidth $\omega_m < \gamma$, then the reflection coefficients will be predominantly real, and the sine term will dominate. If the sideband frequency is larger than the cavity bandwidth $\omega_m < \gamma$, then the reflection coefficients will be imaginary, and the cosine term will dominate.

In figure (4.2) the PDH error signal as a function of cavity detuning for the two different cases is shown. We see that having the sideband frequency be outside the cavity bandwidth gives us the largest error signal with the highest sensitivity to changes in cavity detuning, and this is usually the preferred configuration, for which the resulting error signal will be

$$E_{PDH} \propto -\frac{m}{2}\big|A_{in}^{in}\big|^2\,\mathbb{I}\mathrm{m}\left[R(\Delta)R^*(\Delta+\omega_m) + R(\Delta)R^*(\Delta-\omega_m)\right]. \tag{4.5}$$

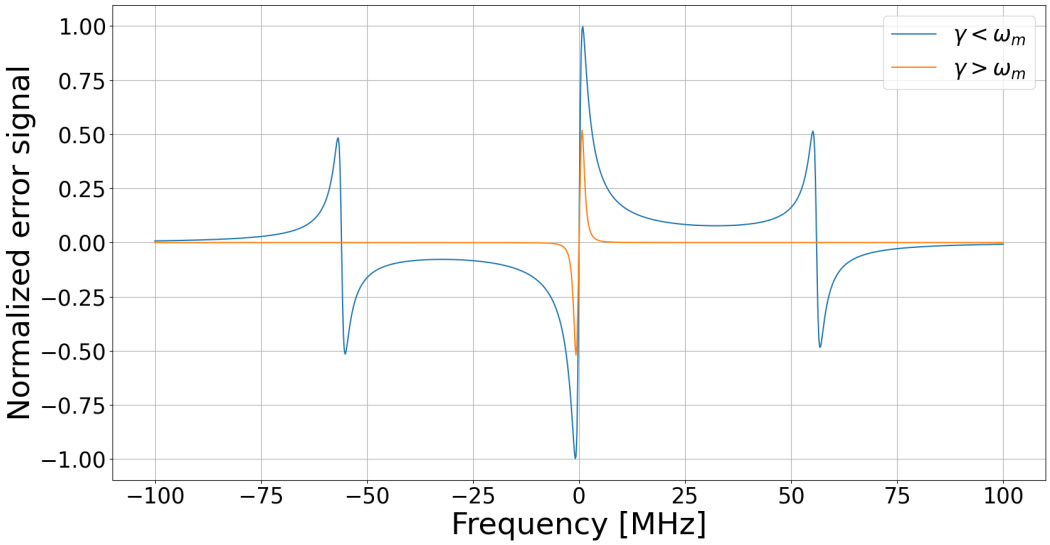

Figure 4.2: The PDH error signal as a function of cavity detuning in the two cases of $\omega_m > \gamma$ and $\omega_m < \gamma$. The cavity parameters are the same as in figure (2.6), with a sideband frequency of 56 MHz in the large frequency case and 700 kHz in the small frequency case.

4.2 Coherent control

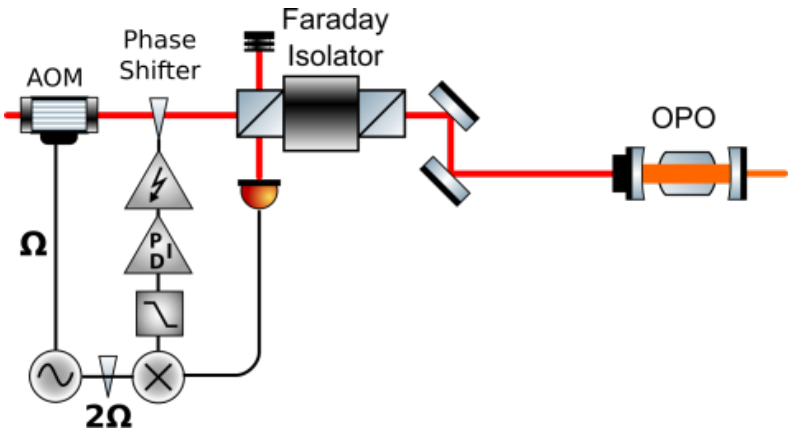

Figure 4.3: A schematic of a typical coherent control setup using a phase shifter to actuate the phase.

Squeezed vacuum does not have a coherent amplitude, and a direct measurement of the relative phase between the local oscillator and the squeezed light is therefore not possible. You could imagine running a maximum/ minimum search algorithm of the squeezed quadrature variance and feed this back to the local oscillator phase, but this would only allow for locking to either the squeezed or anti-squeezed quadrature (not an intermediary angle), and depending on the speed of the algorithm excess phase noise could be added to the measurement.

The way of locking the relative phase involves adding a seed to the squeezing or another field to propagate together with the squeezing to provide a phase reference for the local oscillator. Since we do not want to seed the OPO, we will add a field to the squeezed light which will not add noise to the squeezed state, but will provide a phase reference.

The method we will use is called coherent control [45], which involves phase locking a fre-

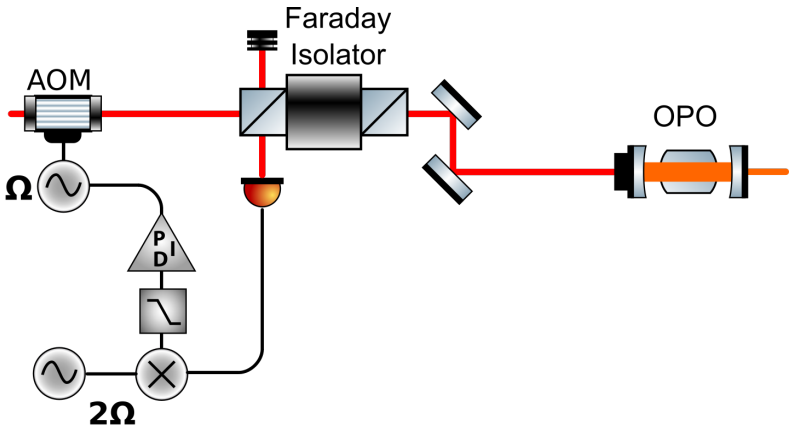

Figure 4.4: A schematic of a coherent control setup using frequency modulation of the AOM to actuate the phase.

quency up-shifted field $\Omega_c + \omega_m$ (called the coherent locking field - CLF) to the pump field and then letting it propagate together with the squeezed light to serve as a reference. Schematics of such a locking scheme is shown in figures (4.3) and (4.4). The up-shifted beam is created using an AOM and only using the positive sideband.

As mentioned in section (3.1), in the non-degenerate case $\omega_s \neq \omega_i$ with the idler field being in the vacuum state difference-frequency-generation (DFG) will take place with a pump photon being split into a signal photon and an idler photon, with this idler having the frequency $2\Omega_c - (\Omega_c + \omega_m) = \Omega_C - \omega_m$. The generation of the idler field is phase sensitive, and the phase of the idler field will obey a strict relationship with the phase of the pump field.

Both signal and idler fields will exit back out of the input port $A^{out}_{tot,in} = A^{out}_{s,in} + A^{out}_{i,in}$ and will be detected on a photo-detector. The detected signal will then be proportional to

$$\begin{aligned}\left|A^{out}_{tot,in}\right| =& \propto \left|A^{out}_{s,in}\right|^2 + \left|A^{out}_{i,in}\right|^2 \\ &+ \cos(2\omega_m t + \phi_s - \phi_i)\,\mathbb{R}\mathrm{e}\left(A^{out}_{s,in}A^{out*}_{i,in}\right) + \sin(2\omega_m t + \phi_s - \phi_i)\,\mathbb{I}\mathrm{m}\left(A^{out}_{s,in}A^{out*}_{i,in}\right)\end{aligned} \tag{4.6}$$

Similarly to the PDH system, we are only interested in the interference terms, so we mix with $\cos(2\omega_m t + \phi_{ELO})$ and low-pass filter to isolate the interference term.

Calculating the explicit form of the error signal involves solving the 3 field OPO cavity dynamics in the steady state assuming no pump-depletion. This has been done in the appendix of the PhD thesis of Erik Oelker of MIT [46] and the approximate result

$$E_{CL} \approx \frac{4\gamma_s^{in}\left|A^{in}_{s,in}\right|^2\sqrt{\frac{P_p}{P_p^{thr}}}}{\gamma_s\sqrt{\left(1-\frac{P_p}{P_p^{thr}}-\left(\frac{\omega_m}{\gamma_s}\right)^2\right)^2+\left(\frac{2\omega_m}{\gamma_s}\right)^2}}\cos(\phi_p - 2\phi_s - 2\mu - \phi_{ELO}), \tag{4.7}$$

$$\mu = \mathrm{atan}\left(\frac{2\omega_m}{\gamma_s\left(1-\frac{P_p}{P_p^{thr}}-\left(\frac{\omega_m}{\gamma_s}\right)^2\right)}\right), \tag{4.8}$$

from which we can see that the lock will ideally full fill the relation $\phi_p - 2\phi_s - 2\mu - \phi_{ELO} = \pi/2n$, where n is an integer. In order to actuate back on the phase of the CLF field you can either use a phase shifter as shown in figure (4.3) or frequency modulate the AOM that creates the CLF-field as shown in figure (4.4). Since frequency is the derivate of phase, then phase can be changed

my creating a slight frequency modulation. The strength of using frequency modulation is that the range of the actuator is much bigger than a traditional phase shifter, and the bandwidth is usually also bigger.

4.3 Homodyne phase lock

The last locking system is the continuation of the coherent control lock, where the phase between the homodyne local oscillator and the CLF-field is to be locked to ensure phase stability between the squeezed field and the local oscillator.

The locked CLF fields (upper and lower sidebands) will propagate together with the squeezed light and interact with the local oscillator at the beam splitter at the homodyne detector. The two fields impinging on the photo-diodes (ignoring fluctuations) are then

$$C = \frac{1}{\sqrt{2}}\left(A^{out}_{s,out} + A^{out}_{i,out} + iA_{LO}\right), \tag{4.9a}$$

$$D = \frac{1}{\sqrt{2}}\left(i\left(A^{out}_{s,out} + A^{out}_{i,out}\right) + A_{LO}\right). \tag{4.9b}$$

The detected photo-currents will contain a DC term containing the total power, an ω_m term containing the interference between the local oscillator and CLF fields and a $2\omega_m$ term containing the interference between the CLF fields. Due to a phase difference between the interference terms, the difference current will however only contain the desired ω_m terms

$$\begin{aligned} C^*C - D^*D &= \frac{i}{2}|A_{LO}|\left(A^{out*}_{s,out}e^{-i\phi_{LO}} + A^{out*}_{i,out}e^{-i\phi_{LO}} - A^{out}_{s,out}e^{i\phi_{LO}} - A^{out}_{i,out}e^{i\phi_{LO}}\right), \\ &= \frac{1}{2}|A_{LO}|\,\mathbb{I}\mathrm{m}\left(A^{out}_{s,out}e^{i\phi_{LO}} + A^{out}_{i,out}e^{i\phi_{LO}}\right). \end{aligned} \tag{4.10}$$

We once again down-mix to DC by mixing the electrical signal with an ELO oscillating at ω_m and lowpass filter to remove the $2\omega_m$ terms. The final form of the error signal has once again been explicitly calculated in the appendix of the PhD thesis of Eric Oelker previously of the LIGO group at the Kavli Institute of MIT [46], and the result is

$$\begin{aligned} E_{HD} = &\frac{4\left|A^{in}_{s,in}A_{LO}\sqrt{\gamma^{in}_s\gamma^{out}_s}\right|}{\gamma_s\sqrt{\left(1 - \frac{P_p}{P^{thr}_p} - \left(\frac{\omega_m}{\gamma_s}\right)^2\right)^2 + \left(\frac{2\omega_m}{\gamma_s}\right)^2}} \\ &\left(\sqrt{\frac{P_p}{P^{thr}_p}}\cos(\phi_p - 2\omega_s - \mu - \phi_{LO} - \phi_{ELO}) + \sqrt{1 + \left(\frac{\omega_m}{\gamma_s}\right)^2}\cos(\nu + \mu + \phi_s - \phi_{LO} + \phi_{ELO})\right), \end{aligned} \tag{4.11}$$

$$\nu = \arctan\left(\frac{\omega_m}{\gamma_s}\right). \tag{4.12}$$

This error signal will allow us to stabilize the phase between the squeezed light and the local oscillator and will in fact allow us to lock to any quadrature value, by varying the demodulation phase ϕ_{ELO}.

4.4 Lock characterization and optimization

The error signals calculated in the previous sections give us signals proportional to the error that we can feed back to the actuator of our feedback system. These actuators only have limited gain

and frequency bandwidth in which the actuator can correct errors. Furthermore, the actuator might have unwanted resonances that could cause instability of our feedback loops.

According to the Nyquist stability criterion [47], in order for a feedback loop to be stable the system should have no gain above the frequency, at which the phase lag hits $-180\,\mathrm{deg}$. Having gain above this frequency causes the feedback loop to become unstable, enhancing errors instead of correcting them, and can in the worst case cause the actuator to start oscillating.

In order to optimize the behaviour of each actuator and to avoid instability, we pass the error signal through a proportional-integral-derivate (PID) controller. The PID controller is a filter with three functions; the proportional term provides a correction proportional to the magnitude of the error (referred to as P-gain), the integral term provides a correction proportional to the magnitude and duration of the error, and the derivative term provides a correction to the magnitude and rate-of-change of the error.

Mathematically, the time response of the PID controller can be written as

$$\Theta_{PID}(t) = K_p\left(E(t) + \frac{1}{T_i}\int_0^t E(\tau)\,\mathrm{d}\tau + T_d\frac{\mathrm{d}E(t)}{\mathrm{d}t}\right), \tag{4.13}$$

where $E(t)$ is the error signal, T_i and T_d are integral and differential time constants. K_p is a common proportionality constant, since all terms are proportional to the magnitude of the error.

It can be more informative to rewrite the time response function as the frequency domain transfer function, for which we have

$$\Theta_{PID}(\omega) = K_p\left(E(\omega) - i\frac{\omega_i}{\omega}E(\omega) + i\frac{\omega}{\omega_d}E(\omega)\right), \tag{4.14}$$

with $\omega_i = 2\pi/T_i$ and $\omega_d = 2\pi/T_d$ being characteristic angular frequencies. We see that the integral term provides gain below ω_i, but causes a $90\,\mathrm{deg}$ negative change in phase, and the derivative term provides gain above ω_d and causes a $90\,\mathrm{deg}$ positive phase change. Using these, we can provide extra gain at frequencies within the bandwidth of the actuator and remove gain outside the bandwidth.

The example data used throughout this section is from the feedback loop used to stabilize the length of the OPO used in chapters (7) and (8).

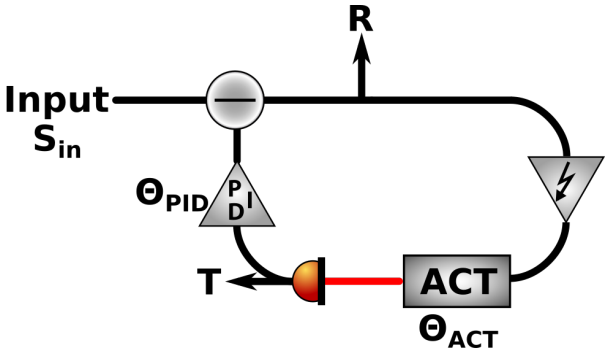

Figure 4.5: Sketch of a typical feedback loop. S_{in}, R, and T are electrical signals and Θ_{ACT} and Θ_{PID} are transfer functions. The red and black lines are optical and electrical connections respectively.

The first step when optimizing a feedback loop is to measure the transfer function of the actuator. A sketched representation of a typical feedback loop using a high-voltage amplifier (HVA) to drive a piezo acting as an actuator is shown in figure (4.5). An input signal (or

disturbance) at a given frequency can be injected via the input port and this signal will propagate through the feedback system being affected by the actuator and the PID described by transfer functions Θ_{ACT} and Θ_{PID} respectively. The photodetector transfer function can usually be ignored, since the photodetector typically has a much wider bandwidth than the actuator. This is not the case for the HVA, but the transfer function of this can be absorbed into Θ_{ACT}.

If we extract the signals marked R and T in figure (4.5), we see that the actuator transfer function will be given by

$$\Theta_{ACT} = \frac{T}{R}, \tag{4.15}$$

which means we can measure the actuator transfer function by doing a T/R measurement using a network analyser. An example of a piezo transfer function is shown in figure (4.6).

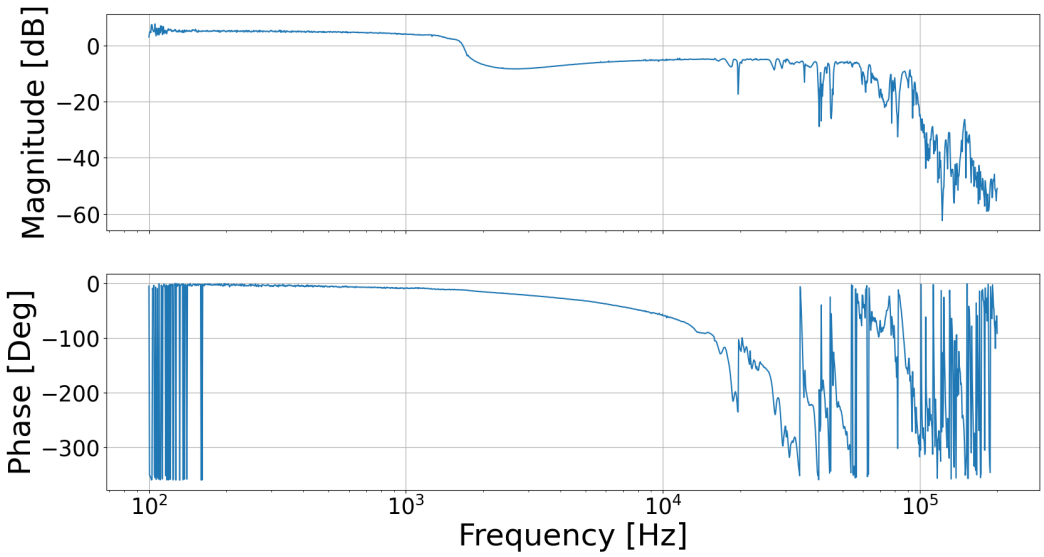

Figure 4.6: Transfer function amplitude and phase of a piezo actuating the length of an OPO. The data is recorded in a T/R measurement on a network analyser recording 1601 points of a logarithmic sweep of driving frequencies from 100 Hz to 100 kHz. The data has manually been adjusted to 0 dB amplitude and 0 deg phase for improved clarity. The low frequency phase behaviour is an artifact of the measurement and not a part the actuator response.

Having measured the actuator transfer function, we can now design our PID to optimize the performance of our feedback loop. The home-made analogue PID modules we use allow for P-gain, two integral or derivate stages, a second-order low-pass filter to further ensure no gain above the instability frequency and two notch filters to remove unwanted resonances. The I/D stages are almost always used as integrators, since derivate stages can add noise at higher frequencies.

The strategy we use when designing filters is to ensure as high a unity gain frequency as possible while still ensuring a nice phase margin (the frequency range from the unity gain frequency and until the instability frequency). Below the unity gain frequency we aim for a $1/f$ behaviour of the gain, and then use the low-pass filter and notch filters to kill off any gain after the instability frequency. We simulate the filter in python using the transfer function data, and the filter used to optimize the actuator in figure (4.6) is shown in figure (4.7). This filter uses two integrators at 100 Hz and 10 kHz respectively and a 10 kHz low-pass filter and P-gain.

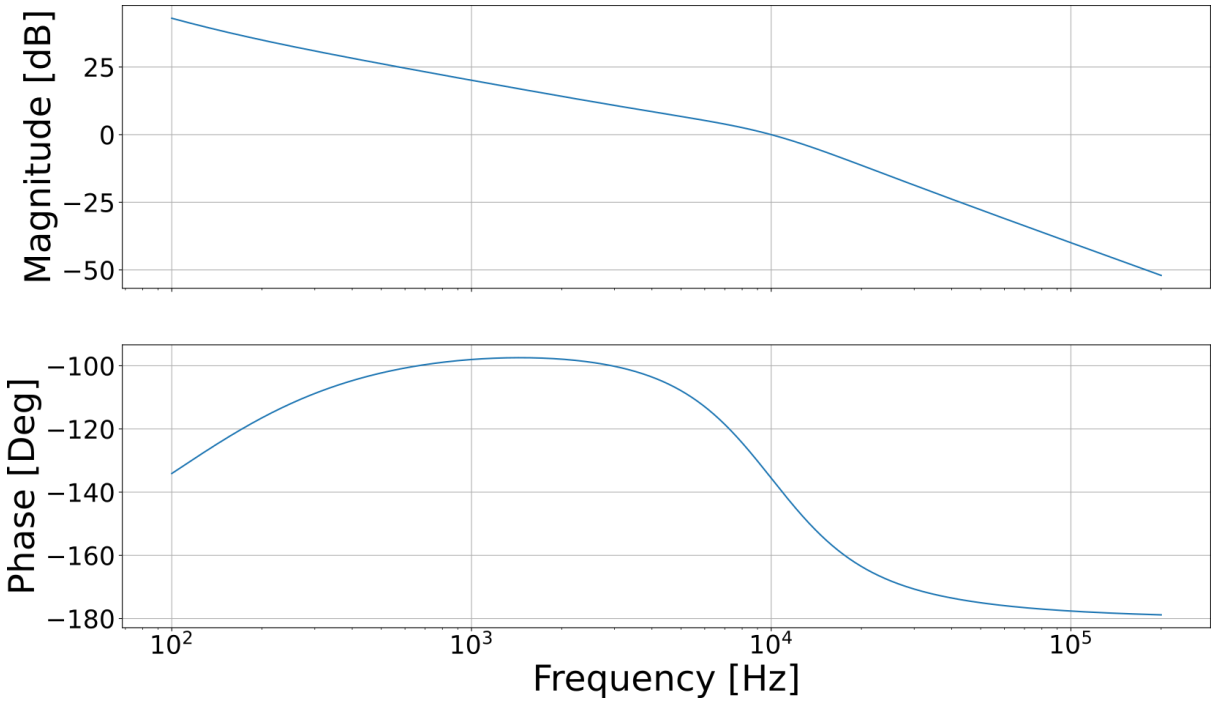

Figure 4.7: Simulated PID transfer function, using P-gain, integrators at 100 Hz and 10 kHz, and a 10 kHz low-pass filter.

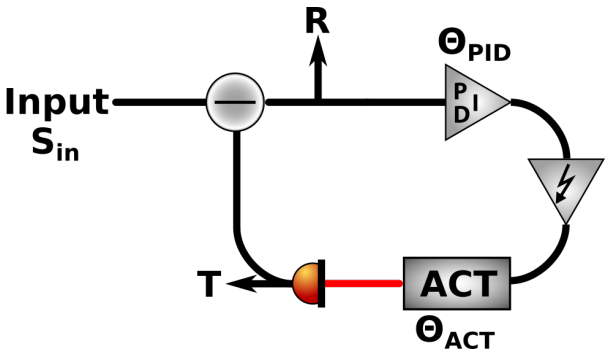

Figure 4.8: Sketch of an open-loop gain measurement in a typical feedback loop.

The final step in optimizing a feedback loop is to evaluate the actual performance of the feedback loop. This is done by measuring the open-loop gain $g_{OL} = \Theta_{PID}\Theta_{ACT}$, which is the gain applied by the filter and actuator in the case of not feeding back the error signal and can be measured by once again doing a T/R measurement, but with T being measured after the PID as shown in figure (4.8).

A measurement of the open-loop gain function of the feedback is shown in figure (4.9) together with the simulated open-loop gain for comparison.

It is quite informative to go through the mathematics of the network of figure (4.8). The signal T is given by

$$T = \Theta_{PID}\Theta_{ACT}R = g_{OL}R, \tag{4.16}$$

and the signal R is given by

$$R = S_{in} - T = S_{in} - g_{OL}R = \frac{S_{in}}{1 + g_{OL}} = g_{CL}S_{in}, \tag{4.17}$$

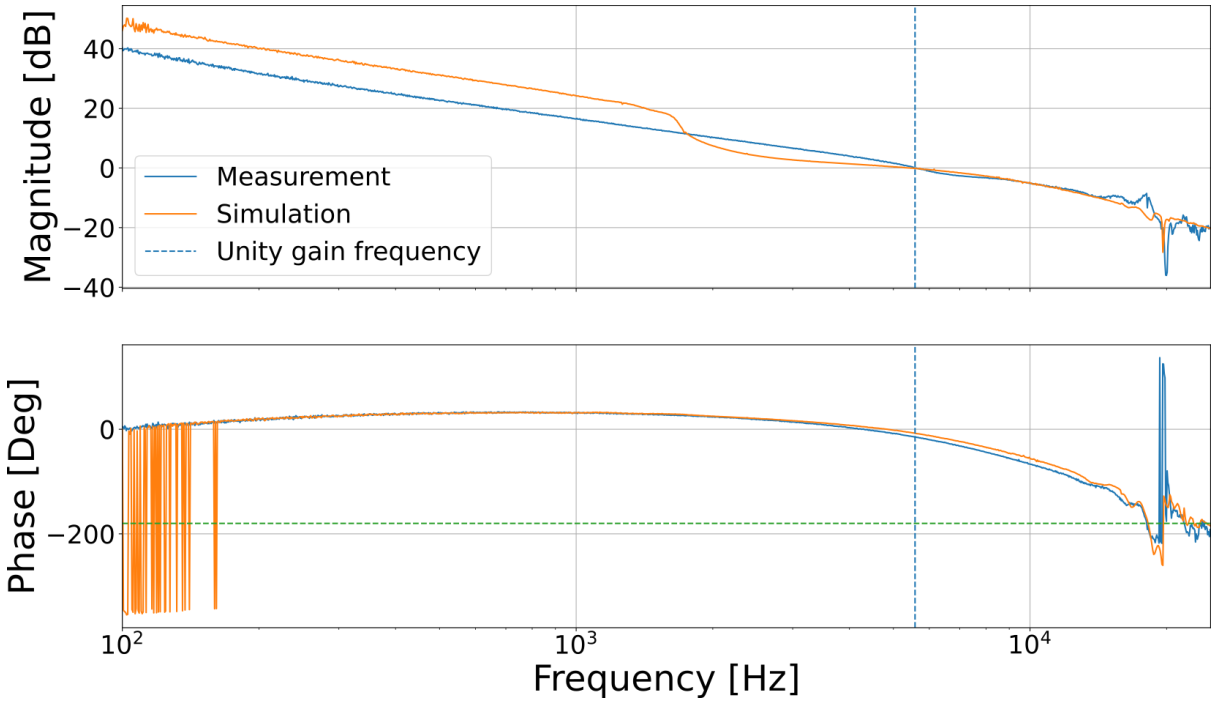

Figure 4.9: Comparison between the measured and simulated open loop gain. The vertical blue line marks the unity gain frequency, and the green line is a guide for the eye to help locate the instability point.

where we have identified the closed-loop gain $g_{CL} = 1/(1 + g_{OL})$, which is the gain applied by closing the feedback loop. The full gain of the feedback loop (also called the round-trip gain g_{RT}) can then be found by substituting equation (4.17) into equation (4.16)

$$T = g_{OL} g_{CL} S_{in} = g_{RT} S_{in} \tag{4.18}$$

The closed loop, open loop and round trip gain functions are all very useful for analysing how noise propagates through a feedback loop (as will be shown in section (6.1.2)). A plot of the magnitude of these gain functions is shown in figure (4.10). Here the a linear fit has been applied to the measured open-loop gain in order to extend it to DC, and the closed-loop and round-trip gain functions are calculated from this.

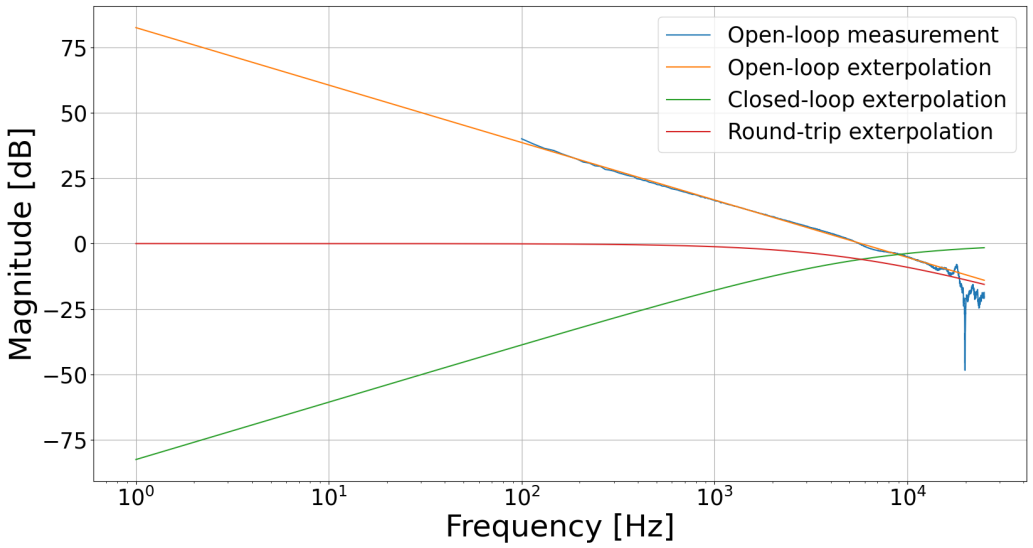

Figure 4.10: Plot of magnitude of the measured open-loop gain function together with an interpolation to extend it to DC. From the interpolation the closed-loop and round-trip gain functions are calculated and plotted.

In fact, the mere act of opening the box will determine the state of the cat, although in this case there were three determinate states the cat could be in: these being alive, dead, and bloody furious.

Lords and Ladies
by Terry Pratchett, 1992

5 Compact Squeezing Source

This chapter is dedicated to an experiment published in a paper: **J. Arnbak, C. S. Jacobsen, R. B. Andrade, X. Guo, J. S. Neergaard-Nielsen, U. L. Andersen, and T. Gehring, "Compact, low-threshold squeezed light source," Opt. Express 27, 37877-37885 (2019)** [48], where we built a compact squeezed light setup. This chapter will start with a short introduction of the setup, including a component overview of the different parts of the setup. I will then motivate the choice of OPO, before I end the chapter by including the paper in its entirety as it was published, but slightly reformatted to fit the format of the thesis.

5.1 Introduction

5.1.1 Fiber-based squeezer

A schematic representation of the fiber based setup is shown in figure (5.1). The setup is supplied by a NKT Photonics ADJUSTIK E-15 fiber laser amplified by a NKT Photonics BOOSTIK fiber amplifier. The laser light is then divided into three parts, and I will go through each section step-by-step.

5.1.1.1 Pump generation

In order to pump the OPO, the light at 1550 nm has to be converted to 775 nm. This part of the setup first uses a fiber coupled phase modulator to add a 100 MHz phase modulation to the light. This is used to stabilize the OPO through the Pound-Drever-Hall stabilization technique, which was introduced in section (4.1). This modulator is a LiNBO3 waveguide that can tolerate a maximum input power of 300 mW and has a 3 dB insertion loss, which limits the power available for frequency conversion to only 150 mW.

The second-harmonic-generation is done via an NTT electronics WH-0775-000-F-B-C wavelength conversion module. This is also a fiber-coupled waveguide module, which we temperature stabilize using a temperature controller.

Finally, the light passes through a circulator before being coupled into free-space and into the OPO. The circulator separates the forward and backwards propagating beams, and the backwards propagating light is used in the PDH lock.

In free-space, the pump beam passes through a half-wave plate to correct the polarization and a set of lenses to mode-match the beam to the cavity. Finally, the pump beam passes

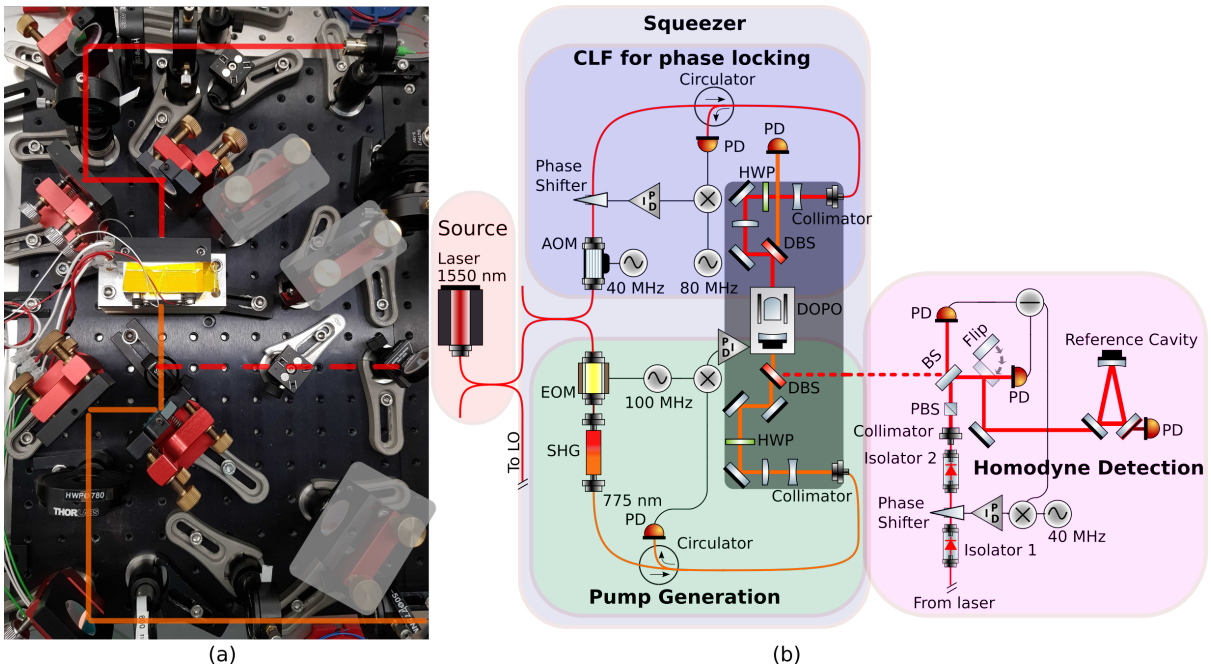

Figure 5.1: (a): Top down photo of the free-space OPO with beam-paths sketched in orange 775 nm and red (1550 nm). The components marked in white have been added later as a part of another project and not relevant to the setup itself. **(b):** Schematic representation of the different parts of the setup. AOM: acousto-optic modulator, EOM: electro-optic modulator, BS: (50/50) beam-splitter, DBS: dichroic beam-splitter, OPO: double-resonant optical parametric oscillator, PD: photo-detector, HWP: half-wave plate, PS: phase-shifter, Iso: isolator, Circ: circulator, Coll: collimator, Flip: flip mirror, CLF: Coherent-locking-field

through a dichroic beam-splitter, which transmits light at 775 nm and reflects light at 1550 nm allowing us to separate the pump light from the squeezed light exiting the cavity.

The OPO is also temperature stabilized by a temperature controller in order to ensure the double resonance condition is fulfilled.

5.1.1.2 CLF generation

The CLF beam used in the coherent locking scheme described in section (4.2) first propagates through a 40 MHz fiber-coupled AOM. This only passes the up-shifted sideband, which propagates through a fiber phase shifter and a circulator before being coupled into free-space for propagation into the OPO.

The free-space part is similar to the pump beam with a half-wave plate and mode-matching lenses. Another dichroic beam-splitter allows us to separate the different wavelengths, sending the transmitted pump beam to a detector to analyse the cavity transmission. A flip mirror and another detector in the path of the squeezed light allows us to analyse the cavity transmission of the CLF beam.

5.1.1.3 Homodyne detection

The final part of the setup of the fiber-based setup to go through is the homodyne detector setup. Even though the entire fiber based part is using polarization-maintaining (PM) fibers, we had some problems with polarization-fluctuations in the local oscillator path. This seems to be correctable by inserting polarization-sensitive components along the fiber path. In the pump

and CLF beams the EOM, AOM and circulators are all polarization sensitive, but in the local oscillator there are none. We therefore inserted polarization-sensitive fiber isolators in the local oscillator path. Besides these another General Photonics phase-shifter allows control of the local oscillator phase for the final phase lock described in section (4.3).

After being coupled out into free-space the local oscillator passes through a half-wave plate and polarization beam-splitter (PBS) to clean the polarization. A 50/50 beam-splitter splits the the light between the two photodiodes of the homodyne detector. In order to ensure as good a visibility as possible between the local oscillator and the squeezed light, after combining on the beam-splitter, both modes are coupled into a triangular reference cavity. If both modes are highly coupled to the cavity, then because they share the same path, they also have to share the same spatial mode, therefore ensuring a large mode-overlap.

5.1.2 The OPO

The first decision to make when designing an OPO is the geometry of the cavity. In section (2.3.5) we introduced the standing (linear) wave and running wave cavities, and while both types can work as OPOs, there are some crucial differences that can influence the choice of geometry.

A running wave cavity has better isolation against back-scattered light, since counter propagating modes of a running-wave cavity exit the cavity at different angles, as opposed to a standing wave cavity, where the counter propagating modes exit on top of each other. This usually makes the running wave cavity the preferred choice of OPO for experiments dealing in single-photon generation or subtraction, since backscattered light can contaminate single-photon detectors. However, due to the natural birefringence of a running wave cavity, the light transmitted from a running wave cavity will therefore exhibit some degree of astigmatism. Finally, a running wave cavity is in general easier to align, since different higher order Hermite-Gaussian and Laguerre-Gaussian modes are nicely separated in resonance frequency, compared to a linear cavity, where they are pair-wise degenerate.

A linear cavity exhibits no astigmatism, is the simplest design, can be made to have the lowest internal-cavity losses of the two types of cavities, but has bad backscatter isolation and is generally harder to align. The pros and cons of each cavity is summarised in table (5.1) For

Property \ Type	Standing wave	Running wave
Astigmatism	No	Yes
Intra-cavity loss	Depends on geometry	Depends on geometry
Backscatter isolation	No	Yes
Alignment	Harder	Easier

Table 5.1: Table summarising the pros and cons of the two different cavity types.

our application, efficiency is of high priority, and we therefore choose to use a linear OPO.

The next step is then the design of the cavity. A linear cavity with a nonlinear medium in general has three configurations.

The first, which I will call the standard, is using two mirrors and then placing the nonlinear crystal in between. The strength of this configuration is that the cavity can be aligned before the nonlinear medium is inserted inside (if the cavity is stable without the nonlinear medium). If the crystal is wedged, then the position of the crystal can be used as a degree of freedom to achieve double-resonance. The down-side to using the "standard" configuration is that there are two air-crystal interfaces per round-trip that can scatter photons, and this will lead to the highest intra-cavity loss of the three configurations, even when the faces of the crystal are anti-reflection

coated. Furthermore, the acoustic stability of the cavity can also be impacted, since it contains three more-or-less independent components that can move relative to each other.

The second configuration, called a hemilithic OPO, replaces one of the mirrors by polishing a radius of curvature and high-reflective coating one of the faces of the crystal. This decreases the number of air-crystal interfaces and independent components by one each and this will lead to decreased intra-cavity loss and improved stability. In a hemilithic cavity, however, the crystal is a permanent part of the cavity, and the position of the crystal can no longer be used to achieve double-resonance.

The final configuration, called a monolithic OPO, removes both mirrors by polishing and coating both faces of the crystal. This removes all air-crystal interfaces and is the most stable of the configurations. The downside to this configuration is that, since there are no mirrors left to actuate upon with a piezo, the laser has to be stabilized by locking the laser frequency to the cavity resonance. Furthermore, the only degrees of freedom available to ensure double-resonance is the crystal temperature and the laser frequency, which can make it challenging to achieve both double-resonance and nonlinear phase-matching.

A sketch of the different configurations is shown in figure (5.2).

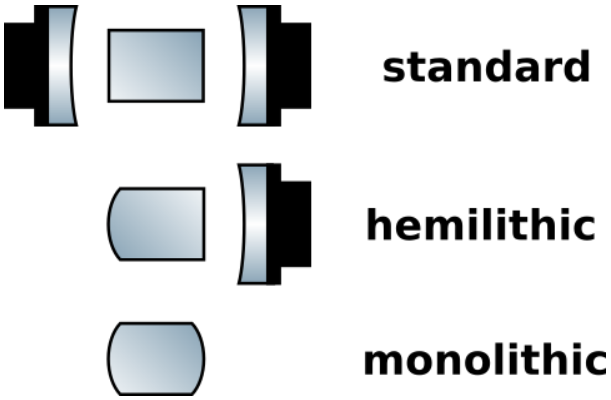

Figure 5.2: Sketch of the three possible configurations of a linear OPO.

For this experiment, we went with the middle ground between practicality and efficiency and chose to work with a hemilithic OPO.

Finally, the physical dimensions of the cavity needed to be chosen. The length of the crystal, the curvature of the mirror and crystal faces, the length of the air gap between mirror and crystal, and the mirror coating reflectivities are all degrees of freedom that can be varied when designing an OPO. The most important OPO properties to consider when choosing parameter values are cavity stability, pump threshold, escape efficiency and higher-order mode isolation, and sadly choosing the right parameters is an iterative process, since the different OPO properties can depend on the same parameters. The parameter dependencies of different OPO properties are summed in table (5.2).

The chosen cavity parameters can be found in the main text of the paper, but below I will motivate the choice of these with regards to the 4 properties described above.

5.1.2.1 Escape efficiency

The escape efficiency is the simplest property to determine, as this only depends on the reflectivity of the mirrors for the signal mode, as defined in section (3.2.3)

$$\eta_{ESC} = \frac{\gamma^{out}}{\gamma^{out} + \gamma^{in} + \gamma^{L}}. \tag{5.1}$$

Property \ Parameter	Air gap	Crystal length	Radii of curvature	Mirror reflectivities
Cavity stability	Yes	Yes	Yes	No
Escape efficiency	No	No	No	Yes
Pump threshold	Yes	Yes	Yes	Yes
Mode isolation	Yes	Yes	Yes	Yes

Table 5.2: Table containing the dependencies of the free parameters of the OPO on the important OPO properties.

The higher the escape efficiency, the higher the maximum available squeezing will be. A high escape efficiency does, however, mean a smaller finesse and a broader linewidth, which will make the filtering properties of the OPO worse. In this experiment our initial goal of the squeezed light source was 10 dB squeezing, and we therefore chose an escape efficiency of 0.98 to have a loss buffer of approximately 8 %, and not impact the linewidth too much.

5.1.2.2 Cavity stability

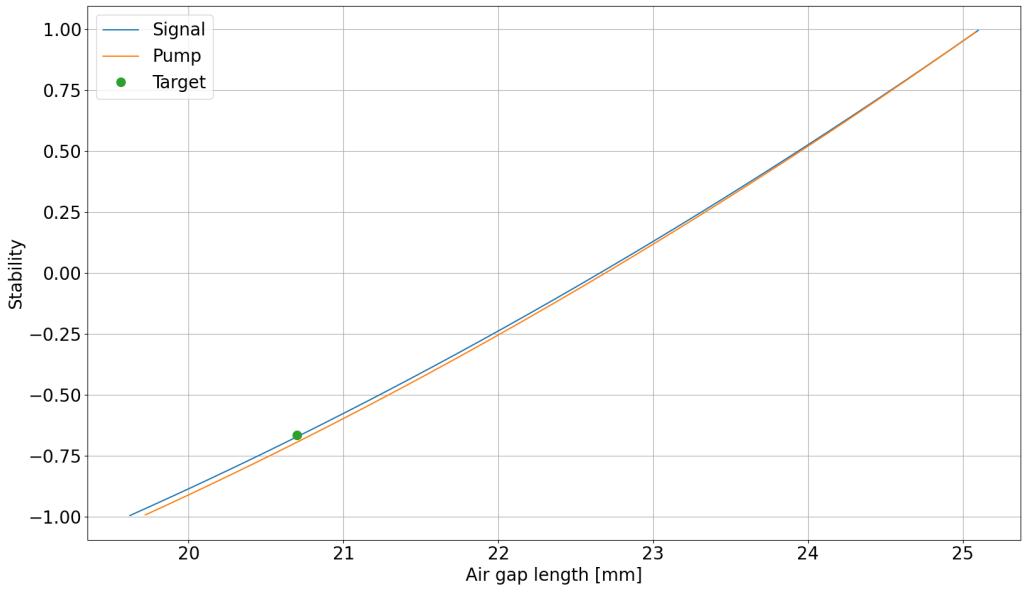

Figure 5.3: Plot of the stability of the signal and pump cavities as a function of the air gap length as well as the target stability. The two curves differ a bit due to the difference in refractive index of the two modes in the nonlinear crystal.

The cavity stability is usually analysed in the framework of ray-optics using the ABCD-matrix formalism [27]. The version of the resonator stability criterion that I use is

$$-1 \leq g_1 g_2 \leq 1, \Rightarrow \tag{5.2}$$

$$0 \leq |g_1 g_2| \leq 1, \tag{5.3}$$

with $g_i = 1 - L/R_i$ being the stability parameter of mirror i, where R_i is the radius of curvature of the cavity mirror, and L is the distance between them. Operating a cavity close to the instability

regions is usually not recommended, as perturbations of the mirror positions or angles can cause the cavity to be unstable, and many higher order modes resonate together with the fundamental mode close to instability. A plot of the OPO stability for the pump and signal modes as a function of the air gap length is shown in figure (5.3).

5.1.2.3 Pump Threshold

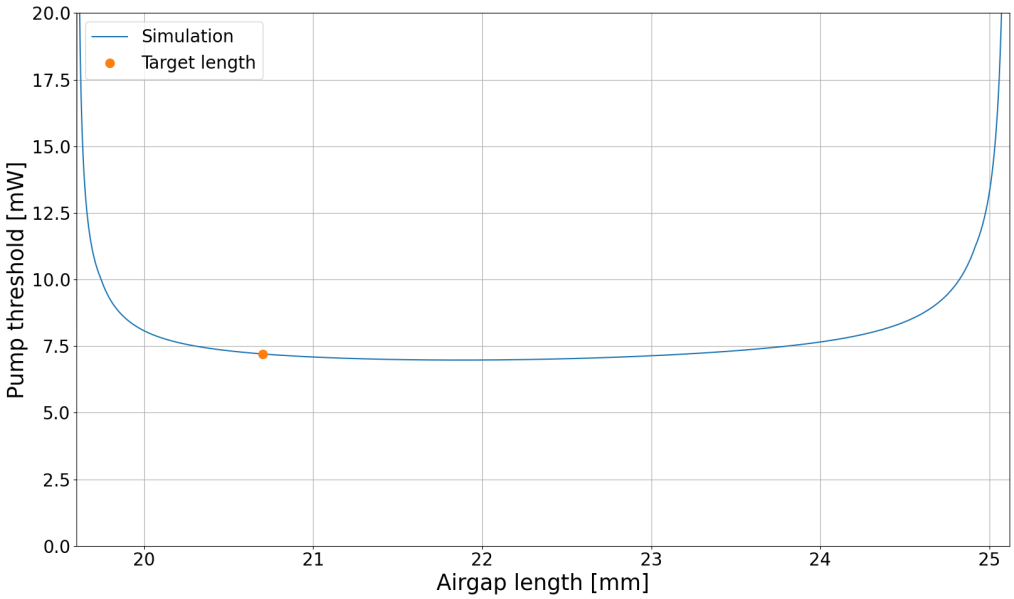

Figure 5.4: Simulation of the OPO threshold power as a function of air gap length.

In section (3.2.2) the pump threshold was introduced as the point where the parametric gain from the pump beam balances out the losses inside the cavity. In the case of no detuning the threshold power can be written as

$$P^{thr} = \frac{(T_{s,in} + T_{s,out} + \mathcal{L}_s)^2}{4E_{NL}} \frac{(T_{p,in} + T_{p,out} + \mathcal{L}_p)^2}{4T_{p,out}}, \tag{5.4}$$

where E_{NL} is the nonlinear power conversion efficiency with units of W^{-1} and is related to the second-harmonic power in the SHG process by $P_p = E_{NL} P_s^2$ keeping to the indexing convention used thus far. The explicit form of this is given by [31]

$$E_{NL} = \frac{16\pi^2 d_{eff}^2 L_c}{\epsilon_0 c \lambda_s n_s n_p} h(\sigma, \xi, \beta, \alpha, \mu) e^{-\alpha L_c}, \tag{5.5}$$

with $h(\sigma, \xi, \beta, \alpha, \mu)$ being the Boyd-Kleinman focusing function (ignoring double-refraction) [38], briefly mentioned in section (3.1)

$$h(\sigma, \xi, \alpha, \mu) = \frac{e^{\mu\alpha L_c}}{4\xi} \left(\int_{-\xi(1-\mu)}^{\xi(1+\mu)} \frac{\sigma \cos(\tau) + \tau \sin(\sigma\tau)}{1+\tau^2} \mathrm{d}\tau \right)^2, \tag{5.6}$$

where $\sigma = \Delta k z_{s,R}$ is a normalized mismatch parameter, $\alpha = \alpha_s + \alpha_p/2$ is an absorption coefficient, $\mu = 2(L_c/2 - z_{s,0})/L_c$ is a normalized focus parameter and $\xi = L_c/(2z_{s,R})$ is a normalized crystal length.

In order to optimize the focusing function, we choose parameters such that the focus is in the middle of the crystal, ensuring $\mu = 0$. We also assume that the temperature controller is keeping the cavity at the optimal phase matching temperature such that $\sigma = 0$. Finally, we vary cavity parameters to maximize the integral in equation (5.6). The resulting threshold power as a function of air gap length is shown in figure (5.4)

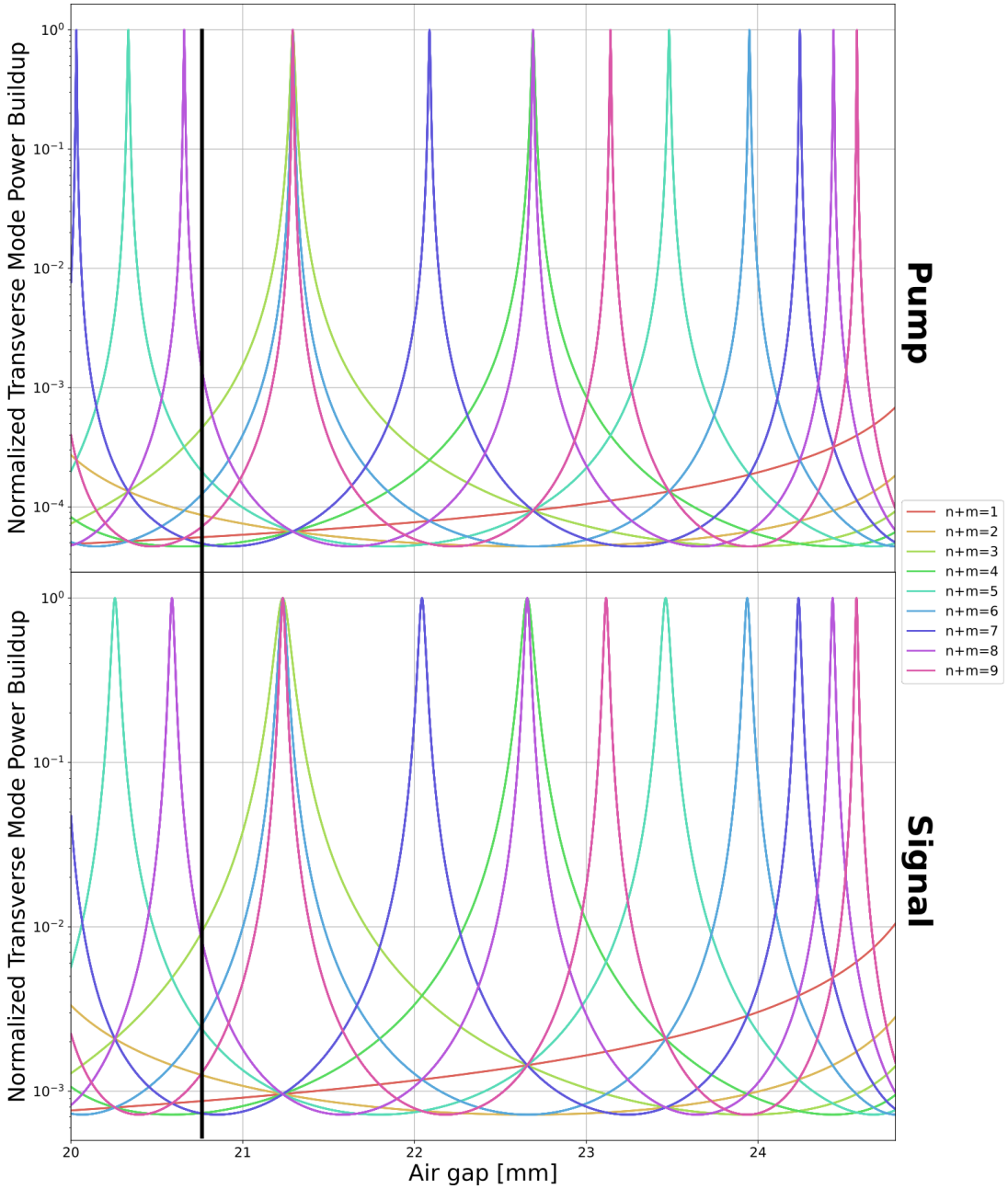

Figure 5.5: Simulation of simultaneous higher-order mode build-up of Hermite-Gaussian modes as a function of air gap length for both pump and signal modes. The black line is a guide for the eye of the desired air gap length.

5.1.2.4 Mode isolation

In an optical cavity the optical mode will acquire a phase shift after completing a roundtrip of the cavity. This is called the round-trip Gouy phase and arises from the Gouy phase of a Gaussian mode integrated throughout the length of the cavity

$$\Phi_{m/p}^{n/l} = \int_0^{L_c} \phi_{m/2p}^{n/l}(z)\mathrm{d}z, \tag{5.7}$$

where m and n indices signify a Hermite-Gaussian mode equation (2.53) and l and p signify a Laguerre-Gaussian mode equation (2.55). Whenever a higher-order Gaussian mode is an integer 2π of the round-trip Gouy phase of the fundamental mode $\Phi_{m/p}^{n/l} = 2\pi\Phi_0^0$, these two modes will resonate together.

As mentioned in section (2.3.5.3), the Gouy phase is given by

$$\phi_m^n(z) = (1+n+m)\,\mathrm{atan}(z/z_R), \qquad \text{(Hermite-Gaussian)}$$
$$\phi_{2p}^l(z) = (1+|l|+2p)\,\mathrm{atan}(z/z_R), \qquad \text{(Laguerre-Gaussian)}$$

from which we can see that the Gouy phase will depend on the cavity length and the radii of curvature of the cavity mirrors. The mode isolation will also depend on the bandwidth of the modes, a narrow bandwidth will give better isolation. This can be seen in figure (5.5), where the simultaneous higher order mode build-up for the pump and signal modes are shown as a function air gap length.

5.2 A compact, low-threshold squeezed light source

J. Arnbak, C. S. Jacobsen, R. B. Andrade, X. Guo, J. S. Neergaard-Nielsen, U. L. Andersen and T. Gehring

Center for Macroscopic Quantum States bigQ, Department of Physics, Technical University of Denmark

5.2.1 Abstract

Strongly squeezed light finds many important applications within the fields of quantum metrology, quantum communication and quantum computation. However, due to the bulkiness and complexity of most squeezed light sources of today, they are still not a standard tool in quantum optics labs. We have taken the first steps in realizing a compact, high-performance 1550 nm squeezing source based on commercially available fiber components combined with a free-space double-resonant parametric down-conversion source. The whole setup, including single-pass second-harmonic generation in a waveguide, fits on a 30 cm × 45 cm breadboard and produces 9.3 dB of squeezing at a 5 MHz sideband-frequency. The setup is currently limited by phase noise, but further optimization and development should allow for a 19" sized turn-key squeezing source capable of delivering more than 10 dB of squeezing.

5.2.2 Introduction

Squeezed quantum states of light are a ubiquitous resource in numerous applications associated with quantum sensing, quantum communication and quantum computation [33, 49–52]. One of the most celebrated examples is the application of squeezed light to improve the sensitivity of gravitational wave interferometers, thereby extending the volume in space within which gravitational events can be observed. [23,53,54]. A recent impressive improvement in observable volume is the eight-fold increase by the detection of 6 dB squeezed light in the gravitational wave detector GEO600 [55]. Quantum-enhanced sensitivity can also be achieved with squeezed light in tracking the motion and estimating bio-physical parameters of single living cells [21,56,57].

Apart from quantum sensing, squeezed light also has applications in quantum cryptography to extend the secure communication distance [58], to improve the cryptographic security [59] and to enable the implementation of quantum secure basic cryptographic primitives [60]. Finally, squeezed light has recently been found to be a viable resource for photonics continuous variable quantum computing due to development of new quantum error correcting codes [61,62] and due to the inherent scalability of the squeezed light source [51, 63–66].

All of the above mentioned applications would naturally benefit from a compact, mobile and robust squeezed light source producing an appreciable amount of squeezing. However, in most experiments to date there have been a sharp trade-off between achieving high degrees of squeezing and the compactness (as well as robustness and transportability) of the source.

On one hand, quantum states have been significantly squeezed by up to 15 dB (that is, a reduction of 97% of the vacuum noise) using a nonlinear crystal embedded in an optical cavity [67–72], but the associated experimental setups have very large footprints and are not easily transportable due to the need for multiple mode-cleaning cavities for the pump and local oscillator to maximize the squeezing and cavity based second harmonic generation to supply the pump which easily exceeds 100 mW. Due to this immobility, the squeezed light sources are often built up around the application.

On the other hand, compact and mobile squeezed light sources have been constructed using either an optical waveguide in a single-pass configuration [73, 74] or as a cavity [75], using a

micron-sized Silicon Nitride ring cavity [76,77] or using a whispering gallery mode resonator [78], but in these systems the squeezing degree have been limited to maximum 3 dB. Using the optical Kerr effect in fibers, the production of 2.4 dB pulsed squeezed light was demonstrated on a mobile platform of 0.3 m^2 [79]. In all of these latter experiments, compactness has been traded with the squeezing degree.

The trade-off has been partially settled in a couple of realizations: The free-space squeezed light source – an optical parametric oscillator – used in the GEO600 gravitational wave detector has a footprint of 1.1 m × 1.3 m, a weight of approximately 70 kg, and produces about 10 dB squeezing [80]. Another free-space squeezed light source without the use of separate lasers for auxiliary beams of size 80 cm × 80 cm has been reported in [81]. Finally, a 50 cm × 60 cm free-space setup producing 6 dB of two-mode squeezed light has recently been demonstrated [82].

5.2.3 Setup

In this article, we present the construction of a compact squeezed light source with a footprint of 30 cm × 45 cm producing 9.3 dB squeezing. While the source itself is a traditional double resonant parametric down-conversion source, we reduced its size by replacing bulky free-space optical components with less effective, but more compact commercially available fiber-alternatives and operate without the use of filter cavities. Only the couplings of the pump beam and the coherent control beam to the nonlinear cavity are obtained by free-space optics, as is the squeezed light output. In particular, the second-harmonic generator consists of a small single-pass waveguide module which produces enough light to saturate our source's low pump power threshold of 5.2 mW—a record for this type of source [72]. The setup is complemented with a 19"-sized laser and 19"-sized control electronics which have roughly the same footprint as our source.

Our experiment is presented in figure (5.6). The 1550 nm squeezed light is generated via parametric down-conversion by pumping a double resonant optical parametric oscillator (OPO) with light at 775 nm below threshold. The OPO itself, as sketched in the yellow inset, is a hemilithic cavity with a planar-convex periodically poled potassium titanyl phosphate (PPKTP) crystal as the nonlinear medium. The crystal has a size of 9.8 mm × 2 mm × 1 mm, the planar facet is coated with an anti-reflection (AR) coating (R<0.1 % @1550 nm, R<0.3 % @775 nm), and the curved facet (radius of curvature (ROC) = 10 mm) is coated with a high-reflection (HR) coating (R=99.95 % @1550 nm, R>99.5 % @775 nm). The output mirror (ROC=25 mm) is coated with a partially reflective coating (R=90 % @1550 nm, R=97.5 % @775 nm). The cavity has a round-trip optical length of around 77 mm resulting in a free spectral range of approximately 3.9 GHz, a finesse of around 58 for the 1550 nm mode (full-width-half-maximum (FWHM) ≈ 66 MHz) and around 200 for the 775 nm mode (FWHM ≈ 17 MHz). The double-resonance is achieved by tuning the temperature of the crystal and the length of the cavity with a piezo-electric transducer.

An NKT Photonics E15 BOOSTIK 1550 nm fiber laser supplies the light to the setup. The light is divided into two paths; one serving as the local oscillator in the homodyne measurement setup. The other path is further split into a pumping path and a path for the coherent control beam [45], in the following called the pilot beam.

The pumping path starts with a 1550 nm electro-optic modulator (EOM) to modulate the phase at 100 MHz for the OPO Pound-Drever-Hall (PDH) lock. The EOM has a maximum input power of 300 mW and an insertion loss of 3 dB. This limits the input power into the $LiNbO_3$ second-harmonic generator (SHG) wave-guide module (NTT Electronics WH-0775-000-F-B-C) to 150 mW, resulting in around 8 mW of 775 nm light to be used to pump the OPO. The reverse configuration, using an SHG before the EOM, was considered but fiber EOMs working at 775 nm are more expensive, have higher insertion losses (up to 5 dB) and much lower maximum input powers (∼ 20 mW) compared to their 1550 nm counterparts, causing us to reject this

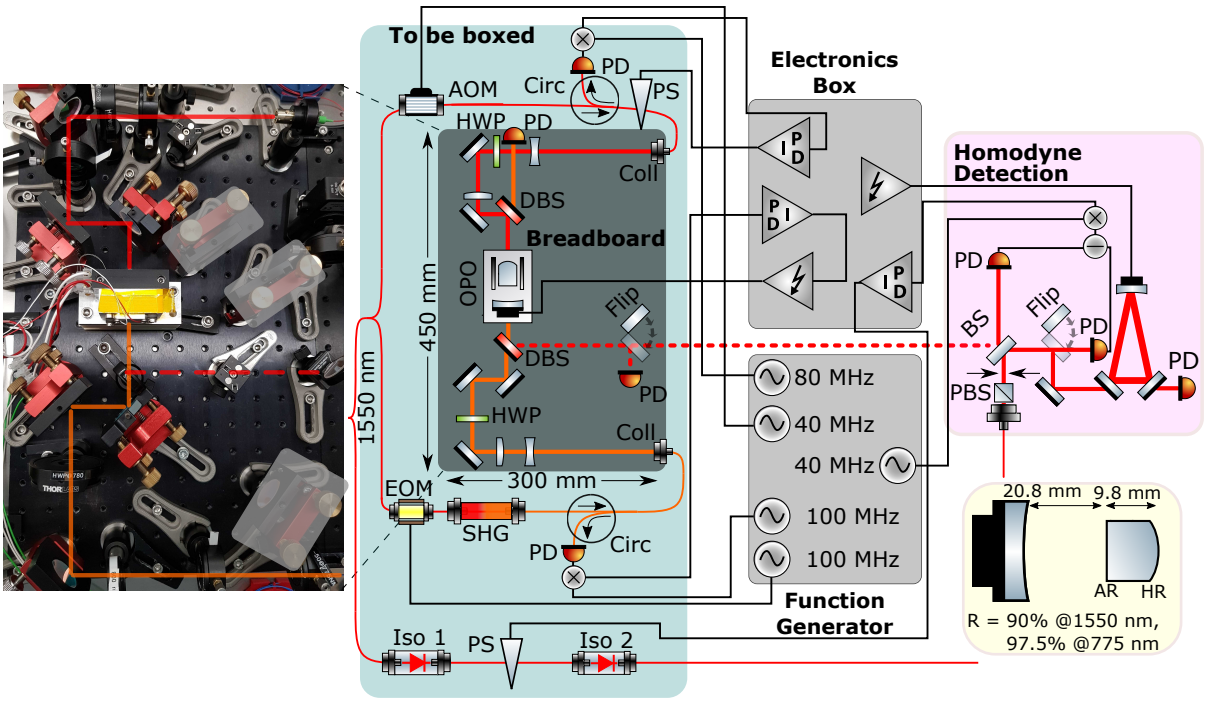

Figure 5.6: Schematic and photographic representation of the experimental setup. The free-space part of the setup is placed on a breadboard measuring 30 cm × 45 cm with the fiber components being placed around for convenience. The plan is to fit both the free-space part and the fiber components (marked by the teal rectangle) into a 19" box. The beam paths are marked in the photo, and the squeezed beam is marked by the dotted line. The grey boxes in the photo mark temporary components of no importance to the setup. The arrows in the LO path mark the point at which the polarization noise is measured.
The 775 nm light, used to generate the squeezed light, is generated in a single-pass $LiNbO_3$ waveguide second-harmonic generator (SHG). A Pound-Drever-Hall lock in the pump path stabilizes the cavity. A coherent-locking scheme for locking the relative phase between pump and local oscillator utilizes a 40 MHz up-shifted pilot tone transmitted together with the squeezed light. The squeezed light is characterized by a balanced homodyne setup that utilizes a reference cavity to help mode-match the squeezed light and local oscillator. Polarization sensitive fiber isolators are inserted along the local oscillator fiber path in order to minimize polarization noise build-up along the fiber path.
AOM: acousto-optic modulator, EOM: electro-optic modulator, BS: (50/50) beam-splitter, DBS: dichroic beam-splitter, OPO: double-resonant optical parametric oscillator, PD: photodetector, HWP: half-wave plate, PS: phase-shifter, Iso: isolator, Circ: circulator, Coll: collimator, Flip: flip mirror.
[Reprinted/Adapted] with permission from [48] © Optica Publishing Group

configuration.

The pilot path implements a coherent-locking scheme for locking the relative phase between the pump light and the local oscillator by using a fiber acousto-optic modulator (AOM) to up-shift the frequency of a 1550 nm beam by 40 MHz. This pilot field enters the OPO through the HR side and interacts with the pump field through difference-frequency generation. The reflected light is detected and down-mixed with an 80 MHz tone to generate an error signal for locking the phase of the pilot field to the pump field. The locked pilot field is transmitted with the squeezing and beats with the local oscillator. After detection in the homodyne detector, it is down-mixed with a 40 MHz tone to provide an error-signal for locking the phase between the local oscillator and the squeezed field.

Both the pump and the pilot beams are coupled out of the fibers and collimated by fiber collimators. Using two mode-matching lenses and two steering mirrors, each of the free-space beams are coupled into the OPO. All free-space optics are placed on the 30 cm × 45 cm bread-board which leaves enough space to place all fiber components on it as well. In the actual experiment, the fiber components were not attached to the breadboard out of convenience, but will be placed in the box in the final version of the device.

The squeezed light is characterized in a balanced homodyne setup which is placed on a neighboring breadboard and uses a bright (10 mW) 1550 nm beam as a local oscillator. The overlap between the squeezed light and the local oscillator is optimized by coupling both fields into a triangular reference cavity. This allows us to achieve a fringe visibility of around 99 %. The homodyne detector uses InGaAs photodiodes ($\eta_{QE} > 99\,\%$). The photo-electric signal is analyzed with a spectrum analyzer.

The setup utilizes polarization maintaining (PM) fiber components, and every time two PM fibers are combined in a mating sleeve, a small polarization mismatch can appear due to an imperfect slow-axes alignment. With many components, such a mismatch can build up and result in quite severe polarization noise. This problem can be circumvented by using a polarization stabilizing feed-back loop, but a simpler solution is to insert polarization filtering components along the path, thus preventing polarization mismatch to build up. The downside to this simple solution is the introduction of some excess amplitude noise.

In our setup, the EOM, AOM, SHG and circulators are all polarization filtering components thus preventing mismatch to build up in the pump and pilot paths. For the local oscillator, however, polarization noise was a problem, and fiber isolators were therefore inserted into the fiber path. While the local oscillator is not a direct part of the squeezed light source, it is required for characterization as well as for potential experiments utilizing the source. We therefore imagine the setup to provide both a squeezed output and a local oscillator. If the polarization of the local oscillator is noisy, this will lead to an unstable shot-noise reference which can falsify measurements as shot noise reference and squeezed light are measured one after another.

We characterize the effect of inserting polarizing components by inserting a power-meter after a polarizing beam-splitter (PBS) measuring at a sampling rate of 1 Hz. Figure 5.7 shows a plot of the overlapped Allan deviation and the power spectral density of these measurements. We measured without any isolators, with isolator 1 and with two isolators, isolators 1 and 2. For their positions see the experimental schematic in figure (5.6). As a baseline, we measure the polarization insensitive amplitude noise. The data is normalized to the mean, and the mean is subtracted in order to get the fluctuations relative to the mean.

From the Allan deviation, we see a large increase in long-term stability of the power when isolator 1 is present. This can also be seen in the power spectral density, with a difference of almost two orders of magnitude between having no polarizing components and having isolator 1. Between having one and two isolators, the difference is negligible for both graphs which is to be expected as no additional fiber components are present after isolator 2. By comparing

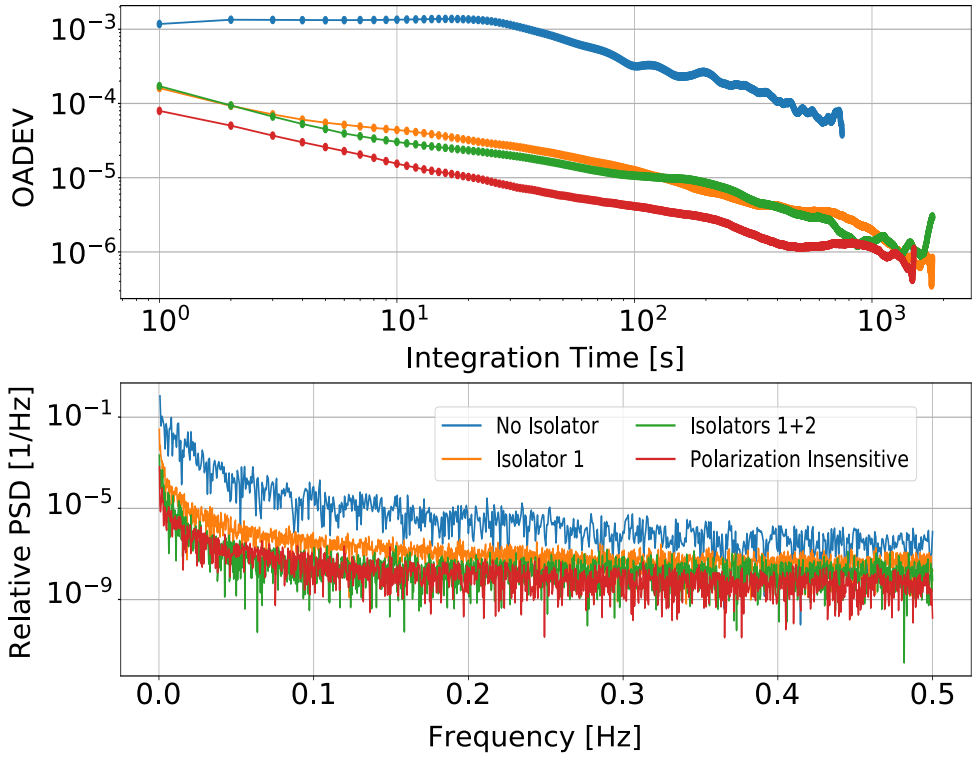

Figure 5.7: Overlapped Allan deviation (OADEV) and power-spectral density of polarization noise measurements in the local oscillator path. The data was taken at a 1 Hz sampling rate and is normalized to the mean and has mean subtracted. The blue trace is without any polarizing components. The yellow trace is with one polarization sensitive isolator and the green trace is with two isolators. The red trace is polarization insensitive amplitude noise. [Reprinted/Adapted] with permission from [48] © Optica Publishing Group

the green/orange traces with the red trace, it seems that the amplitude noise with isolators is in general a bit higher than the intrinsic noise from the laser. This could be due to small polarization mismatches being converted to amplitude noise by the isolators.

5.2.4 Results

The performance of our setup is first characterized by estimating the pump threshold power via a classical gain measurement of a 1550 nm field interacting with the pump field in the crystal. For this measurement, the fiber AOM is removed and the transmitted power of the 1550 nm field is measured while varying the input power of the 775 nm pump field. The gain is then estimated by comparing with the transmitted 1550 nm light when the pump is blocked. The calculated gain values are plotted in figure (5.8). The gain is modelled as [83]

$$g = \frac{1}{\left(1 - \sqrt{\frac{P_p}{P_p^{\mathrm{thr}}}}\right)^2}, \tag{5.8}$$

where P_p is the input pump power and P_p^{thr} is the OPO threshold power. From the fit of the experimental gain values, we can extract an OPO threshold power of $5.12 \pm 0.03\,\mathrm{mW}$. This shows that even though the system only has 8 mW of pump power available due to lossy fiber components, the double resonance allows the squeezer to utilize its full potential, since squeezing is best generated below threshold.

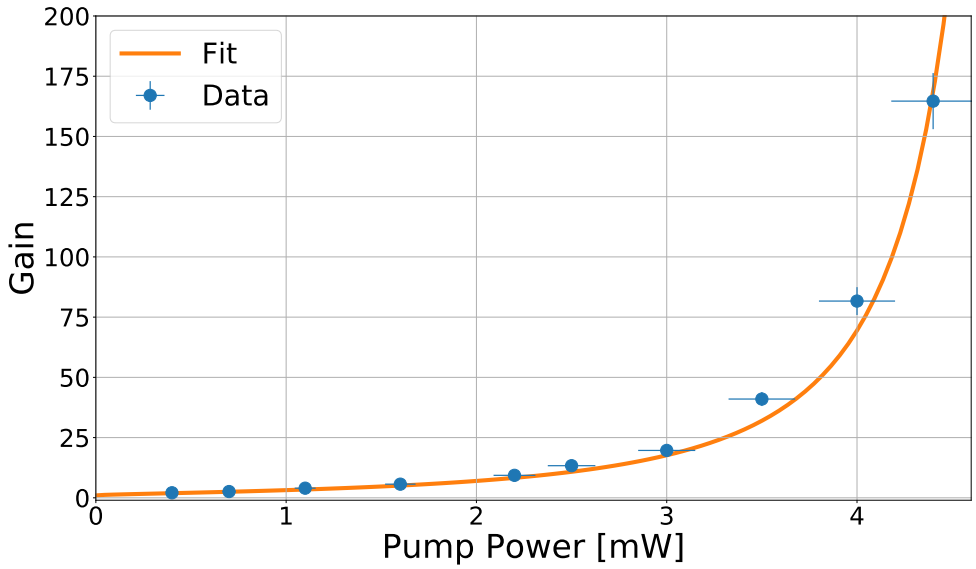

Figure 5.8: Graph showing experimentally obtained gain values (orange dots) as a function of input pump power. The blue line is a fit to equation (5.8), and a threshold value of $5.12 \pm 0.03\,\mathrm{mW}$ is extracted from the model. The error-bars assume a 5% error on the power.
[Reprinted/Adapted] with permission from [48] © Optica Publishing Group

In order to characterize the squeezing performance, we first look at the 5 MHz side-band frequency using a resolution-bandwidth of 300 kHz and video-bandwidth of 300 Hz. We measure for 200 ms and average each trace 100 times. The pump power is varied in the range 0–4 mW, and the local oscillator phase is locked to squeezing and anti-squeezing, respectively. The measured values as a function of pump power are shown in figure (5.9) corrected for electronic noise, which is about 22 dB below shot noise.

The squeezing increases with power until a maximum of around 9.3 dB below shot noise at around 2.5 mW pump power. After this, the squeezing begins to degrade with increasing pump power, suggesting that the measurement suffers from a significant amount of phase noise. The anti-squeezing is almost insensitive to phase noise and increases for all pump powers. The full power dependence of the (anti-)squeezing variance $\sigma^2\left(\delta\hat{\mathbf{X}}\right)_-$ ($\sigma^2\left(\delta\hat{\mathbf{X}}\right)_+$) including phase noise can be modelled as (normalized to shot noise) [83]

$$\sigma^2\left(\delta\hat{X}_\pm\right) \approx$$
$$1 + \eta_{\mathrm{esc}}\eta_{\mathrm{opt}}\mathcal{V}^2\eta_{\mathrm{QE}}\left(\pm\cos^2(\phi)\frac{4\sqrt{\frac{P_p}{P_p^{\mathrm{thr}}}}}{\left(1\mp\sqrt{\frac{P_p}{P_p^{\mathrm{thr}}}}\right)^2+4\left(\frac{\omega}{\gamma}\right)^2}\mp\sin^2(\phi)\frac{4\sqrt{\frac{P_p}{P_p^{\mathrm{thr}}}}}{\left(1\pm\sqrt{\frac{P_p}{P_p^{\mathrm{thr}}}}\right)^2+4\left(\frac{\omega}{\gamma}\right)^2}\right), \tag{5.9}$$

where $\eta_{\mathrm{esc}}\eta_{\mathrm{opt}}\mathcal{V}^2\eta_{\mathrm{QE}} = \eta_{\mathrm{tot}}$ is the total efficiency, with η_{esc} being the escape efficiency, η_{opt} being the optical loss, $\mathcal{V}$ being the fringe visibility of the squeezing and the local oscillator, and η_{QE} being the quantum efficiency of the photo diodes. $\omega = 2\pi\times 5\,\mathrm{MHz}$ is the angular frequency of the measurement side-band and $\gamma = 2\pi\times 66\,\mathrm{MHz}$ is the FWHM bandwidth of the OPO. Finally, ϕ is the RMS value of the phase noise. We note that the equation is only valid for small values of ϕ. The solid lines in figure (5.9) are a fit to equation (5.9). From the fit, we extract a total efficiency $\eta_{\mathrm{tot}} = 0.92 \pm 0.01$. This is in pretty good agreement with our estimated efficiency $\eta_{\mathrm{tot}} \approx 0.93$

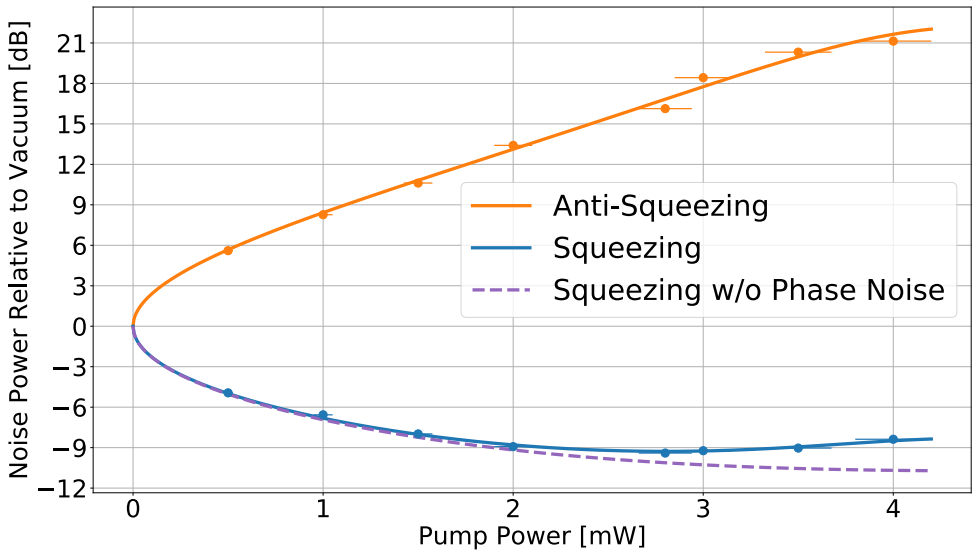

Figure 5.9: Squeezing and anti-squeezing relative to shot noise as a function of pump power at a side-band frequency of 5 MHz. The blue points are squeezing and the orange points are anti-squeezing. The theoretical model of equation (5.9) is fitted to the data and plotted in solid lines. The purple dashed line is the fitted squeezing model in the absence of phase noise. The electronic noise, which is 22 dB below shot noise, was subtracted from the data. The error-bars assume a 5% error on the power.
[Reprinted/Adapted] with permission from [48] © Optica Publishing Group

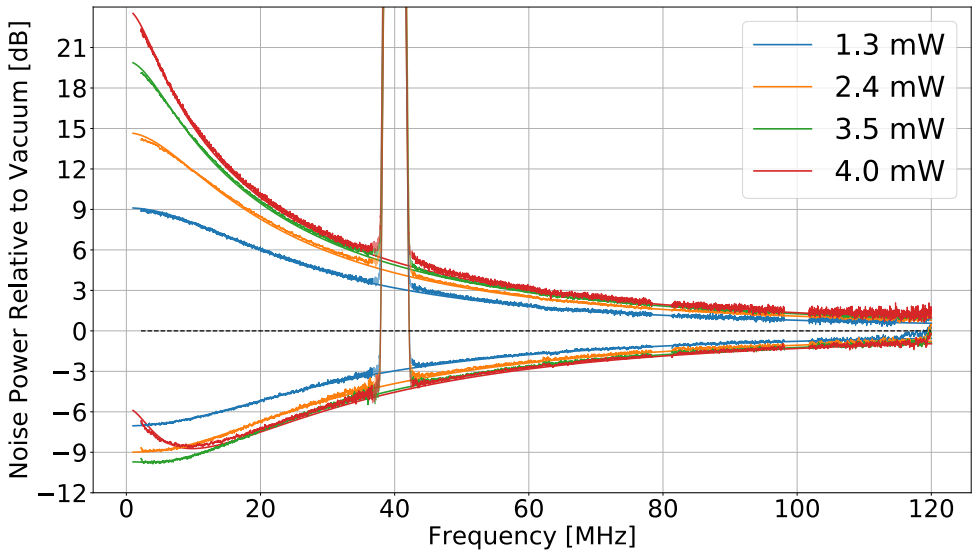

Figure 5.10: Spectrum of the squeezing and anti-squeezing from 1 – 120 MHz for different pump powers. The traces are corrected for electronic noise and normalized to the shot noise. The thin solid lines are fits of equation (5.9). Bands around 40 MHz, 80 MHz and 100 MHz are excluded from the fit as they contain the 40 MHz up-shifted pilot tone and electronic pick-up of modulation signals, and the 80 MHz and 100 MHz peaks are removed from the figure.
[Reprinted/Adapted] with permission from [48] © Optica Publishing Group

that comes from $\eta_{\text{esc}} \approx 0.97$ (estimated from coating specifications, ignoring scattering and absorption), $\mathcal{V} \approx 0.99$, $\eta_{\text{QE}} \approx 0.99$ and $\eta_{\text{opt}} \approx 0.999^7$. The optical loss comes from 5 mirrors and 2 lenses, all of which have an estimated efficiency of 0.999. The discrepancy is likely due to the actual quantum efficiency of the photo-diodes which is quite difficult to estimate precisely. Considering only the escape efficiency of the OPO allows us to determine the squeezing that is available directly out of the cavity, which can go as high as 15 dB close to threshold.

From the fit, we also extract the RMS value of phase noise to be 19 ± 1 mrad. This is quite high as about 3 mrad were observed using the same locking technique before [67], and we believe this to be in part due to disturbances introduced by the fibers and in part due to back-reflections off the photo-diodes and back into the OPO. This issue requires further investigation, as losses have already been optimized quite a bit, and it is therefore more realistic to improve the performance of the squeezer by stabilizing the phase. The theoretical model without phase noise in figure (5.9) indicates that our setup can reach detected squeezing levels beyond 10 dB below shot noise with our current losses.

Figure 5.10 shows the spectrum from 1 to 120 MHz of the squeezing and anti-squeezing for varying pump powers including fits of equation (5.9). As expected, the squeezing follows the bandwidth of the OPO, and is still present all the way out beyond 100 MHz. Once again, for high pump powers the squeezing starts to degrade at low frequencies due to phase noise, and from the fits of the curves, we extract similar values for the efficiency and phase noise. A curious exception is the 3.5 mW trace that surprisingly reaches all the way to 9.6 dB below shot noise for frequencies of 1–7 MHz and only contains about 12 mrad of phase noise from the fit.

5.2.5 Conclusion

In summary, we have demonstrated that a squeezed light source based on a traditional bulk squeezing cavity can be built with a small footprint on an area smaller than what is available in standard 19 inch boxes. We achieved this by replacing most free-space optics with fiber optics except for the in- and out-coupling of the OPO. The result was in particular made possible by a single-pass waveguide SHG module which provided enough pump power for the low threshold of only a couple of milliwatts, which in turn was due to the double-resonance of the OPO.

Further engineering on setup packaging will enable even smaller foot prints. A mobile turn-key squeezed laser in a transportable box might make squeezing a standard tool in quantum optics labs, which are ready to explore many yet undiscovered applications.

Funding

The authors acknowledge support from the Innovation Fund Denmark through the Quantum Innovation Center, Qubiz as well as support from the Danish National Research Foundation, Center for Macroscopic Quantum States (bigQ, DNRF142). Furthermore the authors acknowledge the EU project CiViQ (grant agreement no. 820466) and the EU project UNIQORN (grant agreement no. 820474).

Disclosures

The authors declare no conflicts of interest.

... and by golly it's a wonderful problem, because it doesn't look so easy.

Simulating Physics with Computers
by Richard Feynman, 1982

6 Designing an 18 dB squeezer

As a continuation of chapter (5), this short chapter will deal considerations that went into the design and construction of a high performance OPO able to generate upwards of 18 dB of squeezing. This was for a long time the main project of my PhD, but due to unforeseen problems that I will return to later in the chapter, I was never able to finish construction of the squeezer and had to pivot to the projects described in chapters (7) and (8). None the less, I believe the following information could be of interest for others to read.

This chapter will start out with a discussion of the necessary requirements for measuring 18+ dB of squeezing. I will then move on to describing the design of the OPO capable of meeting said requirements. Finally, this chapter will end by going into some detail with the problems that halted the project and the possible solution that will enable the project to be completed in the future.

6.1 Requirements for high squeezing

From chapter (3), we learned that the two main limitations to measuring high degrees of squeezed quadrature variances are optical loss and phase noise between the squeezed mode and the local oscillator. Of course we need to have enough optical pump power to get high enough parametric gain to get close to the OPO threshold, but the exact amount of optical power needed also depends on the optical losses and phase noise of the system. In the ideal case of no phase noise, optical losses can in part be compensated for by pumping the OPO arbitrarily close to the threshold. Since large parametric gain also means very large anti-squeezed quadrature variances, phase noise complicates the above picture, as some degree of the anti-squeezed quadrature will be mixed into the squeezed quadrature. The desired parametric gain will therefore be found in a compromise between optical loss and phase noise.

Figure (6.1) shows the dependence of pump power on the squeezed variance as us vary either the efficiency or the phase noise. Linear optical loss lowers the maximally measurable squeezed variance, but keeps the optimal pump power the same, whereas phase noise lowers the maximum and pushes it down towards lower pump powers. In order to measure lower than -18 dB of squeezed variance, we need to impose extreme, but in principle achievable requirements on the loss and phase noise, and end on budgets of 1.3 % loss and 1.0 mrad RMS phase noise for which the optimal optical pump power should be around 90 % of the OPO threshold. These numbers form the foundation of the choices made in the next section.

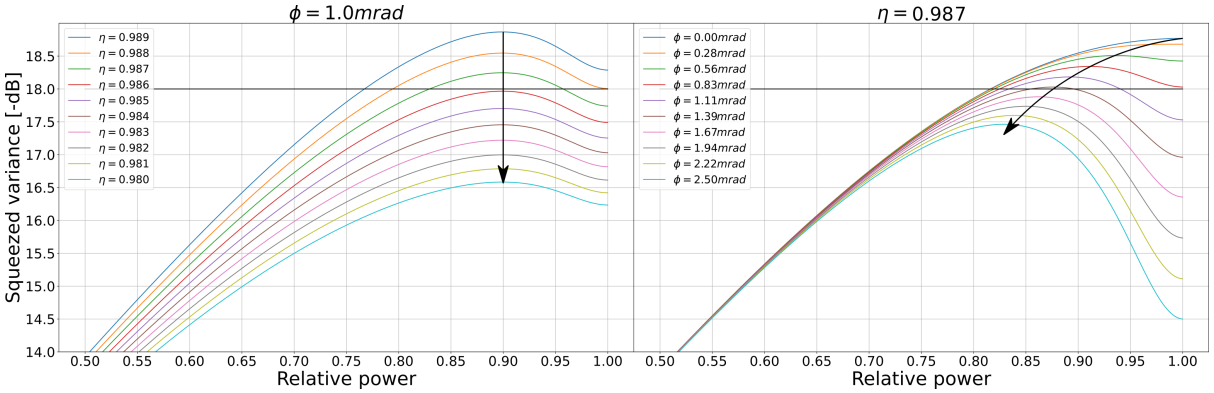

Figure 6.1: Measurable squeezed variance as a function of pump power relative to the threshold power. The y-axis is in -dB, meaning a higher value will correspond to a lower variance. **Left**: Constant phase noise of 1 mrad RMS with varying efficiency. **Right**: Constant efficiency of 0.987 with varying phase noise. The black arrows are guides for the eye to help track the maximum squeezed variance, and the horizontal black line marks the 18 dB level .

6.1.1 The optical loss budget

The total efficiency of a squeezed quadrature variance measurement is given by

$$\eta_{tot} = \eta_{QE}\mathcal{V}^2\eta_{opt}\eta_{ESC}, \tag{6.1}$$

and we start from the right with the escape efficiency η_{ESC}. This efficiency describes, how many of the squeezed photons are extracted from the desired port

$$\eta_{ESC} = \frac{\gamma^{out}}{\gamma^L + \gamma^{in} + \gamma^{out}}. \tag{6.2}$$

γ^{in} is pretty simple to minimize, as this simply involves maximizing the reflectivity of the input-port mirrror. The downside to doing this is that it limits the amount of light power being able to enter the cavity from the input port, requiring us to use more power in the CLF beam, if we want to use the coherent locking scheme described in section (4.2). This can have the unwanted effect of adding more shot noise to the CLF error signal lowering the SNR. γ^{in} is however a major contributor to lowering of the escape efficiency, and we ended up deciding to go with a high reflectivity of $R_{in} = 99.95\,\%$, as we were more concerned with being limited by optical loss.

The intra cavity loss rate γ^L has two main contributions. The first is losses from AR coatings on the crystal. This is the dominating source of intra-cavity loss, as AR coatings on PPKTP crystals cannot be made much better than $R = 0.1\,\%$ due to limitations in the temperatures the crystals can be heated to without destroying the poling. In order to circumvent the losses from AR coatings, we decided to make the OPO monolithic - the crystal itself makes out the cavity as shown in figure (5.2). A monolithic cavity will then only have intra cavity losses determined by the second source; absorption in the crystal. The linear absorption of 1550 nm light in PPKTP was estimated to be, at worst, around $120 \times 10^{-6}\,\mathrm{cm}^{-1}$ in [84]. Using this number, we can try to estimate the absorption losses as a function of cavity length. This is shown in figure (6.2), and we see that compared to the decay rate out of the input port, the absorption decay rate will only contribute a small amount against the escape efficiency. We did however end up deciding on a crystal of shorter rather than longer length, in order to ensure that the squeezed light can be coupled out of the crystal without cutting on the edge of the crystal as the transverse dimensions are only 1.0 mm × 1.2 mm.

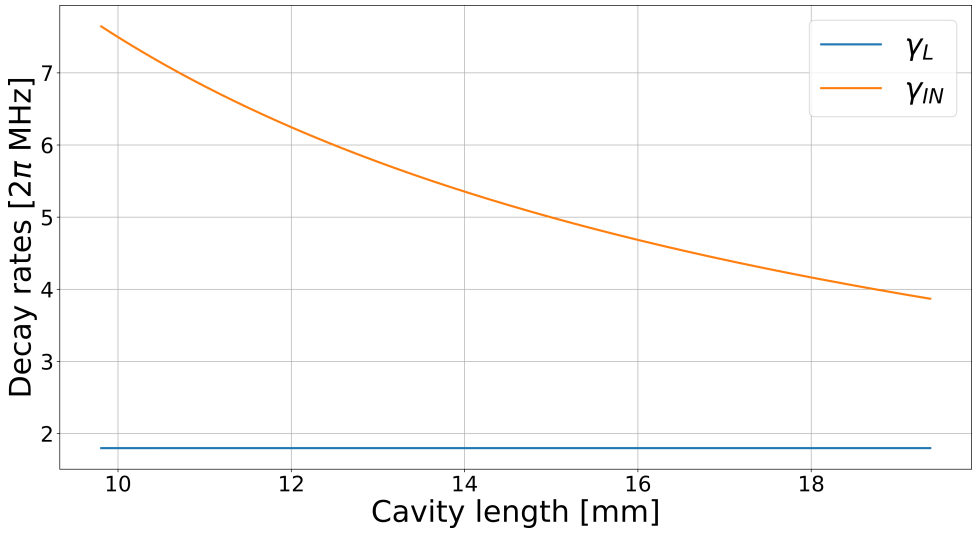

Figure 6.2: Estimated OPO absorption decay rate γ^{α} compared to γ^{in} as a function of cavity round-trip length.

γ^{out} should in principle simply be maximized in order to ensure as large an escape efficiency as possible. However, increasing the transmissivity of the output mirror also has the side-effect of increasing the cavity bandwidth (which is not necessarily a downside) and lowering the cavity finesse (which is a definite downside). Lowering the finesse, increases the pump power necessary to reach threshold and lowers the spatial filtering of the cavity, which can make mode matching the squeezed light to the local oscillator difficult. A large output coupler decay rate is however key to achieving high escape efficiency, and we therefore decided on a output coupler reflectivity of $R_{out} = 75\,\%$, which increases the FWHM bandwidth of the 1550 nm cavity to around 775 MHz and lowers the finesse to around 22. The final escape efficiency is 99.73 %, which leaves room for another 1.03 % loss in the budget.

The next efficiency to consider is the overlap efficiency between the squeezed mode and the local oscillator described by the squared interference visibility $\mathcal{V}^2$. The visibility is extremely important to keep as high as possible, as this factor penalizes the squeezed variance. In order to make sure that the visibility is maximized, a reference cavity, similar to the one mentioned in section (5.2), will be used to assist in matching the two modes. A mode cleaning cavity will also be used to spatially clean the local oscillator, and ideally we would also use one (or an SM fiber) in the CLF beam, as this is the beam most practical for alignment and mode matching after the OPO. Finally, all transmitting optics after the OPO and LO mode cleaning cavity should have stress compensating coatings to prevent beam deformation when passing through beamsplitters or lenses. The target interference visibility is set to 99.8 % to only induce around 0.4 % of loss.

The optical efficiency η_{opt} should be kept high by only using the minimally required number optical components , and the ones that are required should be high-grade custom optical components. We planed to use super polished mirrors, lenses and beamsplitters with high quality Ion beam sputtered coatings to lower the risk of photons scattering off the optical components. To optimize the number of optical components we also planned to use curved mirrors to focus onto the diodes.

Finally, custom diodes with high quantum efficiency η_{QE} should be used. The highest quantum efficiency diodes for telecom wavelengths, I currently know of, are high QE photodiodes from Laser Components that are guaranteed to have a quantum efficiency of minimum 99 %.

The minimum is, however, not good enough to keep within the loss budget, and a little bit of luck is required to find some diodes with $\eta_{QE} \geq 99.3\,\%$. Finally these diodes should also have a large active area to not make focusing the beam onto the diodes too hard. Larger active areas also limit the bandwidth of the detector, and a compromise between bandwidth and ease of focusing should be reached.

6.1.2 The phase noise budget

The phase noise budget is quite difficult to estimate. In general, we would expect the main sources of phase noise to come from locking systems, and careful design of the feedback loops in temperature control, cavity stabilization and phase stabilization systems are therefore required. There are, however, also others effects that can contribute to extra phase noise. When splitting two laser beams, the noise in each mode is correlated common mode noise and can be cancelled, when the beams are combined again (common mode rejection). If the beams propagate different lengths before being recombined, starting from high frequencies, the noise sidebands of the two modes will decouple and no longer cancel as common mode noise. It is therefore of importance to keep this in mind when designing an optical layout, making sure that beam paths are of the same length in order to ensure good common mode rejection.

I will now outline two methods that can in principle be used to estimate and/or troubleshoot the phase noise in the system. The first method uses a framework developed in the appendix of the PhD thesis of Eric Oelker of MIT [46]. This framework builds upon the work done in the thesis of Sheila Dwyer also of MIT [85] and Kirk McKenzie of ANU [86] and generalises and expands upon the nonlinear equations of motion used in chapter (3) to analyse how technical noise in the CLF and pump fields propagate to the squeezed light. The framework ignores shot noise contributions (but can be expanded to also include this), ignores cavity depletion, but includes length and temperature fluctuations of the OPO. The derivation is quite involved, and I will refer to the appendix for the full derivation.

The framework starts in the "two-photon" formalism, where each field includes both the normal propagating mode $\hat{\mathbf{a}}(\omega)$ and the counter propagating mode $\hat{\mathbf{a}}^\dagger(-\omega)$, meaning the intracavity fields and input/output fields are given as

$$\underline{a} = \begin{pmatrix} \hat{\mathbf{a}}_s \\ \hat{\mathbf{a}}_s^\dagger \\ \hat{\mathbf{a}}_i \\ \hat{\mathbf{a}}_i^\dagger \\ \hat{\mathbf{b}} \\ \hat{\mathbf{b}}^\dagger \end{pmatrix}, \underline{A}_k^j = \begin{pmatrix} \hat{\mathbf{A}}_{s,k}^j \\ \hat{\mathbf{a}}_{s,k}^{j\dagger} \\ \hat{\mathbf{a}}_{i,k}^j \\ \hat{\mathbf{a}}_{i,k}^{j\dagger} \\ \hat{\mathbf{b}}_k^j \\ \hat{\mathbf{b}}_k^{j\dagger} \end{pmatrix}, \tag{6.3}$$

where j marks the port in question and k marks the direction of the field, and s and i mark signal and idler fields. Linearizing the operators and looking at the field fluctuations, the intracavity

field fluctuations are given by

$$\delta\underline{a}(\omega) = \left(i\underline{\underline{M}}_{\Omega} - \underline{\underline{M}}\right)^{-1}\left[\underline{\underline{M}}_{in}\delta\underline{A}_{in}^{in}(\omega) + \underline{\underline{M}}_{out}\delta\underline{A}_{in}^{out}(\omega) + \underline{A}_L + \underline{A}_T\right], \tag{6.4}$$

$$\underline{\underline{M}}_j = \begin{pmatrix} \sqrt{2\gamma_s^j} & 0 & 0 & 0 & 0 & 0 \\ 0 & \sqrt{2\gamma_s^j} & 0 & 0 & 0 & 0 \\ 0 & 0 & \sqrt{2\gamma_s^j} & 0 & 0 & 0 \\ 0 & 0 & 0 & \sqrt{2\gamma_s^j} & 0 & 0 \\ 0 & 0 & 0 & 0 & \sqrt{2\gamma_p^j} & 0 \\ 0 & 0 & 0 & 0 & 0 & \sqrt{2\gamma_p^j} \end{pmatrix}, \tag{6.5}$$

$$\underline{\underline{M}}_{\Omega} = \begin{pmatrix} -\Omega+\omega & 0 & 0 & 0 & 0 & 0 \\ 0 & \Omega-\omega & 0 & 0 & 0 & 0 \\ 0 & 0 & \Omega+\omega & 0 & 0 & 0 \\ 0 & 0 & 0 & -\Omega-\omega & 0 & 0 \\ 0 & 0 & 0 & 0 & \omega & 0 \\ 0 & 0 & 0 & 0 & 0 & -\omega \end{pmatrix}. \tag{6.6}$$

The matrix $\underline{\underline{M}}$ contain the nonlinear couplings between the fields

$$\underline{\underline{M}} = \begin{pmatrix} -\gamma_s + i\Delta_s & 0 & 0 & g\beta & g\alpha_i^* & 0 \\ 0 & -\gamma_s - i\Delta_s & g^*\beta^* & 0 & 0 & g^*\alpha_i \\ 0 & g\beta & -\gamma_s + i\Delta_s & 0 & g\alpha_s^* & 0 \\ g^*\beta^* & 0 & 0 & -\gamma_s - i\Delta_s & 0 & g^*\alpha_s \\ -g^*\alpha_i/2 & 0 & -g^*\alpha_s/2 & 0 & -\gamma_p + i\Delta_p & 0 \\ 0 & -g\alpha_i^*/2 & 0 & -g\alpha_s^*/2 & 0 & -\gamma_p - i\Delta_p \end{pmatrix}, \tag{6.7}$$

and finally $\underline{A}_L$ and $\underline{A}_T$ represent interactions caused by cavity length fluctuations of the cavity δL and temperature fluctuations δT

$$\underline{A}_L = \begin{pmatrix} i\alpha_s\frac{\Omega}{L_{cav}}\delta L \\ -i\alpha_s^*\frac{\Omega}{L_{cav}}\delta L^* \\ i\alpha_i\frac{\Omega}{L_{cav}}\delta L \\ -i\alpha_i^*\frac{\Omega}{L_{cav}}\delta L^* \\ i\beta\frac{2\Omega}{L_{cav}}\delta L \\ -i\beta^*\frac{2\Omega}{L_{cav}}\delta L^* \end{pmatrix}, \underline{A}_T = \begin{pmatrix} i\alpha_s\frac{\Omega L_{crystal}}{L_{cav}}\left[\frac{\mathrm{d}n(\Omega)}{\mathrm{d}T} + n(\Omega\alpha_{KTP})\right]\delta T \\ -i\alpha_s^*\frac{\Omega L_{crystal}}{L_{cav}}\left[\frac{\mathrm{d}n(\Omega)}{\mathrm{d}T} + n(\Omega\alpha_{KTP})\right]\delta T^* \\ i\alpha_i\frac{\Omega L_{crystal}}{L_{cav}}\left[\frac{\mathrm{d}n(\Omega)}{\mathrm{d}T} + n(\Omega\alpha_{KTP})\right]\delta T \\ -i\alpha_i^*\frac{\Omega L_{crystal}}{L_{cav}}\left[\frac{\mathrm{d}n(\Omega)}{\mathrm{d}T} + n(\Omega\alpha_{KTP})\right]\delta T^* \\ i\beta\frac{2\Omega L_{crystal}}{L_{cav}}\left[\frac{\mathrm{d}n(2\Omega)}{\mathrm{d}T} + n(2\Omega\alpha_{KTP})\right]\delta T \\ -i\beta^*\frac{2\Omega L_{crystal}}{L_{cav}}\left[\frac{\mathrm{d}n(2\Omega)}{\mathrm{d}T} + n(2\Omega\alpha_{KTP})\right]\delta T^* \end{pmatrix}, \tag{6.8}$$

where α_{KTP} is the linear absorption coefficient and n is the refrative index. From the above equations the intracavity fields can be calculated, converted to quadrature operators $\delta\underline{X} = \underline{\underline{\Gamma}}\delta\underline{a}$

with

$$\underline{\underline{\Gamma}} = \begin{pmatrix} 1 & 1 & & & & \\ i & -i & & & & \\ & & 1 & 1 & & \\ & 0 & i & -i & & 0 \\ & & & & 1 & 1 \\ & & & & i & -i \\ & & & 0 & & \end{pmatrix}, \tag{6.9}$$

$$\delta\underline{X}(\omega) = \begin{pmatrix} \delta\hat{X}_s(\omega) \\ \delta\hat{P}_s(\omega) \\ \delta\hat{X}_i(\omega) \\ \delta\hat{P}_i(\omega) \\ \delta\hat{X}_b(\omega) \\ \delta\hat{P}_b(\omega) \end{pmatrix}. \tag{6.10}$$

The input/output equations can be set up in the form of transfer functions similarly to equations (2.51a) to (2.51d)

$$\delta\underline{X}^{in}_{out} = \underline{\underline{\Theta}}_{[in;in]}\delta\underline{X}^{in}_{in} + \underline{\underline{\Theta}}_{[out;in]}\delta\underline{X}^{out}_{in} + \underline{\underline{\Theta}}_{[\Delta;in]}\left(\underline{A}_L + \underline{A}_T\right) \tag{6.11a}$$

$$\delta\underline{X}^{out}_{out} = \underline{\underline{\Theta}}_{[in;out]}\delta\underline{X}^{in}_{in} + \underline{\underline{\Theta}}_{[out;out]}\delta\underline{X}^{out}_{in} + \underline{\underline{\Theta}}_{[\Delta;out]}\left(\underline{A}_L + \underline{A}_T\right). \tag{6.11b}$$

The quadrature operators can then be related to noise spectra via equations (2.26a) and (2.26b). This model should in principle allow for a analysis of how noise from different sources propagate through the system, but it requires knowledge of the intensity noise and phase noise in the input optical fields, as well as knowledge of the noise spectra of the cavity length and temperature. This information can be difficult to obtain with high precision, but this model could be used to estimate which sources of noise are of the highest importance. I began this, but never had time to finish due to the problems of the project and the need to pivot.

The second method builds on noise measurements of the error signals of the different locking systems. This methods was taught to me by Lee McCuller also of the LIGO group at the Kavli Institute of MIT, and has been used in the LIGO interferometers to give a reasonable estimate of the phase noise in their squeezed light measurements.

For this method, we need to measure noise spectra of the error signal of the CLF locking loop and homodyne locking loop. These should be converted to phase spectra by using the slope of the error signal around the set point. For each of the locks, we then need to measure the open loop gain functions via the method described in section (4.4) and using this extrapolate and calculate the closed loop and round trip gain functions.

Measuring the noise spectrum of the locked error-signal gives us the closed-loop noise spectrum, which is the remaining noise in the feedback loop. We can cast this to open-loop form by dividing the spectrum by the close-loop gain function. The open-loop noise spectrum is then the noise spectrum before the feedback loop is applied. Open- and closed-loop amplitude noise spectra are shown in figure (6.3). This spectrum is the PDH lock of the OPO used in chapters (7) and (8) (not to be confused with a phase noise spectrum of a phase lock).

The open-loop gain function allows us to interpret the contribution of different noise sources by using our knowledge of the shape of the noise spectra: Shot noise (here called sensing noise) is flat in frequency, and classical noise (here called actuator noise) is typically $1/f$ (in amplitude). These contributions are marked in figure (6.3), and we see that above 10 kHz our measurement is shot noise limited and that our lock is able to remove all of the classical noise. The peak at

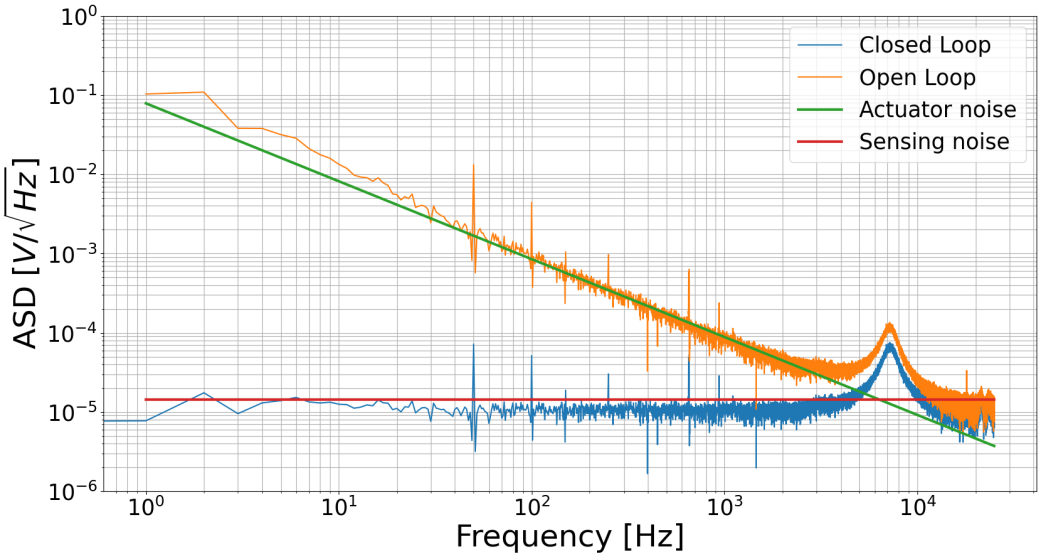

Figure 6.3: Closed- and open-loop amplitude spectral density feedback system. The green line marks the classical (actuator) noise and the red line marks the shot (sensing) noise.

7 kHz seems to be a small oscillation introduced by the feedback loop and is not expected to be a part of the open-loop noise.

Using the decomposed actuator and sensing noise spectra and the gain functions, we can estimate the resulting phase noise spectrum of our squeezed light measurement using the following expression

$$N_{SQZ}^{est} = \Big(\left| N_{act}^{LO} g_{CL}^{LO} \right|^2 + \left| N_{sens}^{LO} g_{RT}^{LO} \right|^2 + \left| N_{act}^{CLF} g_{CL}^{CLF} \right|^2 + \left| N_{act}^{CLF} g_{RT}^{CLF} g_{CL}^{LO} \right|^2 + \left| N_{sens}^{CLF} g_{RT}^{CLF} g_{RT}^{LO} \right|^2 + \left| N_{act}^{CLF} g_{CL}^{CLF} g_{RT}^{LO} \right|^2 \Big)^{-1/2}$$

Calculating the RMS value of the resulting spectrum should then give us the estimate on the total phase noise.

6.2 The OPO and the problems it encountered

Base on the loss calculations done in section (6.1.1), I designed a monolithic OPO, which I will present below. The physical properties of the crystal cavity as well as the optical cavity properties for the pump and fundamental modes are summarized in tables (6.1) and (6.2).

Physical Property	Value
Dimensions	1.0 mm × 1.2 mm × 4.9 mm
Radius of curvature	2.65 mm

Table 6.1: Table containing the physical properties of the 18 dB OPO. The crystal is biconvex with identical radii of curvature.

The monolithic OPO is designed to be double-resonant, and since there is no piezo controlled mirror to move, the only degrees of freedom available to achieve both quasi phase matching AND double resonance are crystal temperature and laser frequency. The combination of these should

Optical property \ Mode value	signal (1550 nm)	pump (775 m)
Input port reflectivity	99.95 %	99.8 %
Output port reflectivity	75 %	0.98 %
Waist size	14.1 μm	9.89 μm
FWHM	774 MHz	58.5 MHz
FSR	16.8 GHz	16.5 GHz
Finesse	21.7	283
Threshold	N/A	119 mW

Table 6.2: Table containing the properties of the 18 dB OPO for both fields. The properties are calculated for a crystal length of 4.9 mm.

in principle be enough, but to give ourselves a better chance of success, we also decided to buy crystals of different length ranging from 5.3 mm to 4.7 mm. For each of these crystals the radius of curvature optimizing the pump threshold and spatial filtering was found, and in general we found this to be $0.54L_{crystal}$.

The optical properties will vary a little bit with the length of the crystal, and simulated plots of the various optical properties as functions of crystal length can be seen in appendix (B). The crystals were procured, polished and coated according to the design decisions in the tables above, and I began setting up and aligning the cavity. It was at this point that the project ran into problems. The first problem was that only some of the crystals seemed to support cavities. For some no amount of mode matching and alignment seemed to allow interference to build up inside the crystal. For the crystals that did support a cavity, the cavity only appeared in the horizontal (p) polarization. This is shown in figure (6.4). This was a major problem, as the crystals are polled to achieve quasi-phase matching only for vertical (s) polarization.

The explanation we found was that the small radius of curvature of the crystals was too sensitive to polishing tolerances, causing some crystals to never have a stable cavity due to misaligning of the end phases of the crystal. For the ones that did have a cavity in p-polarization, due to the birefringence induced difference in the refractive index of the two polarizations, the s-polarization experiences too much refraction, again due to the short radius of curvature, to form a stable cavity or require too extreme an input angle for us to be able to hit. The solution seemed to be to redesign the crystals to have a much longer radius of curvature, making it less sensitive to imperfect polishing and hopefully cause less refraction of the vertical polarization. We settled on a new radius of curvature of $4.1L_{crystal}$, as this relaxed the requirements of the manufacturing tolerances while still keeping the isolation of the fundamental cavity mode high. The property changes caused by this redesign is summarized in table (6.3). We had the crystals

Property	Old value	New value
1550 nm waist	14.1 μm	42.3 μm
775 nm waist	9.89 μm	29.6 μm
Pump threshold	119 mW	356 mW

Table 6.3: Table containing the changes caused by the redesign of the crystal radius of curvature.

sent to polishing and coating, but as this took 4 months, I had to pivot to other projects and never had time to work on this project again. Instead of building this squeezed light source, I ended up building another squeezed light source performance and design wise comparable to the source describe in chapter (5), but completely free-space in stead of partly fiber-coupled.

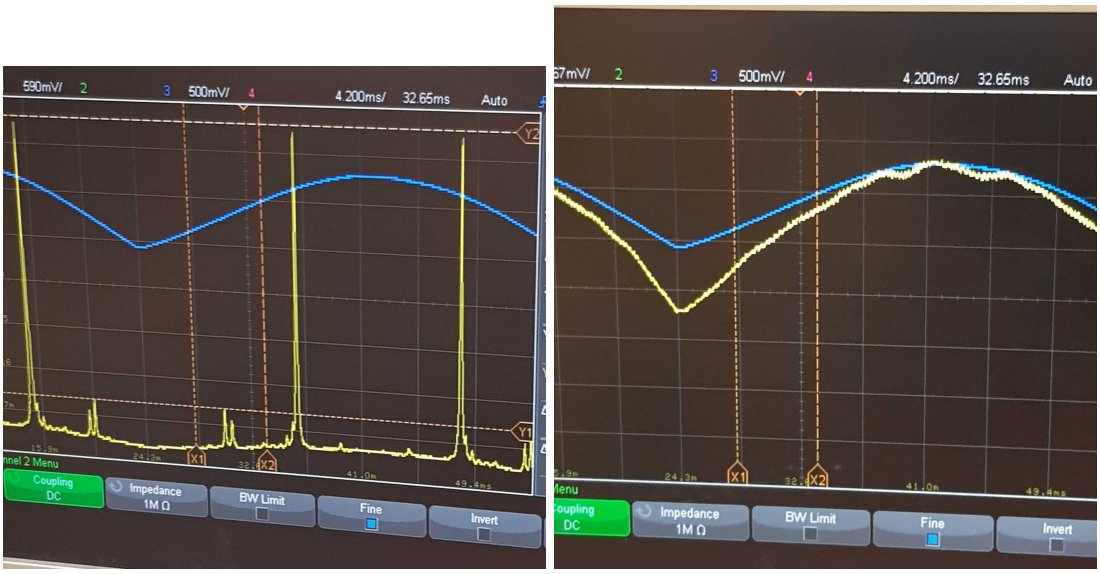

(a) The yellow trace is cavity transmission for p-polarized light.

(b) The yellow trace is the cavity transmission for s-polarized light.

Figure 6.4: Photo of an oscilloscope trace showing the cavity response of the pump mode in the 18 dB OPO. The scale of the yellow traces in the two photos is not the same: (a) has 500 mV / division, and (b) has 57 mV / division. The blue trace is a monitor detector showing power modulation when scanning the laser frequency due to moving in and out of the SHG phase-matching bandwidth.

This squeezer was used in the experiments of chapters (7) and (8). As I was never able to finish this experiment, this chapter can therefore hopefully serve as a summary of my work for new students to build upon and finish in the future.

It was about three o' clock at night when the final result of the calculation lay before me. At first I was deeply shaken. I was so excited that I could not think of sleep. So I left the house and awaited the sunrise on the top of a rock.

Der Teil und das Ganze
by Werner Heinsenberg, 1969

7

Squeezed vacuum phase estimation and sensing

This chapter is dedicated to a phase estimation and sensing experiment using squeezed vacuum states of light. The results of this experiment, we compiled into a manuscript titled " **Deterministic quantum phase estimation beyond the ideal NOON state limit**" by **Jens A H Nielsen, Jonas Schou Neergaard-Nielsen, Tobias Gehring and Ulrik Lund Andersen**. The manuscript was submitted to arXiv the day before the deadline of this thesis. This chapter will introduce the basic ideas of quantum metrology and put them into the context of this experiment. I will then give a short introduction to the experimental setup, before including the manuscript as a whole, but reformatted to fit the format of this thesis. Finally, I will include a small section detailing the method behind the data acquisition and analysis that went in to the figures featured in the manuscript. All sections of this chapter, not part of the main manuscript, are submitted along the manuscript as supplementary information. Most of the theory presented in this chapter is based on the detailed work by Adriano Berni, a former PhD student of our group [87].

7.1 Introduction to quantum metrology

Phase estimation shares the same classical limitation as other optical metrology schemes, the so-called shot noise limit (SNL). This limit arises from the random distribution of photons in a classical laser beam - also called shot noise. This (Poissonian) distribution of photons limits the sensitivity of the measurement [88]

$$\sigma_{SNL} = \frac{1}{2\sqrt{M\,\langle \hat{\mathbf{n}} \rangle}}, \tag{7.1}$$

where $\langle \hat{\mathbf{n}} \rangle$ is the average amount of photons probing the sample, and M is the number of times the measurement is repeated. The sensitivity of the measurement is the minimum detectable phase shift, and using coherent states of light in conjungtion with homodyne detection will have a sensitivity exactly equal to the right-hand side of equation (7.1).

Using non-classical states of light this scaling can be improved upon, and especially maximally entangled states such as the NOON state, $|\psi_{NOON}\rangle = 1/\sqrt{2}(|N,0\rangle \pm |0,N\rangle)$, which, in an interferometer setting, can achieve Heisenberg scaling

$$\sigma_{NOON} = \frac{1}{2\sqrt{M}\,\langle\hat{\mathbf{n}}\rangle}, \tag{7.2}$$

where for NOON states $2\,\langle\hat{\mathbf{n}}\rangle = N$ as only half of the photons will pass through the phase-shifting sample. Phase sensing using NOON states have been demonstrated in polarization [89], spatial [90] and orbital angular momentum (OAM) degrees of freedom [91] (non-exhaustive list), but generation of large NOON states is very difficult without photon resolved detection. Furthermore, the sensitivity of NOON states (and entangled states in general) is severely limited in the presence of loss [92]

$$\sigma_{HS,imp} = \frac{1}{2\sqrt{M}\,\langle\hat{\mathbf{n}}\rangle\,\eta^{\langle\hat{\mathbf{n}}\rangle}\mathcal{V}^2}, \tag{7.3}$$

where η is the total efficiency of the system, and $\mathcal{V}$ is the fringe visibility at the end of the interferometer.

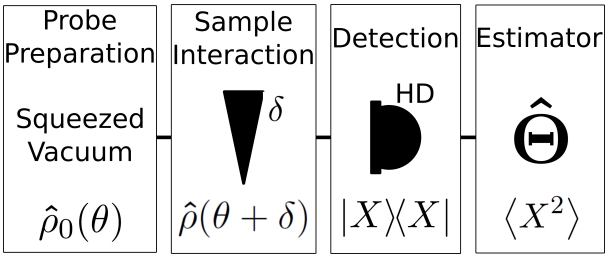

Figure 7.1: Top level schematic of a phase estimation protocol using squeezed vacuum states of light.

In a general phase sensing experiment, as sketched in figure (7.1), a probe state is prepared with a known phase θ. In this experiment the probe state is a squeezed vacuum state $\hat{\rho}_0(\theta) = |r\exp\{i\theta\}\rangle\langle r\exp\{i\theta\}|$, where r is the squeezing strength. The probe interacts with a sample, which transforms it according to $\hat{\rho}(\theta+\delta) = \hat{\mathbf{U}}(\delta)\hat{\rho}_0(\theta)\hat{\mathbf{U}}^\dagger(\delta)$ by inducing a phase shift δ. The probe state is measured in a phase sensitive measurement, and in an optical phase sensing experiment the preferred phase sensitive measurement method is balanced homodyne detection, where the probe state is projected into the quadrature basis $|X\rangle\langle X|$. From the measurement outcomes $\{x\}$ a suitable estimator $\hat{\mathbf{\Theta}}$ is chosen and the total phase $\phi = \theta+\delta$ is estimated. In the phase estimation experiment the total phase ϕ is estimated, but if the system is used for phase sensing, the measured phase shifts would be small compared to the controlled measurement set point θ, $\delta \ll \theta$.

The starting point of most discussions of quantum phase estimation protocols is the analysis of the bounds on the estimation sensitivity $\sigma(\phi)$ - the smallest detectable phase shift giving an SNR of 1 and using M independent samples (a smaller sensitivity is better)

$$\sigma(\phi) \overset{\text{cCR}}{\geq} \sqrt{\frac{1}{MF(\phi)}} \overset{\text{qCR}}{\geq} \sqrt{\frac{1}{MH}}, \tag{7.4}$$

where H is called the quantum Fisher Information and $F(\phi)$ the classical Fisher Information. Starting from the first inequality, called the classical Cramér–Rao (cCR) bound, given a certain estimator, the sensitivity will be larger or equal to the inverse of the the square root of the M-sample, classical Fisher Information $MF(\phi)$, which is the maximal amount of phase information that can be extracted from a given measurement of M samples.

In this experiment, we use squeezed vacuum states as probes together with homodyne detection as the measurement method. The homodyne measurement samples x will be distributed according to the marginal probability distribution $P(x|\phi)$, which can be found by tracing away the p-variable in the squeezed vacuum Wigner function

$$\begin{aligned} P(x|\phi) &= \int \mathrm{d}p \mathcal{W}^{\phi}_{\mathrm{sqz}}(x,p), \\ &= \frac{e^{\frac{-x^2}{2\left(V_- \cos^2(\phi)+V_+ \sin^2(\phi)\right)}}}{\sqrt{2\pi\left(V_- \cos^2(\phi)+V_+ \sin^2(\phi)\right)}}. \end{aligned} \tag{7.5}$$

For a pure squeezed vacuum state $V_\pm = \exp(\pm 2r)$, and we can evaluate the classical Fisher Information as

$$\begin{aligned} F(\phi) &= \int \mathrm{d}x P(x|\phi)\left(\frac{\partial \log(P(x|\phi))}{\partial \phi}\right)^2, \\ &= \frac{2\sinh^2(2r)\sin^2(2\phi)}{\left(e^{-2r}\cos^2(\phi)+e^{2r}\sin^2(\phi)\right)^2}, \end{aligned} \tag{7.6}$$

where the last equality is for a squeezed vacuum state of squeezing strength r and measured at a quadrature angle of ϕ [93]. For a constant squeezing strength, equation (7.6) has an optimal measurement angle $\phi_{opt} = \arccos(\tanh(2r))/2$, where the Fisher Information is maximized $F = 2\sinh^2(2r)$.

If the probe is not a perfectly pure squeezed state, but has experienced some loss, then it can be modelled as a thermal squeezed state with $\langle \hat{\mathbf{n}} \rangle_{th}$ average photons mixed in and a rescaled squeezing strength r_{th}. In this case the squeezed and anti-squeezed variances are $V_\pm = (2\langle \hat{\mathbf{n}} \rangle_{th} + 1)\exp\{\pm 2r_{th}\}$, and the Fisher Information is modified as

$$F(\phi) = \frac{2\sinh^2(2r_{th})\sin^2(2\phi)}{\left(e^{-2r_{th}}\cos^2(\phi)+e^{2r_{th}}\sin^2(\phi)\right)^2}, \tag{7.7}$$

which has the same form as equation (7.6) with a maximum at $\phi_{opt} = \arccos(\tanh(2r_{th}))/2$ and maximal value $F = 2\sinh^2(2r_{th})$. Both the thermal photons added and the re-scaled squeezing strength can be obtained from the squeezed V_- and anti-squeezed V_+ variances (normalized to shot noise).

$$r_{th} = \frac{1}{2}\log\left(\frac{V_+}{\sqrt{V_+ V_-}}\right), \tag{7.8}$$

$$\langle \hat{\mathbf{n}} \rangle_{th} = \frac{\sqrt{V_+ V_-} - 1}{2}, \tag{7.9}$$

and we can calculate the total number of resources in the impure, squeezed vacuum state as

$$\langle \hat{\mathbf{n}} \rangle = \langle \hat{\mathbf{n}} \rangle_{th} \cosh(2r_{th}) + \sinh(r_{th})^2. \tag{7.10}$$

We return to equation (7.4), where the second inequality, known as the quantum Cramér-Rao (qCR) bound, which given a certain measurement puts a lower bound on the sensitivity equal to the inverse of the square root of the M-sample, quantum Fisher Information MH, which describes the phase information contained in the probe state. The quantum Cramér-Rao bound therefore describes how the maximal phase information extractable by a measurement is the phase information contained in the probe state. For pure squeezed vacuum the quantum Fisher

Information can be found to be $H = 8(\langle\hat{\mathbf{n}}\rangle + \langle\hat{\mathbf{n}}\rangle^2)$ [94]. In this case the sensitivity given M measurement samples is

$$\sigma \geq \sqrt{\frac{1}{MH_{sqz}}} = \frac{1}{\sqrt{M8\Big(\langle\hat{\mathbf{n}}\rangle + \langle\hat{\mathbf{n}}\rangle^2\Big)}}, \tag{7.11}$$

In the case of equation (7.11), the sensitivity shows a constant advantage compared to SQL at low photon numbers, but Heisenberg scaling at large photon numbers. The quantum Fisher Information for squeezed vacuum states represent the theoretically best sensitivity achievable in the system, and is in fact the best achievable sensitivity among all Gaussian states.

In the case of pure squeezed vacuum, homodyne detection at the optimal angle is the optimal measurement, saturating the quantum Cramér-Rao bound

$$\begin{aligned} F(\phi_{opt}) &= 2\sinh^2(2r) \\ &= 8\sinh^2(r)\cosh^2(r) \\ &= 8\big(\sinh^4(r) + \sinh^2(r)\big) \\ &= 8\Big(\langle\hat{\mathbf{n}}\rangle + \langle\hat{\mathbf{n}}\rangle^2\Big) = H, \end{aligned} \tag{7.12}$$

since $\langle\hat{\mathbf{n}}\rangle = \sinh^2(r)$ for pure squeezed vacuum. In the case of linear loss the quantum Fisher Information is given by

$$\frac{(2\langle\hat{\mathbf{n}}\rangle_{th} + 1)^2}{2\langle\hat{\mathbf{n}}\rangle_{th}(2\langle\hat{\mathbf{n}}\rangle_{th} + 1) + 1} 2\sinh^2(2r_{th}), \tag{7.13}$$

and as homodyne detection is no longer the optimal measurement, the QCR bound can no longer be saturated.

7.1.1 Bayesian estimation

In order to saturate the classical Cramér–Rao bound, we need to choose a suitable estimator for the phase. Figure (7.2) shows a shot noise normalized homodyne measurement of a squeezed vacuum state with varying homodyne phase. We see the red line $\langle X\rangle$ is effectively zero independently of the phase and would therefore be a bad estimator. The orange lines are the standard deviation, which together with the variance $\langle X^2\rangle$ show a clear dependence on the phase. We therefore choose to use X^2 as our estimator to be plugged into a suitable estimation routine. The two most famously able to saturate the classical Cramér-Rao bound are maximum likelihood estimation (MLE) and Baysian estimation (BE) routines [95]. The choice of routine is arbitrary, as MLE coincides with BE in the case of a uniform prior (which we use), but we choose to work with the Bayesian estimation routine, as it does not depend on the convergence of a minimizer.

The Bayesian estimation routine utilizes Bayes' law, which for M measured samples is given by

$$P(\phi|\{x\}_M)P(\{x\}_M) = P(\{x\}_M|\phi)P(\phi). \tag{7.14}$$

As mentioned before, we assume the a priori probability distribution to be uniform, and as the variance is only uniquely determined for phase angles in the range of $\phi = [0, \pi/2]$, the uniform a priori probability distribution is therefore $P(\phi) = 2/\pi$.

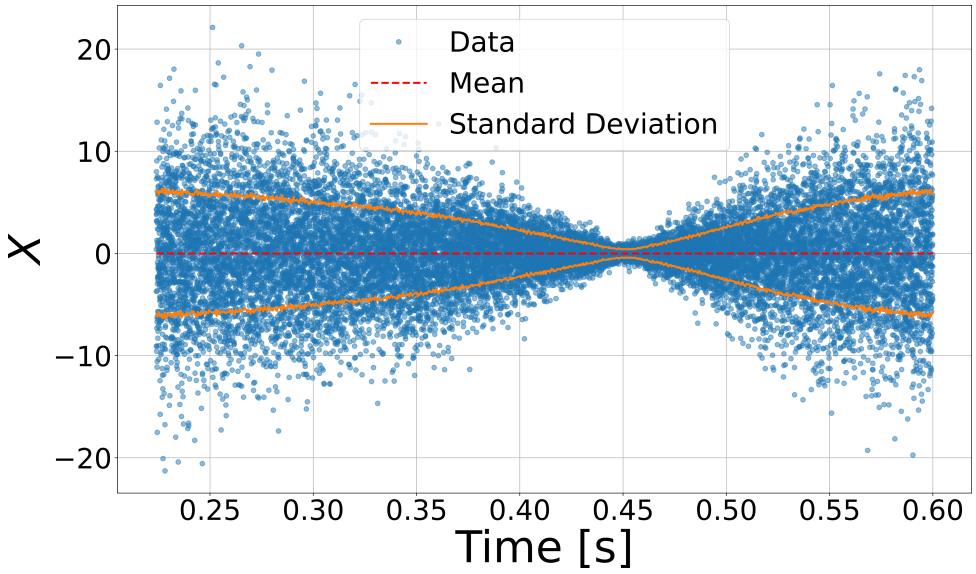

Figure 7.2: Homodyne time trace signal downmixed to the 5 MHz sideband frequency and normalized to shot noise. The orange lines mark the standard deviation, and the red line marks the mean value

$P(\{x\}_M)$ works as a normalization factor, and $P(\{x\}_M|\phi)$ is the probability of measuring the homodyne outcomes $\{x\}_M$ given the phase ϕ. This probability distribution is given by the product of marginal distributions of individual homodyne samples equation (7.5)

$$P(\{x\}_M|\phi) = \prod_{i=1}^{M} P(x_i|\phi). \tag{7.15}$$

The a posteriori phase probability distribution $P(\phi|\{x\}_M)$ can therefore be found using homodyne measurements and knowledge of the squeezed and anti-squeezed variances. The estimated phase is then found as the mode of the posterior probability distribution $\phi_{est} = \arg\max(P(\phi|\{x\}_M))$, and the sensitivity is found from the width. The build-up of the posterior distribution can be seen in figure (7.5)d together with a plot showing the converge of the estimated phase towards a stable value. The grey area of the inset is the associated estimation uncertainty.

7.2 Experimental setup

The squeezed light is generated in a doubly resonant optical parametric oscillator (OPO) using a periodically-poled potassium-titanyl-phosphate (PPKTP) crystal as the non-linear medium. The geometry and design parameters of the cavity are identical to that of [48], and the OPO has a threshold power of 4.7 mW.

The experimental setup is sketched in figure (7.3). An NKT HARMONIK module pumped by an NKT BOOSTIK E15 laser supplies the experiment with 775 nm light, which is used to pump the OPO. The pump beam propagates through an electro-optical modulator (EOM) that creates sidebands at 111 MHz to use in the Pound-Drever-Hall [40] stabilization of the OPO length.

The laser also supplies 1550 nm light, which is used in a coherent locking scheme [45]. This coherent locking field (CLF) is frequency-upshifted by 40 MHz by an acousto-optic modulator

(AOM) and enters the OPO, where it undergoes difference-frequency-generation (DFG) by interacting with the pump beam. The reflected beam, which contains the beat of the +40 and -40 MHz sidebands, is detected and fed back to the AOM in the form of frequency modulation allowing for stabilization of the relative phase between the pump beam and the CLF field at the homodyne detector.

The 1550 nm light is also used as a local oscillator (LO) for the homodyne detector. This LO is cleaned by a 1590 finesse, linear mode-cleaning cavity (MCC) before interacting with the squeezed light and CLF field in the homodyne detector. The relative phase between the LO and the squeezed light is stabilized by phase-locking the LO and CLF fields.

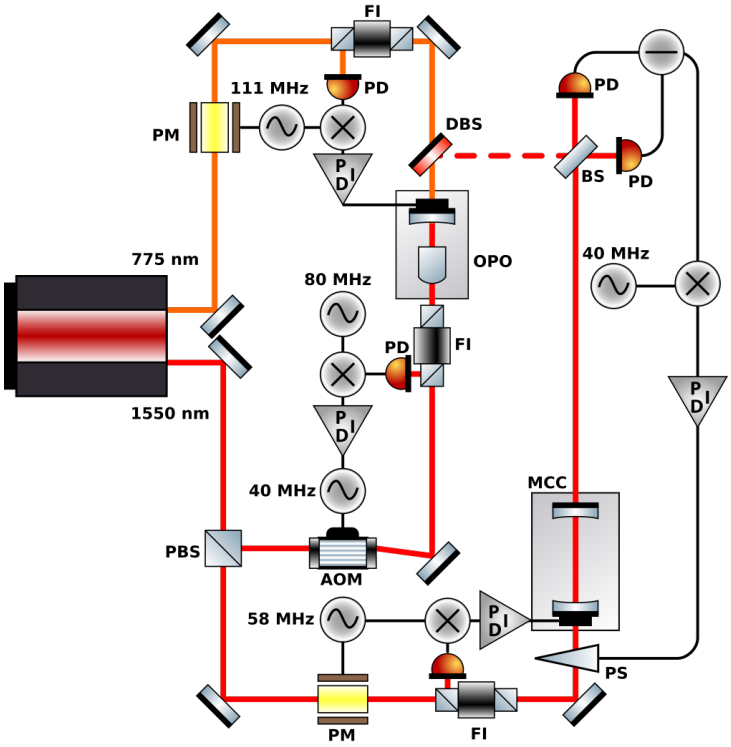

Figure 7.3: Sketch of the optical layout. Orange lines represent the 775 nm mode, and the red lines represent the 1550 nm modes. The dotted line represents the squeezed mode.
AOM: Acousto-optic modulator, BS: Beam-spitter, EOM: Electro-optic modulator, DBS: Dichroic beam-splitter, FI: Faraday Isolator, MCC: Mode-cleaning cavity, OPO: Optical-parametric-oscillator, PBS: Polarizing beam-splitter, PD: Photo-diode.

The squeezer performance as a function of pump power at 5 MHz sideband frequency and as a function of sideband frequency at 3.6 mW pump power are shown in figure (7.5)b. The squeezing generated in an OPO and measured with homodyne detection is given by

$$V_{\pm}^2 = 1 \pm \eta \frac{4\sqrt{\frac{P}{P^{thr}}}}{\left(1 \mp \sqrt{\frac{P}{P^{thr}}}\right)^2 + \left(\frac{\omega}{\gamma}\right)^2}, \tag{7.16}$$

$$V_{\pm}(\phi_{RMS})^2 \approx V_{\pm}^2 \cos^2(\phi_{RMS}) + V_{\mp}^2 \sin^2(\phi_{RMS}), \tag{7.17}$$

where P is the pump power, P^{thr} is the OPO threshold power, $\omega = 2\pi\nu$ is the angular sideband frequency, and γ is the decay rate of the OPO. η is the total efficiency of the system, and ϕ_{RMS} is the RMS phase noise between squeezed light and LO.

The solid lines in figure (7.5)b are fits to equation (7.17) from which we extract $\eta = 88.9(3)\,\%$ and $\phi_{RMS} = 10(2)\,\mathrm{mrad}$. The main sources of loss are intra cavity loss, which limits the escape effeciency to 96 %, the limited efficiency of the photo diodes of approximately 99 % and homodyne visibility of around 97.5 %. The phase noise mainly comes from the phase locks and the PDH lock of the LO, which due to the relatively high finesse of the cavity adds some of phase noise.

7.3 Deterministic quantum phase estimation beyond the ideal NOON state limit

Jens A.H. Nielsen, Jonas S. Neergaard-Nielsen Tobias Gehring and Ulrik L. Andersen

Center for Macroscopic Quantum States (bigQ), Department of Physics, Technical University of Denmark, Fysikvej, 2800 Kgs. Lyngby, Denmark

Abstract

The measurement of physical parameters is one of the main pillars of science. A classic example is the measurement of the optical phase enabled by optical interferometry where the best sensitivity achievable with N photons scales as $1/N$ – known as the Heisenberg limit [22, 96–100]. To achieve phase estimation at the Heisenberg limit, it has been common to consider protocols based on highly complex NOON states of light [101]. However, despite decades of research and several experimental explorations [89, 102–107], there has been no demonstration of deterministic phase estimation with NOON states reaching the Heisenberg limit or even surpassing the shot noise limit. Here we use a phase estimation scheme based on a deterministic source of Gaussian squeezed vacuum states and high-efficiency homodyne detection to obtain phase estimates with an extreme sensitivity that significantly surpasses the shot noise limit and even beats the performance of an ideal, and thus unrealistic, NOON state protocol. Using a high-efficiency setup with a total loss of about 11% we achieve a Fisher Information of $15.8(6)\,\mathrm{rad}^{-2}$ per photon unparalleled by any other optical phase estimation technology. The work represents a fundamental achievement in quantum metrology, and it opens the door to future quantum sensing technologies for the interrogation of light-sensitive biological systems [21].

It is of fundamental interest and practical relevance to investigate the ultimate bounds on the precision in estimating a phase [96,98]. According to classical (that is, approximate) theories of light, phase estimation can in principle be carried out with an arbitrary precision, but due to the inherent corpuscular quantum nature of light phase measurements will in reality be limited in precision – a precision that depends on the probing quantum state of light. If non-entangled states are used, the ultimate precision limit is the shot-noise limit (SNL) where the sensitivity scales as $1/\sqrt{\langle \hat{\mathbf{n}} \rangle}$, with $\langle \hat{\mathbf{n}} \rangle$ being the average number of photons traversing the sample. By exploiting entangled states, it is possible to reach the ultimate Heisenberg limit with superior scaling (see figure (7.4)a).

One of the most celebrated quantum states for reaching the ultimate Heisenberg limit – often referred to as the optimal state for loss-free sensing – is the so-called NOON state [101]: $|\Psi_{NOON}\rangle = 1/\sqrt{2}(|N\rangle|0\rangle + |0\rangle|N\rangle)$ which represents an optical state that is a superposition of N photons across two optical modes. Although a large number of experimental realizations on phase estimation with NOON states have been reported [89, 102–107], as of today, only a single experiment has been able to obtain a sensitivity that violates the SNL [89], and even in this realization, the SNL was only beaten by using a probabilistic source of two-photon NOON states. Due to the high complexity in generating the NOON state and their extreme fragility to loss, it is unlikely that NOON states will be able to reach the Heisenberg limit, or even beat the SNL, for high photon numbers.

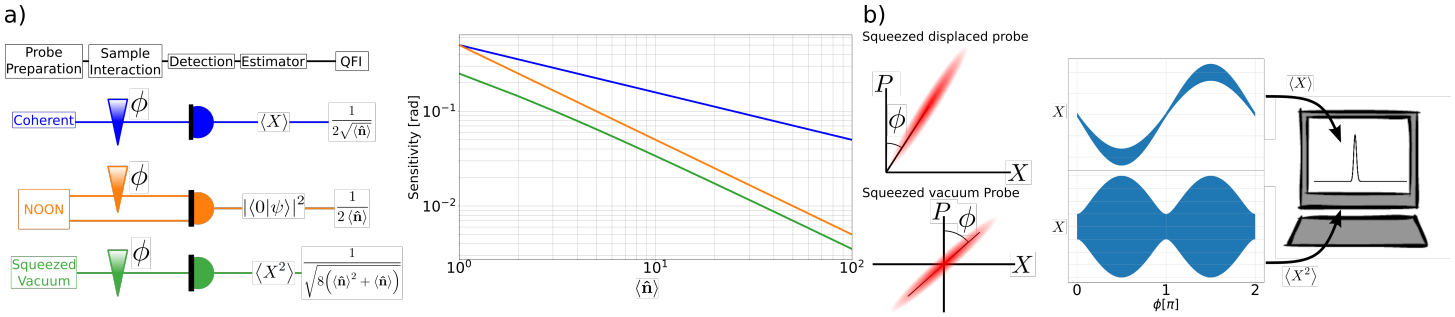

Figure 7.4: Principles and limits of quantum phase estimation. a) Schematics of three different phase estimation schemes. A quantum state of light undergoes a phase shift which is measured with either a homodyne detector (HD) or a NOON-state detector (involving photon counters) from which estimators are used to estimate the phase shift. Note that the NOON-state scheme is based on a two-beam interferometer in which only half of the photons traverse the sample. We therefore use the conservative sensitivity bound of $1/2\,\langle\hat{\mathbf{n}}\rangle$ (where $N = 2\,\langle\hat{\mathbf{n}}\rangle$) for the comparison to our approach. b) The optimal sensitivities for the three schemes. c) Phase space pictures of a displaced squeezed state and a vacuum squeezed state, and the resulting quadrature measurements as a function of the phase. The phase is estimated using the estimators $\langle X\rangle$ or $\langle X^2\rangle$ for the displaced squeezed state and vacuum squeezed state, respectively.

It has been known for decades that the SNL can be more easily surpassed using squeezed states of light [94, 97, 108, 109], which by now has also been realized in several phase estimation experiments [23, 110–113]. However, in most of those experiments, squeezed light is combined with a bright coherent state in an interferometric measurement by which the sensitivity is often limited to $\sqrt{V_-/\langle\hat{\mathbf{n}}\rangle}$ (where V_- is the variance of the squeezed state quadrature normalized to the variance of the vacuum state). Although being superior to the shot noise limit of $1/\sqrt{\langle\hat{\mathbf{n}}\rangle}$, the sensitivity is inferior to the Heisenberg scaling and thus does not reach the fundamental limit of NOON states. In fact, it is often claimed that Heisenberg scaling with squeezed light requires a highly complex measurement strategy [114]. However, in this Letter we show that by employing squeezed vacuum as a probe and a simple quadrature detector as the measurement device, phase estimates at the Heisenberg limit can be attained by evaluating the square of the quadrature outcomes. In addition to a sensitivity scaling similar to that for NOON states, our practical squeezed state estimation protocol is able to reach absolute sensitivities superior to those of the ideal NOON states due to a favorable scaling factor of $\sqrt{1/2}$ [94].

We also note that in contrast to previous NOON state realizations, our scheme is not based on probabilistic sources of light or any post-selection of the measurement outcomes. The conventional approach to squeezing-enhanced phase estimation is based on displaced squeezed states undergoing phase shifts that are estimated using a phase-referenced homodyne detector. The estimator, X, then yields an estimate of the phase with a quadrature uncertainty that depends on the actual phase as illustrated in figure (7.4)b: The best phase estimate is achieved when the response (derivative of $\langle X\rangle$) is maximized and the noise is minimized which, in this case, occurs mid-fringe (at the phases $\phi = n\pi$ where $n = 0, 1, 2\ldots$). Using instead squeezed vacuum as the probe, the measurement of X does not yield information about the phase since in this case $\langle X\rangle = 0$, but if we use X^2 as the estimator, the information is revealed. In this case, however, the phase shift for which the response is the largest is not coinciding with the phases with minimum noise (at $\phi = n\pi$) and thus a trade-off needs to be found for which the sensitivity is optimized. The trade-off is optimized for the phases $\phi = \arccos(\tanh 2r)/2 + n\pi$ at which the Fisher Information is maximized; $F = 2\sinh^2(2r)$ where r is the squeezing parameter. From the Fisher Information, we find the sensitivity $\sigma_{sqz} = 1/\sqrt{2\sinh^2(2r)}$ which can be expressed in

terms of the average photon number (see supplementary material):

$$\sigma_{sqz} = \frac{1}{\sqrt{8(\langle \hat{\mathbf{n}} \rangle^2 + \langle \hat{\mathbf{n}} \rangle)}} \,. \tag{7.18}$$

Here we assume a pure squeezed state; for impure squeezed states see the Supplementary Material. The expression in equation (7.18) exhibits Heisenberg scaling (for $\langle \hat{\mathbf{n}} \rangle \gg 1$), and moreover, it saturates the quantum Cramér–Rao bound which means that the scheme with homodyne detection of squeezed vacuum is optimal among all possible measurement strategies. In addition to being optimal among all Gaussians, it is also clear that it beats the complex estimation strategy of using non-Gaussian NOON states as $\sigma_{sqz} < 1/2 \langle \hat{\mathbf{n}} \rangle$ for all $\langle \hat{\mathbf{n}} \rangle$.

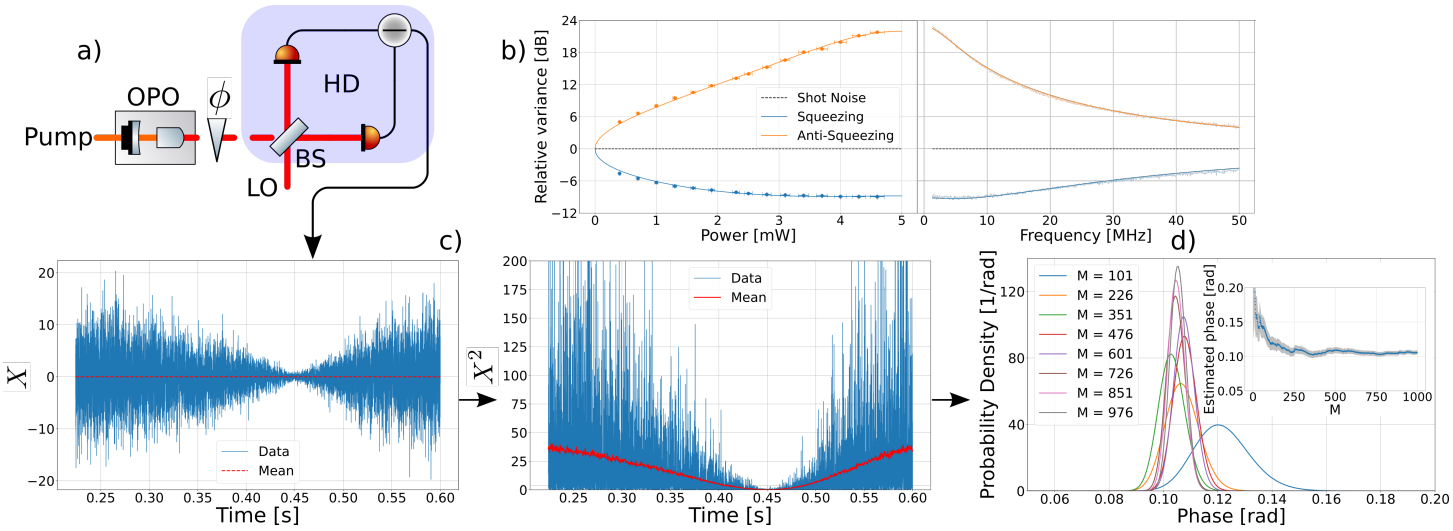

Figure 7.5: Experimental scheme and measurement method. a) Schematic of the experimental setup comprising an optical parametric oscillator (OPO) for squeezed light generation and a high-efficiency homodyne detector with a controllable local oscillator. As the estimated phase shift is relative between the squeezed vacuum and the local oscillator, in the experimental realization, we imposed the phase shift onto the local oscillator. b) Squeezed light spectrum and noise power versus pump power at the sideband frequency of 5 MHz for the squeezed and anti-squeezed quadratures. c) Quadrature measurement outcomes and their squares. The data are acquired while slowly varying the phase of the local oscillator, and down-mixed to a 5 MHz sideband frequency with a bandwidth of 1MHz. d) An example of a posteriori probabilities for the phase for different measurement trials and the associated phase estimates (inset).

A simplified schematic of the experimental setup is shown in figure (7.5)a (see Supplementary Material for details). We employ type 0 parametric down-conversion in a high-quality optical cavity to produce squeezed vacuum in a single spatial mode at the wavelength of 1550 nm. The squeezed vacuum state then experiences a phase shift of ϕ (relative to a reference) before its X quadrature is measured by a homodyne detector. At this detector, the squeezed mode interferes with a phase-referenced local oscillator mode at a balanced beam splitter, the two outputs are detected with high-efficiency photodiodes, and the resulting currents are subtracted, amplified and fed to a computer for phase estimation and analysis.

By paying careful attention to the design and implementation of the source and the detectors, the total absorption and scattering loss was kept below 11% including the loss associated with the source, the propagation and the detector. As a result, we produce squeezed states with a maximum of 9.0 dB of squeezing at a sideband frequency of 5 MHz (see figure (7.5)b). Due to the absorption and scattering losses, the produced squeezed vacuum state is not pure, which eventually leads to a deviation from Heisenberg scaling of the sensitivity.

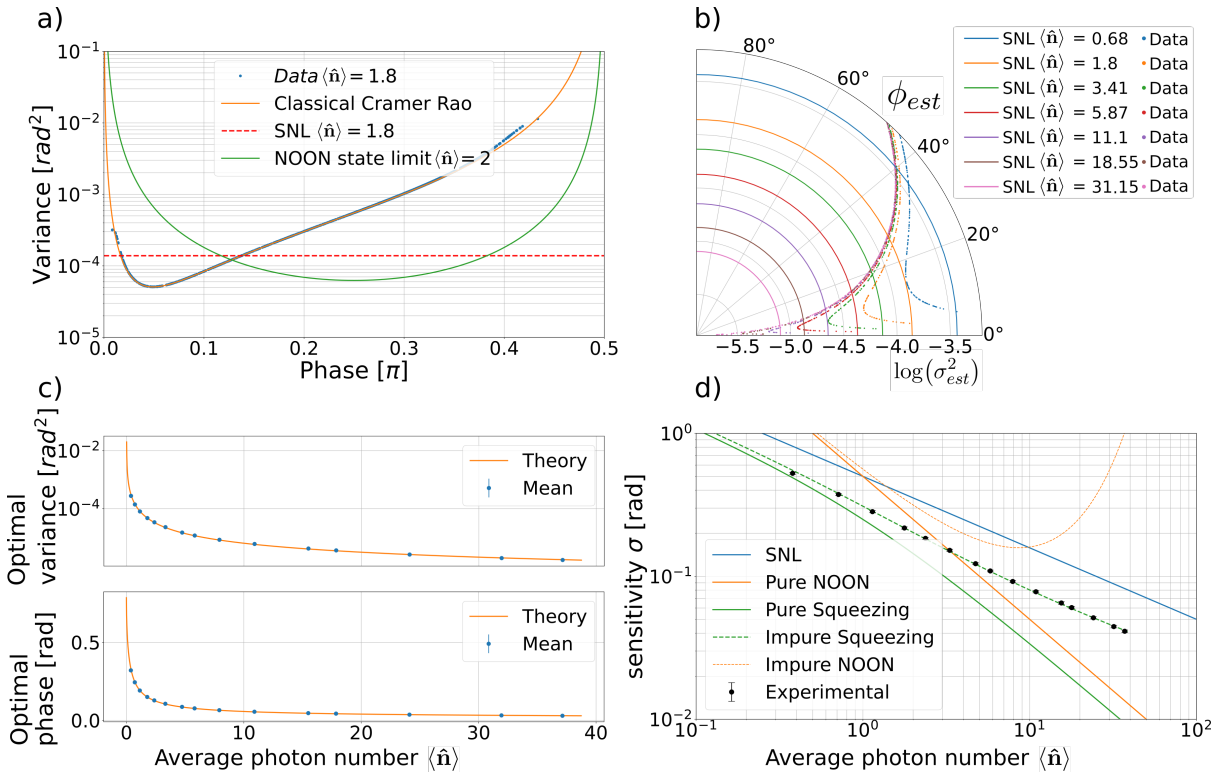

Figure 7.6: Quantum phase estimation results. a) The variance of the phase estimate based on 1000 quadrature measurements of a squeezed vacuum state with 11 photons. This is compared to the SNL and the limit for an ideal NOON state with $2\langle\hat{\mathbf{n}}\rangle = N = 4$. b) The variance of the phase estimated for different average photon numbers represented in a polar diagram and compared to the SNLs of the respective realizations (the curves are color-coded). It is clear from these plots that the variance is minimized for certain phases. The minimal variances and associated phases are presented in c) for different photon numbers and compared with theory. d) The optimized sensitivities versus photon numbers are presented and related to the theoretical predictions for the SNL, squeezed vacuum limit and the NOON state limit. We include theoretical predictions for the ideal limits and the practical limits with 11% loss as measured in our system.

To estimate the phase, ϕ, and the associated uncertainty, we conduct $M = 1000$ quadrature measurements for each phase setting, thereby producing a collection of 1000 data points, $\{x\}_M$. An example of the measured quadrature, X, and the conversion to X^2 for different phases are presented in figure (7.5)c. From these measurements, we find the likelihood of acquiring the set $\{x\}_M$ conditioned on the phase ϕ: $P(\{x\}_M|\phi) = \Pi_{i=1}^{M} P(x_i|\phi)$. The individual measurements are sampled from a Gaussian distribution, $P(x|\phi) = \exp\left(-x^2/2V(\phi)\right)/\sqrt{2\pi V(\phi)}$, with variance $V(\phi) = V_- \cos^2(\phi) + V_+ \sin^2(\phi)$, where V_+ and V_- are the anti-squeezed and squeezed variances, respectively. Using Bayes' theorem, we find the probability distribution for the phase conditioned on the measurement outcomes (the a posteriori probability distribution): $P(\phi|\{x\}_M) = P(\{x\}_M|\phi)P(\phi)/P(\{x\}_M)$ where $P(\{x\}_M)$ is a normalization factor and $P(\phi) = 2/\phi$ is the a priori probability distribution of the phase (assumed to be flat in the range $[0;\pi/2]$). In figure (7.5)d, we plot the a posteriori distribution for different values of M, illustrating the gradual Bayesian updating of the phase estimate. We then determine the estimated phase as the argument of the maximum value of $P(\phi|\{x\}_M)$ (see inset in figure (7.5)d) and the associated phase uncertainty by the width of the distribution. These results are summarized in figure (7.6)a for $\langle\hat{\mathbf{n}}\rangle = 1.8$ and in a polar plot representation in figure (7.6)b for different average photon numbers. It is clear that the phase uncertainty decreases with increasing photon number

(which we realize by varying the squeezing degree) and that it is optimized at specific phases (see figure (7.6)c). The best operating principle of the system is thus to measure small phase shifts relative to the measurement angle for which the phase variance is smallest. In figure (7.6)d, we plot the sensitivity optimized over the phase for different photon numbers, and we clearly observe performance beyond the ideal NOON state limit for photons up to around 3 as well as beyond the SNL and the loss-adapted NOON state limit for photons up to around 40.

Since our states are being produced and measured deterministically, we are in a position to perform real-time measurements of a dynamically varying phase with near-ultimate precision. To do this, we probe an induced 3 kHz phase modulation as well as other low-frequency phase noise components with our sensitive probe which in these measurements contains 6 photons and preset (and locked with a bandwidth of less than approx 1kHz) to the optimal phase. The frequency spectrum of the measured phase signal and noise is shown in figure (7.7)a and the real-time estimate of the dynamically varying phase is shown in figure (7.7)b for $M = 100$. By zooming into a certain time interval, the 3 kHz signal becomes visible (figure (7.7)c).

In summary, we have demonstrated phase sensing close to the ultimate limit, beating the ideal NOON state phase sensing scheme – often viewed as the optimal phase sensing strategy – with up to about 3 photons using solely squeezed vacuum and homodyne detection. To the best of our knowledge this is the best sensitivity per resource achieved in any optical phase sensing experiment: The directly measured Fisher Information per photon in our scheme is $15.8(6)\,\mathrm{rad}^{-2}$ which should be contrasted to the Fisher information of the best NOON state experiment of $\sim 4.2\,\mathrm{rad}^{-2}$ [89]. While we have demonstrated violations of the SNL and the NOON state limit for only a small range of phases, it can be easily extended to phases covering the entire range of $[0;\pi/2]$ by making use of an adaptive feedback approach [93]. We also note that by combining our strategy with a multi-pass metrology protocol [115], the sensitivity can be improved even further as in this case Heisenberg scaling will also apply to the number of measured samples [116]. The development and realization of a practical and loss-tolerant phase sensing scheme that beats the performance of any other current phase sensing strategy is not only of fundamental interest, but is also of practical relevance in phase sensing scenarios, where a low photon flux is needed to avoid the change of dynamics of the interrogated, potentially light-sensitive, sample [117, 118].

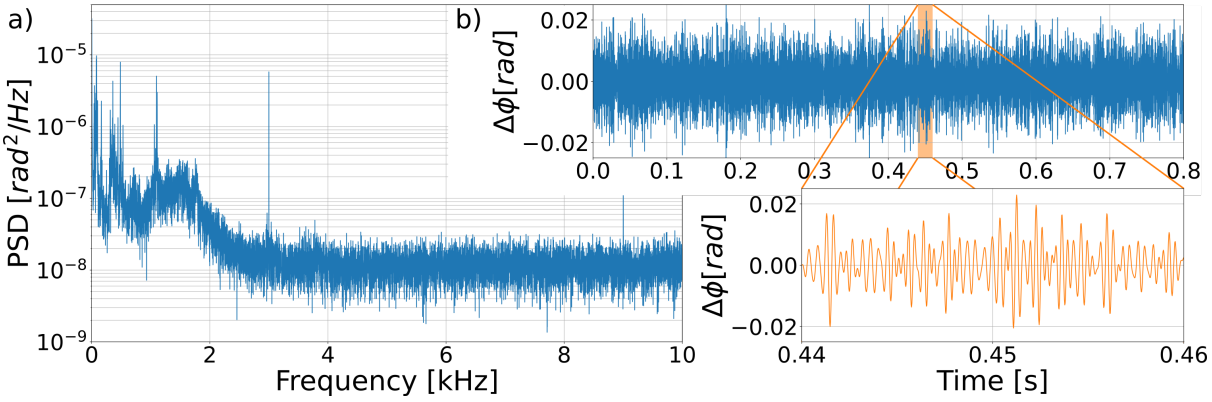

Figure 7.7: Quantum-enhanced tracking of a phase signal. a) Estimated dynamically varying phase signal using squeezed vacuum (with 6 photons) and Bayesian inference (inset) and the associated frequency spectrum. A 3 kHz induced signal as well as some low-frequency noise are apparent. b) Time trace of the same signal but bandpass-filtered at 3 kHz with a 2 kHz bandwidth. The zoom of the time trace as well as the frequency spectrum clearly shows the 3 kHz modulation.The y-axis $\Delta\phi$ is the relative phase shifts compared to the preset measurement phase.

7.4 Experimental method

The proof of principle experiment shown in figure (7.6) is done by slowly scanning the phase of the local oscillator and recording the homodyne detector output in sets of 1 second with a $50\,\mathrm{MSa\,s^{-1}}$ analogue-digital-converter (ADC) acquisition card. To avoid aliasing, an analogue 10 MHz low-pass filter is placed before the acquisition. The electronic noise and shot noise is also recorded in the same way.

The time traces are downmixed digitally to a 5 MHz sideband frequency by multiplying the time traces with a 5 MHz cosine and applying a 1 MHz digital low-pass filter to remove the double-frequency component. The data is also down-sampled to have the same sampling frequency. The signal time traces are normalized to the shot noise standard-deviation, which has had electronic noise subtracted. An example of a down-mixed time trace is shown in figure (7.2).

The variance is calculated from the time traces using sliding window of 1000 samples length, and the squeezed and anti-squeezed variances are extracted to calibrate the estimation.

The time trace is divided into slices of $M = 1000$ quadrature samples for which the marginal distributions are calculated equation (7.5). These 1000 marginal distributions are multiplied together to calculate the posterior distribution, and from this distribution a single phase is estimated as the mode of the distribution, and the uncertainty is found from the the width. The M-sample variance is plotted vs. the estimated phase in figure (7.6)a. It is in excellent correspondence with the theoretical variance given by the inverse classical Fisher Information. The photon expectation value in this trace is $\langle\hat{\mathbf{n}}\rangle = 1.8$ photons, and the SNL variance is calculated as $1/(4M\,\langle\hat{\mathbf{n}}\rangle)$ and the NOON state variance is calculated as $1/M/\left(2\mathcal{V}^2\eta^{\langle\hat{\mathbf{n}}\rangle}\,\langle\hat{\mathbf{n}}\rangle\sin(\langle\hat{\mathbf{n}}\rangle\,\phi)\right)^2$ [89,92], with $1/2N = \langle\hat{\mathbf{n}}\rangle = 2$, since $\langle\hat{\mathbf{n}}\rangle = 1.8$ NOON states are nonphysical, $\mathcal{V} = 1.0$ and $\eta = 1.0$.

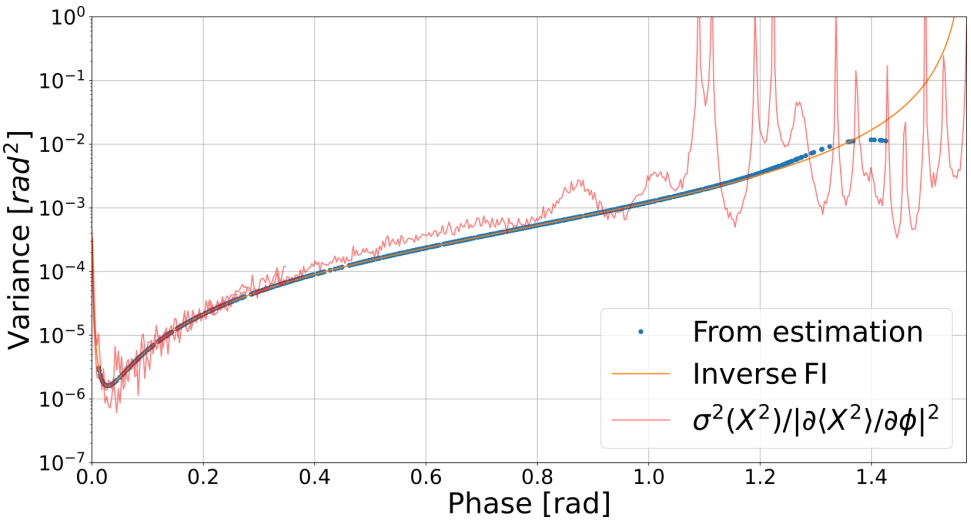

Figure 7.8: Comparison between the estimation variance obtained using the Bayesian estimation routine (blue points), the error propagation formular (red trace) and the theoretical classical Fisher Information (orange trace).

We note that the phase variance can be also deduced using the formula for error-propagation

$$V(\phi) = \frac{V(X^2)}{|dX^2/d\phi|^2}, \tag{7.19}$$

where $V(X^2)$ is the variance of the estimator X^2 and $dX^2/d\phi$ is the derivative of the estimator. These values can be found directly from the measurements of X^2 presented in fig. 2c, and

the result is presented in figure (7.8). It clearly has the same behavior as the one found using Bayesian estimation (Fig. 3a) but the result is more noisy.

We extract the optimal phase angle and the corresponding variance and repeat this process for different pump powers of the OPO (10 measurements per pump power to get some statistics). This gives us the plots shown in figure (7.6)c, where the corresponding photon expectation value has been calculated from the squeezed and anti-squeezed variances (equation (7.10)).

Finally, we can calculate the one-shot sensitivity by multiplying the variance with M = 1000 and taking the square root. The sensitivity as a function of photon number expectation value is shown in figure (7.6)d. The imperfect NOON state has $\eta = 0.89$ to compare with our system. We can also calulate the Fisher Information per photon number, which is shown in figure (7.9), from which we can extract a maximum $15.8(6)\,\mathrm{rad}^{-2}$.

For the phase sensing experiment shown in figure (7.7), we reduce the available squeezed variance to −6 dB (and 14 dB anti-squeezing for the chosen pump power of 3 mW and sideband frequency of 5 MHz). The signal to be measured is a 3 kHz modulation added to the phase-modulator used in the LO path to lock the MCC.

The homodyne angle is locked to the optimal angle of 4°, which is given by the before-mentioned squeezed and anti-squeezed variances. The homodyne signal is measured for 1 second at $50\,\mathrm{MSa\,s}^{-1}$ sampling rate and again down-mixed at 5 MHz. We use $M = 100$ samples per phase. The resulting estimated phase time trace is shown in figure (7.7)a together with the corresponding power-spectral density plot.

We apply a bandpass filter with a bandwidth of 2 kHz around the signal frequency at 3 kHz. The resulting time trace is shown in figure (7.7)c.

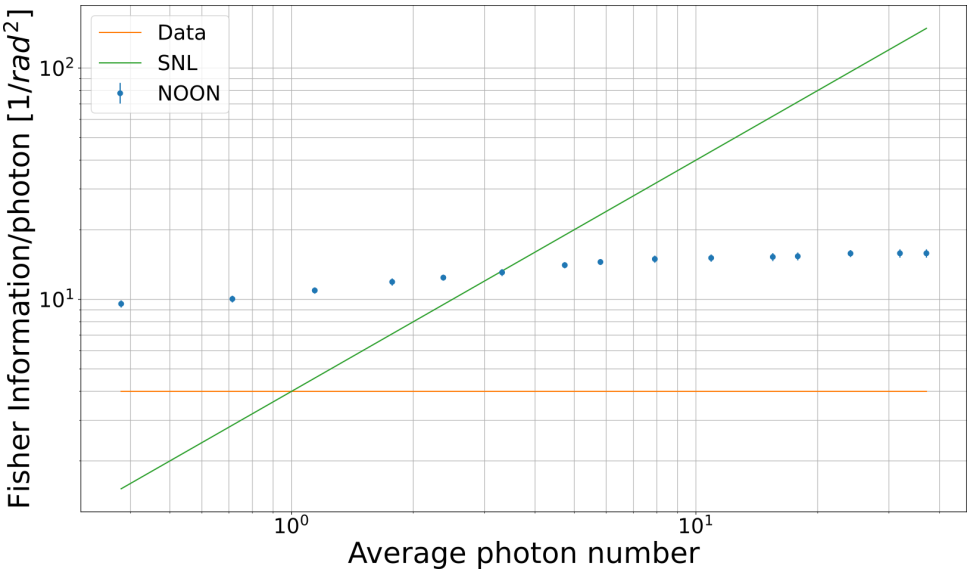

Figure 7.9: Plot of the Fisher Information per photon for our measurements (blue dots), the shot noise limit (orange line) for with the Fisher Information per photon is constant $2\,\mathrm{rad}^{-2}$ and for ideal N00N states (green line).

First Law:
A robot may not injure a human being or, through inaction, allow a human being to come to harm.
Second Law:
A robot must obey the orders given it by human beings except where such orders would conflict with the First Law.
Third Law:
A robot must protect its own existence as long as such protection does not conflict with the First or Second Law.

I, Robot
by Isaac Asimov, 1942

8

VQA assisted optimization of a practical phase estimation probe

In chapter (7) I demonstrated how phase sensing using squeezed vacuum probes breaks the standard quantum limit, performs better than celebrated entangled states such as N00N states and is in theory the optimal Gaussian state to use for phase sensing (in terms of performance per photon). These results were demonstrated in our highly advanced research laboratory, which even with its imperfections, is the near optimal environment for conducting experiments with quantum systems. In order to use quantum technology in practice, it needs to be taken out of the laboratory and applied to the real world. The real world is far from perfect with loss and excess noise of potentially unknown origin, and in these types of environments, squeezed vacuum might not be the optimal probe. Calculating the optimal probe in such a system analytically is not straight forward . In order to find the optimal probe state in a realistic noisy system, usage of a quantum variational algorithm (VQA) has been proposed by our colaborators Johannes Jakob Meyer of Dahlem Center for Complex Quantum Systems, Freie Universität Berlin and Johannes Borregaard of Qutech and Kavli Institute of Nanoscience, Delft University of Technology [119]. This chapter is dedicated to an experimental demonstration of a phase sensing experiment with an VQA optimized probe, which I built and conducted in the final months before my thesis deadline.

I will begin the chapter by introducing the principle behind VQA algorithms. The introductory section is mainly based on a very nice review by Cerezo et al. [120]. I will then move on to describing the setup used in the experiment, before detailing the algorithm used in the experiment. I will present the initial results obtained only weeks before finishing this thesis, and end this chapter with an outlook on the experiment.

The algorithm is adapted to our systems from an algorithm written by Kannan Vijayadharan currently a research assistant at Eindhoven University of Technology. The adaptation was done by Tummas Napoleon Arge, a PhD student in our group, who worked very hard on getting the algorithm up and running in time for us to do the experiment before my thesis deadline. I owe Tummas a great deal of gratitude for his hard work and can do attitude.

8.1 Introduction

The variational quantum algorithm was first proposed in the form of a quantum variational eigensolver (VQE) for ground state and excited state estimation in quantum chemistry [121]. Since then VQAs have been proposed for numerous other applications such as dynamical quantum simulation, quantum circuit optimization, error correction, quantum metrology (which is the application of interest to us) and many more. A VQA is a hybrid classical-quantum algorithm, which takes advantage of classical machine learning and/or optimization algorithms and at the same time take into account the limited performance of currently available Noisy-Intermediate-Scale-Quantum (NISQ) hardware. In fact, quantum variational algorithms has been proposed as the best candidate for demonstrating quantum supremacy in the NISQ era.

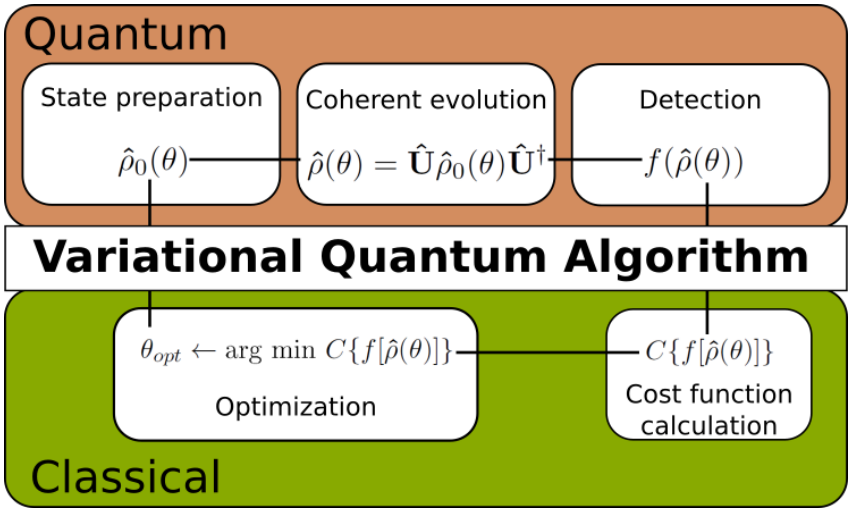

Figure 8.1: Top-level diagram of a typical variational quantum algorithm in the case of a single quantum state.

Figure (8.1) shows a top-level diagram of a typical variational quantum algorithm. A number of quantum states $\sum_k \hat{\rho}_0^k(\vec{\theta})$, parametrized by experimentally controllable parameters $\vec{\theta}$, are prepared. They undergo some coherent evolution $\hat{\rho}^k(\vec{\theta}) = \hat{\mathbf{U}}_k\hat{\rho}_0^k(\vec{\theta})\hat{\mathbf{U}}_k^\dagger$, the final state is measured and from the measurement result $f[\left\{\hat{\rho}^k(\vec{\theta})\right\}]$ a cost function C is extracted. A classical optimization algorithm then iteratively optimizes the experimental parameters by minimizing the cost function. Depending on the application, the optimization algorithm can be supervised or unsupervised.

In this experiment, we will prepare a parametrized input state (also called an anzats), have it undergo a coherent evolution of a phase shift, and detect it in a homodyne detector. From the expectation value and variance of the measurement, we construct a cost function and have a classical minimization algorithm do gradient descent in order to iteratively find optimal parameters. The anzats we use is a general displaced, squeezed probe state $|\alpha, r\rangle = \hat{\mathbf{S}}(r, \phi_r)\hat{\mathbf{D}}(\alpha, \phi_\alpha)|0\rangle$ (the squeezing parameter and coherent amplitude each have been split into amplitude and phase for clarity). The measurement of the state is done in a homodyne detector with full control of the measurement basis ϕ_{HD} The state is therefore parametrized by the four parameters $\alpha, r, \phi_\alpha, \phi_r$ and ϕ_{HD}, but since it is only the relative angles that are of importance, we ignore the squeezed parameter angle ϕ_r.

In the experiment, we have the opportunity to add a phase shift to be measured, however, we will per default work in the small phase regime optimizing the system for small phase shifts

around the set points given by $\delta \ll \phi_{HD}, \phi_\alpha$.

The cost function to be minimized must fulfil certain requirements in order to be useful for the algorithm. Firstly, it must be "faithful", meaning a minimization of the cost function corresponds to finding a solution to the problem at hand. Secondly, it must be efficiently estimable by performing measurements on the quantum system (and with optional classical post processing). Thirdly, the cost function should be "trainable", meaning it can efficiently minimized by optimizing the parameters. Finally, an optional requirement is that it should be meaningful, meaning that a lower cost function corresponds to better performance of the system.

In quantum metrological applications, a cost function satisfying all these requirements is the inverse of the quantum Fisher Information $1/H(\vec{\theta})$ [122], but this is not actually the best candidate, since practical applications are not able to saturate the quantum Cramer Rao bound and can therefore not guarantee that the information actually extracted is being optimized by the algorithm. A better candidate is the inverse of the classical Fisher Information $1/F(\phi, \vec{\theta})$ [119], since the classical Cramer Rao bound can always be saturated, and therefore the classical Fisher Information does represent the amount of information that can be extracted. The classical Fisher Information by itself is, however, a bit misleading, since it can be made arbitrarily large by freely adding displaced photons to the state. It is of more interest to look at the optimal probe state in the case of limited resources, and we will therefore modify the cost function to be the inverse of the classical Fisher Information per photon $C = \left[F(\phi, \vec{\theta}) / \langle n \rangle (\vec{\theta})\right]^{-1}$.

8.2 Setup

The quantum part of the VQA is sketched in the circuit diagram in the top of figure (8.2). A vacuum state is squeezed and displaced, and a phase shift is encoded onto the quantum state. The state propagates through a noisy quantum channel before being detected in a homodyne detector. The experimental setup equivalent of this circuit is also sketched in figure (8.2) and is identical to the setup of chapter (7) up to the OPO. From there the experiment has been changed to allow for a displacement to be added to the squeezed mode.

This displacement is added by from the 1550 nm mode by tapping a bit of light before the mode is split into CLF and LO modes. This tapped light is then coupled into a SM fiber and transported to an GRIN collimator that coupled the light into free space again. In the fiber the light propagates through a manual paddle polarization controller, a polarizer, a wave-guide phase modulator, a waveguide intensity modulator working at quadrature point and a fiber phase shifter. These modulators are needed to add the displacement to the correct sideband frequency, and the phase shifter is needed to lock the phase between the squeezed mode and the displacement mode (and control ϕ_α). After being coupled into free space the displacement is mixed with the squeezed mode on a 99:1 beamsplitter, where the 1 % port is used to detect and lock the phase, and the 99 % port is sent to be mixed with the local oscillator on a PBS. One port of the PBS is used to lock the phase between squeezed mode and local oscillator (and control ϕ_{HD}), and the other port is sent to the homodyne detector.

Before the homodyne detector the beams pass through a quarter waveplate and a half waveplate, which combined with the PBS that splits the light between the homodyne diodes allows an arbitrary phase shift to be encoded between the squeezed light and local oscillator (the same method used in [123]. The two phase locks use the CLF field as a reference to lock the phase as described in sections (4.2) and (4.3).

The noisy quantum channel is added by the same function generators that adds the displacement. This noise is generated by home made white noise generators, and should in principle be added after the phase encoding, but since this noise is Gaussian, it commutes with the other

operations and can be added together with the displacement.

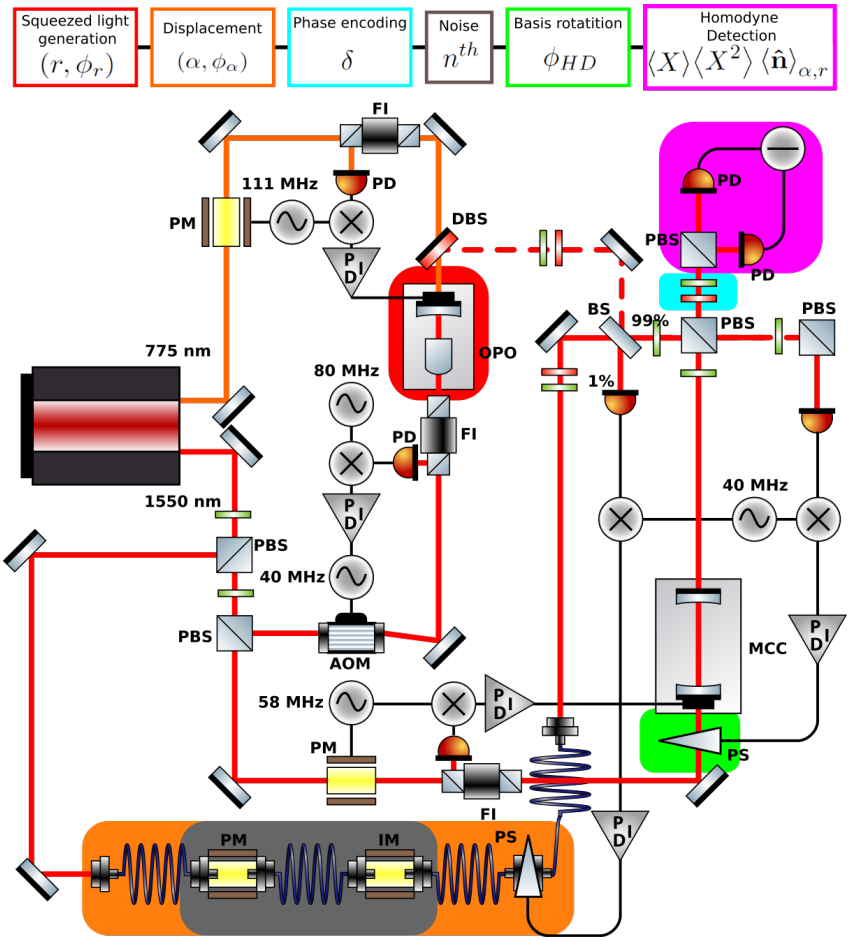

Figure 8.2: Sketch of the setup used in the variational quantum algorithm experiment. The top of the figure shows the circuit of the probe preparation, phase encoding and detection stages color codes with the corresponding components matched in the setup sketch.

8.3 The algorithm and the parameter shift rule

As mentioned in section (8.1), the cost function of the algorithm is the inverse of the photon normalized classical Fisher Information

$$C = \frac{1}{F(\phi,\theta)/\left\langle n(\vec{\theta})\right\rangle} = \frac{\left\langle n(\vec{\theta})\right\rangle}{\int \mathrm{d}x P\left(x|\phi,\vec{\theta}\right)\left(\frac{\partial P\left(x|\phi,\vec{\theta}\right)}{\partial\phi}\right)^2}, \tag{8.1}$$

where the formal definition of the classical fisher information for a single mode is found in [87]. Since our system is Gaussian, equation (8.1) can be evaluated and we find

$$C = \frac{\left\langle n(\vec{\theta})\right\rangle}{\left(\frac{\partial\langle X\rangle(\phi,\vec{\theta})}{\partial\phi}\right)^2 \frac{1}{\sigma_x^2(\phi,\vec{\theta})} + \frac{1}{2}\left(\frac{1}{\left(\sigma_x^2(\phi,\vec{\theta})\right)^2}\frac{\partial\sigma_x^2(\phi,\vec{\theta})}{\partial\phi}\right)^2}, \tag{8.2}$$

where $\langle X \rangle (\phi, \vec{\theta})$ is the expectation value of the homodyne measurement, and $\sigma_x^2(\phi, \vec{\theta})$ is the variance. The algorithm is a fairly rudimentary gradient descent algorithm, which calculates the gradients of the cost function with respect to the parameters and updates the parameters according to

$$\vec{\theta}_{i+1} = \vec{\theta}_i - \vec{\eta} \boldsymbol{\nabla} C(\phi, \vec{\theta}_i), \tag{8.3}$$

where $\vec{\eta}$ is a vector of weights deciding how sensitive each parameter should be to the gradient of the cost function.

As can be seen from equations (8.2) and (8.3) in order to calculate the cost function and the gradients, we need to calculate the partial derivatives of the expectation value and variance with respect to the phase shift and the cost function with respect to the parameters. The gradient can be approximated experimentally by using the finite differences method

$$\frac{\partial f(x_0)}{\partial x} \approx \frac{f(x_0 + s) - f(x_0 - s)}{2s}, \tag{8.4}$$

where s is an infinitesimal change. This is, however, not a very good approximation and is vulnerable to measurement uncertainty and system noise. A better method is the so-called parameter shift rule developed by Xanadu for NISQ quantum systems [124]. According to the parameter shift rule, the analytical gradient of the expectation value of a quantum variable can be calculated via

$$\frac{\partial \langle A \rangle (x_0)}{\partial x} = s\Big[\langle A \rangle (x_0 + \frac{\pi}{4s}) - \langle A \rangle (x_0 - \frac{\pi}{4s})\Big], \tag{8.5}$$

where s is this time a parameter dependent on the parameter to be shifted. The conditions for being able to use the parameter shift rule in continuous variable systems is that the operation encoding the parameter can be decomposed into basic Gaussian operations (squeezing, displacement, rotation and beamsplitting) [119]. Since all our parameters obey this condition, we can set up parameter shift rules for each of the basic Gaussian operations

$$\frac{\partial \langle A \rangle (\phi)}{\partial \phi} = \frac{1}{2}\Big(\langle A \rangle \left(\phi + \frac{\pi}{2}\right) - \langle A \rangle \left(\phi - \frac{\pi}{2}\right)\Big), \tag{8.6a}$$

$$\frac{\partial \langle A \rangle (\alpha)}{\partial \alpha} = \frac{1}{2s}(\langle A \rangle (\alpha + s) - \langle A \rangle (\alpha - s)), \tag{8.6b}$$

$$\frac{\partial \langle A \rangle (r)}{\partial r} = \frac{1}{2\sinh(s)}(\langle A \rangle (r + s) - \langle A \rangle (r - s)), \tag{8.6c}$$

where s is now a finite, but not necessarily infinitesimal step. Higher order derivatives can be evaluated by applying the parameter shift rule multiple times

$$\frac{\partial^2 \langle A \rangle (\phi)}{\partial \phi^2} = \frac{\partial}{\partial \phi}\left(\frac{\partial \langle A \rangle (\phi)}{\partial \phi}\right) = \frac{1}{2}(\langle A \rangle (\phi + \pi) - \langle A \rangle (\phi)), \tag{8.7a}$$

$$\frac{\partial^2 \langle A \rangle (\phi, \alpha)}{\partial \phi \partial \alpha} = \frac{\partial}{\partial \alpha}\left(\frac{\partial \langle A \rangle (\phi, \alpha)}{\partial \phi}\right) = \frac{1}{4s}\left[\langle A \rangle \left(\phi + \frac{\pi}{2}, \alpha + s\right) - \langle A \rangle \left(\phi - \frac{\pi}{2}, \alpha + s\right) - \langle A \rangle \left(\phi + \frac{\pi}{2}, \alpha - s\right) + \langle A \rangle \left(\phi - \frac{\pi}{2}, \alpha - s\right)\right]. \tag{8.7b}$$

In short, this means that by tactically varying the parameters around the set values and doing measurements, we can calculate the cost function and gradients of the cost function, and on the basis of this, we can apply the gradient descent algorithm to our experiment. Equation (8.2) in

principle requires the measured phase to be varied in order to calculate the cost function, but since phases are relative, we use the homodyne basis angle ϕ_{HD} instead to calculate the cost function

From section (8.2), it was described how we can apply squeezing, arbitrary displacement in phase space and rotate the basis of the homodyne detection. Some of these parameters are more practical to vary than others. The squeezing parameter is varied by changing the pump power in the OPO, but since all the phase locks also depend a bit on the pump power, changing this would not only change r, but also change a little bit the angles ϕ_α and ϕ_{HD}. We therefore decided on keeping the squeezing parameter constant during each optimization run, but change it manually between runs to still be able to investigate the behavior for different squeezing parameters.

The thermal noise n_{th} is also changed dynamically between optimization experiments, as the noise generator does not have a function to interface with the computer.

The displacement is done with both an intensity modulator and a phase modulator, but this is redundant as varying the amplitude of both modulators not only varies the degree of displacement α, but also rotates around phase space ϕ_α - a parameter already controlled by changing the set point of the phase lock between the displaced mode and the squeezed mode. We therefore ended up only using the intensity modulator.

In total we have three parameters we can change dynamically α, ϕ_α and ϕ_{HD} in the algorithm, and two parameters r and n_{th}, which are changed manually between runs.

When the algorithm is started it sends initial values of the parameters to the equipment. It then first applies the parameter shift rules and time trace measurements around the initial parameters to estimate the initial value of the cost function. Each time trace measurement is $100\,\mu$s with a 50 MSa/per/second acquisition rate. The time trace is downmixed to a 5 MHz sideband frequency (this is the default choice of frequency), and the expectation value and variance is calculated. From the parameter shifts of the expectation value and variance the cost function is calculated, and the algorithm then proceeds to calculate the gradient of the cost function by performing further parameter shifts, and once the full gradient is estimated, the parameters are updated according to equation (8.3), and the process is repeated until it (in principle) reaches the convergence condition that two consecutive cost-function values are approximately the same.

8.4 Calibration of the system

The cost function equation (8.2) depends on the photon expectation value, which in turn depends on the squeezing parameter r and displacement amplitude α. Since we manually change r and dynamically change α, we need to know for all values the photon expectation value $\langle n\rangle(r,\alpha) = \langle n\rangle_{sqz}(r) + \langle n\rangle_{disp}(\alpha)$. The function generators that drive the modulators use a scale of [0:1] when changing the amplitude (where 1 corresponds to -9 dBm of RMS power), and we need to map this scale to α and $\langle n\rangle_{disp}(\alpha)$ at a given sideband frequency. Similarly, we need to map the pump power into the OPO to r and $\langle n\rangle_{sqz}(r)$ at a given sideband frequency. Finally, we need to be able to map the thermal noise added to the average number of thermal photons added in the noise. We will begin with describing the calibration of the latter, then move on to describing the calibration of squeezing and displacement.

8.4.1 Thermal noise calibration

This subsection will very shortly outline how we calibrate the thermal noise added to the system. When we add thermal noise, we first do a shot noise measurement on the spectrum analyzer around the frequency of interest (5 MHz in this case). We then add the thermal noise and

compare the noise power to that of the shot noise. Since, per the definition set in chapter (2), the shot noise variance is $V_{SN} = 1$, and the thermal noise variance is $V_{th} = 2\langle n \rangle_{th} + 1$ per equation (2.18), we can find the average photon number via

$$\langle n \rangle_{th} = \frac{1}{2}\left(\frac{V_{th}}{V_{SN}} - 1\right) \tag{8.8}$$

8.4.2 Squeezing calibration

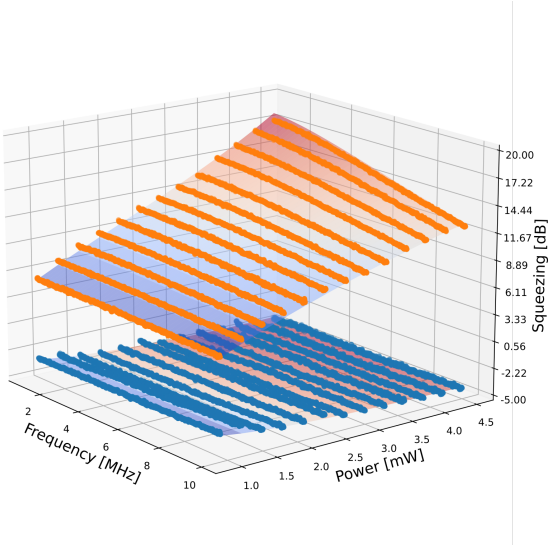

(a) 3D plot of the squeezed variance (blue dots) and anti-squeezed variance (orange dots) relative to shot noise as a function of frequency and power. The superimposed area is the fitted model from equation (5.9), and the color scale of the squeezed variance area has its color scale inverted to go to varmer colors at higher degrees of squeezing.

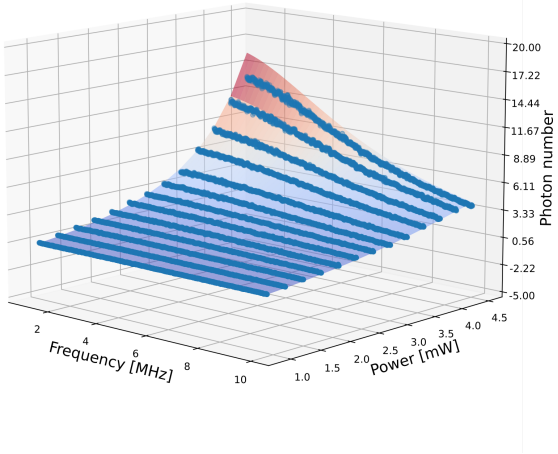

(b) Squeezed photon number expectation value as a function of frequency and power. The blue dots are calculated from measured values. The superimposed area is calculated from the fit

Figure 8.3

The experiment had to be be constructed from the setup described in chapter (7) in a very short period of time. Due to this time pressure, not a lot of time could be dedicated to optimizing the squeeed light performance. In this experiment we therefore only have about 65 % efficiency, which corresponds to around 4.5 dB of squeezed light available. This was nevertheless enough for us to perform the experiment, and in order to calibrate the squeezed light, the squeezed and anti-squeezed variances were measured on a spectrum analyzer as functions of pump power and sideband frequency. These measurements we then fitted to equation (5.9). The fit parameters are summarized in table (8.1). The measurements and corresponding fitted model are shown in figure (8.3a) as a function of sideband frequency and pump power.

From the squeezed and anti-squeezed variances we can estimate effective squeezing parameter r_{th} and the average number of thermal photons $n_{th,sqz}$ in the squeezed light via equation (2.23)

$$r_{th} = \frac{1}{2}\log\left(\frac{V_+}{\sqrt{V_+ V_-}}\right), \tag{8.9a}$$

$$n_{th,sqz} = \frac{\sqrt{V_+ V_-} - 1}{2}, \tag{8.9b}$$

Parameter	Value
Efficiency η	65.6(1) %
Phase nose ϕ_{RMS}	17.5(5) mrad
Pump threshold P^{thr}	6.7(1) mW
OPO bandwidth γ	65.9(1) MHz

Table 8.1: Table showing the fitted parameters of equation (5.9) to spectrum analyzer measurements. The threshold is higher than the expected 4.7 mW due to a slight temperature mismatch in the double resonance.

and from these the squeezed photon expectation value as [87]

$$\langle n \rangle_{sqz} = n_{th} \cosh(2r_{th}) + \sinh(r_{th})^2. \tag{8.10}$$

The expectation value of the squeezed photon number is plotted as a function of frequency and power in figure (8.3b). We now have a continuous model for the squeezed photon number expectation value as a function of our system parameters.

8.4.3 Displacement calibration

The idea behind the displacement calibration is similar to the squeezing calibration. We record a time trace while scanning the phase of the displacement beam. This gives us fringes as the displaced mode is rotated around the phase space. We record 20 ms with a sampling rate of $50\,\mathrm{MSa\,s^{-1}}$, and the time trace is downmixed to the frequency of the displacement and normalized to a shot noise calibration. The top of a fringe is identified and fitted with a parabola shape $ax^2 + bx + c$ and the height of the top point is extracted as $\langle X \rangle (\phi_\alpha = 0) = max(ax^2 + bx + c)$. This is done to get around the measurement noise and an example of this is shown in figure (8.4).

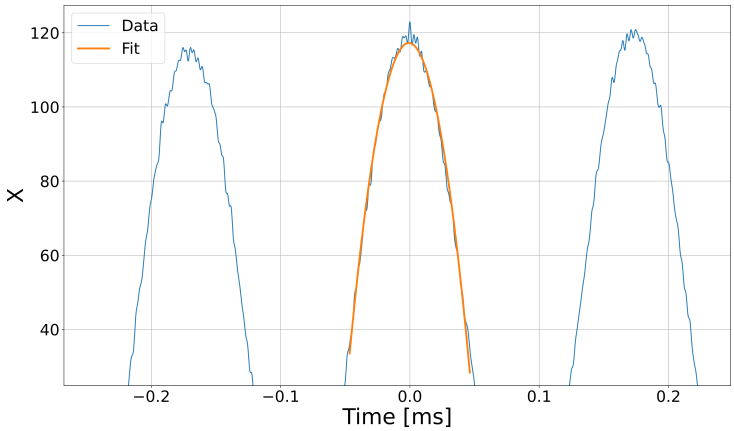

Figure 8.4: Measurement of the displacement while scanning the phase. The orange trace is a fitted parabola to extract the top of the fringe without noise.

Since we are still using $V_{SN} = 1$, the coherent amplitude can be calculated from equation (2.3a) as $\alpha = 1/2 \langle X \rangle (\phi_\alpha = 0)$ and $\langle n \rangle_{disp} = |\alpha|^2$. We extract α and $\langle n \rangle_{disp}$ for varying values of the intensity modulator amplitude and frequency.

The extracted values of α and $\langle n \rangle_{disp}$ are shown in figures (8.5a) and (8.5b) as functions of frequency and amplitude. In order to get a continuous model of α, we fitted the data with the empirical function

$$\alpha = (B\nu + C)A_{IM}, \tag{8.11}$$

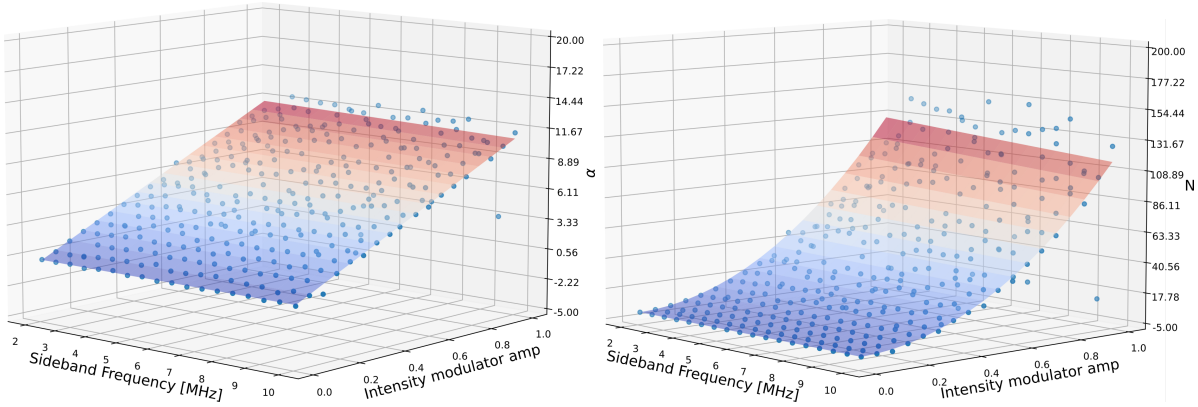

(a) Calibration of α as a function of frequency and amplitude (blue dots). The superimposed area is the fitted model described in the text.

(b) Calibration of $\langle n \rangle_{disp}$ as a function of frequency and amplitude (blue dots). The superimposed area is the fitted model described in the text.

Figure 8.5

where B and C are fitting parameters, ν is the sideband frequency and A_{IM} is the modulator amplitude. This fit model is superimposed the data in figures (8.5a) and (8.5b). We now also have a continuous model for α and $\langle n \rangle_{disp}$, which allows us to translate between the physical parameters and system parameters.

8.5 Preliminary results

The data represented in this section are quite rough and represent the first measurements done just weeks from the thesis deadline, while there are obvious problems with the data, I still believe they show some interesting systematic behavior that is worth discussing. I will also discuss the current known problems with the experiments and how these might affect the measurements. I will present two experimental series of the VQA algorithm. The first has no thermal noise, but varies the squeezing parameter by changing the power between 1 and 4.5 mW. The second measurement series has constant squeezing (3 mW of pump power corresponding to around 4 dB squeezing), but has varying degrees of thermal noise. These measurements are done at a 5 MHz frequency sideband, and the alogrithm is allowed to run for 40 optimization steps before it is terminated (due to systematic problems that will become apparent, the algorithm will never reach the convergence condition). For both measurement the gradient weight vector $\vec{\eta}$ was set to be 0.001 in all parameters.

8.5.1 Varying the squeezing parameter

For the variable squeezing series, we let the initial state with $\alpha = 0.5, \phi_\alpha = 1.5, \phi_{HD} = 2.09$. This corresponds to the squeezed variance being aligned with the X-axis of the homodyne measurement and with a small displacement slightly rotated approximately 33° away from the X-axis. As mentioned above, we then let the algorithm run for 40 iterations (in the figures called epochs). As mentioned above, the algorithm is never able to converge, and if we look at the calculated cost function values for different values of pump powers shown in figure (8.6).

From figure (8.6) we can clearly see that cost functions change randomly, with the only clear behavior being that the cost function might be acting more erratic with higher pump powers. This is quite a big problem, as this seems to suggest that the cost function parameter space is extremely noisy, and the algorithm will have problems finding minima (or even navigating) this

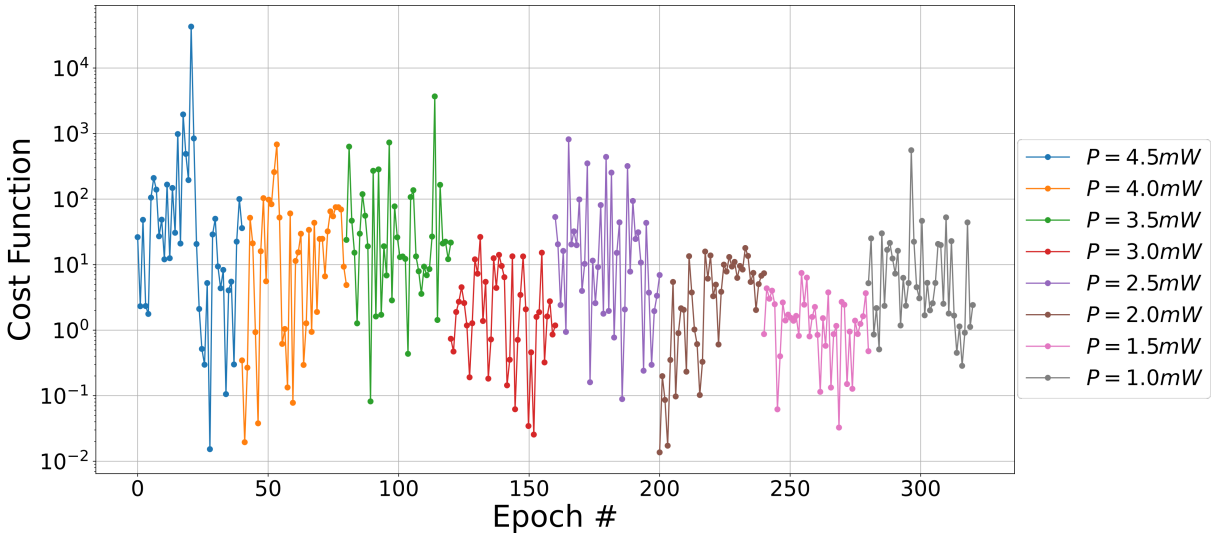

Figure 8.6: Plot of the cost function as a function of iteration epochs for varying pump powers. Each run for different pump powers has been displaced horizontally to increase clarity.

noise landscape. A possible reason for this can be seen in figure (8.7).

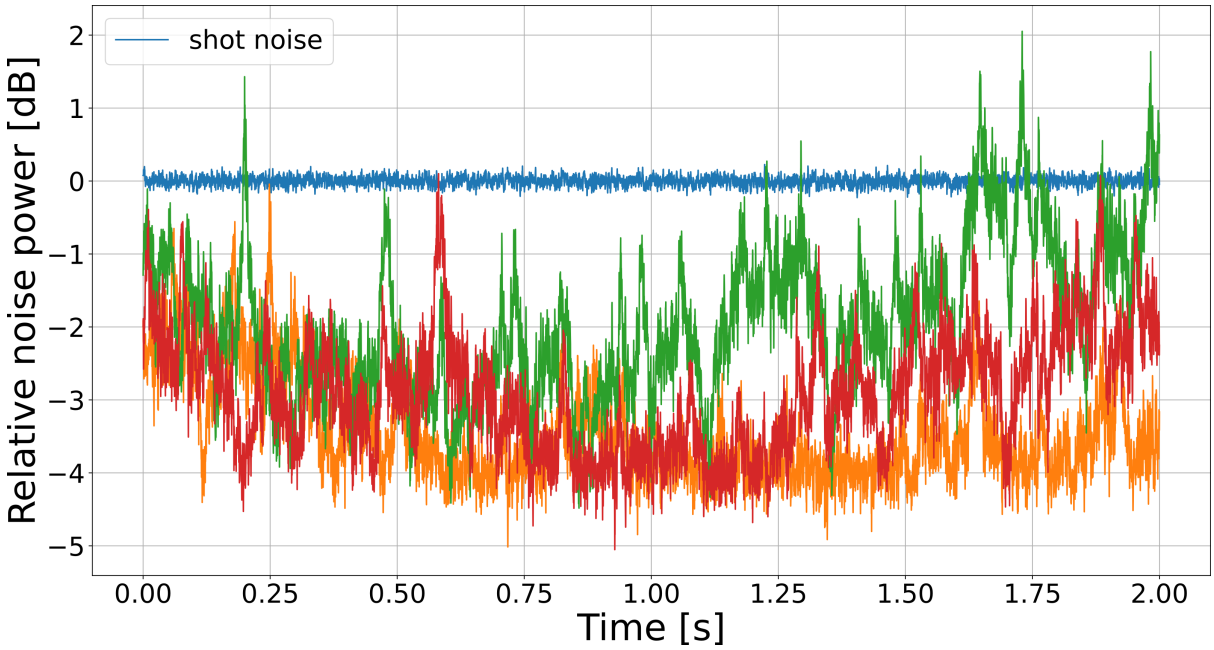

Figure 8.7: Plot of the shot noise variance as a function of time (blue trace), and homodyne variance as a function of time locked to the squeezed quadrature (orange, green and red).

Figure (8.7) shows time traces of the homodyne variance phase locked to the squeezed quadrature. We clearly see that even though the variance should be locked to squeezing, some disturbance either in the locking system or after the lock causes the variance to take some very drastic excursions from the lock point. During these excursions the lock never breaks, meaning in principle it should be keeping the phase stable, and no matter how I tried to vary the lock parameters, this could not be fixed. The instability of the phase can also explain, why it appears as is the cost function looks to be more unstable for higher pump powers, where the anti-squeezed variance is higher.

Based on the unstable behavior of the cost function, we might expect the parameters also to show the same erratic behavior. This is however not quite the case. Even though the cost function is very noisy, the system seems to be able to find some systematic gradients to follow. This can be seen in figure (8.8), where ϕ_α, ϕ_{HD} and the difference between the two are plotted.

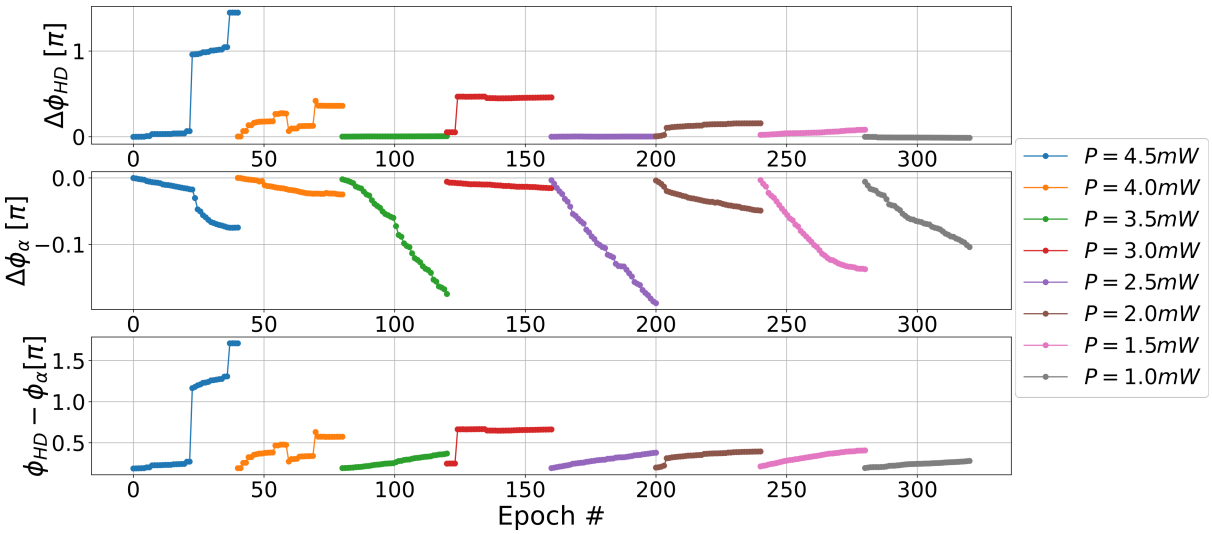

Figure 8.8: Plots of the change in ϕ_{HD} (topmost figure), ϕ_α (center figure) and the difference between the two $\phi_{HD} - \phi_\alpha$ (bottommost figure) for different pump powers. Each run for different pump powers has been displaced horizontally to increase clarity.

In figure (8.8) we see that there are two general behaviors of the angle parameters. The first (which I call type 1) is where ϕ_{HD} very quickly and abruptly moves away from the squeezed quadrature $\Delta\phi_{HD} = 0$ and towards the anti-squeezed quadrature (integers of $\pi/2$), putting the relative angle also at integers of $\pi/2$, meaning the displacement will be put into the P quadrature. For this "type 1" behavior the displacement angle ϕ_α only varies very little.

The other type of behavior (type 2) is where ϕ_{HD} stays down around the squeezed quadrature, and this time ϕ_α seems to move to put the relative angle be $\pi/2$ and the displacement into the P-quadrature.

These two types of behavior seems to have some dependence on the pump power, with the type 1 behavior happening more for higher pump powers and type 2 behavior happening more for lower pump powers. As I was writing up this result, I discovered a bug in the code, which could explain this dependence on the pump power. Equation (8.2), the inverse photon normalized classical Fisher Information, is the cost function we want the algorithm to minimize, but the bug, which sadly seems to have gone unnoticed through several iterations of the code, normalizes the following cost function

$$C_{bug} = \frac{1}{\left(\frac{\partial\langle X\rangle(\phi,\vec{\theta})}{\partial\phi}\right)^2 \frac{1}{\sigma_x^2(\phi,\vec{\theta})} + \frac{1}{2\langle n(\vec{\theta})\rangle}\left(\frac{1}{\left(\sigma_x^2(\phi,\vec{\theta})\right)^2}\frac{\partial\sigma_x^2(\phi,\vec{\theta})}{\partial\phi}\right)^2}, \tag{8.12}$$

where we see that only the variance part of the cost function is penalized by the photon number. This basically causes the variance contribution to the cost function be invisible to the algorithm for high pump powers (and therefore high photon numbers). The algorithm incorrectly sees only a coherent state, which it more or less correctly optimizes by putting the displacement into P quadrature. For lowers photon numbers the variance contribution becomes visible, and the algorithm seems to correctly identify the squeezed quadrature as the optimal, while slowly

moving the displacement up towards the P quadrature, which we would expect to be close to the optimal probe for sensing with a displaced squeezed probe.

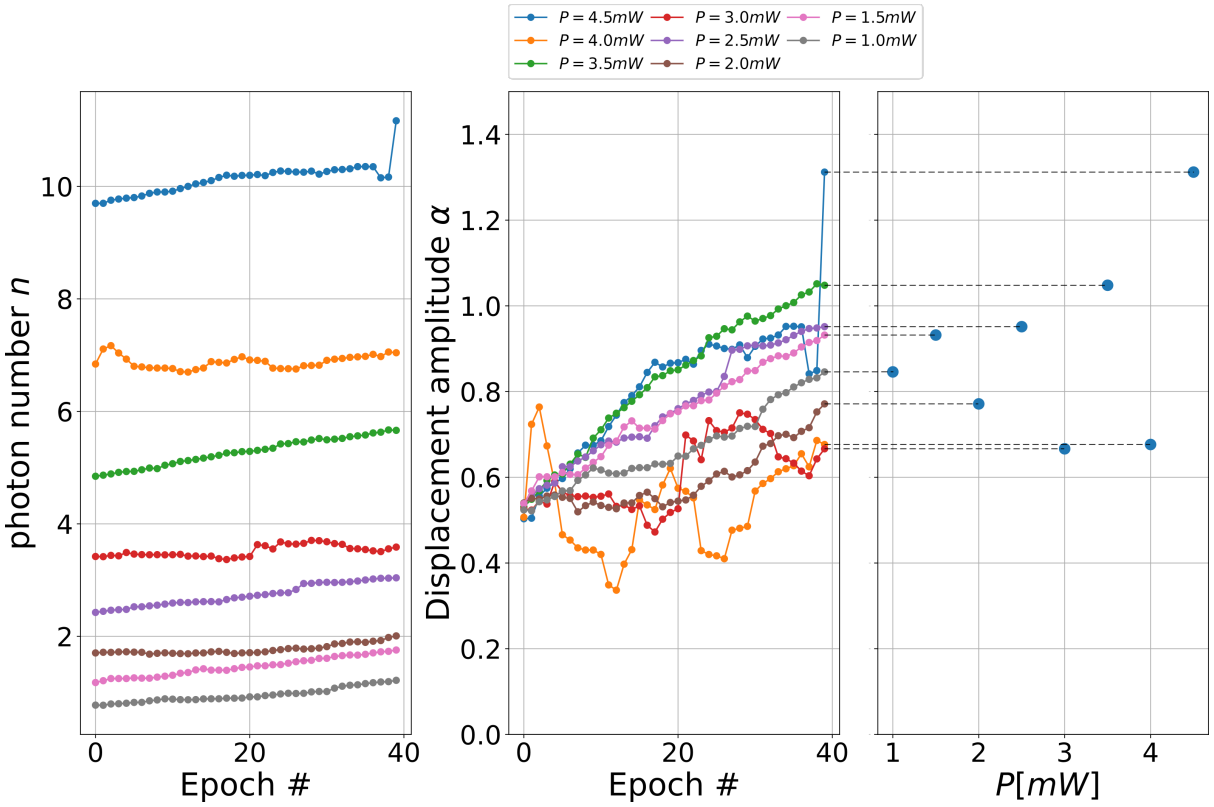

Figure 8.9: Plots of the total photon number $\langle n \rangle$ (rightmost figure), displacement amplitude α (center figure) for different pump powers. The rightmost plot shows the final coherent amplitude value as a function of pump power. The dotted lines are guides for the eye.

In terms of the displacement amplitude, in figure (8.9), we see that there is not the same tendency to systematic movement of the amplitude, and the photon number is mainly dominated by the squeezed photons. From chapter (7), we saw that ideally the displacement should be removed in the case of no noise, but given the bug in the algorithm, the fact that this does not happen is not surprising. The fact that te amplitude is not simply increased, however, is a bit surprising, and I do not at this point in time have a good answer as to why.

8.5.2 Varying the thermal noise

In the experiment with thermal noise, the starting parameters were $\phi_\alpha = 1.5$, $\phi_{HD} = 2.7$, meaning the starting quadrature is slightly off the squeezed quadrature with the displacement at a 68° angle relative to the measurement quadrature. The displacement amplitude was $\alpha = 3$ for the first 3 measurements, and then 5 and 7 for the last two runs for reasons that should become clear. The thermal noise photon expectation value was varied between 0 and 2.

The cost function figure (8.10) shows the same random behavior, this time however with no clear dependence on the thermal noise level. In terms of the phases in figure (8.11), not much seems to happen either for most of the runs. The homodyne phase seems to stay around the starting value or move closer to anti-squeezing, but it is not as clear as it was in figure (8.8). The displacement angle also does not change much and the relative angle is kept close to $\pi/2$ for most of the runs, making it look like the type 1 behavior mentioned above.

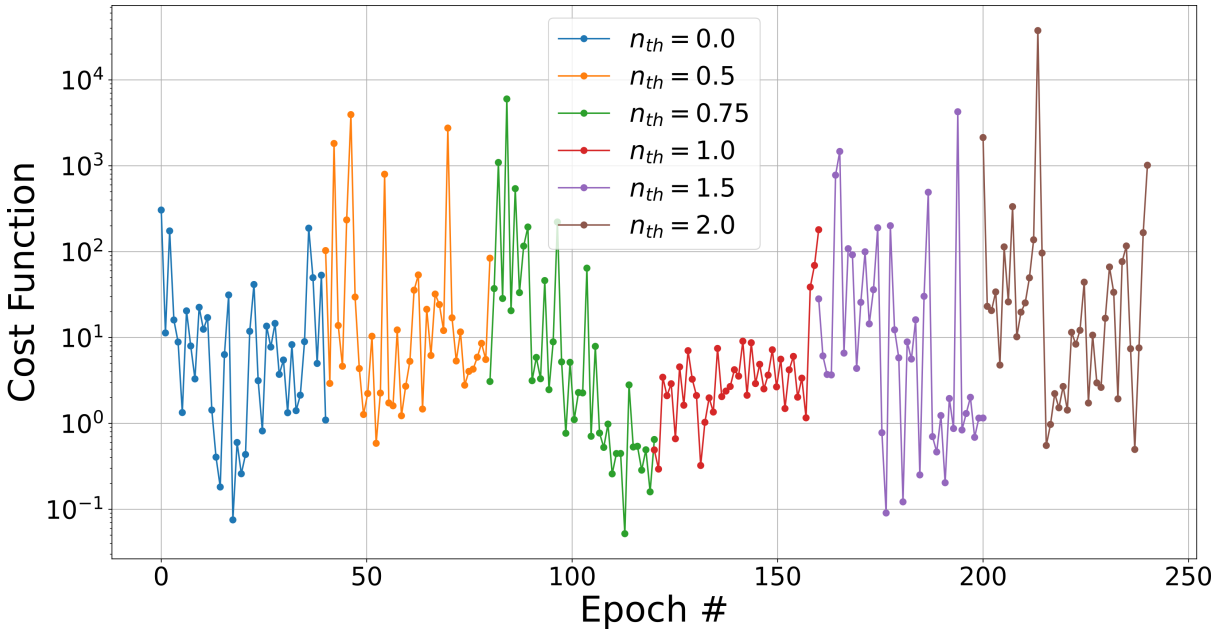

Figure 8.10: Plot of the cost function as a function of iteration epochs for varying thermal noise level. Each run for different pump powers has been displaced horizontally to increase clarity.

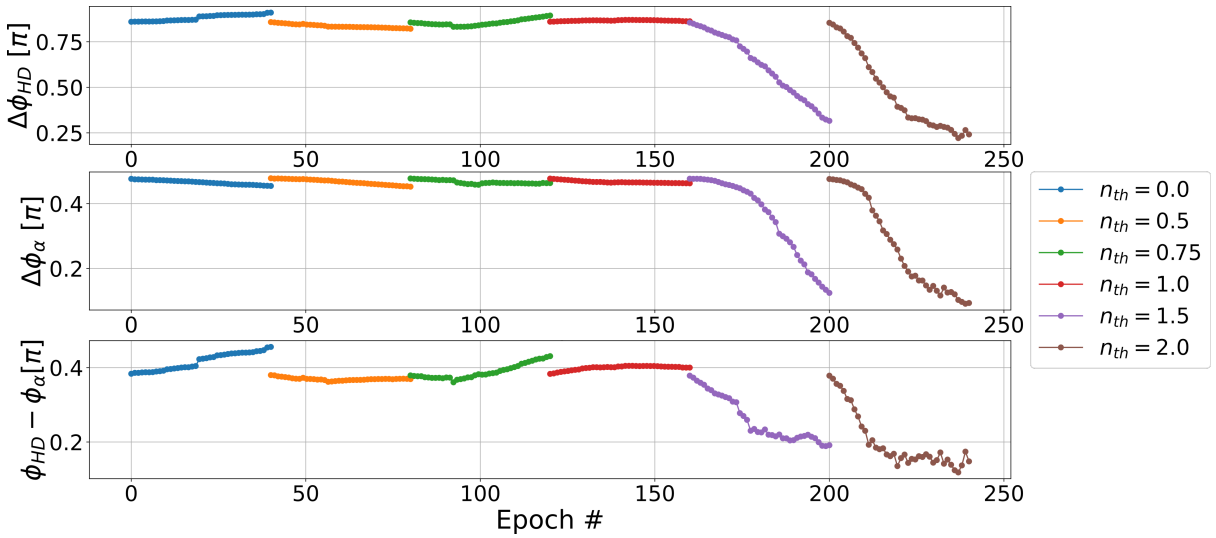

Figure 8.11: Plots of the change in ϕ_{HD} (topmost figure), ϕ_{α} (center figure) and the difference between the two $\phi_{HD} - \phi_{\alpha}$ (bottommost figure) for different thermal noise levels. Each run for different thermal noise levels has been displaced horizontally to increase clarity.

For the last two runs with the highest levels of thermal noise, both angles change a lot with ϕ_{HD} seemingly going towards zero which still corresponds to passing through the squeezed quadrature and returning to the anti-squeezed quadrature. ϕ_{disp} curiously follows such as to eliminate the relative phase between them, and I do not currently have a good reason for why this happens.

When looking at the displacement amplitude in figure (8.12), we see the first three runs with non-zero thermal noise (orange, green and red) start with the same amplitude, but pretty quickly move apart. This seemed to suggest that increasing thermal noise leads to the algorithm wanting to increase the displacement amplitude. Since it only runs for 40 iterations, I wanted

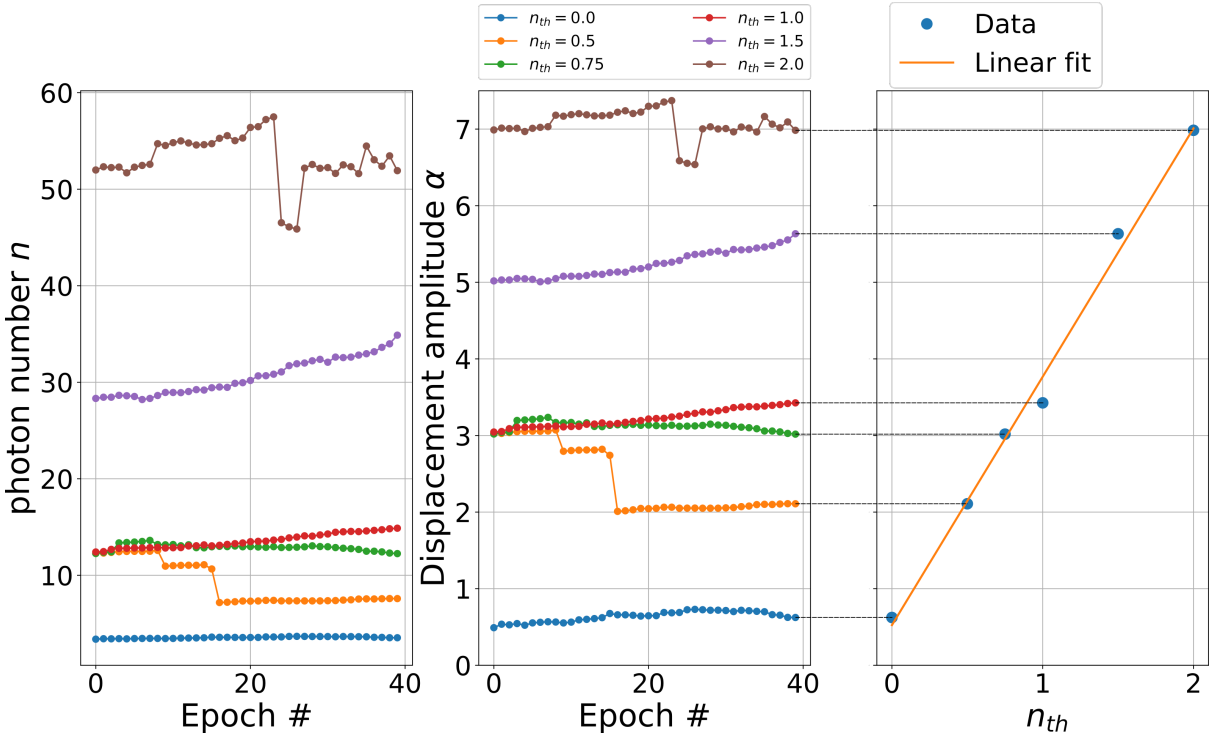

Figure 8.12: Plots of the total photon number $\langle n \rangle$ (rightmost figure), displacement amplitude α (center figure) for different pump powers. The rightmost plot shows the final coherent amplitude value as a function of pump power. The dotted lines are guides for the eye, and the orange line is a linear fit to the data.

to help the algorithm along, and this lead to changing the starting values of the final two runs. This trend seemed to continue, and in the end there seems to be a tendency for higher levels of thermal noise to lead to higher amplitudes of the displacement. This conclusion should of course be drawn with some level of caution, as we know the algorithm has a bug that causes the amplitude to not be penalized with increasing photon numbers, but the leftmost plot of figure (8.12) seems to show a very nice linear dependence on the thermal noise average photon numbers.

8.6 Conclusion and outlook

To finish this chapter off, I will conclude that we have built an experiment realizing a variational quantum algorithm in order to optimize a general displaced squeezed probe for sensing small phases. I have presented the absolute initial results of running this algorithm with different values of the squeezing parameter and thermal noise photon numbers. While the experiment has obvious problems in the form of phase instability and a very unfortunate bug in the algorithm, the resulting optimized parameters show some interesting systematic behavior in an increase of the displacement amplitude for increasing thermal noise levels and a general tendency for the displacement to be moved into the P-quadrature.

The outlook of this project would be to diagnose and remove the source of the phase noise and remove the bug in the algorithm. Besides these obvious points of improvement, a general optimization of the experiment to be able to measure higher degrees of squeezing would be beneficial. The algorithm itself also has a lot of parameters that can be investigated and optimized (measurement time, parameter shift step size, gradient weight etc.).

Besides changing the squeezing parameter and thermal noise levels, we can also change the size of the phase shift encoded into the probe state.

Finally, the squeezing parameter can be semi-included as an optimization parameter, by allowing the system to dynamically change the frequency at which the displacement is added and the measurement is done. We know from figure (3.3) that the squeezed and anti-squeezed variances change with frequency, and this can be modelled as a frequency dependent squeezing parameter for which the parameter shift rule can be applied.

Macroscopic quantum states are robust against loss and noise... right?

Jens A H Nielsen
On his first day as a PhD student
QPIT retreat 2018

9 Conclusion

In this thesis, I have investigated the generation of squeezed states of light, first theoretically in chapter (3), where it was explained how the generation and measurement of squeezed light is limited by optical loss and phase noise of the squeezed quadrature measurement. The generation of squeezed light was also investigated experimentally in chapter (5), where we built a squeezed light source with a small footprint producing around 9.3 dB limited in practice by phase noise.

If this project were to be continued, it would be of great interest to create a portable squeezed light source by reducing the footprint even further and packing the source into a box with integrated electronics. I would also be nice to increase the performance a bit further. To do this, the source of phase noise would have to be investigated and corrected. Finally, it could be interesting to couple the squeezed light into a fiber in order to make the source more flexible and practical (even though this would probably come with a penalty to the squeezed light variance).

In chapter (6) it was described, how a squeezed light source capable of measuring upwards of 18 dB would have to be designed with an extremely tight loss budget of 1.3 % and phase noise budget of 1 mrad RMS. It was also reported, how an initial attempt to built such a source had to be postponed due to the initial design seemingly having too severe requirements on the tolerances of the crystal manufacturing process.

The crystals have since then been redesigned, and are now ready for another PhD student to try to finish the construction of the source.

In chapter (8), a variational quantum algorithm was implemented to optimize a general squeezed phase estimation probe under noisy conditions, where the results from chapter (7) would no longer be valid. The results presented in this chapter were only very early results and far from ideal. The experiment had problems with phase noise, and there was an unfortunate bug in the algorithm, but these initial results seemed to suggest that in the case of thermal noise in the system, a displacement of the squeezed state could improve the performance of the phase estimation.

A conclusion of this project would certainly be desirable, but in order to do this the algorithm has to be corrected, the phase noise problem has to be fixed and the general parameters of both the experimental system and the algorithm should be optimized.

In chapter (7) the results of a phase estimation and sensing experiment were reported. The experiment, which involved using squeezed vacuum as a probe, showed an performance beyond

the shot noise limit. The experiment also showed performance beyond the limit set by ideal NOON states for low photon expectation values, and beyond comparable practical NOON states for all average photon numbers. Furthermore, in terms of Fisher Information per photon this experiment set, to the best of our knowledge, a new record of $15.8(6)\,\mathrm{rad}^{-2}$ beating all previously reported estimation protocols. This estimation protocol was also used successfully in a sensing experiment, where a 3 kHz sine wave phase modulation added to the local oscillator was sensed.

As a continuation of this project, real spatial phase imaging of physical samples could be of interest, but modifications would have to be made to the experimental setup in order to be able to do these types of measurements.

Appendices

A

Calculation of transmitted field variances

We start this appendix with the field fluctuations transmitted through the output coupler equation (3.18a)

$$\delta\widetilde{\mathbf{X}}^{out}_{s,out} = \sqrt{2\gamma_s^{out}}\frac{\left[\gamma_p + i\omega\right]\widetilde{\mathbf{N}}^{x}_{s} + g\alpha\widetilde{\mathbf{N}}^{x}_{p}}{|g|^2|\alpha|^2 + (\gamma_s + i\omega - g\beta)(\gamma_p + i\omega)} - \delta\widetilde{\mathbf{X}}^{out}_{s,in}, \tag{A.1a}$$

$$\delta\widetilde{\mathbf{P}}^{out}_{s,out} = \sqrt{2\gamma_s^{out}}\frac{\left[\gamma_p + i\omega\right]\widetilde{\mathbf{N}}^{p}_{s} + g\alpha\widetilde{\mathbf{N}}^{p}_{p}}{|g|^2|\alpha|^2 + (\gamma_s + i\omega + g\beta)(\gamma_p + i\omega)} - \delta\widetilde{\mathbf{P}}^{out}_{s,in}. \tag{A.1b}$$

We now calculate the variance of the operators, and as we assume the mean value to be zero, we get $\sigma^2\left(\delta\widetilde{\mathbf{A}}\right) = \left\langle \delta\widetilde{\mathbf{A}}^{\dagger}\delta\widetilde{\mathbf{A}} \right\rangle$. We assume all the noise terms to be uncorrelated noise. We start with the easiest terms $\left\langle \delta\widetilde{\mathbf{X}}^{out\dagger}_{s,in}\delta\widetilde{\mathbf{X}}^{out}_{s,in} \right\rangle$ and $\left\langle \delta\widetilde{\mathbf{P}}^{out\dagger}_{s,in}\delta\widetilde{\mathbf{P}}^{out}_{s,in} \right\rangle$.

$$\left\langle \delta\widetilde{\mathbf{X}}^{out\dagger}_{s,in}\delta\widetilde{\mathbf{X}}^{out}_{s,in} \right\rangle = 1, \tag{A.2a}$$

$$\left\langle \delta\widetilde{\mathbf{P}}^{out\dagger}_{s,in}\delta\widetilde{\mathbf{P}}^{out}_{s,in} \right\rangle = 1, \tag{A.2b}$$

since we have defined the shot noise normalized to unity and assume there is only vacuum coming from the output-coupler for the fundamental mode (the seed is inputted via the input-coupler). The other terms are much less trivial to solve. We start with the terms proportional to $\left\langle \widetilde{\mathbf{N}}^{x\dagger}_{s}\widetilde{\mathbf{N}}^{x}_{s} \right\rangle$

and $\left\langle \widetilde{\mathbf{N}}_s^{p\dagger}\widetilde{\mathbf{N}}_s^{p}\right\rangle$

$$\frac{\sqrt{2\gamma_s^{out}}\left[\gamma_p - i\omega\right]}{|g|^2|\alpha|^2 + (\gamma_s - i\omega - g\beta)(\gamma_p - i\omega)}\frac{\sqrt{2\gamma_s^{out}}\left[\gamma_p + i\omega\right]}{|g|^2|\alpha|^2 + (\gamma_s + i\omega - g\beta)(\gamma_p + i\omega)}\left\langle \widetilde{\mathbf{N}}_s^{x\dagger}\widetilde{\mathbf{N}}_s^{x}\right\rangle$$
$$= \frac{2\gamma_s^{out}\left\langle \widetilde{\mathbf{N}}_s^{x\dagger}\widetilde{\mathbf{N}}_s^{x}\right\rangle}{\left[\frac{|g|^2|\alpha|^2\gamma_p}{\gamma_p^2+\omega^2} + \gamma_s - g\beta\right]^2 + \left[\omega - \frac{|g|^2|\alpha|^2\omega}{\gamma_p^2+\omega^2}\right]^2} = \frac{4\gamma_s^{out}\left(\gamma_s + \gamma_s^{in}\mathcal{V}_s^{x}\right)}{\left[\frac{|g|^2|\alpha|^2\gamma_p}{\gamma_p^2+\omega^2} + \gamma_s - g\beta\right]^2 + \left[\omega - \frac{|g|^2|\alpha|^2\omega}{\gamma_p^2+\omega^2}\right]^2}, \tag{A.3a}$$

$$\frac{\sqrt{2\gamma_s^{out}}\left[\gamma_p - i\omega\right]}{|g|^2|\alpha|^2 + (\gamma_s - i\omega + g\beta)(\gamma_p - i\omega)}\frac{\sqrt{2\gamma_s^{out}}\left[\gamma_p + i\omega\right]}{|g|^2|\alpha|^2 + (\gamma_s + i\omega + g\beta)(\gamma_p + i\omega)}\left\langle \widetilde{\mathbf{N}}_s^{p\dagger}\widetilde{\mathbf{N}}_s^{p}\right\rangle$$
$$= \frac{2\gamma_s^{out}\left\langle \widetilde{\mathbf{N}}_s^{p\dagger}\widetilde{\mathbf{N}}_s^{p}\right\rangle}{\left[\frac{|g|^2|\alpha|^2\gamma_p}{\gamma_p^2+\omega^2} + \gamma_s + g\beta\right]^2 + \left[\omega - \frac{|g|^2|\alpha|^2\omega}{\gamma_p^2+\omega^2}\right]^2} = \frac{4\gamma_s^{out}\left(\gamma_s + \gamma_s^{in}\mathcal{V}_s^{p}\right)}{\left[\frac{|g|^2|\alpha|^2\gamma_p}{\gamma_p^2+\omega^2} + \gamma_s + g\beta\right]^2 + \left[\omega - \frac{|g|^2|\alpha|^2\omega}{\gamma_p^2+\omega^2}\right]^2}, \tag{A.3b}$$

where we have allowed the seed entering from the input coupler to have excess noise in both amplitude $\mathcal{V}_s^x$ and phase $\mathcal{V}_s^p$.
We now look at the terms proportional to $\left\langle \widetilde{\mathbf{N}}_p^{x\dagger}\widetilde{\mathbf{N}}_p^{x}\right\rangle$ and $\left\langle \widetilde{\mathbf{N}}_p^{p\dagger}\widetilde{\mathbf{N}}_p^{p}\right\rangle$

$$\frac{\sqrt{2\gamma_s^{out}}g\alpha}{|g|^2|\alpha|^2 + (\gamma_s - i\omega - g\beta)(\gamma_p - i\omega)}\frac{\sqrt{2\gamma_s^{out}}g\alpha}{|g|^2|\alpha|^2 + (\gamma_s + i\omega - g\beta)(\gamma_p + i\omega)}\left\langle \widetilde{\mathbf{N}}_p^{x\dagger}\widetilde{\mathbf{N}}_p^{x}\right\rangle$$
$$= \frac{2\gamma_s^{out}|g|^2|\alpha|^2\left\langle \widetilde{\mathbf{N}}_p^{x\dagger}\widetilde{\mathbf{N}}_p^{x}\right\rangle}{\left[|g|^2|\alpha|^2 + \gamma_s\gamma_p - \omega^2 - g\beta\gamma_p\right]^2 + \left[\omega\left(\gamma_s + \gamma_p - g\beta\right)\right]^2}$$
$$= \frac{4\gamma_s^{out}|g|^2|\alpha|^2\left(\gamma_p + \gamma_p^{out}\mathcal{V}_p^{x}\right)}{\left[|g|^2|\alpha|^2 + \gamma_s\gamma_p - \omega^2 - g\beta\gamma_p\right]^2 + \left[\omega\left(\gamma_s + \gamma_p - g\beta\right)\right]^2}, \tag{A.4a}$$

$$\frac{\sqrt{2\gamma_s^{out}}g\alpha}{|g|^2|\alpha|^2 + (\gamma_s - i\omega + g\beta)(\gamma_p - i\omega)}\frac{\sqrt{2\gamma_s^{out}}g\alpha}{|g|^2|\alpha|^2 + (\gamma_s + i\omega + g\beta)(\gamma_p + i\omega)}\left\langle \widetilde{\mathbf{N}}_p^{p\dagger}\widetilde{\mathbf{N}}_p^{p}\right\rangle$$
$$= \frac{2\gamma_s^{out}|g|^2|\alpha|^2\left\langle \widetilde{\mathbf{N}}_p^{p\dagger}\widetilde{\mathbf{N}}_p^{p}\right\rangle}{\left[|g|^2|\alpha|^2 + \gamma_s\gamma_p - \omega^2 + g\beta\gamma_p\right]^2 + \left[\omega\left(\gamma_s + \gamma_p + g\beta\right)\right]^2}$$
$$= \frac{4\gamma_s^{out}|g|^2|\alpha|^2\left(\gamma_p + \gamma_p^{out}\mathcal{V}_p^{p}\right)}{\left[|g|^2|\alpha|^2 + \gamma_s\gamma_p - \omega^2 + g\beta\gamma_p\right]^2 + \left[\omega\left(\gamma_s + \gamma_p + g\beta\right)\right]^2}, \tag{A.4b}$$

where once again we have allowed the pump to have excess noise in both amplitude and phase. Finally we have the cross terms proportional to $\left\langle \widetilde{\mathbf{N}}_s^{x\dagger}\delta\widetilde{\mathbf{X}}_{s,in}^{out}\right\rangle$, $\left\langle \delta\widetilde{\mathbf{X}}_{s,in}^{out\dagger}\widetilde{\mathbf{N}}_s^{x}\right\rangle$, $\left\langle \widetilde{\mathbf{N}}_s^{p\dagger}\delta\widetilde{\mathbf{P}}_{s,in}^{out}\right\rangle$ and $\left\langle \delta\widetilde{\mathbf{P}}_{s,in}^{out\dagger}\widetilde{\mathbf{N}}_s^{p}\right\rangle$

$$
\begin{aligned}
&- \frac{\sqrt{2\gamma_s^{out}}\left[\gamma_p - i\omega\right]\left\langle \widetilde{\mathbf{N}}_s^{x\dagger}\delta\widetilde{\mathbf{X}}_{s,in}^{out}\right\rangle}{|g|^2|\alpha|^2 + (\gamma_s - i\omega - g\beta)(\gamma_p - i\omega)} - \frac{\sqrt{2\gamma_s^{out}}\left[\gamma_p + i\omega\right]\left\langle \delta\widetilde{\mathbf{X}}_{s,in}^{out\dagger}\widetilde{\mathbf{N}}_s^{x}\right\rangle}{|g|^2|\alpha|^2 + (\gamma_s + i\omega - g\beta)(\gamma_p + i\omega)} \\
&= - \frac{\sqrt{2\gamma_s^{out}}\left[\frac{|g|^2|\alpha|^2\gamma_p}{\gamma_p^2+\omega^2} + \gamma_s - g\beta + i\omega\left[1 - \frac{|g|^2|\alpha|^2}{\gamma_p^2+\omega^2}\right]\right]\left\langle \widetilde{\mathbf{N}}_s^{x\dagger}\delta\widetilde{\mathbf{X}}_{s,in}^{out}\right\rangle}{\left[\frac{|g|^2|\alpha|^2\gamma_p}{\gamma_p^2+\omega^2} + \gamma_s - g\beta\right]^2 + \left[\omega - \frac{|g|^2|\alpha|^2\omega}{\gamma_p^2+\omega^2}\right]^2} \\
&- \frac{\sqrt{2\gamma_s^{out}}\left[\frac{|g|^2|\alpha|^2\gamma_p}{\gamma_p^2+\omega^2} + \gamma_s - g\beta - i\omega\left[1 - \frac{|g|^2|\alpha|^2}{\gamma_p^2+\omega^2}\right]\right]\left\langle \delta\widetilde{\mathbf{X}}_{s,in}^{out\dagger}\widetilde{\mathbf{N}}_s^{x}\right\rangle}{\left[\frac{|g|^2|\alpha|^2\gamma_p}{\gamma_p^2+\omega^2} + \gamma_s - g\beta\right]^2 + \left[\omega - \frac{|g|^2|\alpha|^2\omega}{\gamma_p^2+\omega^2}\right]^2} \\
&= - \frac{4\gamma_s^{out}\left[\frac{|g|^2|\alpha|^2\gamma_p}{\gamma_p^2+\omega^2} + \gamma_s - g\beta\right]}{\left[\frac{|g|^2|\alpha|^2\gamma_p}{\gamma_p^2+\omega^2} + \gamma_s - g\beta\right]^2 + \left[\omega - \frac{|g|^2|\alpha|^2\omega}{\gamma_p^2+\omega^2}\right]^2},
\end{aligned}
\tag{A.5a}
$$

$$
\begin{aligned}
&- \frac{\sqrt{2\gamma_s^{out}}\left[\gamma_p - i\omega\right]\left\langle \widetilde{\mathbf{N}}_s^{p\dagger}\delta\widetilde{\mathbf{P}}_{s,in}^{out}\right\rangle}{|g|^2|\alpha|^2 + (\gamma_s - i\omega + g\beta)(\gamma_p - i\omega)} - \frac{\sqrt{2\gamma_s^{out}}\left[\gamma_p + i\omega\right]\left\langle \delta\widetilde{\mathbf{P}}_{s,in}^{out\dagger}\widetilde{\mathbf{N}}_s^{p}\right\rangle}{|g|^2|\alpha|^2 + (\gamma_s + i\omega + g\beta)(\gamma_p + i\omega)} \\
&= - \frac{\sqrt{2\gamma_s^{out}}\left[\frac{|g|^2|\alpha|^2\gamma_p}{\gamma_p^2+\omega^2} + \gamma_s + g\beta + i\omega\left[1 - \frac{|g|^2|\alpha|^2}{\gamma_p^2+\omega^2}\right]\right]\left\langle \widetilde{\mathbf{N}}_s^{p\dagger}\delta\widetilde{\mathbf{P}}_{s,in}^{out}\right\rangle}{\left[\frac{|g|^2|\alpha|^2\gamma_p}{\gamma_p^2+\omega^2} + \gamma_s + g\beta\right]^2 + \left[\omega - \frac{|g|^2|\alpha|^2\omega}{\gamma_p^2+\omega^2}\right]^2} \\
&- \frac{\sqrt{2\gamma_s^{out}}\left[\frac{|g|^2|\alpha|^2\gamma_p}{\gamma_p^2+\omega^2} + \gamma_s + g\beta - i\omega\left[1 - \frac{|g|^2|\alpha|^2}{\gamma_p^2+\omega^2}\right]\right]\left\langle \delta\widetilde{\mathbf{P}}_{s,in}^{out\dagger}\widetilde{\mathbf{N}}_s^{p}\right\rangle}{\left[\frac{|g|^2|\alpha|^2\gamma_p}{\gamma_p^2+\omega^2} + \gamma_s + g\beta\right]^2 + \left[\omega - \frac{|g|^2|\alpha|^2\omega}{\gamma_p^2+\omega^2}\right]^2} \\
&= - \frac{4\gamma_s^{out}\left[\frac{|g|^2|\alpha|^2\gamma_p}{\gamma_p^2+\omega^2} + \gamma_s + g\beta\right]}{\left[\frac{|g|^2|\alpha|^2\gamma_p}{\gamma_p^2+\omega^2} + \gamma_s + g\beta\right]^2 + \left[\omega - \frac{|g|^2|\alpha|^2\omega}{\gamma_p^2+\omega^2}\right]^2}.
\end{aligned}
\tag{A.5b}
$$

We put everything together and compute the full variance of the quantum fluctuations

$$\begin{aligned}
\sigma^2\left(\delta\widetilde{\mathbf{X}}^{out}_{s,out}\right) =& 1+\frac{4\gamma_s^{out}\left(\gamma_s+\gamma_s^{in}\mathcal{V}_s^x\right)}{\left[\frac{|g|^2|\alpha|^2\gamma_p}{\gamma_p^2+\omega^2}+\gamma_s-g\beta\right]^2+\left[\omega-\frac{|g|^2|\alpha|^2\omega}{\gamma_p^2+\omega^2}\right]^2}-\frac{4\gamma_s^{out}\left[\frac{|g|^2|\alpha|^2\gamma_p}{\gamma_p^2+\omega^2}+\gamma_s-g\beta\right]}{\left[\frac{|g|^2|\alpha|^2\gamma_p}{\gamma_p^2+\omega^2}+\gamma_s-g\beta\right]^2+\left[\omega-\frac{|g|^2|\alpha|^2\omega}{\gamma_p^2+\omega^2}\right]^2}\\
&+\frac{4\gamma_s^{out}|g|^2|\alpha|^2\left(\gamma_p+\gamma_p^{out}\mathcal{V}_p^x\right)}{\left[|g|^2|\alpha|^2+\gamma_s\gamma_p-\omega^2-g\beta\gamma_p\right]^2+\left[\omega\left(\gamma_s+\gamma_p-g\beta\right)\right]^2}\\
=& 1+\frac{4\gamma_s^{out}g\beta}{\left[\frac{|g|^2|\alpha|^2\gamma_p}{\gamma_p^2+\omega^2}+\gamma_s-g\beta\right]^2+\left[\omega-\frac{|g|^2|\alpha|^2\omega}{\gamma_p^2+\omega^2}\right]^2}+\frac{4\gamma_s^{out}\left[\gamma_s^{in}\mathcal{V}_s^x-\frac{|g|^2|\alpha|^2\gamma_p}{\gamma_p^2+\omega^2}\right]}{\left[\frac{|g|^2|\alpha|^2\gamma_p}{\gamma_p^2+\omega^2}+\gamma_s-g\beta\right]^2+\left[\omega-\frac{|g|^2|\alpha|^2\omega}{\gamma_p^2+\omega^2}\right]^2}\\
&+\frac{4\gamma_s^{out}|g|^2|\alpha|^2\left(\gamma_p+\gamma_p^{out}\mathcal{V}_p^x\right)}{\left[|g|^2|\alpha|^2+\gamma_s\gamma_p-\omega^2-g\beta\gamma_p\right]^2+\left[\omega\left(\gamma_s+\gamma_p-g\beta\right)\right]^2}, \qquad \text{(A.6a)}\\
\sigma^2\left(\delta\widetilde{\mathbf{P}}^{out}_{s,out}\right) =& 1+\frac{4\gamma_s^{out}\left(\gamma_s+\gamma_s^{in}\mathcal{V}_s^p\right)}{\left[\frac{|g|^2|\alpha|^2\gamma_p}{\gamma_p^2+\omega^2}+\gamma_s+g\beta\right]^2+\left[\omega-\frac{|g|^2|\alpha|^2\omega}{\gamma_p^2+\omega^2}\right]^2}-\frac{4\gamma_s^{out}\left[\frac{|g|^2|\alpha|^2\gamma_p}{\gamma_p^2+\omega^2}+\gamma_s+g\beta\right]}{\left[\frac{|g|^2|\alpha|^2\gamma_p}{\gamma_p^2+\omega^2}+\gamma_s+g\beta\right]^2+\left[\omega-\frac{|g|^2|\alpha|^2\omega}{\gamma_p^2+\omega^2}\right]^2}\\
&+\frac{4\gamma_s^{out}|g|^2|\alpha|^2\left(\gamma_p+\gamma_p^{out}\mathcal{V}_p^p\right)}{\left[|g|^2|\alpha|^2+\gamma_s\gamma_p-\omega^2+g\beta\gamma_p\right]^2+\left[\omega\left(\gamma_s+\gamma_p+g\beta\right)\right]^2}\\
=& 1-\frac{4\gamma_s^{out}g\beta}{\left[\frac{|g|^2|\alpha|^2\gamma_p}{\gamma_p^2+\omega^2}+\gamma_s+g\beta\right]^2+\left[\omega-\frac{|g|^2|\alpha|^2\omega}{\gamma_p^2+\omega^2}\right]^2}+\frac{4\gamma_s^{out}\left[\gamma_s^{in}\mathcal{V}_s^x-\frac{|g|^2|\alpha|^2\gamma_p}{\gamma_p^2+\omega^2}\right]}{\left[\frac{|g|^2|\alpha|^2\gamma_p}{\gamma_p^2+\omega^2}+\gamma_s+g\beta\right]^2+\left[\omega-\frac{|g|^2|\alpha|^2\omega}{\gamma_p^2+\omega^2}\right]^2}\\
&+\frac{4\gamma_s^{out}|g|^2|\alpha|^2\left(\gamma_p+\gamma_p^{out}\mathcal{V}_p^x\right)}{\left[|g|^2|\alpha|^2+\gamma_s\gamma_p-\omega^2+g\beta\gamma_p\right]^2+\left[\omega\left(\gamma_s+\gamma_p+g\beta\right)\right]^2} \qquad \text{(A.6b)}
\end{aligned}$$

This is in theory the result we are looking for, however, we want to put equations (A.6a) and (A.6b) on a more useful form. We do this by defining the escape efficiency of the squeezed light $\eta_{esc}=\gamma_s^{out}/\gamma_s$ and use the fact that $P_p/P_p^{thr}=(g\beta/\gamma_s)^2$. This gives us

$$\sigma^2\left(\delta\widetilde{\mathbf{X}}^{out}_{s,out}\right) = 1 + \eta_{esc}\frac{4\sqrt{\frac{P_p}{P_{th}}}}{\left[1-\sqrt{\frac{P_p}{P_{th}}}+\frac{|g|^2|\alpha|^2}{\gamma_p^2+\omega^2}\frac{\gamma_p}{\gamma_s}\right]^2+\left[\frac{\omega}{\gamma_s}\left(1+\frac{|g|^2|\alpha|^2}{\gamma_p^2+\omega^2}\right)\right]^2}$$
$$+\eta_{esc}\frac{4\left[\frac{\gamma_s^{in}}{\gamma_s}\mathcal{V}_s^x-\frac{|g|^2|\alpha|^2}{\gamma_p^2+\omega^2}\frac{\gamma_p}{\gamma_s}\right]}{\left[1-\sqrt{\frac{P_p}{P_{th}}}+\frac{|g|^2|\alpha|^2}{\gamma_p^2+\omega^2}\frac{\gamma_p}{\gamma_s}\right]^2+\left[\frac{\omega}{\gamma_s}\left(1+\frac{|g|^2|\alpha|^2}{\gamma_p^2+\omega^2}\right)\right]^2}$$
$$+\eta_{esc}\frac{4|g|^2|\alpha|^2\left[\frac{\gamma_p}{\gamma_s}+\frac{\gamma_p^{out}}{\gamma_s}\mathcal{V}_p^x\right]}{\gamma_p^2\left[\frac{|g|^2|\alpha|^2-\omega^2}{\gamma_s\gamma_p}+\left(1-\sqrt{\frac{P_p}{P_{th}}}\right)\right]^2+\omega^2\left[1-\sqrt{\frac{P_p}{P_{th}}}+\frac{\gamma_p}{\gamma_s}\right]^2}, \tag{A.7a}$$

$$\sigma^2\left(\delta\widetilde{\mathbf{P}}^{out}_{s,out}\right) = 1 - \eta_{esc}\frac{4\sqrt{\frac{P_p}{P_{th}}}}{\left[1+\sqrt{\frac{P_p}{P_{th}}}+\frac{|g|^2|\alpha|^2}{\gamma_p^2+\omega^2}\frac{\gamma_p}{\gamma_s}\right]^2+\left[\frac{\omega}{\gamma_s}\left(1+\frac{|g|^2|\alpha|^2}{\gamma_p^2+\omega^2}\right)\right]^2}$$
$$+\eta_{esc}\frac{4\left[\frac{\gamma_s^{in}}{\gamma_s}\mathcal{V}_s^p-\frac{|g|^2|\alpha|^2}{\gamma_p^2+\omega^2}\frac{\gamma_p}{\gamma_s}\right]}{\left[1+\sqrt{\frac{P_p}{P_{th}}}+\frac{|g|^2|\alpha|^2}{\gamma_p^2+\omega^2}\frac{\gamma_p}{\gamma_s}\right]^2+\left[\frac{\omega}{\gamma_s}\left(1+\frac{|g|^2|\alpha|^2}{\gamma_p^2+\omega^2}\right)\right]^2}$$
$$+\eta_{esc}\frac{4|g|^2|\alpha|^2\left[\frac{\gamma_p}{\gamma_s}+\frac{\gamma_p^{out}}{\gamma_s}\mathcal{V}_p^p\right]}{\gamma_p^2\left[\frac{|g|^2|\alpha|^2-\omega^2}{\gamma_s\gamma_p}+\left(1+\sqrt{\frac{P_p}{P_{th}}}\right)\right]^2+\omega^2\left[1+\sqrt{\frac{P_p}{P_{th}}}+\frac{\gamma_p}{\gamma_s}\right]^2}. \tag{A.7b}$$

While complete, equations (A.7a) and (A.7b) can be simplified quite a bit by neglecting the terms proportional to $|g|^2|\alpha|^2/(\gamma_p^2+\omega^2)$.

$$\sigma^2\left(\delta\widetilde{\mathbf{X}}^{out}_{s,out}\right) = 1 + \eta_{esc}\frac{4\sqrt{\frac{P_p}{P_{th}}}}{\left[1-\sqrt{\frac{P_p}{P_{th}}}\right]^2+\left[\frac{\omega}{\gamma_s}\right]^2}+\eta_{esc}\frac{4\frac{\gamma_s^{in}}{\gamma_s}\mathcal{V}_s^x}{\left[1-\sqrt{\frac{P_p}{P_{th}}}\right]^2+\left[\frac{\omega}{\gamma_s}\right]^2}$$
$$+\eta_{esc}\frac{4|g|^2|\alpha|^2\left[\frac{\gamma_p}{\gamma_s}+\frac{\gamma_p^{out}}{\gamma_s}\mathcal{V}_p^x\right]}{\gamma_p^2\left[\frac{|g|^2|\alpha|^2-\omega^2}{\gamma_s\gamma_p}+\left(1-\sqrt{\frac{P_p}{P_{th}}}\right)\right]^2+\omega^2\left[1-\sqrt{\frac{P_p}{P_{th}}}+\frac{\gamma_p}{\gamma_s}\right]^2}, \tag{A.8a}$$

$$\sigma^2\left(\delta\widetilde{\mathbf{P}}^{out}_{s,out}\right) = 1 - \eta_{esc}\frac{4\sqrt{\frac{P_p}{P_{th}}}}{\left[1+\sqrt{\frac{P_p}{P_{th}}}\right]^2+\left[\frac{\omega}{\gamma_s}\right]^2}+\eta_{esc}\frac{4\frac{\gamma_s^{in}}{\gamma_s}\mathcal{V}_s^p}{\left[1+\sqrt{\frac{P_p}{P_{th}}}\right]^2+\left[\frac{\omega}{\gamma_s}\right]^2}$$
$$+\eta_{esc}\frac{4|g|^2|\alpha|^2\left[\frac{\gamma_p}{\gamma_s}+\frac{\gamma_p^{out}}{\gamma_s}\mathcal{V}_p^p\right]}{\gamma_p^2\left[\frac{|g|^2|\alpha|^2-\omega^2}{\gamma_s\gamma_p}+\left(1+\sqrt{\frac{P_p}{P_{th}}}\right)\right]^2+\omega^2\left[1+\sqrt{\frac{P_p}{P_{th}}}+\frac{\gamma_p}{\gamma_s}\right]^2}. \tag{A.8b}$$

B

Plots of the 18 dB OPO optical properties

This appendix will contain plots of the optical properties of the 18 dB OPO as a function of crystal length. The first section will be on the old crystal design, and the second section will be on the modified crystal design. In the section on the modified cavity, I will only include figures of properties that change drastically.

B.1 Old crystal design

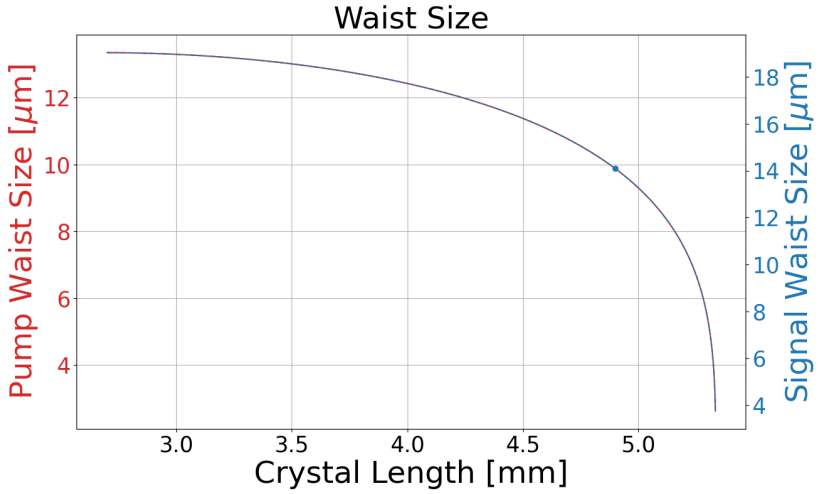

Figure B.1: Cavity waist vs crystal length

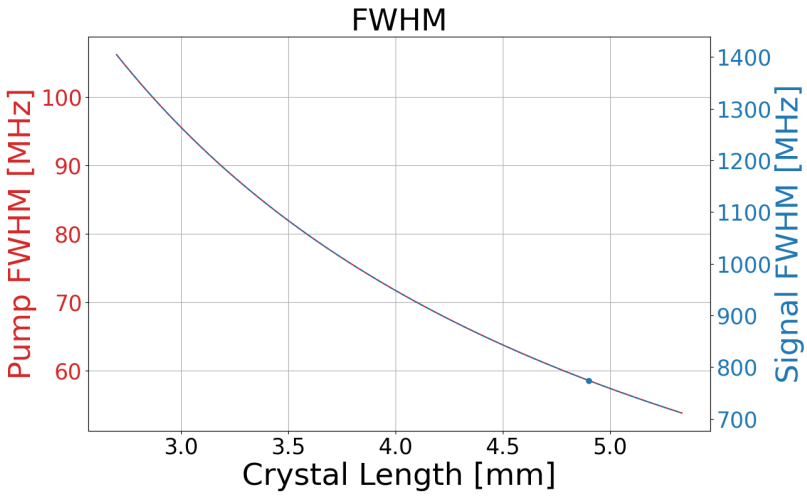

Figure B.2: Cavity FWHM vs crystal length

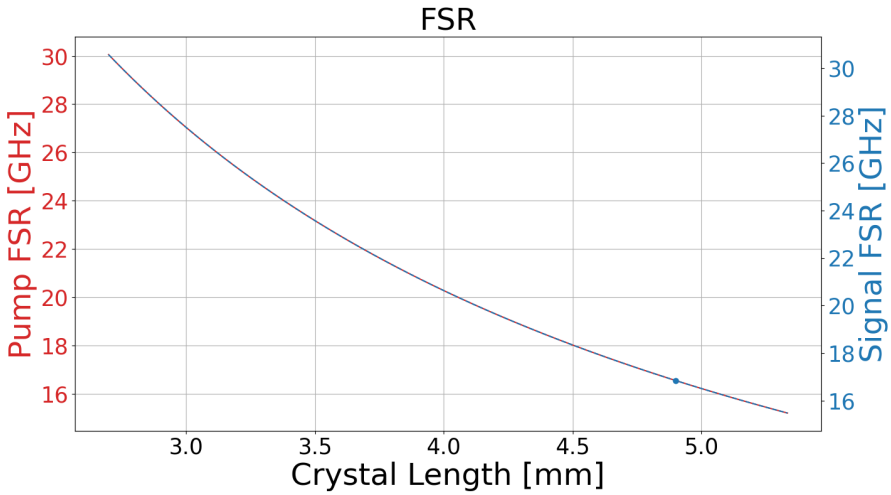

Figure B.3: Cavity FSR vs crystal length

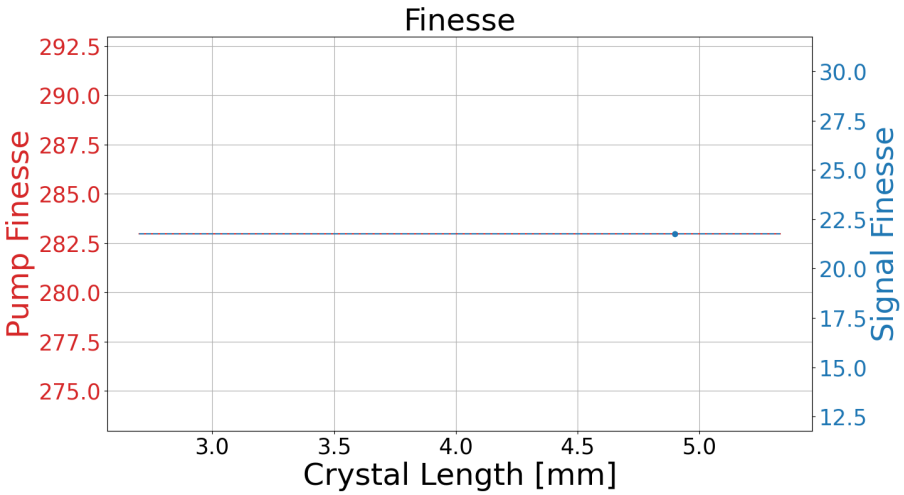

Figure B.4: Cavity finesse vs crystal length

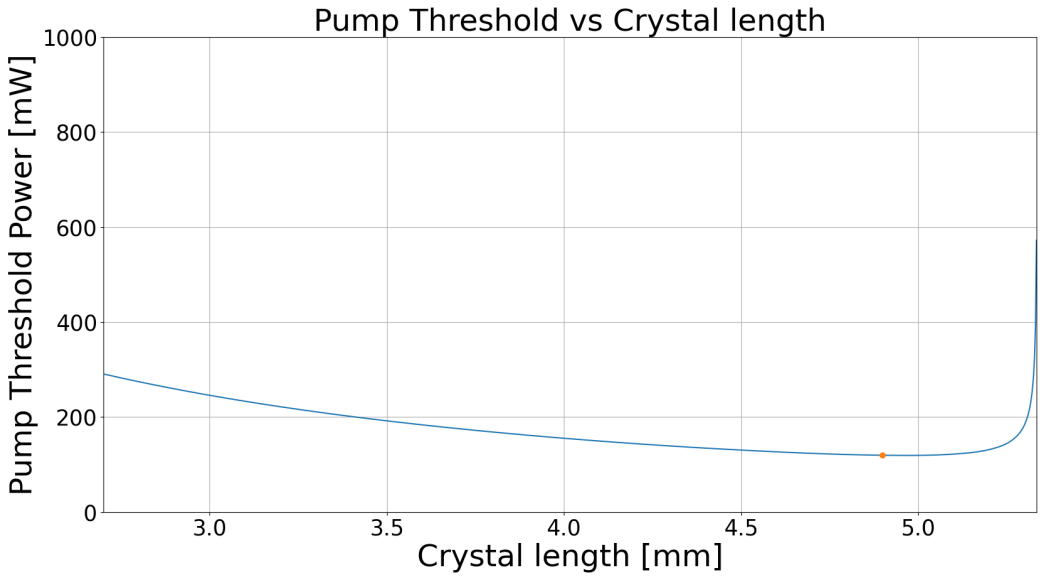

Figure B.5: OPO threshold vs crystal length

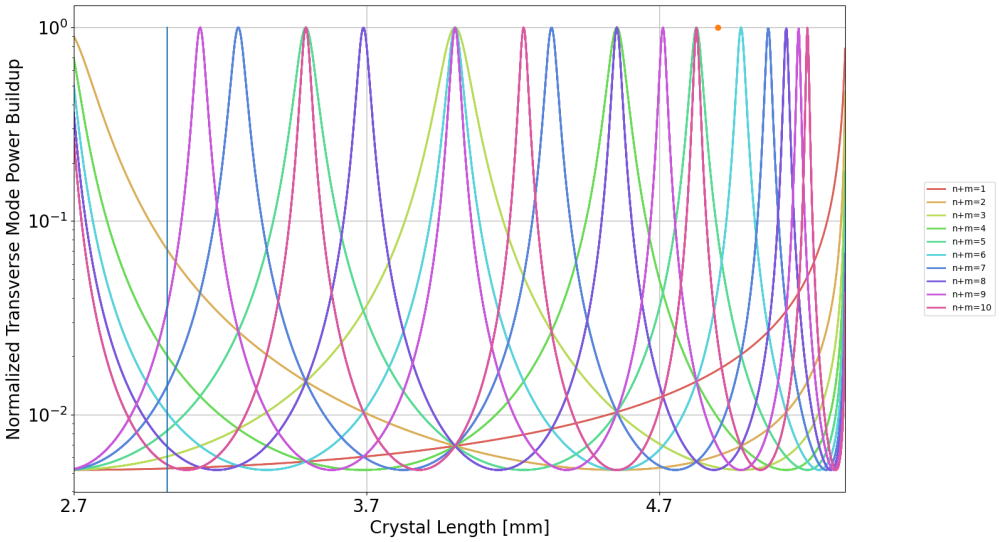

Figure B.6: Higher order mode build-up for 1550 nm vs crystal length

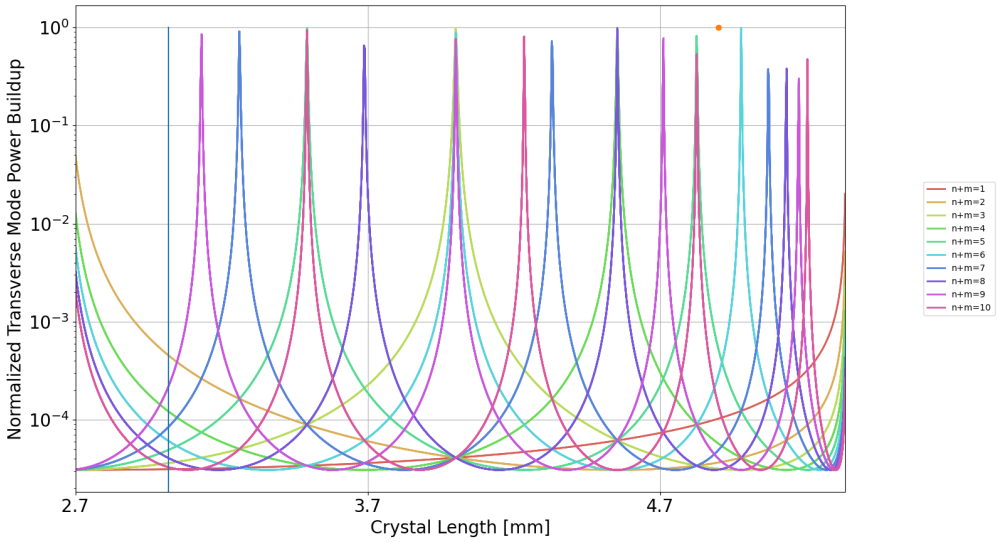

Figure B.7: Cavity waist vs crystal length

B.2 Modified crystal design

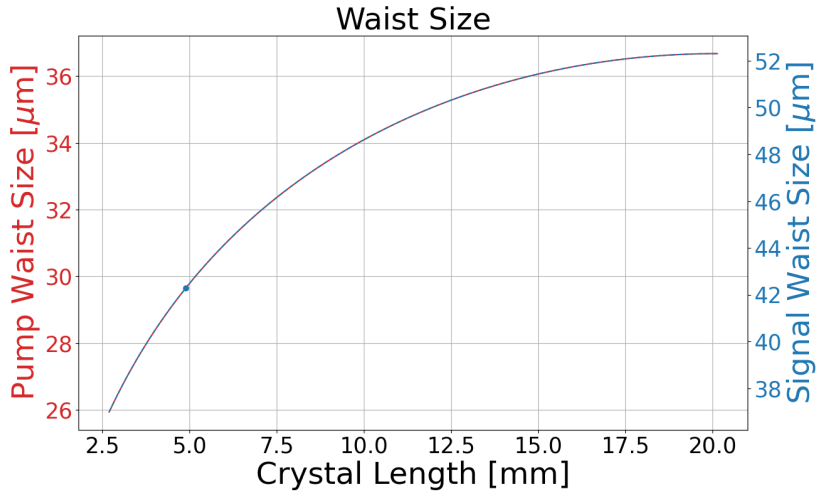

Figure B.8: Cavity waist vs crystal length

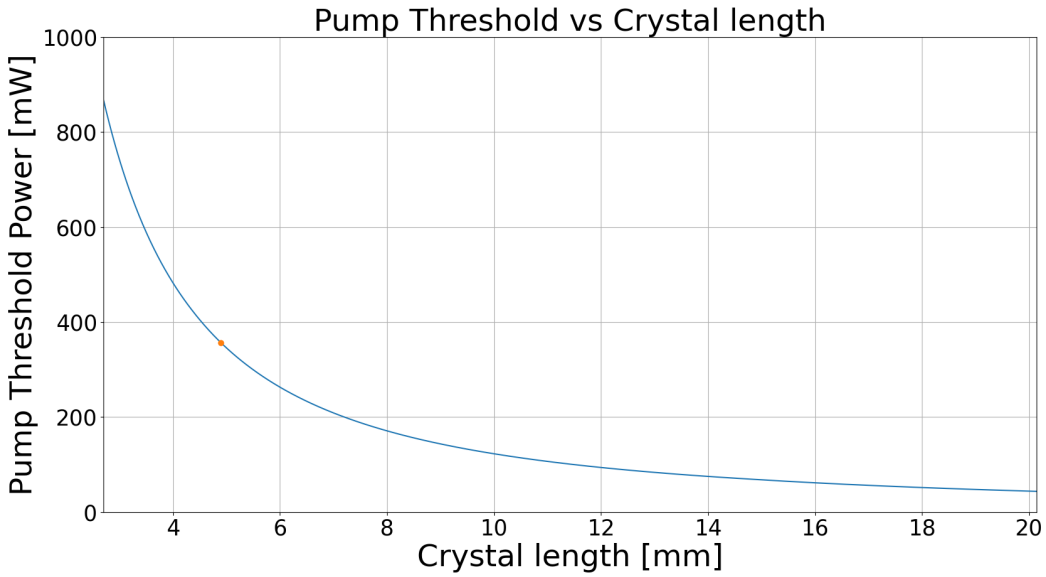

Figure B.9: OPO pump threshold vs crystal length

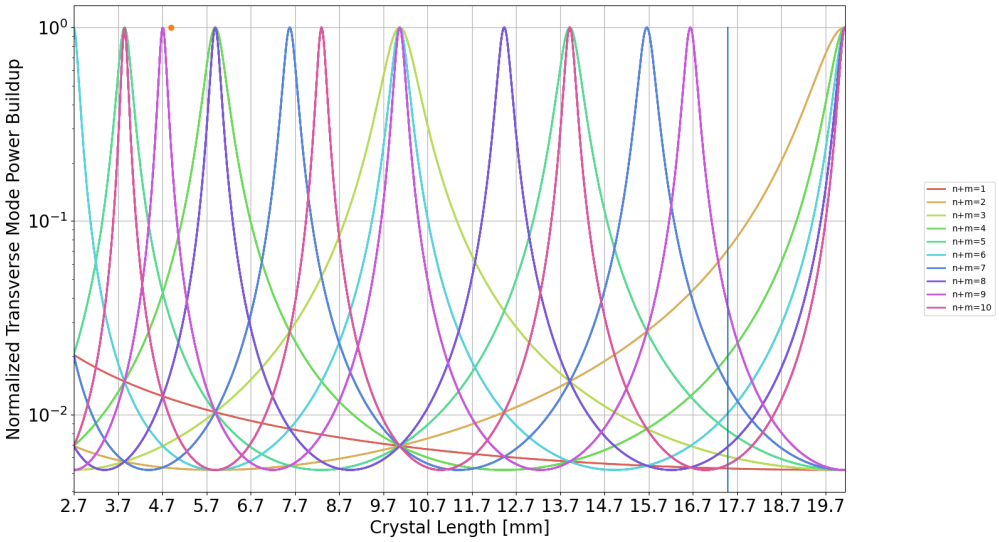

Figure B.10: Higher order mode build-up for 1550 nm vs crystal length

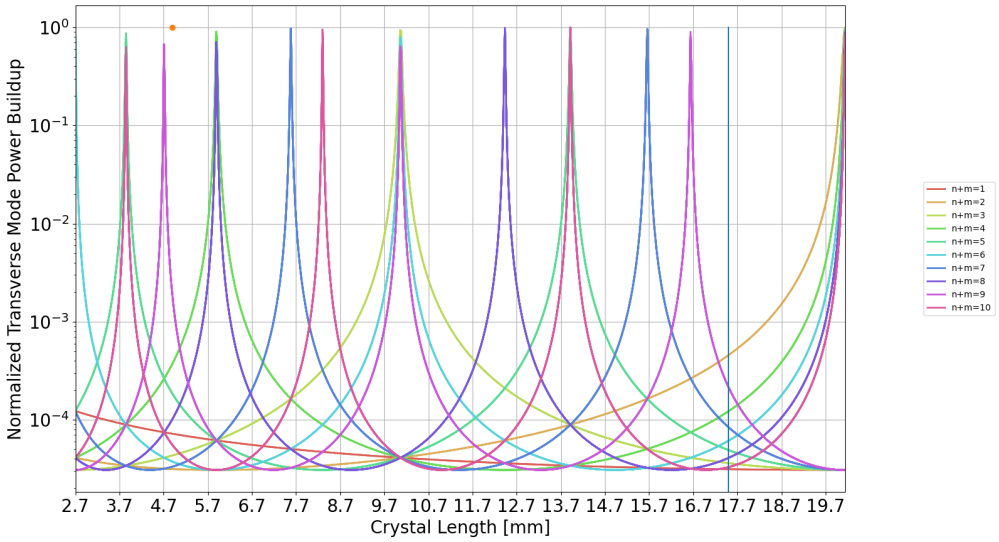

Figure B.11: Cavity waist vs crystal length

Bibliography

[1] M. Planck, *The theory of heat radiation*. P. BLAKISTON'S SON & CO., 1913.

[2] A. B. Arons and M. B. Peppard, "Eistein's propoal of the photon concept - a translation of the annalen der physik paper of 1905," *American Journal of Physics*, vol. 33, 1965.

[3] N. Bohr, "I. on the constitution of atoms and molecules," *The London, Edinburgh, and Dublin Philosophical Magazine and Journal of Science*, vol. 26, no. 151, pp. 1–25, 1913.

[4] L. de Broglie, "Waves and quanta," *Nature*, vol. 112, no. 2815, p. 540, 1923.

[5] W. A. Fedak and J. J. Prentis, "The 1925 born and jordan paper "on quantum mechanics"," *American Journal of Physics*, vol. 77, no. 2, pp. 128–139, 2009.

[6] E. Schrödinger, "An undulatory theory of the mechanics of atoms and molecules," *Phys. Rev.*, vol. 28, pp. 1049–1070, 1926.

[7] A. G. J. MacFarlane, J. P. Dowling, and G. J. Milburn, "Quantum technology: the second quantum revolution," *Philosophical Transactions of the Royal Society of London. Series A: Mathematical, Physical and Engineering Sciences*, vol. 361, no. 1809, pp. 1655–1674, 2003.

[8] G. Moore, "Cramming more components onto integrated circuits," *Electronics Magazine*, vol. 38, no. 8, 1965.

[9] R. Landauer, "Irreversibility and heat generation in the computing process," *IBM Journal of Research and Development*, vol. 5, no. 3, pp. 183–191, 1961.

[10] C. H. Bennett, "Logical reversibility of computation," *Ibm Journal of Research and Development*, vol. 17, pp. 525–532, 1973.

[11] R. P. Feynman, "Simulating physics with computers," *International Journal of Theoretical Physics*, p. 467–488, 1982.

[12] R. P. Feynman, "Quantum mechanical computers," *Foundations of Physics*, p. 507–531, 1986.

[13] D. Deutsch and R. Penrose, "Quantum theory, the church-turing principle and the universal quantum computer," *Proceedings of the Royal Society of London. A. Mathematical and Physical Sciences*, vol. 400, no. 1818, pp. 97–117, 1985.

[14] D. E. Deutsch and R. Penrose, "Quantum computational networks," *Proceedings of the Royal Society of London. A. Mathematical and Physical Sciences*, vol. 425, no. 1868, pp. 73–90, 1989.

[15] P. W. Shor, "Algorithms for quantum computation: discrete logarithms and factoring," in *Proceedings 35th Annual Symposium on Foundations of Computer Science*, pp. 124–134, 1994.

[16] J. Preskill, "Quantum Computing in the NISQ era and beyond," *Quantum*, vol. 2, p. 79, 2018.

[17] F. Arute *et al.*, "Quantum supremacy using a programmable superconducting processor," *Nature*, vol. 574, no. 7779, pp. 505–510, 2019.

[18] H.-S. Zhong *et al.*, "Quantum computational advantage using photons," *Science*, vol. 370, no. 6523, pp. 1460–1463, 2020.

[19] H.-S. Zhong *et al.*, "Phase-programmable gaussian boson sampling using stimulated squeezed light," *Phys. Rev. Lett.*, vol. 127, p. 180502, 2021.

[20] Y. Wu *et al.*, "Strong quantum computational advantage using a superconducting quantum processor," *Phys. Rev. Lett.*, vol. 127, p. 180501, 2021.

[21] M. A. Taylor and W. P. Bowen, "Quantum metrology and its application in biology," *Physics Reports*, vol. 615, pp. 1–59, 2016.

[22] E. Polino, M. Valeri, N. Spagnolo, and F. Sciarrino, "Photonic quantum metrology," *AVS Quantum Science*, vol. 2, no. 2, p. 024703, 2020.

[23] The LIGO Scientific Collaboration, "Enhanced sensitivity of the LIGO gravitational wave detector by using squeezed states of light," *Nature Photonics*, vol. 7, p. 613, 2013.

[24] M. Tse *et al.*, "Quantum-enhanced advanced ligo detectors in the era of gravitational-wave astronomy," *Phys. Rev. Lett.*, vol. 123, p. 231107, 2019.

[25] A. Buikema *et al.*, "Sensitivity and performance of the advanced ligo detectors in the third observing run," *Phys. Rev. D*, vol. 102, p. 062003, 2020.

[26] J. Lough, E. Schreiber, F. Bergamin, H. Grote, M. Mehmet, H. Vahlbruch, C. Affeldt, M. Brinkmann, A. Bisht, V. Kringel, H. Lück, N. Mukund, S. Nadji, B. Sorazu, K. Strain, M. Weinert, and K. Danzmann, "First demonstration of 6 db quantum noise reduction in a kilometer scale gravitational wave observatory," *Phys. Rev. Lett.*, vol. 126, p. 041102, 2021.

[27] Peter W. Milonni and J. H. Eberly, *Laser Physics*. John Wiley & Sons, Inc., 2010.

[28] C. C. Gerry and P. L. Knight, *Introductory Quantum Optics*. Cambridge University Press, 2005.

[29] H.-A. Bachor and T. C. Ralph, *A Guide to Experiments in Quantum Optics*. Wiley-VCH Verlag GmbH & Co. KGaA, 2004.

[30] T. Eberlei, *Realization of Finite-Size Quantum Key Distribution based on Einstein-Podolsky-Rosen Entangled Light*. PhD thesis, Gottfried Wilhelm Leibniz University of Hannover, 2013.

[31] J. S. Neergaard-Nielsen, *Generation of single photons and Schrödinger kitten states of light.* PhD thesis, University of Copenhagen, 2008.

[32] J.J. Sakurai and J. J. Napolitano, *Modern Quantum Mechanics.* Pearson, 2014.

[33] A. I. Lvovsky, "Squeezed light," *ArXiv e-prints*, 2016.

[34] C. Kittel, *Introduction to Solid State Physics.* John Wiley and Sons, Inc, 2005.

[35] A. Freise, *Finesse 2 Manual.* Andreas Freise, 2018.

[36] D. Z. Anderson, "Alignment of resonant optical cavities," *Appl. Opt.*, vol. 23, no. 17, pp. 2944–2949, 1984.

[37] K. Rottwitt and P. Tidemand-Lichtenberg, *Nonlinear Optics: Principles and Applications.* CRC Press, 2015.

[38] G. D. Boyd and D. A. Kleinman, "Parametric interaction of focused gaussian light beams," *Journal of Applied Physics*, vol. **39**, no. 8, 1968.

[39] P. K. Lam, *Applications of Quantum Electro-Optic Control and Squeezed Light.* PhD thesis, Australian National University, 1998.

[40] R. Drever, J. L. Hall, F. Kowalski, J. Hough, G. M. Ford, A. J. Munley, and H. Ward, "Laser phase and frequency stabilization using an optical resonator," *Applied Physics B*, vol. 31, pp. 97–105, 1983.

[41] E. D. Black, "An introduction to pound–drever–hall laser frequency stabilization," *American Journal of Physics*, vol. 69, no. 1, pp. 79–87, 2001.

[42] J. Miller and M. Evans, "Length control of an optical resonator using second-order transverse modes," *Opt. Lett.*, vol. 39, no. 8, pp. 2495–2498, 2014.

[43] D. A. Shaddock, M. B. Gray, and D. E. McClelland, "Frequency locking a laser to an optical cavity by use of spatial mode interference," *Opt. Lett.*, vol. 24, no. 21, pp. 1499–1501, 1999.

[44] T. W. Hansch and B. Couillaud, "Laser frequency stabilization by polarization spectroscopy of a reflecting reference cavity," *Optics Communications*, vol. 35, no. 3, pp. 441–444, 1980.

[45] H. Vahlbruch, S. Chelkowski, B. Hage, A. Franzen, K. Danzmann, and R. Schnabel, "Coherent control of vacuum squeezing in the gravitational-wave detection band," *Phys. Rev. Lett.*, vol. 97, p. 011101, 2006.

[46] E. Oelker, *Squeezed States for Advanced Gravitational Wave Detectors.* PhD thesis, Massachusetts Institute of Technology, 2016.

[47] A. Abramovici and J. Chapsky, *FEEDBACK CONTROL SYSTEMS: A Fast-Track Guide for Scientists and Engineers.* Springer Science+Business Media, LLC, 2000.

[48] J. Arnbak, C. S. Jacobsen, R. B. Andrade, X. Guo, J. S. Neergaard-Nielsen, U. L. Andersen, and T. Gehring, "Compact, low-threshold squeezed light source," *Opt. Express*, vol. 27, no. 26, pp. 37877–37885, 2019.

[49] U. L. Andersen, T. Gehring, C. Marquardt, and G. Leuchs, "30 years of squeezed light generation," *Physica Scripta*, vol. **91**, no. 5, 2016.

[50] U. L. Andersen, J. S. Neergaard-Nielsen, P. van Loock, and A. Furusawa, "Hybrid discrete- and continuous-variable quantum information," *Nature Physics*, vol. 11, no. 9, pp. 713–719, 2015.

[51] C. Weedbrook, S. Pirandola, R. García-Patrón, N. J. Cerf, T. C. Ralph, J. H. Shapiro, and S. Lloyd, "Gaussian quantum information," *Reviews of Modern Physics*, vol. 84, no. 2, pp. 621–669, 2012.

[52] S. Pirandola, B. R. Bardhan, T. Gehring, C. Weedbrook, and S. Lloyd, "Advances in photonic quantum sensing," *Nature Photonics*, vol. 12, no. 12, pp. 724–733, 2018.

[53] R. Schnabel, N. Mavalvala, D. E. McClelland, and P. K. Lam, "Quantum metrology for gravitational wave astronomy," *Nature Communications*, vol. 1, no. 8, p. 121, 2010.

[54] The LIGO Scientific Collaboration, "A gravitational wave observatory operating beyond the quantum shot-noise limit," *Nature Physics*, vol. 7, no. 12, pp. 962–965, 2011.

[55] GEO600, "Gravitational-wave detectors begin third observation run." URL: http://www.geo600.org/1897380/gravitational-wave-detectors-begin-third-observation-run, 2019.

[56] M. A. Taylor, J. Janousek, V. Daria, J. Knittel, B. Hage, H.-A. Bachor, and W. P. Bowen, "Biological measurement beyond the quantum limit," *Nature Photonics*, vol. 7, p. 229, 2013.

[57] M. A. Taylor, J. Janousek, V. Daria, J. Knittel, B. Hage, H.-A. Bachor, and W. P. Bowen, "Subdiffraction-Limited Quantum Imaging within a Living Cell," *Physical Review X*, vol. 4, no. 1, p. 011017, 2014.

[58] L. S. Madsen, V. C. Usenko, M. Lassen, R. Filip, and U. L. Andersen, "Continuous variable quantum key distribution with modulated entangled states.," *Nature Communications*, vol. 3, p. 1083, 2012. Article number:1083.

[59] T. Gehring, V. Handchen, J. Duhme, F. Furrer, T. Franz, C. Pacher, R. F. Werner, and R. Schnabel, "Implementation of continuous-variable quantum key distribution with composable and one-sided-device-independent security against coherent attacks," *Nature Communications*, vol. 6, p. 8795, 2015.

[60] F. Furrer, T. Gehring, C. Schaffner, C. Pacher, R. Schnabel, and S. Wehner, "Continuous-variable protocol for oblivious transfer in the noisy-storage model," *Nature Communications*, vol. 9, no. 1, 2018.

[61] D. Gottesman, A. Kitaev, and J. Preskill, "Encoding a qubit in an oscillator," *Phys. Rev. A*, vol. **64**, 2001.

[62] N. C. Menicucci, "Fault-tolerant measurement-based quantum computing with continuous-variable cluster states," *Phys. Rev. Lett.*, vol. **112**, 2014.

[63] K. Marshall, C. S. Jacobsen, C. Schäfermeier, T. Gehring, C. Weedbrook, and U. L. Andersen, "Continuous-variable quantum computing on encrypted data," *Nature Communications*, vol. 7, p. 13795, 2016.

[64] S. Yokoyama, R. Ukai, S. C. Armstrong, C. Sornphiphatphong, T. Kaji, S. Suzuki, J.-I. Yoshikawa, H. Yonezawa, N. C. Menicucci, and A. Furusawa, "Ultra-large-scale continuous-variable cluster states multiplexed in the time domain," *Nature Photonics*, vol. 7, pp. 982–986, 2013.

[65] M. V. Larsen, X. Guo, C. R. Breum, J. S. Neergaard-Nielsen, and U. L. Andersen, "Deterministic generation of a two-dimensional cluster state," *Science*, vol. 366, no. 6463, pp. 369–372, 2019.

[66] M. Chen, N. C. Menicucci, and O. Pfister, "Experimental realization of multipartite entanglement of 60 modes of a quantum optical frequency comb," *Phys. Rev. Lett.*, vol. 112, p. 120505, 2014.

[67] H. Vahlbruch, M. Mehmet, K. Danzmann, and R. Schnabel, "Detection of 15 db squeezed states of light and their application for the absolute calibration of photoelectric quantum efficiency," *Phys. Rev. Lett.*, vol. **117**, 2016.

[68] Y. Takeno, M. Yukawa, H. Yonezawa, and A. Furusawa, "Observation of -9 dB quadrature squeezing with improvement of phase stability in homodyne measurement," *Optics Express*, vol. 15, no. 7, pp. 4321–7, 2007.

[69] T. Eberle, S. Steinlechner, J. Bauchrowitz, V. Händchen, H. Vahlbruch, M. Mehmet, H. Müller-Ebhardt, and R. Schnabel, "Quantum Enhancement of the Zero-Area Sagnac Interferometer Topology for Gravitational Wave Detection," *Physical Review Letters*, vol. 104, no. 25, p. 251102, 2010.

[70] M. Mehmet, S. Ast, T. Eberle, S. Steinlechner, H. Vahlbruch, and R. Schnabel, "Squeezed light at 1550 nm with a quantum noise reduction of 12.3 db," *Opt. Express*, vol. **19**, no. 25, 2011.

[71] S. Shi, Y. Wang, W. Yang, Y. Zheng, and K. Peng, "Detection and perfect fitting of 13.2 dB squeezed vacuum states by considering green-light-induced infrared absorption," *Optics Letters*, vol. 43, no. 21, p. 5411, 2018.

[72] A. Schönbeck, F. Thies, and R. Schnabel, "13 db squeezed vacuum states at 1550 nm from 12 mw external pump power at 775 nm," *Opt. Lett.*, vol. 43, no. 1, pp. 110–113, 2018.

[73] F. Mondain, T. Lunghi, A. Zavatta, É. Gouzien, F. Doutre, M. De Micheli, S. Tanzilli, and V. D'Auria, "Chip-based squeezing at a telecom wavelength," *Photonics Research*, vol. 7, no. 7, pp. 36–39, 2019.

[74] N. Takanashi, T. Kashiwazaki, T. Kazama, K. Enbutsu, R. Kasahara, T. Umeki, and A. Furusawa, "Detection of 3-dB continuous-wave squeezing at 1.55 um from a fiber-coupled single-pass PPLN ridge waveguide," *arXiv*, p. 1906.09749, 2019.

[75] M. Stefszky, R. Ricken, C. Eigner, V. Quiring, H. Herrmann, and C. Silberhorn, "A waveguide cavity resonator source of squeezing," *Physical Review Applied*, vol. 7, p. 044026, 2017.

[76] A. Dutt, K. Luke, S. Manipatruni, A. L. Gaeta, P. Nussenzveig, and M. Lipson, "On-chip optical squeezing," *Phys. Rev. Applied*, vol. 3, p. 044005, 2015.

[77] V. D. Vaidya, B. Morrison, L. G. Helt, R. Shahrokhshahi, D. H. Mahler, M. J. Collins, K. Tan, J. Lavoie, A. Repingon, M. Menotti, N. Quesada, R. C. Pooser, A. E. Lita, T. Gerrits, S. W. Nam, and Z. Vernon, "Broadband quadrature-squeezed vacuum and nonclassical photon number correlations from a nanophotonic device," *arXiv e-prints*, p. arXiv:1904.07833, 2019.

[78] A. Otterpohl, F. Sedlmeir, G. Shafiee, T. Dirmeier, U. Vogl, G. Schunk, D. V. Strekalov, H. G. Schwefel, T. Gehring, U. L. Andersen, G. Leuchs, and C. Marquardt, "Squeezed vacuum states from a whispering gallery mode resonator," *arXiv*, p. 1905.07955, 2019.

[79] C. Peuntinger, B. Heim, C. R. Müller, C. Gabriel, C. Marquardt, and G. Leuchs, "Distribution of squeezed states through an atmospheric channel," *Physical Review Letters*, vol. 113, p. 060502, 2014.

[80] H. Vahlbruch, A. Khalaidovski, N. Lastzka, C. Gräf, K. Danzmann, and R. Schnabel, "The GEO 600 squeezed light source," *Classical and Quantum Gravity*, vol. 27, no. 8, 2010.

[81] A. Schönbeck, *Compact squeezed-light source at 1550 nm.* PhD thesis, Fakultät für Mathematik, Informatik und Naturwissenschaften Fachbereich Physik der Universit ät Hamburg, 2018.

[82] Y.-J. Wang, W.-H. Yang, Y.-H. Zheng, and K.-C. Peng, "A compact einstein–podolsky–rosen entangled light source," *Chinese Physics B*, vol. 24, no. 7, p. 070303, 2015.

[83] T. Aoki, G. Takahashi, and A. Furusawa, "Squeezing at 946nm with periodically poled ktiopo4," *Optics Express*, vol. 14, no. 15, pp. 6930–6935, 2006.

[84] J. Steinlechner, S. Ast, C. Krüger, A. P. Singh, T. Eberle, V. Händchen, and R. Schnabel, "Absorption measurements of periodically poled potassium titanyl phosphate (ppktp) at 775 nm and 1550 nm," *Sensors*, vol. 13, no. 1, pp. 565–573, 2013.

[85] S. E. Dwyer, *Quantum noise reduction using squeezed states in LIGO.* PhD thesis, Massachusetts Institute of Technology, 2013.

[86] K. McKenzie, *Squeezing in the Audio Gravitational Wave Detection Band.* PhD thesis, Australian National University, 2008.

[87] A. A. Berni, *Continuous Variables Quantum Information in Noisy Environments.* PhD thesis, Technical University of Denmark, 2014.

[88] V. Giovannetti, S. Lloyd, and L. Maccone, "Quantum metrology," *Phys. Rev. Lett.*, vol. 96, p. 010401, 2006.

[89] S. Slussarenko, M. Weston, H. Chrzanowski, L. Shalm, V. Verma, S. Nam, and G. Pryde, "Unconditional violation of the shot noise limit in photonic quantum metrology," *Nature Photonics*, vol. 11, 2017.

[90] K. Edamatsu, R. Shimizu, and T. Itoh, "Measurement of the photonic de broglie wavelength of entangled photon pairs generated by spontaneous parametric down-conversion," *Phys. Rev. Lett.*, vol. 89, p. 213601, 2002.

[91] M. Hiekkamäki, F. Bouchard, and R. Fickler, "Photonic angular super-resolution using twisted N00N states," *arXiv e-prints*, p. arXiv:2106.09273, 2021.

[92] K. J. Resch, K. L. Pregnell, R. Prevedel, A. Gilchrist, G. J. Pryde, J. L. O. Brien, and A. G. White, "Time-Reversal and Super-Resolving Phase Measurements," *Phys. Rev. Lett.*, vol. 223601, no. JUNE, pp. 2–5, 2007.

[93] A. Berni, T. Gehring, B. Nielsen, V. Händchen, M. Paris, and U. Andersen, "Ab initio quantum-enhanced optical phase estimation using real-time feedback control," *Nature Photonics*, vol. 9, no. 9, pp. 577–582, 2015.

[94] A. Monras, "Optimal phase measurements with pure gaussian states," *Phys. Rev. A*, vol. 73, p. 033821, 2006.

[95] L. Pezzé, A. Smerzi, G. Khoury, J. F. Hodelin, and D. Bouwmeester, "Phase detection at the quantum limit with multiphoton mach-zehnder interferometry," *Phys. Rev. Lett.*, vol. 99, p. 223602, 2007.

[96] C. W. Helstrom, "Quantum detection and estimation theory," *Journal of Statistical Physics*, vol. 1, no. 2, pp. 231–252, 1969.

[97] C. Caves, "Quantum-mechanical noise in an interferometer," *Physical Review D*, vol. 23, no. 8, pp. 1693–1708, 1981.

[98] S. L. Braunstein and C. M. Caves, "Statistical distance and the geometry of quantum states," *Physical Review Letters*, vol. 72, no. 22, pp. 3439–3443, 1994.

[99] V. Giovannetti, S. Lloyd, and L. MacCone, "Advances in quantum metrology," *Nature Photonics*, vol. 5, no. 4, pp. 222–229, 2011.

[100] R. Demkowicz-Dobrzański, M. Jarzyna, and J. Kołodyński, "Quantum Limits in Optical Interferometry," *Progress in Optics*, vol. 60, pp. 345–435, 2015.

[101] J. P. Dowling, "Quantum optical metrology – the lowdown on high-n00n states," *Contemporary Physics*, vol. 49, no. 2, pp. 125–143, 2008.

[102] M. W. Mitchell, J. S. Lundeen, and A. M. Steinberg, "Super-resolving phase measurements with a multiphoton entangled state," *Nature*, vol. 429, no. 6988, pp. 161–164, 2004.

[103] P. Walther, J.-W. Pan, M. Aspelmeyer, R. Ursin, S. Gasparoni, and A. Zeilinger, "De Broglie wavelength of a non-local four-photon state," *Nature*, vol. 429, no. 6988, pp. 158–161, 2004.

[104] T. Nagata, R. Okamoto, J. L. O'Brien, K. Sasaki, and S. Takeuchi, "Beating the standard quantum limit with four-entangled photons," *Science*, vol. 316, no. 5825, pp. 726–729, 2007.

[105] S. Daryanoosh, S. Slussarenko, D. W. Berry, H. M. Wiseman, and G. J. Pryde, "Experimental optical phase measurement approaching the exact Heisenberg limit," *Nature Communications*, vol. 9, no. 1, pp. 1–6, 2018.

[106] W.-b. Gao, C.-y. Lu, X.-c. Yao, P. Xu, O. Gühne, A. Goebel, Y.-a. Chen, C.-z. Peng, Z.-b. Chen, and J.-w. Pan, "Experimental demonstration of a hyper-entangled ten-qubit Schrödinger cat state," *Nature Physics*, vol. 6, no. March, pp. 331–335, 2010.

[107] X.-L. Wang, L.-K. Chen, W. Li, H.-L. Huang, C. Liu, C. Chen, Y.-H. Luo, Z.-E. Su, D. Wu, Z.-D. Li, H. Lu, Y. Hu, X. Jiang, C.-Z. Peng, L. Li, N.-L. Liu, Y.-A. Chen, C.-Y. Lu, and J.-W. Pan, "Experimental ten-photon entanglement," *Phys. Rev. Lett.*, vol. 117, p. 210502, 2016.

[108] M. Aspachs, J. Calsamiglia, R. Muñoz-Tapia, and E. Bagan, "Phase estimation for thermal Gaussian states," *Physical Review A - Atomic, Molecular, and Optical Physics*, vol. 79, no. 3, 2009.

[109] O. Pinel, J. Fade, D. Braun, P. Jian, N. Treps, and C. Fabre, "Ultimate sensitivity of precision measurements with intense gaussian quantum light: A multimodal approach," *Phys. Rev. A*, vol. 85, p. 010101, 2012.

[110] P. Grangier, R. E. Slusher, B. Yurke, and A. LaPorta, "Squeezed-light–enhanced polarization interferometer," *Phys. Rev. Lett.*, vol. 59, pp. 2153–2156, 1987.

[111] K. McKenzie, D. A. Shaddock, D. E. McClelland, B. C. Buchler, and P. K. Lam, "Experimental demonstration of a squeezing-enhanced power-recycled michelson interferometer for gravitational wave detection," *Phys. Rev. Lett.*, vol. 88, p. 231102, 2002.

[112] S. Pradyumna, E. Losero, I. Ruo-Berchera, P. Traina, M. Zucco, C. Jacobsen, U. Andersen, I. Degiovanni, M. Genovese, and T. Gehring, "Twin beam quantum-enhanced correlated interferometry for testing fundamental physics," *Communications Physics*, vol. 3, no. 1, 2020.

[113] B. J. Lawrie, P. D. Lett, A. M. Marino, and R. C. Pooser, "Quantum sensing with squeezed light," *ACS Photonics*, vol. 6, no. 6, pp. 1307–1318, 2019.

[114] P. M. Anisimov, G. M. Raterman, A. Chiruvelli, W. N. Plick, S. D. Huver, H. Lee, and J. P. Dowling, "Quantum metrology with two-mode squeezed vacuum: Parity detection beats the heisenberg limit," *Phys. Rev. Lett.*, vol. 104, p. 103602, 2010.

[115] B. L. Higgins, D. W. Berry, S. D. Bartlett, H. M. Wiseman, and G. J. Pryde, "Entanglement-free Heisenberg-limited phase estimation," *Nature*, vol. 450, no. 7168, pp. 393–396, 2007.

[116] J. Borregaard, "Super sensitivity and super resolution with quantum teleportation," *npj Quantum Information*, no. July 2018, pp. 1–6, 2019.

[117] M. P. Landry, P. M. Mccall, Z. Qi, and Y. R. Chemla, "Characterization of Photoactivated Singlet Oxygen Damage in Single-Molecule Optical Trap Experiments," *Biophysj*, vol. 97, no. 8, pp. 2128–2136, 2009.

[118] S. Wäldchen, J. Lehmann, T. Klein, S. V. D. Linde, and M. Sauer, "Light-induced cell damage in live- cell super-resolution microscopy," *Nature Publishing Group*, pp. 1–12, 2015.

[119] J. J. Meyer, J. Borregaard, and J. Eisert, "A variational toolbox for quantum multiparameter estimation," *npj Quantum Information*, vol. 7, p. 89, 2021.

[120] M. Cerezo, A. Arrasmith, R. Babbush, S. C. Benjamin, S. Endo, K. Fujii, J. R. McClean, K. Mitarai, X. Yuan, L. Cincio, and P. J. Coles, "Variational Quantum Algorithms," *arXiv e-prints*, p. arXiv:2012.09265, 2020.

[121] A. Peruzzo, J. McClean, P. Shadbolt, M.-H. Yung, X.-Q. Zhou, P. J. Love, A. Aspuru-Guzik, and J. L. O'Brien, "A variational eigenvalue solver on a photonic quantum processor," *Nature Communications*, vol. 5, p. 4213, 2014.

[122] B. Koczor, S. Endo, T. Jones, Y. Matsuzaki, and S. C. Benjamin, "Variational-state quantum metrology," *New Journal of Physics*, vol. 22, no. 8, p. 083038, 2020.

[123] X. Guo, C. Breum, J. Borregaard, S. Izumi, M. Larsen, T. Gehring, M. Christandl, J. Neergaard-Nielsen, and U. Andersen, "Distributed quantum sensing in a continuous variable entangled network," *Nature Physics*, vol. 16, p. 281–284, 2020.

[124] M. Schuld, V. Bergholm, C. Gogolin, J. Izaac, and N. Killoran, "Evaluating analytic gradients on quantum hardware," *Phys. Rev. A*, vol. 99, p. 032331, 2019.